The role of radiation in the nocturnal boundary layer : the origin of the lifted temperature minimum

A Thesis
Submitted for the Degree of
Doctor of Philosophy

by

V.K.Ponnulakshmi

Engineering Mechanics Unit
Jawaharlal Nehru Centre for Advanced Scientific Research
(A Deemed University)
Bangalore – 560 064

FEBRUARY 2014

Family and Suryakanthi

DECLARATION

I hereby declare that the matter embodied in the thesis entitled "**The role of radiation in the nocturnal boundary layer : the origin of the lifted temperature minimum**" is the result of investigations carried out by me at the Engineering Mechanics Unit, Jawaharlal Nehru Centre for Advanced Scientific Research, Bangalore, India under the supervision of **Prof. Ganesh Subramanian** and that it has not been submitted elsewhere for the award of any degree or diploma.

In keeping with the general practice in reporting scientific observations, due acknowledgment has been made whenever the work described is based on the findings of other investigators.

V.K.Ponnulakshmi

CERTIFICATE

I hereby certify that the matter embodied in this thesis entitled "**The role of radiation in the nocturnal boundary layer : the origin of the lifted temperature minimum**" has been carried out by **Ms. V.K.Ponnulakshmi** at the Engineering Mechanics Unit, Jawaharlal Nehru Centre for Advanced Scientific Research, Bangalore, India under my supervision and that it has not been submitted elsewhere for the award of any degree or diploma.

Prof. Ganesh Subramanian
(Research Supervisor)

Acknowledgements

I owe my deepest gratitude to *Prof. Ganesh subramanian* for his constant encouragement and support. His deep physical and mathematical understanding, dedication to research and teaching is a great source of inspiration . His immense patience with me helped me to pass through difficult times. His friendly nature and advice on all fronts helped me a lot. I take this opportunity to thank his family members for their support.

I am grateful to Prof. K.R.Sreenivas for fruitful discussions and his heat transfer course. I would like to thank him for the financial assistance that helped me to attend the summer school.

I am grateful to *Prof. Rama Govindarajan* for her course on fluid mechanics and her pep talks that helped me to manage both my family and research.

I thank *Prof. Ansumali* for discussions on Brownian dynamics. I thank him for his financial support towards the end of my PhD.

I thank *Prof. Mehaboob Alam* for his course on Mathematics which benefited me a lot.

I thank J.Sreenivasan, Prof. Joseph Mathew, Prof. O.N.Ramesh for their course which was stimulating and very helpful.

I thank *Mukund* and *Dhiraj* for discussions on experiments and their deep understanding of the problem helped me a lot.

My life in JNC was memorable because of emuites. It is my honor to thank everyone. 'Non stop non-sense FM' Ratul dasgupta - for all the advice and fundes, 'baby hungry dinosaur'Anubhab Roy for entertainment, discussions and "senior" advice, 'Mr. Perfect' Sumesh P.T. for all discussions ranging from fluid mechanics to personal, 'Grandpa' Harish - introducing me to matlab, Gayathri akka to introduce me to jnc, Vivek for being a good friend, good times with Raja, Rajaram, Priyanka,Ashish Malik, Vineetha Snehalatha - for constant support and love, standing by my side all the times and teaching me Maths, Aditya, Vivek N.P for weekend experiments and funny chasing all around EMU, Bale for group study and teasing, Rakshith, Kopal, Dinesh, 'Hermite'Ujjayan and Vinay for fun times, Srikanth for all the discussions, 'Jumping post-doc' Vishwanath shastry Saikishan - for discussions on Indian cricket team and CSK, PP for his funde sorry 'opinions' 'Dude of Jnc' Rajesh , Tank Jose, 'Care taker' Rohith Navaneeth Cheta, 'Captain' Milind Mamta, 'Comrade' Sunil, shashank, Siddharth, Vybhav, Deepthi for being wonderful friend, Rashmi - a great source of inspiration (I learnt a lot from her to manage research and family), Deepak - a good brother and in the last day helping me to take thesis print-outs and for his songs, 'item song' Chakri, Paaji, Shiwani, Manjusha, Reddy,Saikat, Ramki shajahan and Ansari for fun times, 'KD' Sankalp, Pheriphery walking partner Vicky, Reddy, Rahul Karyappa, Tapan, Lavanya, Vivek Raja, Mirunalini, Charu and Chandra Prakash are few to mention. I thank all my other JNC friends.

I thank JNC for giving me best friends and advisor. Rekha, Sree and Thanuja for being very supportive, caring, roaming around places in bangalore and helping me in all the situations.

I thank Senjuiti, Priyanka Sen and Aswathy for good food, fun times and making my life happy.

I thank my yoga teacher Rajeshwari for being very supportive.

I thank our Administrative officer, admin staff, academic staff especially Sukanya from various help from time to time. I thank JNC bus drivers and other members of JNC community to make my life easy in jnc. I acknowledge ISAC-CNR and IRS 2010 for providing me with financial assistance which helped me to attend conferences.

I thank JNC and DST for providing me all the financial and infrastructural support to pursue my PhD here and I am sincerely grateful to them.

Finally nothing would have been possible with out support from my family members. I am indebted to them.

Abstract

The nocturnal boundary layer(NBL) that develops over land is important in weather forecasting, climate modeling and in the dispersion of pollutants. Physical transport mechanisms such as radiation and turbulence play a strong role in the formation and evolution of the NBL as characterized by the vertical temperature profile above the ground. Characterizing radiation and its interaction with other transport processes(such as turbulence, advection, subsidence etc.), and the effect of these interactions on the thermal structure of the NBL, is not yet fully understood. In this thesis, we mainly address the issue of frequency parameterization in modeling radiation over a surface with arbitrary emissivity and varying directional characteristics. Further, we discuss in detail, the implication of this issue with regard to the origin of a specific micrometeorological phenomenon called the Ramdas layer; a phenomenon that concerns the radiation-driven non-monotonic vertical distribution of temperature in the lowest decimeters of air on calm clear nights.

Frequency-parameterized radiation schemes

Modeling radiative transfer in a gaseous participating medium in general is very complex owing to (a) the non-local and directional nature of radiant energy transport by photons, (b) the absorption and emission processes being very sensitively dependent on wavelength, and (c) the radiative inhomogeneity of the path through which the photon travels (owing to the variation of the absorption characteristics of the participating medium with temperature and pressure). Radiative parameterization aims to provide a simple, accurate and efficient method of calculating radiative fluxes by suitable approximation of one or more of the above aspects.

Frequency-parameterized radiative transfer schemes are often employed to model infrared radiative exchanges in the atmosphere. At the coarsest level in frequency parameterization are computationally efficient broadband schemes. The central quantity in such schemes is the flux-emissivity which may be interpreted as the emissivity of an isothermal column of the participating medium. These schemes have mostly been used for cases where the bounding surfaces are radiatively black. An extension of the above formulation to non-black surfaces (ground in the NBL context) that has often been used to analyze the NBL, employs the surface emissivity to divide the up-welling flux into emission and reflection contributions, each of which is attenuated by the complement of the flux-emissivity. This naive extension, developed by an analogy with the emission of solid surfaces, is erroneous, however. It is shown here that such an extension leads to a spurious near-surface cooling in the opaque bands. The error occurs because of an incorrect transmissivity used in the aforementioned extension which attributes a fraction of energy in the reflected radiation, in the opaque bands, to the transparent bands, allowing it to escape to the

upper atmosphere and beyond. The surface emissivity enters the formulation in a more subtle manner, and we present the correct emissivity scheme for non-black surfaces that eliminates the spurious cooling. The correct formulation is then used to examine the thermal structure of the NBL. It is shown that earlier studies which attempt to study the influence of the ground emissivity on NBL temperature profiles have exaggerated the effect of the ground emissivity on the radiative cooling-rate profiles due to the aforementioned intense spurious cooling contribution. The correct formulation predicts only a modest, and more importantly, a qualitatively different dependence of the NBL temperature profile on the ground emissivity. The basic emissivity scheme is then extended to allow for a non-isothermal atmosphere, multiple reflections between a pair of reflective surfaces (a configuration commonly employed in laboratory experiments, and also of relevance to cloudy atmospheres), and an angular dependence of the radiant intensity. This later generalization enables one to rigorously account for the directional characteristics of surface emission and reflection and thereby avoids the use of a diffusivity factor approximation. Finally, it is argued that the extension, based on the analogy with solid surfaces, leads to an error in any frequency-parameterized scheme, involving non-black emitting surfaces, and that does not fully resolve the emission spectrum of the participating medium. Earlier narrow-band calculations affected by this error are discussed, and the inherent superiority of the correlated-k method in this regard is highlighted.

The Ramdas layer

The near-surface vertical distribution of air temperature in the atmosphere is an important aspect of studies in agricultural and boundary layer meteorology. The Ramdas layer concerns the formation of an elevated minimum in the vertical temperature profile within the NBL, and thereby, defies the traditional notion of a post-sunset inversion layer where the ground is at the lowest temperature. On calm and cloudless nights the temperature minimum occurs a few decimeters above the ground. It is the resulting layer of cold air that is referred to as the Ramdas layer; the phenomenon is also known as the lifted temperature minimum(LTM). That the layer is colder than the ground and other layers in its neighborhood, suggests that the phenomenon must be radiative in origin.

The prevailing explanation for this counter-intuitive phenomenon is based on the naive extension of the broadband flux-emissivity scheme to gray surfaces, described above. The model predicts an LTM to occur only over a non-black surface and in a homogeneous night-time atmosphere (here, homogeneity implies compositional homogeneity of water vapor, the principal radiatively participating component) due to the aforementioned spurious cooling. However, our study based on the correct formulation conclusively shows that such a preferential cooling cannot occur in a homogeneous atmosphere. The implication is that an inhomogeneity on the length scale of the Ramdas layer is necessary to explain this phenomenon. The heterogeneity is proposed to arise from the presence of a varying aerosol concentration near the ground. Lab experiments [1], which have recently examined the radiative forcing as a function of the varying

[1]The laboratory experiments have been carried out by another group and those details are not discussed in this thesis which solely focusses on modeling the experimental observations. Experimental details are presented in Mukund et al, 2010, *Phys.Scripta*, T142,014041 and Mukund et al, 2013, *Quart.J.Roy.meteor.Soc, in press,DOI:*

heterogeneity of the participating medium, strongly support this hypothesis.

To study the radiative forcing by the aforementioned heterogeneity due to suspended aerosol particles, a first set of experiments has been carried out in the traditional two plate geometry (used for the classical Rayleigh-Benard problem) wherein the plates are maintained at (different) constant temperatures corresponding to a stable stratification. For this configuration, fixing the plate temperatures also fixes the radiative boundary conditions. This is unlike the LTM where the radiative boundary conditions are decoupled from the boundary conditions driving the local heat transfer processes (conduction and convection). The radiative-conductive equilibria obtained with unfiltered air exhibit a pronounced deviation from the linear conduction profile in comparison to earlier studies, and more importantly, the nature of the deviation is crucially dependent on the plate emissivities. The theoretical temperature profiles are obtained from a solution of the energy equation in a radiatively inhomogeneous medium, with radiation being modelled using the Milne-Eddington approximation. The theoretical equilibria compare well with the experiments for an absorptivity stratification arising from an assumed exponential distribution of aerosol particles.

A second set of experiments attempts to mimic the LTM conditions in the atmosphere. Towards this end, a cold source is added to the two-plate configuration that interacts with the aerosol-laden air-layers via the transparent upper plate. The addition of a separate source helps decouple the radiative and conductive boundary conditions which is crucial to the formation of the LTM without violating the second law of thermodynamics. With this decoupling, the experiments could successfully simulate LTM on the laboratory scales. We have modelled this theoretically in a manner similar to that described above for the two-plate experiments, and the predicted radiative conductive equilibrium profiles compare well with experimental observations, again for an exponential distribution of aerosol particles.

The role of the aerosol-induced heterogeneity is then re-examined in the atmospheric context. Based on the relative magnitudes of the ground and (aerosol-laden)air cooling rates, a non dimensional number called the Ramdas-Zdunkowski factor (R_f) is defined and is expected to discriminate between inversion and LTM-type profiles. Motivated by the laboratory context, we model the radiative response of a concentrated (yet optically transparent) aerosol layer near the ground based on a Newtonian cooling approximation. The solution of the governing equations is shown to depend on two dimensionless parameters - the surface emissivity and the Ramdas-Zdunkowski factor. However, the sign of the radiative slip at the ground is shown to be governed almost entirely by R_f. Next, we include the effect of conduction that smears out the radiative slip, and leads to a lifted temperature minimum. For small R_f, conduction retards the transition from an inversion to an LTM-type profile. Finally, we carry out dynamic simulations, based on the flux-emissivity formulation for an inhomogeneous aerosol-laden atmosphere, to examine the evolution of the vertical temperature profile starting from an initial lapse-rate profile at sunset. In the absence of aerosols, as expected on physical grounds, water-vapor-driven cooling leads to a monotonic variation of the temperature in the lowest decimeters. The inclusion of the aerosol contribution shows that an LTM-type profile emerges above a threshold concentration that corresponds to an R_f value of order unity.

10.1002/qj.2113

Nomenclature

α_L	Line width
α_p	Emissivity of the polythene sheet
α_w	Absorption coefficient in window band
α_{nw}	Absorption coefficient in non-window band
$\bar{T_v}$	mean virtual temperature
β	diffusivity factor ≈ 1.66 (Chapter 1)
β	surrogate cooling rate (Chapter 5)
χ	ratio of radiative to thermal conductivities $\chi = \frac{\sigma T_g^3}{[\rho_w(0)\dot{\epsilon}^f_{nw}(0)k]}$
ΔT	strength of the inversion layer
δ	Thermodynamic scaling exponent
ϵ	non-isothermal emissivity for ground emission
$\epsilon^f(u)$	Isothermal broadband flux transmissivity as a function of height
$\epsilon^f(u)$	Isothermal broadband flux-emissivity as a function of height
ϵ_g	emissivity of cloud
ϵ_g	ground emissivity
$\epsilon_{g-crossover}$	crossover emissivity
$\epsilon_{g\nu}(\Omega)$	directional spectral surface emissivity
η	ratio of radiative to conductive fluxes $\frac{\sigma T_c^4 h}{k(T_1 - T_0)}$.
η_a	Ratio of initial conductive flux in air to emission from ground $= \frac{\frac{k_a T_{g0}}{H}}{\sigma T_{g0}^4}$
η_s	Ratio of initial conductive flux in soil to emission from ground $= \frac{\frac{k_s T_{g0}}{H}}{\sigma T_{g0}^4}$

$\frac{g}{T_v}$	buoyancy parameter
Γ	adiabatic lapse rate $= -9.8\,\mathrm{Kkm}^{-1}$
$\hat{\alpha}$	optical thickness based on the test section height
$\hat{\epsilon}$	non-isothermal emissivity for reflected flux
$\hat{A}$	non-isothermal absorptivity for reflected flux
κ_s	thermal diffusivity of soil
μ	Ratio of radiative time scale to the conductive time scale in soil
μ	cosθ
μ_1	Ratio of radiative time scale to the conductive time scale in air
Ω	solid angle
Ω_d	diurnal frequency
ψ	normalized total flux in the medium.
ρ	Concentration of the participating medium
ρ	Density of air
ρ_c	reflectivity of cloud
ρ_g	reflectivity of ground
$\rho_s C_{ps}$	soil heat capacity
ρ_s	reflectivity of a diffuse surface
ρ_s	reflectivity of a specular surface
ρ_w	density of water vapor
$\rho_{g\nu\Omega'\to\Omega}$	bidirectional spectral reflectivity
σ	Stefen-Boltzmann constant
$\tau_{aerosol}$	flux transmissivity of aerosol laden-atmosphere
τ_{rad}	radiative relaxation time
τ_{wv}	flux transmissivity of water-vapor-laden-atmosphere
f	Coriolis parameter
h	Planck's constant
k	Boltzmann's constant

k	Von Karman constant
θ	Mean potential temperature
θ'	temperature fluctuation.
θ_a	Normalized temperature profile in air
θ_s	Normalized temperature profile in soil
$\varrho^{aero}C_p^{aero}$	Heat capacity of aersol particles
ζ_0	Ratio of aerosol radiative cooling to water vapor heating contribution$\zeta_0 = \frac{f_w Q_{ext} An(0)}{[(1-f_w)\rho_w(0)\dot{\epsilon}_{nw}^f(0)]}$
A	non-isothermal absorptivity for ground emission
B_j	Planck function in band j
$B\nu$	Planck source function
c_o	speed of light in vacuum
C_p	specific heat capacity at constant pressure
F	Net radiative flux
$F^{\downarrow}$	Total downward flux
$F_a^{\downarrow}(u)$	the cumulative upward emission of air layers in the interval u and u_t
$F^{\uparrow}$	Total upward flux
$F_a^{\uparrow}(u)$	the cumulative upward emission of air layers in the interval $(0, u)$
$F_{eg}^{\uparrow}(u)$	Ground emission which is attenuated by the participating medium that reaches level u
$F_{rg}^{\uparrow}(u)$	Upwelling reflected flux that reaches level u
F_s	net radiative flux from the surface
f_w	fractions of the total radiant energy in the window band
f_{nw}	fractions of the total radiant energy in the non-window band
g	acceleration due to gravity
H	Scale height
H	scale height of aerosol concentration layer
h	height of the test section height
I_ν	Monochromatic intensity

k_a	thermal conductivity of air
k_s	thermal conductivity of soil
k_s	thermal conductivity of soil
$k\nu$	absorption coefficient corresponding to the frequency ν
L	Obukhov length scale
M	Total number of bands
$m^{aero}C_p^{aero}$	heat capacity of the aerosol particle
n	refractive index
$n(u)$	aerosol concentration profile
nA	specific interfacial area of a particle
nV	volume fraction
p	pressure (Nm^{-2})
Q_{ext}	extinction efficiency
R	Non dimensional temperature profile $R(z) = \frac{T}{T_g}$
R_f	Ramdas-Zdunkowski factor
Ra_R	Radiative Rayleigh number
Ri	Richardson number
Ri_c	Critical Richardson number = 0.25
S	Line intensity
T	Temperature (K)
T_*	Characteristic temperature scale $T_* = \dfrac{-\overline{w'\theta'}}{u_*}$.
T_g	ground temperature
T_s	soil temperature
T_{g0}	temperature of initial isothermal atmosphere
T_{rad}	radiative equilibrium temperature
T_{sky}	effective outer-space temperature
T_{sky}	temperature of the radiative sink
u	scaled absorber amount

u', w'	Turbulent velocities in the horizontal and vertical directions.
u, v	Two horizontal velocity components
u_*	The frictional velocity $u_* = -\sqrt{\overline{(u'w')}_0}$
u_g, v_g	Components of the geostrophic wind speed
u_t	scale height of the participating medium
z	vertical coordinate
Z_d	penetration depth
z_t	total height of the atmosphere

List of Figures

List of Tables

Contents

Chapter 1

Introduction

Radiant energy transfer through participating media that can absorb, emit and scatter radiation is important in a wide range of fields such as furnaces [Hottel & Egbert (1941)], engine combustion chambers at high pressures and temperatures [Viskanta & Mengüç (1987)], rocket propulsion, hypersonic shock layers [Vincenti & Traugott (1971)], glass manufacturing [Frank & Klar (2011)] and the earth's atmosphere [Goody (1964); Siegel & Howell (2002)]. In general, in a rigorous analysis of radiation in any physical situation, one has to account for the directional nature of the photon trajectories, the spectral dependence of the participating medium and variation of the absorption characteristics of the participating medium with pressure and temperature which may vary from one point to another in the domain of interest. Radiation parameterization essentially revolves around the suitable approximation of one or more of the aforementioned features, thereby providing an efficient yet accurate method of calculating the radiative fluxes and flux divergences (cooling rates).

1.1 Radiative transfer equation

The amount of energy passing in a given direction is expressed in terms of the *intensity of radiation* [Sparrow & Cess (1967)]. Intensity (I_ν) is basically the radiant energy leaving a surface in a given direction, per unit area *normal* to the pencil of rays in that direction, per unit solid angle and per unit time. The energy flux from the surface into the hemispherical space above can be obtained by

$$F_\nu = \int_\Omega I_\nu cos\theta d\Omega \tag{1.1}$$

where $\Omega \equiv (\theta, \phi)$ denotes the direction on the unit sphere with $d\Omega = -d\mu d\phi$ being the differential solid angle element, and $\mu = \cos\theta$; $\cos\theta d\Omega$ is the differential element projected normal to the pencil of rays.

The intensity of a pencil of radiation traversing a medium is usually changed by its interaction with matter. If the change in intensity in a given direction, after travelling a distance ds through a medium is given by dI_ν, then this change may be attributed to the following physical mechanisms [Sparrow & Cess (1967)]:

1. Attenuation due to both absorption and scattering.
2. Augmentation as a result of emission from the elemental volume.
3. Augmentation by energy scattered, from all incident beams of energy, into the given direction.

If one neglects the effects of scattering, and considers the system to be in local-thermodynamic

equilibrium (LTE) [1] then,

$$\frac{dI_\nu}{ds} = k_\nu(B_\nu - I_\nu), \tag{1.2}$$

where B_ν is the Planck source function and k_ν is the absorption coefficient corresponding to the frequency ν. For a system in local thermodynamic equilibrium, the emission depends only on the absolute temperature (T) and the frequency (ν). The spectral distribution function of emission is completely characterized by the Planck function given by [Sparrow & Cess (1967)]:

$$B_\nu = \frac{2\pi h\nu^3 n^2}{c_o^2(e^{\frac{h\nu}{kT}} - 1)} \tag{1.3}$$

where c_o is the speed of light in vacuum, n is the refractive index, k is Boltzmann's constant and h is Planck's constant.

For a plane-parallel formulation, the medium is assumed to be infinite in the horizontal direction and homogeneous and hence, the radiant intensities and fluxes are function of the vertical coordinate z only. The intensity of radiation can be divided into two contributions: the intensity directed along the upper hemisphere is denoted as $I_\nu^\uparrow(\Omega, z)$ and that directed along the lower hemisphere is denoted as $I_\nu^\downarrow(\Omega, z)$. The above equation, written as a differential equation in the vertical coordinate z, by relating the differential element dz to the differential arc length ds as $ds = \frac{dz}{\cos\theta}$, can be solved with the boundary conditions:

$$I_\nu^\uparrow(z, \Omega) = I_\nu^\uparrow(0, \Omega), \tag{1.4}$$

$$I_\nu^\downarrow(z, \Omega) = I_\nu^\downarrow(z_t, \Omega), \tag{1.5}$$

where $I_\nu^\uparrow(0, \Omega)$ and $I_\nu^\downarrow(z_t, \Omega)$ are the radiosities [2] emanating from the boundaries at $z = 0$ and $z = z_t$, and include both the surface emission and reflection. For a cloud-free atmosphere the boundary conditions are:

$$I_\nu^\uparrow(0, \Omega) = \underbrace{\epsilon_{g\nu}(\Omega)B_\nu(z = 0) + \int_{\Omega'} \mu' d\Omega' \rho_{g\nu\Omega'\to\Omega} I_\nu^\downarrow(z = 0, \Omega')}_{\text{radiosity emanating from the ground}}, \tag{1.6}$$

$$I_\nu^\downarrow(z_t, \Omega) = 0. \tag{1.7}$$

where $\epsilon_{g\nu}$ is the directional spectral surface emissivity and $\rho_{g\nu\Omega'\to\Omega}$ is the bidirectional spectral reflectivity.

The resultant fluxes obtained by solving (1.2) with the aid of boundary conditions (1.6) and

[1] Here, local thermodynamic equilibrium implies that any time scale that characterizes the 'macroscopic system' (for instance, the time scale that corresponds to the energy input to the system) is larger than the collision time scale between the molecules. Due to the large number of molecular collisions, the redistribution of absorbed energy in each energy state occurs rapidly and the distribution of molecules in each energy state is given by the equilibrium distribution at any given location. The consequence of LTE is that the emission from the element depends only on the temperature at that instant regardless of the spectral distribution of incident energy and the emission is given by equation (1.3). Non-LTE conditions are prevalent in rarefied gases, and are relevant to the upper atmosphere, where the redistribution of absorbed energy by collisions is slow.

[2] The rate at which radiant energy streams away from a surface per unit area is termed as radiosity [Sparrow & Cess (1967)]

(1.7), followed by integration over the relevant hemisphere, are given by

$$F^{\uparrow}(z) = \int_{\Omega} \mu d\Omega \left[\int_0^{\infty} \epsilon_{g\nu} B_\nu(z=0) \tau_\nu(z, z=0, \mu) d\nu + \int_0^{\infty} \int_0^{z} B_\nu(z') \frac{d\tau_\nu}{dz'}(z, z', \mu)\, dz' d\nu \right.$$
$$\left. - \int_0^{\infty} d\nu\, \tau_\nu(z, z=0, \mu) \int_0^{\infty} \left[\int_{\Omega'} \mu' d\Omega' \rho_{g\nu\Omega' \to \Omega} B_\nu(z') \frac{d\tau_\nu}{dz'}(0, z', \mu') \right] dz' \right], \quad (1.8)$$

$$F^{\downarrow}(z) = -\int_{\Omega} \mu d\Omega \left[\int_0^{\infty} \int_z^{\infty} B_\nu(z') \frac{d\tau_\nu}{dz'}(z, z', \mu)\, dz' d\nu \right], \quad (1.9)$$

where

$$\tau_\nu(z, z', \mu) = \exp\left[-\frac{1}{\mu} \int_{u(z)}^{u(z')} k_\nu(p, T) du \right], \quad (1.10)$$

is the monochromatic transmittance function. Physically, the integral terms (say, in the upwelling radiation from the ground to any height z) can be interpreted as summing the emission contribution of each element from ground up until the height z, with an attenuation, over the appropriate optical path, by the transmittance function above. The flux expressions above involve integrals over frequency, zenith angle and over the path through the photon travels via the transmittance function in equation (2.7). These integral expressions, when used in the energy equation, that includes the other heat transport mechanisms, lead to a complicated integro-differential equation, and the solution of this equation is computationally expensive. In this chapter, an overview of the existing parameterizations to simplify the integrals involved in equations (1.8)-(1.9) will be presented.

1.2 Directional characteristics

There are many approximate methods available in the literature to account for the angular dependence of the surface and the medium emissions (see equations (1.6) and (2.7) .

A powerful and elegant method was developed by Chandrasekhar (1960) for application to the transfer of radiation in planetary scattering atmospheres wherein the unit sphere is divided into a given number of sectors and the intensity in each of these sectors (discrete 'streams') is assumed to be uniform. Further, the integral involving the scattering kernel is approximated by a quadrature summation. As a result, the original integro-differential equation is reduced to solving a system of ODE's for the intensities of the discrete streams. This method is known as the *discrete ordinates*, S_N, or *multi-flux* method [Siegel & Howell (2002)]. The discrete ordinate method has been found to be efficient and accurate for calculations of the scattered intensity and fluxes. The simplest multi-flux approximation for an absorbing and scattering medium is the so-called two-stream approach. The assumption in this case is that the intensity is the same for all directions within a given hemisphere, although it can take on different value in the two hemispheres. That is to say,

$$I_\nu(\mu, x) = I_\nu^{\uparrow}(x) \quad \text{for} \quad 0 < \mu \leq 1$$
$$I_\nu(\mu, x) = I_\nu^{\downarrow}(x) \quad \text{for} \quad -1 \leq \mu \leq 0 \quad (1.11)$$

where μ is the direction cosine and x is the spatial coordinate.

Another method accounts for the angular dependence of the intensity by expanding in terms of spherical harmonics, which, for the axisymmetric case, are *Legendre polynomials*. This method is called P_N (Spherical Harmonics) method. In the general P_N method, the integral equations of radiative transfer are reduced to a set of ordinary differential equations by taking moments of the governing equation [Siegel & Howell (2002)]. The moments are obtained by multiplying the radiative transfer equation (1.2) by powers of the cosine of the angle between the coordinate direction and the direction of the intensity, and then integrating over the solid angle. Proceeding in this way results in a closure problem, that is, the number of moment equations generated is one less than the number of unknowns. To find the relationship between lower and higher order moments, the local intensity is expressed in terms of a truncated series in spherical harmonics, the truncation leading to a finite-dimensional system of ODE's [Siegel & Howell (2002)].

In the atmospheric context, the angular dependence of the intensity is often approximated by a diffusivity factor (β). In this approximation, the average of the transmission over all zenith angles is replaced by the transmission along an average path at a zenith angle $\theta = \cos^{-1}(1/\beta)$ [Goody (1964); Liou (2002)]:

$$2\int_0^1 \tau_\nu(z, z', \mu)\mu d\mu \propto \tau_\nu(z, z', 1/\beta), \tag{1.12}$$

where $\beta \approx 1.66$. With this approximation the flux expressions given earlier in equation (1.8) and (1.9) only involve integrals over frequency, and are given by:

$$\begin{aligned} F^{\uparrow}(z) &= \int_0^\infty \pi\epsilon_{g\nu}B_\nu(0)\tau_\nu^f(z,0)d\nu + \int_0^\infty d\nu \int_0^z \pi B_\nu(z')\frac{d\tau_\nu^f}{dz'}(z,z')\,dz' \\ &\quad + \int_0^\infty d\nu\,(1-\epsilon_{g\nu})\tau_\nu^f(z,0)\int_0^{z_t}\pi B_\nu(z')\frac{d\tau_\nu^f}{dz'}(0,z')\,dz', \qquad (1.13) \\ F^{\downarrow}(z) &= \int_0^\infty d\nu \int_z^{z_t} \pi B_\nu(z')\frac{d\tau_\nu^f}{dz'}(z,z')\,dz'. \qquad (1.14) \end{aligned}$$

The directional dependence of surface emission (and reflection) may also be accounted for, in addition to the directional dependence of medium emission above. Surfaces are usually assumed to be diffuse emitters with the reflection ranging from being diffuse to specular. 'Diffuse' signifies that the directional emissivity and absorptivity do not depend on direction [Sparrow & Cess (1967)], while specular surfaces or mirror like surfaces obey Snell's law of reflection.

1.3 Frequency Parameterization

Figure 1.1 shows the spectrum of solar radiation that reaches the earth's surface and the spectrum of the upwelling earth's emission transmitted through the atmosphere. The red shaded area shows the absorption by greenhouse gases in the atmosphere like H_2O, CO, O_2, CH_4, N_2O etc. The absorption characteristics of the atmospheric medium are sensitively dependent on

wavelength [3] (figure 1.1). Absorption occurs only at specific wavelengths, and the upwelling thermal spectrum of the earth's emission shows in particular, that the atmosphere is transparent in the infrared (IR) regime (8-14 μm). This spectral interval is termed as the atmospheric window in the literature.

There are four distinguishable frequency scales in the spectrum (figure 1.2) [Goody (1964);Stephens (1984)]. In decreasing order, they correspond to

1. the slow variation of the Planck function,

2. the shorter-range variation of the principal band contours. In case of the water vapor molecule, which is of immense importance in atmospheric studies (on account of being principal absorbing gas in the troposphere), the band contours are by far the widest, with the width to half-intensity ranging upto 300 cm^{-1}. For computational purposes, this region has to be further divided into smaller intervals of the order of 50 cm^{-1} so that one can assume Planck function to be constant in the resulting smaller wavelength interval.

3. the inter-line spacing $(1 - 5\,\mathrm{cm}^{-1})$, and

4. the scale on which Lambert's law of absorption is obeyed which is a small fraction of the elementary line width (the line width varies from $2 \times 10^{-2}\,\mathrm{cm}^{-1}$ for collisional pressure broadening at atmospheric pressure to about $2 \times 10^{-4}\,\mathrm{cm}^{-1}$ for Doppler broadening).

The disparity between the inter-line spacing and the elementary line width above is responsible for the absorption coefficient being a sensitive function of wavelength.

The spectrum of a water vapor molecule contains of the order of 10^5 absorption lines and calculating the emission contribution for each line, and summing up over all lines to get the total radiative flux requires a lot of computing power. Hence, one needs frequency parameterization to express the absorption properties of the participating medium in terms of a frequency averaged quantity (applicable to the coarser intervals) such that the parameterized quantity reflects the fine-scale features of the spectrum. Several models are available in the literature based on the level at which one wants to resolve the different scales in the absorption spectrum. Line-by-line calculations resolve the finest structure of the spectrum and serve as a benchmark for other models [Ellingson *et al.* (1991)]. At the next (lower) level of accuracy is the relatively less expensive narrow-band method. This formulation can be obtained by integrating the monochromatic fluxes in equation (1.13) and (1.14) over a frequency interval much larger than the average inter-line spacing but smaller than the length scale of variation of the Planck function. The next level in frequency parameterization is the wide-band model wherein the resolution is at the level of the entire band. At the coarsest level in the frequency parameterization are the broadband emissivity schemes wherein the absorption characteristics over the entire frequency interval of interest are modelled by a gray flux-emissivity [Goody (1964)]. This scheme is computationally inexpensive and has been used in the literature to study the interaction of radiation with other heat transfer mechanisms.

[3] This strong dependence on wavelength is only true for gases at moderate pressure. In the case of solids and liquids, strong molecular interactions and the resulting broadening leads to the spectrum exhibiting a smoother dependence on wavelength space. On the other hand, for gases, molecular interactions are negligible, leading to discrete spiky lines in the spectrum which reflect the specificity of the photon-induced transitions between the energy levels of a single non-interacting molecule.

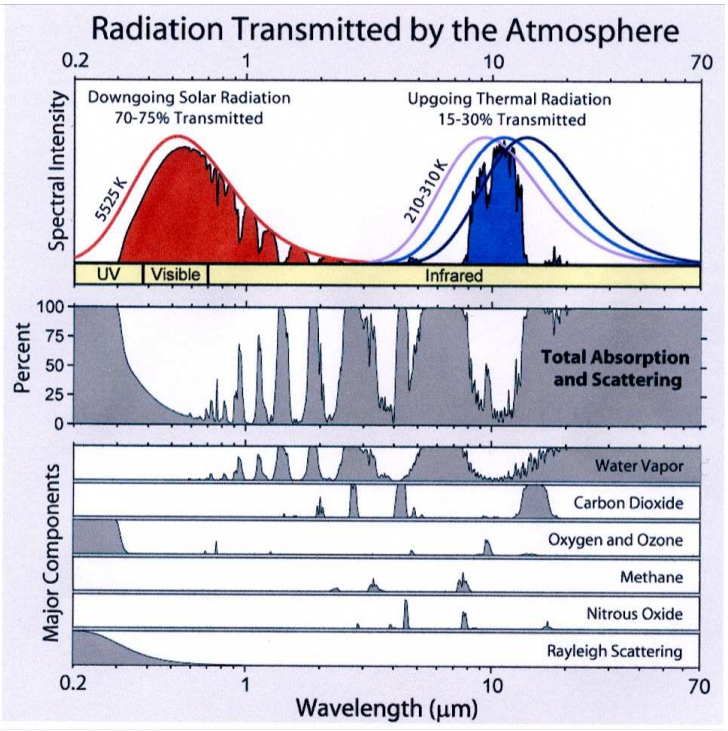

Figure 1.1: Solar and earth emission spectra and the absorption of gases in the atmosphere. Picture source:http://www.barrettbellamyclimate.com/page15.htm

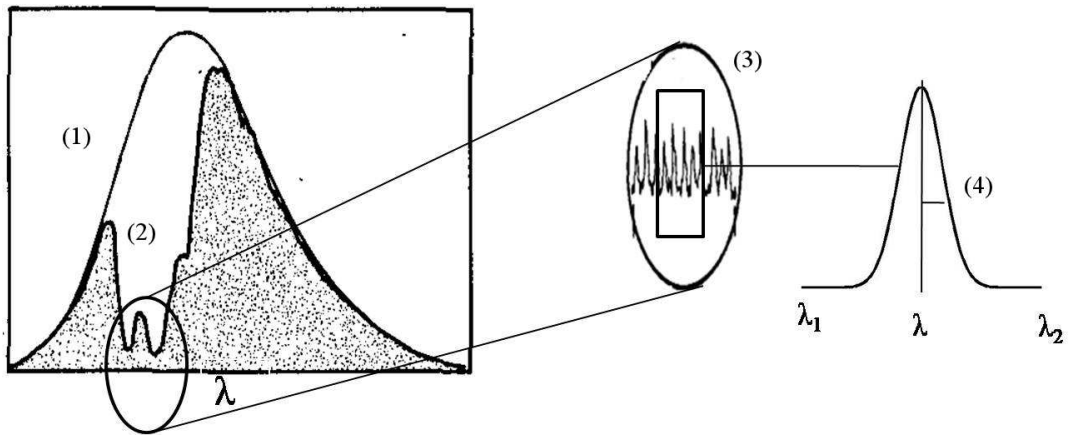

Figure 1.2: Figure shows different frequency scales present in the spectrum. (1) represents the scale over which the Planck function varies, (2) is the length scale that characterizes unresolved band contour, (3) shows the inter-line spacing and (4) shows the elementary line-width [Stephens (1984)]

.

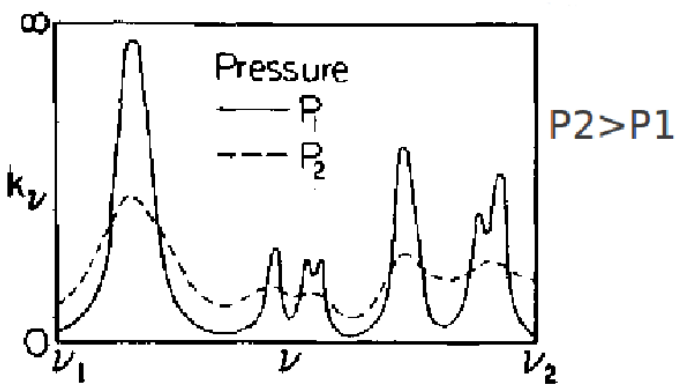

Figure 1.3: A schematic of absorption line spectra at two different pressures [Stephens (1984)]. At low pressure the natural or pressure broadening is small and the line shows spiky structures.

1.4 Inhomogeneity-Scaling approximation

Equation (2.7) for the monochromatic transmittance function involves an integration of the monochromatic absorption coefficient of the medium over the path through which the photon travels. This integration is complicated by the dependence of k_ν on pressure, temperature and the variation of both of these along a generic photon trajectory. Figure 1.3 illustrates the dependence of absorption spectrum on pressure. The pressure dependence arises because the width of the absorption line, on account of collisional broadening is proportional to the pressure, while the temperature dependence is associated with the line intensity (and reflects the dependence of underlying transition probability). This dependence on thermodynamic variables have to be taken into account to calculate the attenuation of the radiative flux along thermodynamically inhomogeneous paths. Two commonly used approximations in the literature are briefly discussed below. These approximations aims at developing a solution for the absorption along inhomogeneous paths in the atmosphere by reduction to an equivalent homogeneous path with appropriately scaled absorber amount $\tilde{u}$, temperature $\tilde{\theta}$ and pressure $\tilde{p}$ [Goody (1964)].

The simplest approximation is the so-called one-parameter scaling approximation wherein the absorption along an inhomogeneous path is described in terms of the absorption along a homogeneous path with an appropriately scaled absorber amount. Such a scaling works only when the monochromatic absorption coefficient exhibits a separable dependence on frequency and the thermodynamic variables, with a function of the latter variables acting as the scale for the absorber amount. This separable dependence is true in the asymptotic weak-line and strong-line limits. The resulting scaling functions for the absorber amount are different, however, and therefore, the choice of a particular scaling function ensures accuracy in either limit, but not both. The next method is the two-parameter scaling approximation, an example of which is the Curtis-Gordon approximation wherein the equivalent homogeneous path is defined in terms of both a scaled absorber amount and an equivalent pressure (or line width). The two parameter scaling allows asymptotic accuracy in both the weak and strong line limits, and remains reasonably accurate for atmospheric paths at moderate pressures [Goody (1964)].

1.5 Organization of the thesis

In this thesis, we address the fundamental issue of frequency parameterization, and to a lesser extent, the parameterization of directional characteristics, in the context of modelling radiative transfer in the infrared regime. As mentioned in section 1.3, with the present computing resources, frequency parameterization is still necessary for one to study the interaction of radiation with other heat transfer processes which occur in many physical scenarios. Frequency parameterized schemes, including broadband flux-emissivity schemes in particular, were initially formulated for black surfaces (surface emissivity $\epsilon_g = 1$). Later, in the context of the nocturnal boundary layer, both the broadband emissivity schemes and narrow-band formulations have been extended to include non-black surfaces [Garratt & Brost (1981); Savijärvi (2006)]. The first part of the thesis shows this extension is erroneous and leads to a spurious yet intense near-surface cooling in the opaque bands of the participating medium, and thence, an erroneous thermal structure of the NBL. The latter part of the thesis deals with the consequences of the erroneous frequency parameterization for the micrometeorological phenomenon known as the Ramdas layer. The remainder of the thesis is organized as follows:

- In chapter 2 it is shown that the error in the formulation for non-black surfaces is due to the use of an incorrect transmissivity to attenuate the reflected flux, and leads to a spurious cooling near the surface. It is shown that a careful treatment of the reflection term leads to the correct emissivity scheme, and eliminates the aforementioned spurious cooling. A detailed discussion on earlier NBL calculations affected by this error is presented.

- In chapter 3, we extend the correct emissivity scheme to account for multiple reflections between a pair of reflective surfaces and for an angular dependence of the radiant intensity. The latter generalization avoids the use of a diffusivity factor and enables one to rigorously account for directional characteristics of surface emission and reflection. Reflective surfaces are commonly employed in laboratory configurations. Accounting for the multiple reflections is also shown to be important in the atmospheric context, the specific instance being the appearance of a cloud over a non-black ground. Further, it is shown that the error discussed in chapter 2 is not only restricted to flux-emissivity schemes, and is present in all frequency-parameterized schemes, involving non-black emitting surfaces, when the scheme does not fully resolve the emission spectrum of the participating medium. Thus, Line-by-line calculations remain the only ones exempt from this error.

- In chapter 4 we discuss a longstanding unsolved micrometeorological paradox eponymously known as the Ramdas layer after its original discovery by Ramdas and Atmanthan [Ramdas & Atmanathan (1932)]. This micro-meteorological phenomenon concerns the formation of a minimum in the vertical temperature profile close to the ground within the NBL. The layer of cold air close to the ground is referred to as the Ramdas layer; the phenomenon is also known as the lifted temperature minimum(LTM). The prevailing explanation for this phenomenon [Vasudevamurthy *et al.* (1993)] is based on a broadband flux-emissivity scheme. The model predicts an LTM to occur only over non-black surfaces. It is shown herein that the prediction of an elevated temperature minimum is based on the aforementioned incorrect extension of the broadband emissivity scheme to non-black surfaces. A

preferential cooling leading to a temperature minimum near the surface cannot occur in a homogeneous atmosphere (here, homogeneity implies compositional homogeneity of the principal radiatively participating component). Heterogeneity on the length scale of the LTM is necessary to explain this phenomenon. The steep concentration gradient of suspended aerosols near the ground is proposed to be responsible for the preferential cooling. A theoretical formulation that includes the radiative effects of suspended aerosol particles is then presented. A non dimensional parameter is defined based on the relative magnitudes of radiative heating by water vapor and radiative cooling by aerosol particles via the atmospheric window. Next, an initial analysis, in the asymptotic regime, corresponding to a weak aerosol induced cooling, is presented for ground at a fixed temperature. This serves as a proof-of-principle demonstration of the existence of a minimum arising from participating medium heterogeneity, presented for a specific case where aerosol cooling is assumed to be dominant in all the spectral intervals. The aerosol radiative contribution is modeled using Newtonian cooling approximation. Based on the ground and air cooling rate a non dimensional number is proposed and its significance on demarcating between LTM and inversion profile is discussed.

- In chapter 5, a detailed analysis which accounts for the variation in ground temperature and water vapor in addition to the contribution of the suspended aerosols, is presented. First, we consider the radiative response of the aerosol particles alone, in the optically thin limit, and the results show that the evolution of the temperature profile close to the ground depends on two dimensionless parameters - the surface emissivity and what we call the Ramdas-Zdunkowski factor. The direct dependence of the evolution on the surface emissivity is relatively weak. The Ramdas-Zdunkowski factor, defined as the ratio of the cooling rates of the aerosol-laden air layers to that of ground, is therefore the principal factor that demarcates the LTM regime and the traditional inversion regime. Next, we carry out dynamic simulations, based on the flux-emissivity formulation for an inhomogeneous aerosol-laden atmosphere, to examine the evolution of the vertical temperature profile starting from an initial lapse-rate profile at sunset. In the absence of aerosols, as expected on physical grounds, water-vapor-driven cooling leads to a monotonic variation of the air temperature in the lowest decimeters regardless of the ground cooling-rate and surface emissivity. The inclusion of the aerosol contribution shows that an LTM-type profile emerges above a threshold concentration that corresponds to an R_f value of order unity, consistent with the evolution of the simplified analysis, based on a Newtonian cooling approximation, and that only considers the aerosol contribution.

- In chapter 6 we discuss the theoretical model for the Ramdas layer reproduced in a laboratory set up. Experiments on the laboratory Ramdas layer have successfully demonstrated the role of aerosol radiative forcing on the origin of the phenomenon. Two sets of experiments have been carried out to study the radiative forcing of suspended aerosol particles. In the first set, experiments are carried in a traditional Rayleigh-Benard setup where the participating medium is confined between two parallel *opaque* plates leading to monotonic non-linear radiative-conductive equilibrium profiles. Then, to mimic the night-time atmospheric conditions (required to produce an LTM) a cold sink is added. The participating

medium can then interact with the cold sky through the upper plate that is now transparent, thereby leading to a de-coupling of the radiative and conductive boundary conditions. The resultant equilibrium profiles are LTM-type profiles. We have modeled the two sets of experiments and the theoretical results compare well with the experimental findings for an exponentially decaying aerosol concentration profile.

- Finally we conclude and provide a perspective on future work in chapter 7

Chapter 2

Broadband flux-emissivity scheme - Structure of nocturnal boundary layer

The material in this chapter is reproduced, in part, in J.atmos.sci, 69, 2892-2905, 2012

2.1 Abstract

The nocturnal stable boundary layer (NBL) that develops over land, under calm and clear conditions, is important in understanding pollution control, radiation fog and in other micrometeorological phenomena. Under these conditions, radiation is an important heat transport mechanism throughout the NBL. This is in contrast to the daytime boundary layer where convection is the dominant mode of heat transfer, and is responsible for transport of heat throughout the boundary layer. Turbulence due to natural convection, driven by solar heating, is spatially continuous; on the other hand, during night time, turbulence tends to be weak and spatially intermittent under calm, clear conditions [Mahrt & Vickers (2006)]. Hence, characterizing other transport processes such as radiation, advection and subsidence is important to study the evolution of the NBL under calm conditions. Frequency-parameterized radiative transfer schemes are often used in the literature to study the interaction of radiation with other heat transport processes. The coarsest level of frequency parameterization leads to broadband flux-emissivity schemes Such schemes have been mostly used for the cases where the bounding surfaces are black. In 1981, in an important article, Garratt & Brost (1981) extended the prevailing flux-emissivity scheme to non-black surfaces (ground), in an attempt to examine the influence of the ground emissivity on the thermal structure of the NBL. In this chapter, it is shown that Garratt & Brost (1981) extension of the flux-emissivity formulation, to model radiation over non-black surfaces, is fundamentally inconsistent. There is an error in the reflected component which produces a strong intense cooling near the surface. The correct formulation which eliminates the above error is presented and the resulting thermal structure of NBL is discussed.

2.2 Introduction

The part of the atmosphere which is directly influenced by the presence of the *surface* (ground) and responds to surface forcing with a time scale of about an hour or less is termed as the atmospheric boundary layer [Stull (1988)]. During daytime, the earth's surface absorbs solar radiation, and it is at a higher temperature than the overlying air layers. This unstable stratification results in turbulent convection and a transfer of heat to the overlying air layers. Typically,

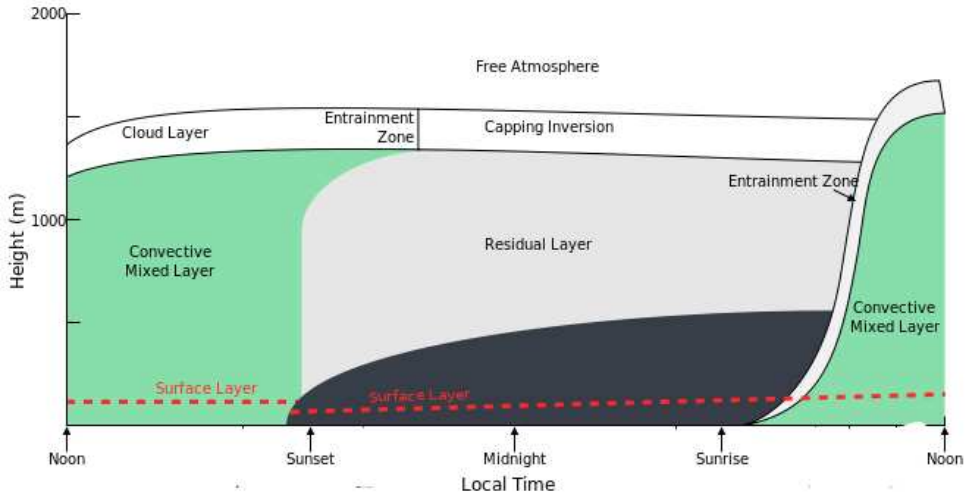

Figure 2.1: A schematic of a typical atmospheric boundary layer observed during daytime and night time is shown. The diurnal boundary layer comprises of surface layer (where the turbulent fluxes are almost constant), convectively mixed layer which is capped by an inversion. Similarly during night time, the surface layer is followed by a residual layer (remnant of daytime convectively well mixed layer) and then there is a transition to free atmosphere.Picture source:http://commons.wikimedia.org/wiki/File:Atmospheric-boundary-layer.svg

the diurnal boundary layer that forms over land extends to a height of the order of kilometers [Stull (1988)]. The *surface layer*, which typically occupies the lowest 10% of the boundary layer, is the region where the turbulent fluxes almost remain a constant [Stull (1988)] and the observed temperature gradient exceeds the adiabatic lapse-rate. Above the surface layer is the well *mixed layer* which is capped by an inversion. The base of the capping inversion is usually taken as the height of the daytime boundary layer. The wind velocity and temperature profiles in the surface layer are well described by the Monin-Obukhov theory. Monin and Obuhkov hypothesized that in a constant flux layer, in the absence of advection and for a stationary steady state, turbulent statistics such as gradients, variances and covariances when normalized by appropriate powers of the characteristic velocity, that is, the frictional velocity(u_{*0}) [1], and the characteristic temperature scale T_* [2], become a function of the non-dimensional height $\frac{z}{L}$, where L is the Obukhov length scale [Kaimal & Finnigan (1994)]. Physically, the Obukhov length scale is the height over which the buoyancy and shear terms are of the same order in a local balance, and thereby, remain [Garratt (1994)]. The Obukhov length scale is defined as $L = \frac{u_*^2}{k\frac{g}{\bar{T}_v}T_*}$ where $\bar{T}_v$ is the mean virtual temperature, $\frac{g}{\bar{T}_v}$ is the buoyancy parameter and k is the von Karman constant. A schematic sketch of diurnal boundary layer is shown in figure 2.1.

At night, in the absence of advection, conventional wisdom dictates that, starting at sunset, the earth's surface, being a good emitter in the infrared regime, cools radiatively much faster than the air layers (careful temperature measurements near the ground shows this is not actually the case, however. The air layers closest to the ground, in fact, cool much faster than

[1]The frictional velocity is defined as $u_* = -\sqrt{\overline{(u'w')}_0}$ where u' and w' are the rapidly varying turbulent velocities in the horizontal and vertical directions.

[2]The characteristic temperature scale is defined as $T_* = \frac{-\overline{w'\theta'}}{u_*}$.

the ground resulting in a non monotonic temperature profile typically known as the Ramdas layer. The origin of this phenomenon will be discussed in Chapters 4 and 6). The resultant stable inversion temperature profile, unlike the diurnal boundary layer, is not well understood [Edwards (2009a)]. The structure of the NBL is expected to depend on the relative magnitude of shear generated turbulence and dampening effect due to buoyancy, and this determines the vertical profiles of the various variables. Hence, the stable boundary layer (SBL) could be well mixed or non-turbulent depending upon the dominant mechanism. One can classify the nocturnal boundary layer into two types; weakly stable boundary layer (WSBL) and Very strong boundary layer(VSBL). The weakly stable boundary layer which occurs during windy and cloudy conditions, is characterized by continuous turbulent activity and the turbulence can be well described by local similarity scaling [Nieuwstadt (1984)]. On the other hand VSBL is characterized by temporally intermittent turbulent activity.

In the absence of clouds, and under calm conditions, turbulence can, in fact, be subdominant and longwave radiation may play a dominant role in determining the vertical structure of the NBL. Radiation plays two distinct roles in the NBL [Edwards (2009a)]. It influences the surface skin temperature (directly affecting the establishment of the inversion layer) and the differential radiative heating or cooling of the air layers across the NBL affect the evolution indirectly. The latter effect is less well understood and it has been the main focus of research in recent years. Unlike the diurnal boundary layer as discussed above, the height of the stable NBL and the nocturnal inversion layer are difficult to define [Andre & Mahrt (1981)]. The height of the NBL is usually taken as the height of the turbulent layer (the altitude at where the sensible heat flux is 5% of its surface value) and this turbulent layer occupies the lower part of the inversion layer. There exist alternate definitions of the NBL height. For instance, Yu (1978) proposed the inversion layer height to be the altitude where the temperature gradient vanishes. The main focus of this thesis is on the role of radiation on the evolution of NBL (the lower meters thereof) under calm, clear conditions.

Initial studies assumed the role of the longwave radiative flux divergence to be very small when compared to the turbulent heat exchanges in the lowest atmospheric layers [Gaevskaya *et al.* (1962)]. The argument in favor of this view was based on the apparent agreement between observations and theoretical calculations of air temperature that included turbulence alone. The calculation of the air temperature was based on solving the heat conduction equation which takes into consideration the turbulent heat exchange by way of an eddy-diffusivity. But, later theoretical calculations [Gaevskaya *et al.* (1962)] indicate that the radiative cooling is always greater than the observed cooling rate. This clearly suggests the role of radiation in changing the air temperature. In what follows, we will give a brief overview of the existing observational studies to understand the direct and indirect effect of radiation on the development of the NBL, and then we will discuss the theoretical studies which attempt to study the effect of various factors on NBL development.

An early observational study by Funk (1960) measured the vertical distribution of radiative flux near the ground in the *developing* NBL. The radiative cooling rate, obtained by taking the difference between the measured fluxes at different heights, was found to be always higher than the actual cooling rate implying the importance of radiation in the formation of an inversion

layer. The maximum radiative cooling rate was found to be $300\,\mathrm{Kday}^{-1}$. The averaged radiative flux- divergence profile (where the averaging time was more than an hour) showed radiative cooling between $0.5 - 1.5\,\mathrm{m}$ and the radiative cooling rate increased with height. There were instances where the observed profiles also exhibited radiative warming. Further, there was a discrepancy between the observed radiative cooling rate and the estimated radiative cooling (using Deacon's radiation chart). The underestimation of the radiative flux-divergence by the theory was attributed to the omission of the radiative effect due to an invisible haze layer near the ground.

On the other hand, observations by Lieske & A.Stroschein (1967) showed a radiative warming over snow in the lowest 5 m and a radiative cooling from $20 - 200\,m$. The maximum radiative heating measured was $160\,\mathrm{Kday}^{-1}$. The theoretical prediction was, however unable to reproduce the observed flux divergence. Nkemdirim (1978) reported a radiative cooling over grass and snow, over a height of $1 - 3\,m$, in opposition to the Lieske & A.Stroschein (1967) observations.

Sun *et al.* (2003) measured the difference between the radiative fluxes at heights of 2 m and 48 m over a grass surface. The maximum radiative cooling was found to occur during *early evening*, under calm conditions, and thus, radiation controlled the initial formation of an inversion layer. The role of radiation was to cool the layers between 2 m and 48 m and was found to be relatively insignificant later in the night. The history such as the amount of solar radiance, determines the radiative cooling at early evening and the cooling also depends on the gradient of the temperature profile. The study also emphasized the role of advection to the energy balance. The Monin-Obukhov theory (valid only when the vertical sensible heat flux in the surface layer varies only by 10% or less) was found to be *invalid* because of the significant variation in the sensible heat flux divergence.

Hoch (2005) measured the radiative flux divergence over the ice sheet in Greenland, throughout the night, over a period of 14 months. The flux divergence during the night showed radiative warming next to the surface, implying a sign change in the radiative cooling profile near the surface. Further, the theoretically evaluated radiative flux divergence using MODTRAN compared well with the experiments. The main theoretical results were that the effect of surface emissivity on the radiative cooling rate was small, and that the flux divergence had a weak dependence on the amount of water vapor present in the air.

Steeneveld (2007) measured radiative fluxes over grass at 1.3 m, 10 m and 20 m. The maximum radiative cooling was observed immediately after sunset which was similar to the conclusion drawn by Sun *et al.* (2003) and then decreased with time. Further, the author performed a Large eddy simulations (LES) to study the turbulent structure in the stable boundary layer (SBL). The radiative flux divergence was estimated using a flux-emissivity scheme. The results were compared with CASES-99 observations (Sun *et al.* (2003)). The main conclusion is that the coupling between land and surface plays a crucial role in forecasting the SBL. Further, the radiative cooling was found to be dominant when the wind speed is very small.

The above discussion mainly concerns existing observations that study the role of radiation and turbulence in determining the structure of the NBL. We now present an overview of the theoretical analyses which have attempted to study the role of the different heat transfer modes in establishing and controlling the growth of the NBL. Before proceeding to the review, we write

down the governing equations for the evolution of the mean temperature and velocity fields by assuming molecular conduction and viscosity to be negligible, and the atmosphere to be plane-parallel, divergent free, and barotropic. The resulting system of governing equations is given by:

$$\frac{\partial \theta}{\partial t} = -\frac{\partial \overline{w'\theta'}}{\partial z} - \frac{1}{\rho C_p}\frac{\partial F_z}{\partial z}, \tag{2.1}$$

$$\frac{\partial u}{\partial t} = f(v - v_g) - \frac{\partial \overline{w'u'}}{\partial z}, \tag{2.2}$$

$$\frac{\partial v}{\partial t} = -f(u - u_g) - \frac{\partial \overline{w'v'}}{\partial z}, \tag{2.3}$$

where θ, u and v are the mean potential temperature, and the two horizontal velocity components, u_g and v_g are components of the geostrophic wind speed (obtained from the balance between Coriolis force and pressure gradient; in general, the geostrophic wind speed is specified when studying the NBL.), f is the Coriolis parameter and the covariances of the fluctuating components in (2.2) and (2.3) are the turbulent heat and momentum fluxes. Several closure models are available in the literature to approximate the covariances of the fluxes. In the above equations, the role of advection is neglected and with the aid of the Boussinesq approximation, the effect of density variation on the inertial terms has also been neglected. The theoretical studies below differ in terms of the models used to approximate the turbulent fluxes and radiative flux divergences and our focus is principally on the radiative fluxes. Consistent with this focus, we will attempt to organize the thermal structure of the NBL based on the radiative cooling-rate profiles. As will be seen below, alternate classifications exist on the relative dominance of turbulence and radiative flux-divergence. Note that many authors have studied the evolution of the boundary layer height under stable conditions as a function of time [for instance, Nieuwstadt & Tennekes (1981)]. These models, however, neglect the effect of radiative cooling.

The earliest studies in the literature calculated the radiative flux divergence using radiation charts and tables. Using the radiation tables by Brooks (1950), Fleagle (1953) calculated the vertical distribution of radiative flux divergence. The flux divergence profile, predicted for an inversion layer, exhibited a two-layer structure, a radiative warming near the ground, and a subsequent transition to radiative cooling [Fleagle (1955)] over a length scale of a few centimeters for a water vapor-laden atmosphere. He correctly reasoned that the warming was due to the radiative exchanges between the lowest air layers with the overlying warmer layers.

Elliott (1963) obtained the vertical profile of sensible heat flux by subtracting the calculated longwave flux divergence contribution from the observed mean cooling in a nearly *neutral* NBL. The longwave radiative contribution was estimated using an emissivity scheme and the emissivity values were again taken from Brooks (1950). The unresolved temperature profile near the ground was modeled using a *slip*. The computed turbulent heat flux contribution was warming and the maximum value occurred at a height of 10m. This suggests that there was a strong radiative cooling in the lowermost air layers.

Garratt & Brost (1981) studied the effect of radiative cooling on the evolution of the NBL. The radiative flux divergence was calculated using a flux-emissivity scheme which employs different emissivities for upward and downward trajectories [Rodgers (1967)] (discussed in detail

in section 2.3). The authors also studied, for the first time, the effect of the surface emissivity (ϵ_g) on NBL evolution. These simulations were performed for only one value of the geostrophic wind speed $10\,m\,s^{-1}$, and for a surface emissivity value of 0.8 and 1. They concluded that, thermodynamically (that is, from the point of view of the temperature profile), the boundary layer developed into a three-layer structure where the bottom $0.1h$, (h being the boundary-layer height) and uppermost ($0.2h$ thick) was influenced by radiative cooling and the *bulk* ($0.7h$ thick) was determined by turbulence. The height at which the Richardson number (The Richardson number Ri, is a dimensionless parameter, that represents the relative importance of buoyancy and shear in stratified flows) first equals the critical value ($\mathrm{Ri}_c = 0.25$) was defined as the boundary layer height. The authors distinguished the aforementioned layers by comparing the layer-averaged turbulent and radiative cooling-rates to the calculated total cooling-rate. This three-layer structure was observed for all the simulations performed under strong wind conditions with the separation being clear over a gray surface. From the perspective of the radiative flux-divergence profile, the NBL again exhibited three regimes where the lower and topmost layers were cooled by radiation and the intermediate layers were warmed by radiation. The effect of reducing the surface emissivity from unity was found to significantly *enhance* the radiative cooling near the surface. Further, the predicted sensible heat flux profile showed a maximum at around $0.05h$ over a non-black surface; a feature that was absent for simulations done over a black surface.

Andre & Mahrt (1981) analyzed the nocturnal boundary layer data obtained during the Wangara and Voves experiments [Clarke *et al.* (1971);Andre & Lacarrère (1980)]. The authors concluded that the turbulent heat exchange and radiative cooling, on average, contribute equally to the development of the NBL. For a black surface, the calculations using a flux-emissivity scheme predicted a radiative warming in the lowest air layers, and turbulence determined the profile in the bulk. The topmost layer was influenced by clear-air radiative cooling and is responsible for the development of an inversion layer. However, the radiative warming near the ground changed to a *cooling* for a gray surface with a slightly reduced emissivity $\epsilon_g = 0.965$. Further, the results showed that the stratification normally decreases with height corresponding to the negative curvature of the potential temperature profile. When the level of turbulence increased, the negative curvature weakened and became positive for a well-mixed flow. Under calm conditions, the flux-divergence profile pointed to a two-layer NBL, where the bottom layer was heated radiatively and with a transition to radiative cooling at greater heights. However, under strong wind conditions, the flux divergence profile showed three distinct layers where the layers close to the surface and the inversion layer were cooling radiatively and in the intermediate regime, the layers were warmed by radiation. This is similar to the results obtained by Garratt & Brost (1981).

The effect of geostrophic wind speed on NBL evolution was studied by Claude & Guedalia (1985). The radiative flux divergence was calculated using Goody's random narrow-band model [Goody (1964)] with a spectral resolution of $20\,cm^{-1}$. For weak wind speeds, the radiative cooling is dominant: Under these conditions, the height of the inversion layer (defined as the height at which the gradient of the potential temperature reaches $-3.5 \times 10^{-3} K\,m^{-1}$) increases during the night even as the height of the turbulent layer shows little variation with respect to

time. The computed radiative flux-divergence showed a two-layer structure under weak wind conditions, where near the ground radiative *warming* occurred and the warming decreases with height with an eventual transition to radiative cooling. The maximum radiative cooling occurred at 20 m. Under strong wind conditions, the depth of the stable layer overlying the turbulent layers remains nearly constant. In this case, a classification based on the relative magnitude of turbulence and radiation again led to a two-layer NBL structure where, in the lowest tens of meters, turbulence is dominant, and above which the layers cool radiatively with turbulence usually being absent. Under strong wind conditions, the radiative warming near the ground is replaced by a strong radiative cooling (although still sub-dominant related to turbulence) which decreases with height.

Räisänen (1996) analyzed the effect of vertical resolution on the radiative fluxes using two radiation codes. The main conclusion with regard to the NBL is that the detailed temperature profile near the ground governs the sign of the radiative flux divergence. The estimated flux divergence for a temperature profile with a discontinuity produced a large radiative cooling rate, near the surface, while a logarithmic inversion profile without any discontinuity in temperature produced radiative warming near the surface.

Gopalakrishan *et al.* (1997) studied the evolution of the nocturnal inversion layer under weak wind conditions. Radiation was again modeled using a flux-emissivity scheme and turbulence using an eddy diffusivity model. The predicted turbulent heat flux at the surface reduced when the speed decreased. For low geostrophic wind speed, the nocturnal inversion layer was found to grow throughout the night, while for strong wind conditions, the height of the inversion layer attained an equilibrium value similar to the conclusion drawn by Claude & Guedalia (1985). Further, the predicted radiative flux divergence showed cooling near the surface both under weak and strong wind conditions. In the simulations under strong wind conditions, the NBL develops a three layer structure similar to Garratt & Brost (1981). Interpretation using both classification leads to the same structure. Later, Ramakrishna *et al.* (2003) also arrived at the same conclusion, but the turbulence in their studies was modeled using a mixing-length closure model and the rest of the modeling was same as that of Gopalakrishan *et al.* (1997).

Ha & Mahrt (2003) concluded that the detailed nature and curvature of the temperature profile determined the vertical structure of the radiative fluxes. The same conclusions were obtained earlier by Andre & Mahrt (1981) and Räisänen (1996). They modeled radiation using a flux-emissivity scheme which accounts for the non-isothermality of the atmosphere [Ramanathan & Downey (1986)]. The predicted radiative flux divergence close to ground was found to be cooling which occurs next to the ground and the cooling was found to depend upon the moisture content. The cooling close to the ground was due to an assumed temperature difference between the ground and the lowermost air layer and the magnitude of this cooling strongly depend on the assumed temperature difference.

Savijärvi (2006) studied the diurnal evolution of the clear-sky midlatitude summertime (MLS) boundary layer. Radiation was modeled again using Goody's random narrow-band model. The surface emissivity, geostrophic wind speed and the structure of the temperature profile near the surface were found to affect the radiative cooling close to the ground. The effect of radiation close to the ground was found to be *warming* at all geostrophic wind speeds. The

windy nocturnal inversion layer develops into a four-layer structure where a thin radiative warming close to the surface transitions to radiative cooling which decreases with height, the overlying bulk of the boundary layer is dominated by turbulent cooling, and finally, the radiative cooling dominates the top of the inversion layer. Note that the radiative warming next to the ground was absent in the previous studies [Garratt & Brost (1981),Gopalakrishan *et al.* (1997),Ramakrishna *et al.* (2003)] which also studied the development of NBL under strong geostrophic wind speed. For the weak wind case, the NBL evolves into a two-layer structure where the radiative cooling is important in the bulk and turbulent cooling dominates near the surface. These results were obtained earlier by Andre & Mahrt (1981) and Claude & Guedalia (1985). Based on the sign of the radiative flux divergence the NBL also showed a two layer structure under weak-wind condition similar to that found by Andre & Mahrt (1981) and Claude & Guedalia (1985), and under strong wind conditions, the distribution of radiative-flux divergence vertically showed a four layer structure where close to the ground there was a radiative warming and then there was a transition to radiative cooling, the radiative cooling decreased with height there being a second transition to a radiative warming and finally, the topmost layer was found to cool radiatively. The fourth layer, the near-surface radiative warming zone, in the earlier efforts due to a combination of an inadequate resolution and an incorrect radiation scheme.

Edwards (2009a) studied the role of radiation under both weak and strong wind conditions and as a function of the spectral and directional characteristics of the surface. Radiation was modeled using a correlated k-distribution method [Lacis & Oinas (1991);Liou (2002)] with high spectral and vertical resolution. The evening transitional developing boundary layer was found to be described in terms of radiative cooling to the surface although, as the night progresses, the exchanges between air layers was found to govern the radiative contribution. Radiation was found to heat the air layers near the surface, there being a transition to cooling at greater heights. The maximum radiative cooling occurred at a height of the order of meters and the height over which cooling occurs was found to increase over time. The decrease in surface emissivity was found to enhance the radiative heating near the surface. Further, the study emphasized the need to account for the directional characteristics of the surfaces in determining the radiative cooling rate. The interaction between radiation and turbulence was analyzed by Edwards (2009b). Under strong wind conditions, the vertical distribution of the radiative flux divergence has four regions as obtained by earlier Savijärvi (2006). The top of the boundary layer is influenced by radiative cooling, the bulk of the boundary layer is affected by radiative heating, which again transitions to a cooling near the surface. Finally, the fourth layer is the radiative warming closest to the surface first resolved by Savijärvi (2006). As mentioned above, a decrease in the surface emissivity is found to lead to an increase the warming in this region.

A summary of the observational studies of the NBL, which measure the radiative flux divergences, is given in table 2.1.

Reference	**Details about the measurement**	**Radiative flux divergence(RFD)**

Funk (1960)	1. Measurement were done over grass in Australia at the time of the evening transitional boundary layer (5pm-8pm). 2. Height - up to 8m. 3. The surface temperature was calculated from the radiative flux measured at 1.5 m	1. Finite difference between different vertical levels to calculate the divergence. 2. Both warming and cooling were observed. 3. RFD, averaged over an hour, resulted in cooling. Maximum cooling rate was 300 $\mathrm{K\,day^{-1}}$
Lieske & A.Stroschein (1967)	1. Measurements were done over snow in Alaska throughout the night time (9 pm-5 am). 2. Near-surface temperature measurements done at 1,2,3,4,5 m and a tower measured temperatures up to 250 m. 3. The ground temperature was obtained by extrapolation from temperatures measured at 1 and 2 m.	1. Finite difference to calculate the flux divergence. 2. Observed near-surface radiative warming and the flux divergence changes to cooling at greater heights. 3. Maximum heating observed was 160 $\mathrm{K\,day^{-1}}$.

Nkemdirim (1978)	1. Measurements were done over snow and grass from 3 pm-11 pm. 2. Humidity, temperature, wind speed and radiative fluxes were measured at 1m and 3m.	1. Finite difference to calculate the flux divergence. 2. The time-averaged radiative contribution was a cooling of the air layers. 3. The maximum cooling observed was $264\,\mathrm{Kday}^{-1}$ over grass and $160\,\mathrm{Kday}^{-1}$ over snow.
Sun *et al.* (2003)	1. Measurements were done over grass with different surface roughness. 2. Radiative fluxes were measured at 2 m and 48 m.	1. Finite difference to calculate the flux divergence. 2. The maximum cooling rate measured in the early evening was $18\,\mathrm{Kday}^{-1}$.
Hoch (2005)	1. Measurements were done over snow and covered all seasons. 2. Temperatures were measured at eight levels $(0.5, 1, 2, 5, 10, 19, 34, 48\,m)$	1. Observed radiative warming near the ground and the maximum heating observed between 2m and 8m was $200\,\mathrm{Kday}^{-1}$. 2. A sign change in radiative cooling observed near the surface and the maximum cooling recorded between 2m and 10m is $10\,\mathrm{Kday}^{-1}$

Steeneveld (2007)	1. Measurements were done over grass in Netherlands. 2. Air temperature was measured at 0.1 m and the wet bulb temperature at 1.5 m. 3. Radiative fluxes were measured at 1.3 m,10 m and at 20 m	1. Finite difference to calculate the flux divergence. 2. Maximum cooling was observed after sunset and the cooling decreased with height. 3. The maximum cooling recorded between 1.3 m-1 0m was 72 Kday^{-1}, and between 10 m and 20 m was 36 Kday^{-1}.

Table 2.1: Summary of observational studies which measured the radiative flux divergence during night time.

A summary of both theoretical and computational studies that examine the role of radiation in the NBL and the predicted RFD, is given in table 2.2.

Reference	**Model used**	**Surface emissivity**	**Slip**	**Radiative flux divergence(RFD)**
Fleagle (1953)	Emissivity model (values taken from Brooks (1950))	1	-	Radiative warming next to the surface
Funk (1960)	Emissivity model (Deacon chart)	1	-	Radiative cooling between 0.5 m - 1.5 m 107 Kday^{-1}
Elliott (1963)	Emissivity model	1	3-4 K	Radiative cooling 24 Kday^{-1} near the surface.
Lieske & A.Stroschein (1967)	Emissivity model where the emissivity values are taken from Elsasser	1	-	Radiative warming next to the surface.
Garratt & Brost (1981)	Emissivity model	1 0.8	-	Radiative cooling at 2 m 17 Kday^{-1} 77 Kday^{-1}
Andre & Mahrt (1981)	Emissivity model	1 0.965	-	Radiative warming 57.6 Kday^{-1} Radiative cooling 288 Kday^{-1}

Claude & Guedalia (1985)	Goody random narrow-band model	1	-	Radiative warming $7.2\,\mathrm{Kday}^{-1}$
Gopalakrishan *et al.* (1997)	Emissivity model	1	-	Radiative cooling at 2 m
Ha & Mahrt (2003)	Emissivity model	1	1.5 K	Radiative cooling at 1 m
Ramakrishna *et al.* (2003)	Emissivity model	1	-	Radiative cooling at 2 m
Savijärvi (2006)	Goody random narrow-model	0.96	-	Radiative warming
Steeneveld (2007)	Flux emissivity model	0.96	-	Radiative cooling
Edwards (2009a)	k-distribution method	1 0.8	- -	Radiative warming near the surface Modest increase in radiative warming.

Table 2.2: Summary of theoretical study which study the role of radiation in the nocturnal boundary layer.

The above discussion suggests that there is a strong disagreement regarding the sign of the radiative flux divergence near the surface and the importance of radiation in determining the vertical structure of NBL.

This thesis has been influenced by the following list of questions, some of which (those concerning radiation) are partially or fully answered in later chapters.

1. The sign of the flux divergence remains controversial. On one hand we have radiative heating first observed by Lieske & A.Stroschein (1967), and most recently Hoch (2005) and on the other hand, radiative cooling observed by Funk (1960),Nkemdirim (1978),Sun *et al.* (2003),Steeneveld (2007). The theoretical studies are also inconclusive because some models predict radiative warming [Fleagle (1953),Claude & Guedalia (1985), Edwards (2009a) and Hoch (2005)], while others predict cooling [Garratt & Brost (1981), Andre & Mahrt (1981),Gopalakrishan *et al.* (1997),Ramakrishna *et al.* (2003)]. Is there really a contradiction in the observed radiative flux-divergence and the theoretical predictions, or is the bridge between the observation and theoretical studies missing?

2. Is there really a change in sign of the flux divergence near the surface as predicted by Fleagle (1953), Savijärvi (2006),Hoch (2005), Edwards (2009a)?

3. How does the surface emissivity affect the radiative cooling rate in the NBL?

4. How does the radiative flux vary with height? Will it increase [Funk (1960)] or decrease [Steeneveld (2007)] with height?

In the following sections we will examine the role of radiation in determining the thermal structure of NBL and the effect of surface emissivity on the RFD profiles. To understand the

NBL structure, in section 2.3, we first present the existing flux-emissivity formulation for a black surface, and its extension to non-black surfaces proposed originally by Garratt & Brost (1981). The flux-emissivity formulation is the simplest model which captures the essential feature, that is, the multiplicity of photon mean-free-paths that characterize the water vapor spectrum, via a gray flux-emissivity (see section 1.3 that deals with the frequency parameterization in Chapter 1). It will be shown that the existing formulation for non-black surfaces is incorrect. The error is due to the use of the same transmissivity to attenuate both emitted and reflected radiation. A physical explanation of the consequences of using the erroneous transmissivity will be given in section 2.3.2, and a derivation of the correct transmissivity to eliminate the aforementioned error will then be presented. The corrected scheme helps clarify the relative influences of the radiative and sensible flux divergences on NBL structure and evolution - an important issue in micrometeorology [Hoch (2005)]. After obtaining the correct reflected flux, the radiative flux-divergence (cooling-rate) profiles are determined in section 2.4, for model atmospheres, using both the prevailing erroneous and the correct formulations; these include a model inversion layer with an exponential increase in temperature with height. Tiny departures from a radiatively black surface lead to qualitative differences in the cooling-rate profiles obtained from the erroneous and correct schemes. We discuss the implications of these differences for existing NBL calculations in section 2.5. In section 2.6, we present the extension of the basic isothermal flux-emissivity formulation to include the non-isothermality of the atmosphere over non-black surfaces. Finally, we conclude the results for this chapter with a discussion of the results in section 2.7.

2.3 Broadband flux emissivity model

Broadband flux-emissivity schemes are computationally efficient and typically used in studies where the primary focus is not on the radiation modelling alone, but also its interaction with turbulence, stratification, surface characteristics, etc. [Penner *et al.* (2009); Justin *et al.* (2009); Abraha & Savage (2008); Brubaker & Entekhabi (1996)]. Examples include micrometeorological phenomena that influence or are influenced by the thermal structure of the NBL - the formation and growth of inversion layers after sunset, the onset of radiation fog, etc. As indicated in chapter 1, such schemes correspond to the coarsest level of frequency resolution of the absorption spectrum of the participating medium. The broadband fluxes, obtained from the corresponding spectral expressions (1.8 -1.9) by an integration over frequency, with a diffusivity-factor being used to model the angular dependence of the intensity [Goody (1964); Liou (2002)] over a black surface are as follows:

$$F^{\downarrow}(u) = \int_{u}^{u_t} \sigma T^4(u') \dot{\epsilon}^f(u' - u) du', \tag{2.4}$$

$$F^{\uparrow}(u) = \sigma T_g^4 [1 - \epsilon^f(u)] + \int_{0}^{u} \sigma T^4(u') \dot{\epsilon}^f(u - u') du', \tag{2.5}$$

where the dot denotes differentiation with respect to the argument, and $\epsilon^f(u)$ is the isothermal broadband flux-emissivity.

The basic definition of the flux-emissivity is [Rodgers (1967)]:

$$\epsilon^f(z,z') = \int_0^\infty \frac{B_\nu(z')}{\sigma T^4(z')}[1-\tau_\nu(z,z')]d\nu, \tag{2.6}$$

and

$$\tau_\nu(z,z',\mu) = \exp\left[-\frac{1}{\mu}\int_{u(z)}^{u(z')} k_\nu(p,T)du\right], \tag{2.7}$$

The absorption coefficient k_ν is a function of pressure and temperature which varies throughout the atmosphere. This may be seen, for instance, in case of a single Lorentz shape line, for which the optical thickness between two levels (1) and (2) is given by

$$\tau_\nu(1,2) = \int_1^2 \frac{Sda}{\pi}\frac{\alpha_L}{\alpha_L^2+\nu^2} \tag{2.8}$$

where α_L is the line width, S is the line intensity (defined as the area under the absorption coefficient $(k_\nu) - \nu$ curve, and a is the absorber amount. The absorption is affected by temperature through the Boltzmann factor affecting the line strengths (which reflects the underlying probability of the transition), by both pressure and temperature via their effect on the line widths, and by absorber amount through Beer's law [Goody (1964);Rodgers (1967)]. As discussed in section 1.4 the inhomogeneity of the atmosphere could be taken into account via suitable scaling approximation. The simplest approximation with respect to temperature is to assume it to be a constant. Thus, for the isothermal flux-emissivity formulation, the broadband flux emissivity is defined as [Liou (2002)]:

$$\epsilon^f(u) = \int_0^\infty \pi B_\nu(T)[1-\tau_\nu(u,1/\beta)]\frac{d\nu}{\sigma T^4}. \tag{2.9}$$

Here, u is the scaled absorber amount which includes the effect of pressure and temperature and β is the diffusivity factor which models the angular dependence of the participating medium. A non-isothermal flux emissivity formulation was developed by Ramanathan & Downey (1986) which takes care of the temperature difference between the emitting and absorbing levels. The emissivity parameterization in principle, also by Rodgers (1967) accounts for an anisotropy, between the flux-emissivities defined for upward and downward trajectories ($\epsilon^{f\uparrow}$ and $\epsilon^{f\downarrow}$). These flux emissivities are distinct functions of u (the anisotropy apparently arises from accounting for temperature and pressure corrections in addition to those incorporated via the absorber path-length).

For a homogeneous atmosphere, and with other additional assumptions with regard to the thermodynamic scaling properties of the absorption paths, the central quantity in the broadband flux expressions (2.4-2.5) is the broadband flux-emissivity, $\epsilon^f(u)$, which may be defined as the ratio of the spectrally integrated emission from an isothermal column of participating medium of mass-absorption path-length u to that of a black body; here, u is related to the actual column height z by $u = \int_0^z \rho(z')\{\frac{p(z')}{p(0)}\}^\delta dz'$ $(0.5 < \delta < 1)$, δ being a thermodynamic scaling exponent, $\rho(z')$ being the concentration of the participating component, $p(z')$ the pressure at the level z'. Thus, an isothermal column emission at temperature T_0 is $F_{column}(u) = \epsilon^f(u)\sigma T_0^4$. Here,

$\epsilon^f(u) \to 0\,(1)$ for $u \to 0\,(\infty)$, so that short columns are nearly transparent while the emission of infinitely long columns is the same as that of a black body (see figure 2.2a).

The broadband flux-emissivity $\epsilon^f(u)$ is plotted in figure 2.2b as a function of the path length, and the expression used is based on an empirical parameterization developed by Zdunkowski and Johnson (1965) for a water-vapor-laden participating medium. The plot emphasizes the non-exponential variation of $\epsilon^f(u)$ with u for a non-gray medium - in this case, a water-vapor-laden atmosphere. An initial sharp increase, for small u, due to opaque-band emissions, is followed by a much slower increase due to weak emission in the transparent bands. The flux-emissivities for other atmospheric gases exhibit a similar dependence on u. This deviation of $\epsilon^f(u)$ from the exponential increase (shown as a dashed line in the figure 2.2b) characteristic of a gray medium is important. Since all natural surfaces are not perfectly black, Garratt & Brost (1981) first examined the effect of surface emissivity on the evolution of the NBL. In this case, there is an additional contribution to the radiative flux divergence from the attenuated reflected flux and, the authors used the same transmissivity to attenuate both the emitted and the reflected radiation. Although, by the very definition of $\epsilon^f(u)$, participating medium emission appears in a manner analogous to a solid surface, with $\epsilon^f(u)$ playing the role of the surface emissivity, the same is true for the attenuated reflected flux only for a gray medium wherein the spectral dependence of the intensity follows the Planck function. For a non-gray medium with a multiplicity of photon path-lengths, attenuation depends on the spectral contents of the incident radiation, and there can be no universal transmissivity. In particular, the attenuation corresponding to a broadband transmissivity defined by $\tau^f(u) = 1 - \epsilon^f(u)$ applies only to a gray incident radiation. The prevailing scheme for non-black surfaces proposed by Garrat and Brost (1981) fails to recognize this difference, and the authors used the same transmissivity to attenuate both the emitted and reflected radiation. Correctly capturing the variability of the *appropriate* reflected flux on local, regional and global scales is crucial to an accurate estimate of both the upwelling longwave fluxes and land surface temperatures via remote sensing in the thermal infrared [Wang *et al.* (2005)], and elimination of the aforementioned error in frequency-parameterized schemes is thus of considerable significance. Determination of the spatial variations in the surface emissivity, via flux measurements, would also allow a sensible classification of surface types [Running *et al.* (1994)].

2.3.1 The prevailing broadband flux-emissivity formulation for reflective ground

For an atmosphere bounded below by black ground, it is convenient to write the flux contributions as follows:

$$F^{\uparrow}_{eg}(u) = \sigma T_g^4 \tau^f(u), \tag{2.10}$$

$$F^{\uparrow}_{a}(u) = \int_0^u \sigma T^4(u') \dot{\epsilon}^f(u - u') du', \tag{2.11}$$

$$F^{\downarrow}_{a}(u) = \int_u^{u_t} \sigma T^4(u') \dot{\epsilon}^f(u' - u) du'. \tag{2.12}$$

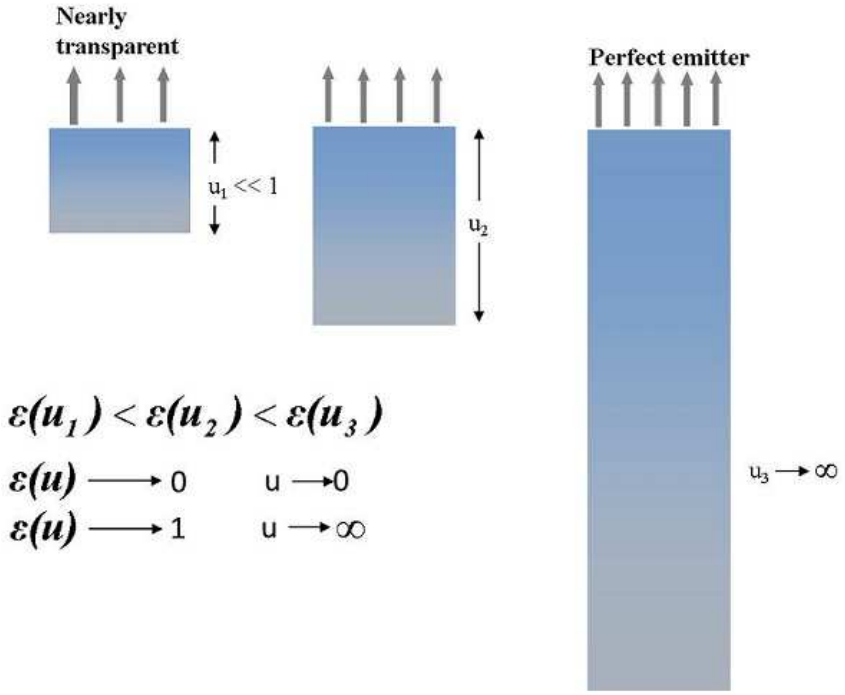

(a) Emission from an isothermal air column of height u

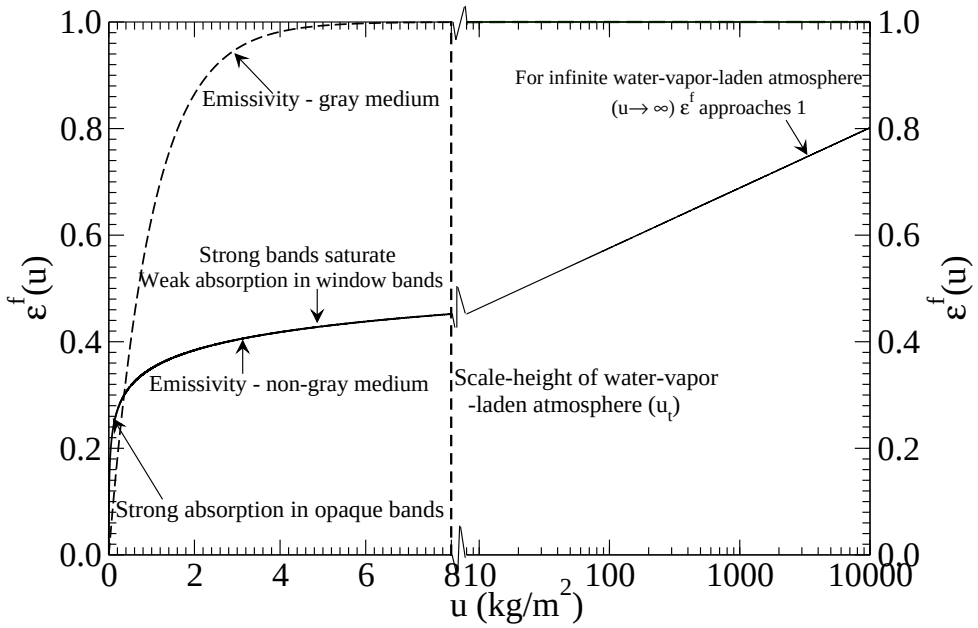

(b) Flux emissivity of water-vapor-laden atmosphere

Figure 2.2: A schematic of $\epsilon^f(u)$ as a function of the mass absorber path length u; the expression used is given in section 2.4 (see equation (2.51)). The flux emissivity for a gray medium, a simple exponential, is also shown with a photon mean-free-path of 200 m.

Here u_t is the scale height of the participating medium i.e water vapor in the present case. $F^{\uparrow}_{eg}(u)$ is the ground emission attenuated by the broadband flux- transmissivity $\tau^f(u)$ where $\tau^f(u) = 1 - \epsilon^f(u)$, $F^{\uparrow}_{a}(u)$ is the cumulative upward emission of air layers in the interval $(0, u)$, $F^{\downarrow}_{a}(u)$ is the cumulative downward emission of air layers between u and u_t and the dot in (2.11) and (2.12) denotes differentiation. Further, T_g is the ground temperature, $T(u)$ is the atmospheric temperature profile with u being the mass-absorber path length. In the absence of pressure-temperature scalings necessary for inhomogeneous paths [Garratt & Brost (1981)], and with water vapor as the only participating component, $u = \int_0^z \rho_w(z')dz'$, ρ_w being the water-vapor density. Thus, u may be regarded as a proxy height; the scale height of the water-vapor-laden atmosphere above is $u_t \approx 2.7km$. Water vapor is the dominant contributor to tropospheric radiative exchanges in the infrared (in the absence of clouds) and the smaller contributions of other gases are neglected here. The isothermality assumption in (2.6) restricts the magnitude of temperature variations within the region of interest, and the formulation above typically applies to each of many (nearly isothermal) layers [Liou (2002)]. This detail is again not central to the arguments presented here with regard to the sensitivity of the NBL thermal structure to surface emissivity ϵ_g, and (2.10)-(2.12) shall be applied to the entire atmosphere. A non-isothermal emissivity scheme has been given by Ramanathan and Downey (1986), and we return to the extension of this scheme to non-black surfaces at the end of this chapter.

As discussed briefly in the earlier section, Garrat and Brost (1981) were the first to extend the above formulation to a gray surface with emissivity ϵ_g as follows:

$$F^{\uparrow}_{eg}(u) = \epsilon_g \sigma T_g^4 \tau^f(u), \tag{2.13}$$

$$F^{\uparrow}_{a}(u) = \int_0^u \sigma T^4(u', t)\dot{\epsilon}^f(u - u')du', \tag{2.14}$$

$$F^{\downarrow}_{a}(u) = \int_u^{u_t} \sigma T^4(u', t)\dot{\epsilon}^f(u' - u)du', \tag{2.15}$$

$$F^{\uparrow}_{rg}(u) = (1 - \epsilon_g)F^{\downarrow}_{a}(0)\tau^f(u). \tag{2.16}$$

An additional contribution, the upwelling reflected flux $F^{\uparrow}_{rg}(u)$ proportional to $(1-\epsilon_g)$ arises, the ground emission itself being weakened by ϵ_g. Both the emission and reflection contributions in (2.13) and (2.16) are attenuated by $\tau^f(u)$. This is, however, incorrect due to the differing spectral characteristics of the two fluxes. Figure 2.4 highlights this difference between the spectra of $\epsilon_g F^{\uparrow}_{eg}(0)$ and $(1-\epsilon_g)F^{\downarrow}(0)$. While it is reasonable to approximate the spectral distribution of the ground emission by the Planck function $(B_\nu(T))$, the reflected flux departs sharply from such a gray approximation. Since the reflected flux at the surface represents the weakened downward emission of the entire water-vapor-laden air column, its spectral distribution may be inferred from that of water vapor emission. The latter is dominated by vibration-rotation transitions, and as a result, within wavelength intervals corresponding to the principal band-centers, relatively short columns behave as perfect emitters, while in the atmospheric window $(8 - 14\mu)$, the entire atmosphere remains a deficient emitter (see figure 2.3). As will be seen, not accounting for this difference between the emitted and reflected radiation spectra leads to a crucial error in the calculated cooling rates. The dashed line in figure 2.5 shows the transmissivity $\tau^f(u)$ appropriate

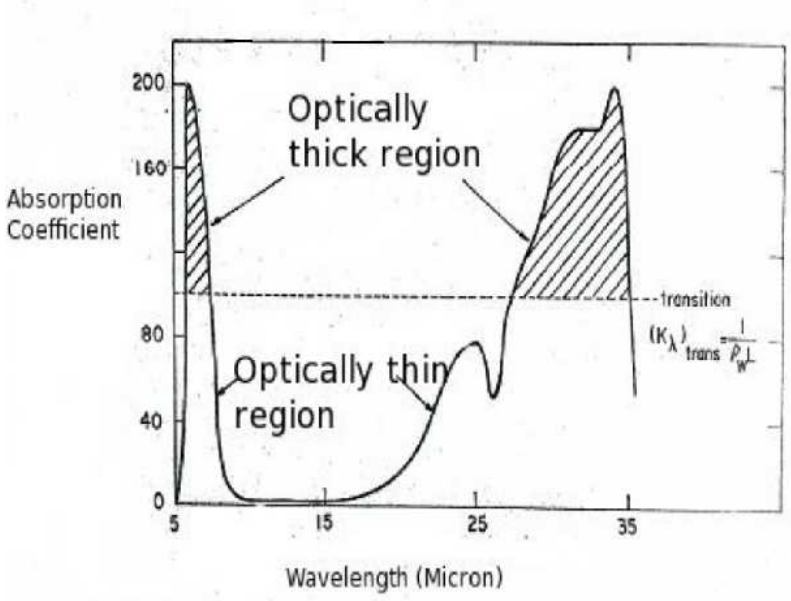

Figure 2.3: The water vapor spectrum shows the highly absorbing regions ($6.3\mu m$) where the medium behaves like a black body and the optically thin region ($8-14\mu m$) where the medium is effectively transparent over the water vapor scale height ($\approx 2.7km$).

for an incident radiation that has energy distribution like a Planckian. An initial steep decrease is due to the rapid removal of energy by the strongly absorbing wavelength intervals followed by a weaker attenuation in the atmospheric window. The reflected flux is already deficient in the transparent bands, and the initial rapid removal of opaque-band energy implies near-complete attenuation (the solid line in figure 2.5). The use of $\tau^f(u)$ for $(1-\epsilon_g)F^{\downarrow}(0)$ attributes a fraction of the incident opaque-band energy to the transparent bands, allowing it to escape to the upper atmosphere and beyond. The resulting deficiency over short length scales of $(O[\rho_w(0)\dot{\epsilon}^f(0)]^{-1})$ leads to a spurious near-surface cooling.

The error in using (2.16) can also be seen explicitly from the equations by noting that the broadband flux-emissivity is intended to capture the multiplicity of photon mean-free-paths in the IR spectrum shown in figure 2.3 and it is this multiplicity that is responsible for the deviation of $\tau^f(u)$ from a single exponential, and thence, the error discussed above. For the purpose of illustration, we consider a participating medium whose emission spectrum consist of two bands one corresponds to a strongly absorbing (opaque) wavelength interval and the other to a weakly absorbing one. The spectrum is intended as a simplistic model for the Janus-faced, nature of the water vapor emission-spectrum shown in figure 2.3. The two-band medium is characterized, by the following simple expression for the gray flux-emissivity:

$$\epsilon^f(u) = 1 - f_w \mathrm{e}^{-\alpha_w u} - f_{nw}\mathrm{e}^{-\alpha_{nw} u}. \tag{2.17}$$

Here, the subscripts 'w' and 'nw', respectively, denote the transparent window band and the strongly absorbing non-window band. The corresponding absorption coefficients are α_w and α_{nw}, with the fractions of the total radiant energy in the window and non-window bands being f_w and f_{nw}; thus, $f_w + f_{nw} = 1$. The above expression may be obtained from the exact expression for the gray flux-emissivity (see equation (2.9)) by assuming a constant absorption coefficient in each

of the two bands, and then, defining the fraction of energy in each band as $f_i = \int_{\lambda_i}^{\lambda_i+1} \frac{B_\lambda}{\sigma T^4} d\lambda$ and approximating the resulting exponential damping of the radiant intensity along any given direction by an angularly averaged exponential in the vertical coordinate. Thus, the inverses of the absorption coefficients in the individual bands are to be interpreted as angularly averaged photon mean-free-paths in the relevant frequency intervals. The length scales in the problem are ordered as $\alpha_{nw}^{-1} \ll u_t \ll \alpha_w^{-1}$; in other words, the atmosphere is transparent in the window band, while being nearly opaque in the non-window band. Thus, the linear combination of exponentials in equation 2.17 retains the most important characteristic of the flux-emissivity (see figures 2.2b and 2.3)- the initial steep increase to a value of $(1 - f_w)$ over a length scale of $O(\alpha_{nw}^{-1})$ on account of the strongly absorbing bands, and a much slower increase thereafter to unity, over a length scale of $O(\alpha_{nw}^{-1})$, indicative of a saturation of the opaque bands and subsequent weak absorption in the window band [Zdunkowski *et al.* (1966)]. Saturation of the latter, of course, doesn't happen over an atmosphere of height u_t, since $u_t \ll \alpha_w^{-1}$ as assumed above. Thus, in the domain $(0, u_t)$, to a good approximation, (2.17) may be interpreted as $\epsilon^f(u) \approx (1 - f_w)(1 - \mathrm{e}^{-\alpha_{nw} u})$.

Considering an isothermal atmosphere for simplicity, and using (2.17), the flux divergence can now be calculated from (2.13)-(2.16). The contributions for the two-band model are given by:

$$\frac{dF_{eg}^{\uparrow}}{du} = -\epsilon_g \sigma T_0^4 [f_w \alpha_w \mathrm{e}^{-\alpha_w u} + f_{nw} \alpha_{nw} \mathrm{e}^{-\alpha_{nw} u}], \tag{2.18}$$

$$\frac{dF_{a}^{\uparrow}}{du} = \sigma T_0^4 [f_w \alpha_w \mathrm{e}^{-\alpha_w u} + f_{nw} \alpha_{nw} \mathrm{e}^{-\alpha_{nw} u}], \tag{2.19}$$

$$\frac{dF_{a}^{\downarrow}}{du} = \sigma T_0^4 [f_w \alpha_w \mathrm{e}^{-\alpha_w (u_t - u)} + f_{nw} \alpha_{nw} \mathrm{e}^{-\alpha_{nw} (u_t - u)}], \tag{2.20}$$

$$\frac{dF_{rg}^{\uparrow}}{du} = -(1 - \epsilon_g) \epsilon(u_t) \sigma T_0^4 [f_w \alpha_w \mathrm{e}^{-\alpha_w u} + f_{nw} \alpha_{nw} \mathrm{e}^{-\alpha_{nw} u}], \tag{2.21}$$

where a negative sign denotes a heating contribution. The net radiative flux divergence in the Garratt & Brost (1981) formulation is given by the sum of the individual (signed) contributions, and may be written as

$$\frac{dF}{du} = \sigma T_0^4 \Big[(1-\epsilon_g)(f_w \alpha_w \mathrm{e}^{-\alpha_w u} + f_{nw} \alpha_{nw} \mathrm{e}^{-\alpha_{nw} u}) f_w \mathrm{e}^{-\alpha_w u_t} + f_w \alpha_w \mathrm{e}^{-\alpha_w (u_t - u)} \Big]. \tag{2.22}$$

Here, we have assumed $\mathrm{e}^{-\alpha_{nw} u_t} \approx 0$, so that $\epsilon^f(u_t) \approx (1 - f_w)$. The final term in (2.22) denotes the 'cooling to space' contribution, and arises on account of the transparency of the atmosphere in the window band. As expected, this contribution, being proportional to α_w, predicts a weak cooling, and a flux divergence that increases with height over a length scale of $O(\alpha_w^{-1})$. In other words, the upper air layers cool to space more efficiently. In the absence of a temperature discontinuity at the ground, and for a non-black surface, the dominant contribution to the cooling in the near-surface layers of air $(u \ll u_t)$ comes from the first term. If we neglect the much smaller contribution proportional to α_w which would be true for $u \leq O(\alpha_{nw}^{-1})$, this cooling of the near-surface air layers is seen to primarily arise due to the attenuation of the missing window-band-energy in the reflected radiation, $(1 - \epsilon_g) f_w \mathrm{e}^{-\alpha_w u_t} \approx (1 - \epsilon_g) f_w$, by the transmissivity

in the non-window band ($e^{-\alpha_{nw}u}$). In contrast to the cooling-to-space contribution, the cooling rate is now largest near the ground, being proportional to α_{nw}, and *decays* over a much shorter length scale of $O(\alpha_{nw}^{-1})$. In addition, this near-surface cooling relies crucially on a non-black surface and a transparent atmosphere ($\epsilon^f(u_t) < 1$). In the original formulation ((2.13)(2.16)), for the non-isothermal atmosphere, and for a general flux-emissivity function, the flux divergence is given by

$$\frac{dF}{du} = \frac{dF^{\uparrow}}{du} - \frac{dF^{\downarrow}}{du}, \tag{2.23}$$

$$= \sigma T_0^4[\dot{\epsilon}^f(u_t - u) + \dot{\epsilon}^f(u)(1-\epsilon_g)(1-\epsilon^f(u_t))], \tag{2.24}$$

where the (2.24) causes an increased cooling near the ground. But, the predicted cooling in (2.24) and (2.22), which is a simplified form of the original with in the two-band framework, is spurious. There can be no inter-band interaction as amplified since the window and non-window bands correspond to mutually exclusive wavelength intervals. Simply put, a photon of a given frequency cannot trigger a transition (in the infra-red range of interest, a vibration or a vibration-rotation transition) at a rate commensurate with the absorption coefficient in a different frequency interval. That such a coupling between different bands, which we call a 'band cross-talk', is erroneous is evident from the more fundamental spectral form of the flux-emissivity formulation [Liou (2002)], wherein the radiant energy balance is carried out separately at each wavelength (or frequency). In the context of the above simplistic analysis, however, the inconsistency in the above gray formulation is more easily seen by comparing its results with a two-band formulation which naturally avoids the aforementioned cross-talk between the bands. In the bandwise formulation, one defines flux-emissivities separately in the two bands as:

$$\epsilon_w^f(u) = (1 - e^{-\alpha_w u}), \tag{2.25}$$

$$\epsilon_{nw}^f(u) = (1 - e^{-\alpha_{nw} u}), \tag{2.26}$$

The calculation of the flux divergences, using the above band-emissivities, proceeds in an analogous fashion, and one obtains:

$$\frac{dF_w}{du} = f_w(\sigma T_0^4)[\alpha_w e^{-\alpha_w u}(1-\epsilon_g)e^{-\alpha_w u_t} + \alpha_w e^{-\alpha_w(u_t-u)}], \tag{2.27}$$

$$\frac{dF_{nw}}{du} = f_{nw}(\sigma T_0^4)[\alpha_{nw} e^{-\alpha_{nw} u}(1-\epsilon_g)e^{-\alpha_{nw} u_t} + \alpha_{nw} e^{-\alpha_{nw}(u_t-u)}]. \tag{2.28}$$

for the flux divergences in the two bands in an isothermal atmosphere where $f_w\sigma T_0^4$ and $f_{nw}\sigma T_0^4$ denote the radiant energies in the two-bands . The total flux divergence is

$$\frac{dF}{du} = \frac{dF_w}{du} + \frac{dF_{nw}}{du},$$

$$= \sigma T_0^4[(1-\epsilon_g)(f_w\alpha_w e^{-\alpha_w(u+u_t)} + f_{nw}\alpha_{nw}e^{-\alpha_{nw}(u+u_t)}) + (f_w\alpha_w e^{-\alpha_w(u_t-u)}$$

$$+ f_{nw}\alpha_{nw}e^{-\alpha_{nw}(u_t-u)}]. \tag{2.29}$$

As expected (2.29) predicts that, there is no band cross-talk, and thence, no preferential cooling of air layers near the ground. The terms proportional to $(1-\epsilon_g)$ in both (2.27) and (2.28) remain

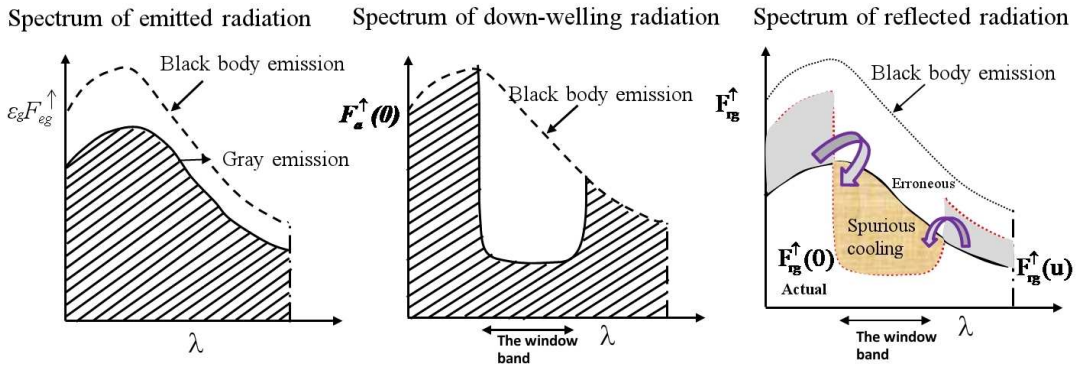

Figure 2.4: The spectral energy distribution of the gray-ground emission ($F_{eg}^{\uparrow}$), downwelling surface flux ($F_a^{\downarrow}(0)$) and reflected flux ($F_{rg}^{\uparrow}(0)$).

smaller than the respective cooling-to-space contributions, and the flux divergence profiles do not differ qualitatively for black and non-black surfaces. In either case, the cooling-rate profile exhibits a weak *increase* with height over a scale of kilometers. The strong interaction present in the gray theory is now absent even in the non-window band, since any cooling on short length scales is weakened by the opacity of the band. Indeed, since $e^{-\alpha_{nw} u_t} \approx 0$, in general, the near-surface air layers in opaque bands can never cool to outer space. All radiative exchanges in such a band are restricted to the immediate nearly isothermal neighborhood of a given air layer (this neighborhood being of the order of a photon mean-free path in the opaque bands).

The error committed above is, in a sense, obvious since the broadband transmissivity must respect the spectral distribution of the incident energy. There can be no universal frequency-averaged transmissivity and even $\tau^f(u)$ in (2.13) is the correct transmissivity only for ground that is radiatively gray. For a water-vapor-laden atmosphere, however, information regarding the spectral distribution of radiant energy, as a function of the path length traversed, is contained in $\epsilon^f(u)$, and it is thus possible to obtain the correct transmissivity ($\tau_r^f(u)$) as a function of the actual $\epsilon^f(u)$ rather than the simplified two-band model treated in this section. In what follows, we obtain $\tau_r^f(u)$ (to be used in (2.16) in place of $\tau^f(u)$).

2.3.2 The correct flux-emissivity formulation

Herein, we first obtain the broadband transmissivity, and thence, the reflected flux, for an isothermal atmosphere. The expression for the reflected flux is then generalized to the case of a non-isothermal atmosphere.

An isothermal clear atmosphere with reflective ground

The correct transmissivity is obtained via two approaches. The first approach although indirect is the easier one as it relies only on the definition of the flux-emissivity. Here, the attenuated reflected flux as a function of u is obtained and the correct transmissivity is a consequence. The second approach is more direct in seeking to obtain the correct transmissivity for the upwelling reflected flux at the surface.

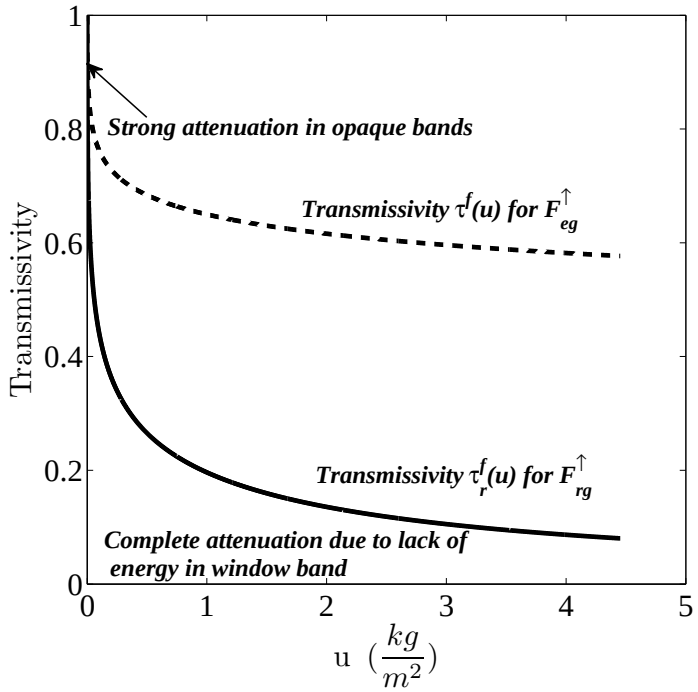

Figure 2.5: The broadband transmissivities for attenuating emitted photons from ground and the correct transmissivity to attenuate the reflected flux (see equation (2.31)).

.

Approach 1

By definition of the flux-emissivity, an infinite water-vapor-laden air column would be a perfect emitter (see figure 2.2a). Thus, accounting for the non-Planckian spectrum of the correct reflected flux implies accounting for the finite path length ($\sim O(u_t)$) of the reflected photons. Now, reflection only weakens the radiant intensity by a factor $(1-\epsilon_g)$, leaving the spectrum unchanged. Hence, rather than separately account for the downward emission from a column of height u_t, and subsequent attenuation of the upwelling reflected flux through a further distance u, it is convenient to instead consider the combined emission of a hypothetical isothermal air column of height $(u+u_t)$; the essential idea is illustrated in figure 2.6. The expression for this extended column emission is immediate viz. $\epsilon^f(u+u_t)\sigma T_0^4$, and the reflection interaction simply amounts to weakening this emission by $(1-\epsilon_g)$. The resulting emission includes the (weakened) upward emission contribution of the air column of height u. Since the latter is already accounted for in $F_a^{\uparrow}(u)$, it must be removed. Doing so, one obtains the following expression for the attenuated reflected flux at height u as:

$$F_{rg}^{i\uparrow}(u) = (1-\epsilon_g)[\epsilon^f(u+u_t) - \epsilon^f(u)]\sigma T_0^4, \tag{2.30}$$

for an isothermal atmosphere. Since the downwelling surface flux, $F_a^{i\downarrow}(0) = \epsilon^f(u_t)\sigma T_0^4$, the implied transmissivity for the reflected radiation is $\tau_r^f(u) = (\epsilon^f(u+u_t) - \epsilon^f(u))/\epsilon^f(u_t)$ in an isothermal atmosphere

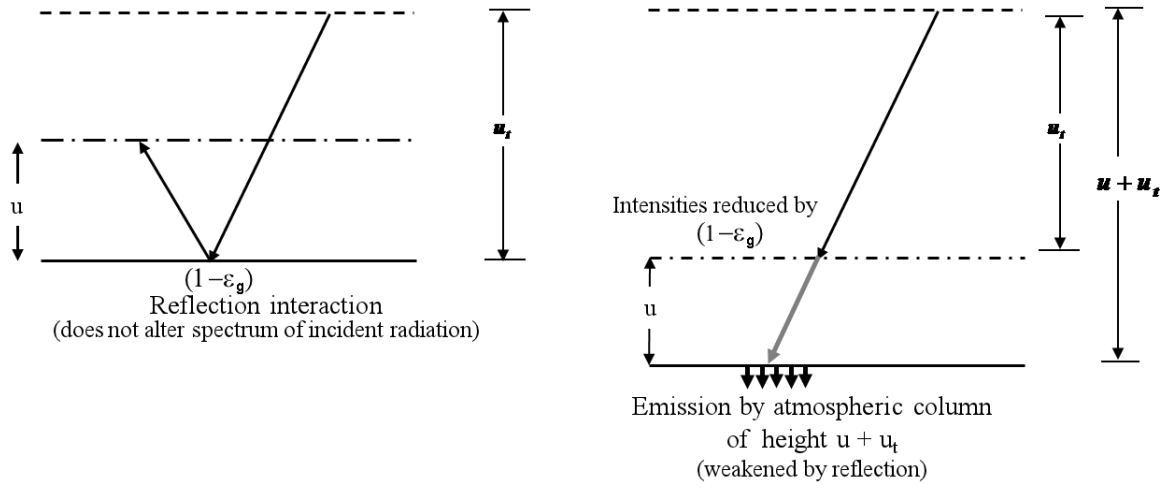

Figure 2.6: Obtaining the correct expression for the attenuated reflected flux at height u.

Approach 2

Having argued for the inappropriateness of $\tau^f(u)$ for $F^{\uparrow}_{rg}$ in (2.16), it is natural ask for the correct transmissivity to be used for attenuating the reflected radiation. In order to obtain $\tau^f_r(u)$ directly, rather than via the flux-emissivity as in the approach above, we first note that $\tau^f(u)$ corresponds to the attenuation, over a distance u, of an incident radiation with a spectral energy distribution that follows the Planck function. Then, $\tau^f(u+u_t)$ denotes a similar attenuation over the distance $(u+u_t)$; in other words, the additional attenuation, over a distance u, of incident radiation with band energies that survive after traversing a water-vapor-laden air column of height u_t. Said differently, $\tau^f(u+u_t)$ denotes the attenuation, over a distance u, of an incident radiation with energies in those bands that cannot be absorbed by an air column of height u_t. From Kirchhoff's law, what cannot be absorbed cannot be emitted; thus, $\tau^f(u+u_t)$ may therefore be regarded as the attenuation, over a distance u, of incident radiation with band energies that cannot be emitted by an air column of height u_t. The difference, $\tau^f(u)-\tau^f(u+u_t)$, therefore corresponds to attenuating, over u, an incident radiation whose band energies correspond precisely to the emission of a column of height u_t. Thus, $\tau^f_r(u)$ must be proportional to $(\tau^f(u)-\tau^f(u+u_t))$. With the appropriate normalization, so that $\tau^f_r(0)=1$, we have

$$\tau^f_r(u) = \frac{(\tau^f(u)-\tau^f(u+u_t))}{(1-\tau^f(u_t))}, \tag{2.31}$$

$$= \frac{(\epsilon^f(u+u_t)-\epsilon^f(u))}{\epsilon^f(u_t)}. \tag{2.32}$$

which is consistent with (2.30) for the reflected flux.

From (2.31), we note that $\tau^f_r(u)$ reduces to $\tau^f(u)$ only in two limiting instances. The first is for a hypothetical infinite atmosphere $(u_t \to \infty;\ \tau^f(u_t), \tau^f(u+u_t) \to 0)$. In this case, the downwelling flux at the surface corresponds to the emission of an infinitely high air column, and must therefore have a spectral energy distribution that follows a Planck function without any windows. The second limit is that of a radiatively gray participating medium wherein photons

of all wavelengths are attenuated, on average, over the same distance. Denoting this average path-length as α^{-1}, both $\tau^f(u)$ and $\tau_r^f(u)$ reduce to $\mathrm{e}^{-\alpha u}$. The requirement of radiatively gray behavior may be seen with a little more rigor by equating (2.31) to $\tau^f(u)$. The necessary and sufficient condition for this equality to hold is given by

$$\tau^f(u+u_t) = \tau^f(u)\tau^f(u_t). \tag{2.33}$$

The only continuous solution of the above Cauchy functional equation is an exponential function [continuity at even a single point is sufficient for uniqueness Aczel (1996)]. Neither of the above limits is, of course, realized in practice. On one hand, the density scale height of water vapor is finite as already stated earlier, $u_t \approx 2.7$ km. On the other hand, the absorption coefficients of atmospheric gases exhibit an enormous wavelength sensitivity (for reasons discussed in chapter 1) as a result of which, over any spectral interval larger than a small fraction of an elementary line width, the frequency-averaged transmittance will no longer be a decaying exponential as stipulated by Beer-Lambert's law. The resulting discrepancy between the transmissivities $\tau^f(u)$ and $\tau_r^f(u)$ will necessary lead to an error in the radiative flux divergence, calculated using (2.13)-(2.16), for an isothermal atmosphere.

In summary, the various contributions to the net radiative flux, for an isothermal atmosphere with reflective ground, may be written as:

$$F_{eg}^{i\uparrow}(u) = \epsilon_g \sigma T_0^4 \tau^f(u), \tag{2.34}$$

$$F_a^{i\uparrow}(u) = \epsilon^f(u)\sigma T_0^4, \tag{2.35}$$

$$F_a^{i\downarrow}(u) = \epsilon^f(u_t-u)\sigma T_0^4, \tag{2.36}$$

$$F_{rg}^{i\uparrow}(u) = (1-\epsilon_g)[\epsilon^f(u+u_t) - \epsilon^f(u)]\sigma T_0^4. \tag{2.37}$$

The radiative flux divergence obtained from (2.34)-(2.37) is given by:

$$\frac{dF}{du} = \sigma T_0^4[\dot{\epsilon}^f(u_t-u) + (1-\epsilon_g)\dot{\epsilon}^f(u+u_t))] \tag{2.38}$$

Note that near the ground, where $u \ll u_t$, both terms in (2.38) are approximately proportional to $\dot{\epsilon}^f(u_t)$ and exhibit only a weak variation with increasing height. As a result, unlike the flux divergence obtained from the naive formulation (see 2.24 and 2.22), the additional factor of $(1-\epsilon_g)$ makes the second term much smaller than the cooling-to-space contribution for ϵ_g close to unity.

Non-isothermal clear atmosphere with reflective ground

To generalize (2.30) to the case of a non-isothermal atmosphere, we note from (4.3) that the downward emission of a non-isothermal air column extending from u to u_t is given by

$$F_a^{\downarrow}(u) = \int_u^{u_t} \sigma T^4(u',t)\dot{\epsilon}^f(u'-u)du', \tag{2.39}$$

and the emission, $\epsilon^f(u+u_t)\sigma T_0^4$, of an isothermal air column of height $(u+u_t)$ now takes the form

$$F_a^{\downarrow}(-u) = \int_{-u}^{u_t} \sigma T^4(|u'|,t)\dot{\epsilon}^f(u'+u)du', \tag{2.40}$$

in a non-isothermal atmosphere. Here the lower limit, $-u$, implies the (conceptual) reversal of the reflected trajectory illustrated in figure 2.6. The argument of the temperature field is $|u'|$ rather than u' since the photons that make up the reflected flux traverse the region $(0,u)$ twice in arriving at u. Subtracting (4.2) for the upward air emission, and adding the pre-factor $(1-\epsilon_g)$, one obtains

$$F_{rg}^{\uparrow}(u) = (1-\epsilon_g)\left[\int_{-u}^{u_t} \sigma T^4(|u'|,t)\dot{\epsilon}^f(u'+u)du' + \int_0^u \sigma T^4(u',t)\dot{\epsilon}^f(u-u')du'\right]. \tag{2.41}$$

Splitting the range of integration in the first term into $(-u,0)$ and $(0,u_t)$, and using the variable transformation $u' \leftrightarrow -u'$ in the first integral, (2.41) simplifies to:

$$F_{rg}^{\uparrow}(u) = (1-\epsilon_g)\int_0^{u_t} \sigma T^4(u',t)\dot{\epsilon}^f(u+u')du'. \tag{2.42}$$

The above expression also has an easier interpretation. Writing the argument, $(u+u')$, of the flux-emissivity as $u-(-u')$, we note that $-u'$ denotes the path-length of the photon before reflection that contributes to the upward emission at u. The length of this downward trajectory alone extends from 0 to u_t which fixes the range of integration of u' in (2.42). Including both the upward and downward trajectories, the reflected photons must then have a total path-length whose magnitude is at least u extending up to a maximum of $(u+u_t)$.

Correct Reflected term from monochromatic radiative balance

The expression, (2.42), for the reflected flux may also be directly obtained from the frequency-dependent expression for the monochromatic reflected flux. The upward $F_\nu^{\uparrow}$ and downward $F_\nu^{\downarrow}$ monochromatic radiative fluxes at any height z is given by:

$$\begin{aligned} F_\nu^{\uparrow}(z) =& \epsilon_{g\nu}\pi B_\nu(z=0)\tau_\nu^f(z,z=0) + \int_0^z \pi B_\nu(z')\frac{d\tau_\nu^f}{dz'}(z,z')\,dz' \\ &- \tau_\nu^f(z)\int_0^\infty (1-\epsilon_{g\nu})\pi B_\nu(z')\frac{d\tau_\nu^f}{dz'}(0,z')\,dz', \end{aligned} \tag{2.43}$$

$$F_\nu^{\downarrow}(z) = -\int_0^\infty \int_z^\infty \pi B_\nu(z')\frac{d\tau_\nu^f}{dz'}(z,z')\,dz'd\nu, \tag{2.44}$$

which are the same as that given earlier in chapter 1 (see equation 1.9). The monochromatic reflected component at any height z is given by

$$F_{rg\nu}^{\uparrow}(z) = -\int_0^\infty (1-\epsilon_{g\nu})\pi B_\nu(z')\frac{d\tau_\nu^f(z')}{dz'}\tau_\nu(0,z)\,dz', \tag{2.45}$$

which generalizes equation (1.8) in chapter 1 to the case of a non-black surface with an arbitrary spectral dependence, (neglecting the angular dependence of the surface emissivity). For a wave-

length interval which is much less than the half width of the line (the region over which Beer Lambert's law obeyed) the transmissivity can be written in terms of exponential as indicated in chapter 1 (see (2.7)) and using the scaling approximation to account for the variation of the absorption characteristics of the participating medium, the above expression can be simplified and reduced to

$$F^{\uparrow}_{rg\nu}(z) = -\int_0^{\infty} (1-\epsilon_{g\nu})\pi B_\nu(z')\frac{d\tau_\nu(z+z')}{dz'}\,dz' \tag{2.46}$$

At a single wavelength, $\tau_\nu(z)\tau_\nu(z') = \tau_\nu(z+z')$ holds because of the exponential nature of the transmissivity. This naturally avoids the error since the path length of the reflected photon has been accounted properly. Now, the integration over wavelength can be carried out and defining the emissivity as in equation (2.6) gives the corrected reflected component defined in (2.50).

To summarize, the broadband flux-emissivity formulation, for a non-isothermal atmosphere with reflective (gray) ground, may now be summarized as:

$$F^{\uparrow}_{eg}(u) = \epsilon_g \sigma T_g^4 \tau^f(u), \tag{2.47}$$

$$F^{\uparrow}_{a}(u) = -\int_0^{u} \sigma T^4(u')\dot{\epsilon}^f(u-u')du', \tag{2.48}$$

$$F^{\downarrow}_{a}(u) = \int_u^{u_t} \sigma T^4(u')\dot{\epsilon}^f(u'-u)du', \tag{2.49}$$

$$F^{\uparrow}_{rg}(u) = (1-\epsilon_g)\int_0^{u_t} \sigma T^4(u')\dot{\epsilon}^f(u+u')du'. \tag{2.50}$$

Note that the difference between the Garratt & Brost (1981) formulation, as given by equations (2.13)-(2.16), and the above corrected formulation is the expression for the reflected flux.

2.4 Cooling-rate profiles for model atmospheres

We now examine the cooling-rate (flux-divergence) profiles obtained from the two formulations, viz. (2.13)-(2.16) and(2.47)-(2.50), for model atmospheres. The $\epsilon^f(u)$ used in these calculations (plotted in Figure 2.2b) is given by Zdunkowski & Johnson (1965):

$$\epsilon^f(u) = a_1 \ln(1+b_1 u) \quad \text{for} \quad u \le 10^{-2}\text{kgm}^{-2}, \tag{2.51}$$

$$= a_2 \ln(1+b_2 u) \quad \text{for} \quad u > 10^{-2}\text{kgm}^{-2}, \tag{2.52}$$

where $a_1 = 0.04902$, $a_2 = 0.05624$, $b_1 = 1263.5\text{m}^2\text{kg}^{-1}$ and $b_2 = 875\text{m}^2\text{kg}^{-1}$. The above expressions were originally proposed by Zdunkowski and Johnson (1965) since the temperature profile determined by solving the energy equation, using (2.51) and (2.52), was found to compare well with lab experiments [Corradini & Severini (1975)]. The piecewise continuous profile described by (2.51) and (2.52), has a kink however, that leads to a discontinuity in $\dot{\epsilon}^f(u)$, and thence, in the calculated cooling-rate profiles. We therefore approximate $\epsilon^f(u)$ over the entire range of u by (2.51) alone. The focus of the calculations in this section is on the near-surface flux divergence, and (2.51) is the relevant representation close to the surface. The approximation leads to an error of less than $20\,\text{Wm}^{-2}$ in the calculated fluxes, and is sufficiently accurate for

the proof-of-principle calculations here. That the use of (2.51) alone for $\epsilon^f(u)$ leads only to insignificant numerical differences has already been verified by Vasudevamurthy et.al (2005).

The flux-divergence profiles over the lowest 10 m for the simplest model atmosphere, an isothermal water-vapor-laden atmosphere, obtained from the two flux-emissivity formulations ((2.13)-(2.16) and (2.47)-(2.50)), are compared in figure 2.7. The comparison is in terms of the predicted cooling rates given by $\left(\frac{\rho_w}{\rho_a c_p}\frac{dF}{du}\right)$ with $F(u) = F^{\uparrow}(u) - F^{\downarrow}(u)$. The two cooling rate profiles are coincident for $\epsilon_g = 1$ as they must be. For $\epsilon_g < 1$, the deficiency of the reflected flux in the erroneous formulation, on length scales of $O[(\rho_w(0)\dot{\epsilon}^f(0))^{-1}]$, leads to a pronounced cooling in a region of the same extent. Even for a surface that is nearly black, that is, for an emissivity of $\epsilon_g = 0.9$, the spurious cooling rate close to the surface is more than two orders of magnitude greater than its actual value. This heightened sensitivity to surface emissivity is absent in the correct formulation. The latter continues to predict a cooling rate that increases with increasing height, although this is not obvious in the comparisons for $\epsilon_g = 0.8$ and $\epsilon_g = 0.9$ owing to the enormous disparity in the cooling rate magnitudes. The cooling rate profile predicted using (2.34)-(2.37) is also in accordance with intuition since layers higher-up in an isothermal atmosphere receive relatively smaller amounts of downwelling warming flux from the overlying atmosphere. Simply put, in a compositionally homogeneous atmosphere, that is, on length scales much smaller than the water-vapor scale height and for a fixed ground temperature, air layers closer to the cold source cool faster.

Figure 2.8 compares the cooling-rate profiles as a function of ϵ_g for an adiabatic lapse-rate atmosphere with $T(z) = T_g - \Gamma z$ and $T_g = 300\,\mathrm{K}$; here, Γ is the specified lapse rate, and $T_g = T(0)$, so there is no temperature discontinuity at the ground. For the chosen value of $\Gamma\,(-9.8\,\mathrm{Kkm}^{-1})$, the cooling rate decreases with height in contrast to the isothermal case above, since the cooling-to-space contribution is overwhelmed by the upwelling flux from the ground and the underlying warmer air layers. This is consistent with earlier LBL calculations for a water-vapor-laden tropical atmosphere [Chou *et al.* (1993)]. For $\epsilon_g = 1$ the flux divergences calculated from the two formulations are again coincident as they must be. For $\epsilon_g < 1$ the deficient reflected flux in the erroneous formulation again leads to a pronounced cooling near the ground. For $\epsilon_g = 0.9$, the erroneous surface cooling rate is already more than two orders of magnitude greater than its actual value, and there continues to be a substantial deviation even at 10 m.

The standard inversion profile under calm cloudless condition is usually modeled using an exponential profile [Stull (1988);Ha & Mahrt (2003)] and that under stronger wind conditions is modeled using an oscillating profile [Ha & Mahrt (2003)]. Figure 2.9 shows the cooling-rate profiles for an inversion layer, characterized by $T(z) = T_g + (\Delta T)(1 - e^{-\frac{z}{H}})$, and with $\epsilon_g = 1$; H here is specified *apriori* and ranges from 0.001 m to 10 m, and ΔT is assumed to be 5 K in the calculations. In principle, H must be obtained from solving the energy equation, and is then found to be a time-dependent quantity that increases through the night starting from very small values in the evening transitional layer [Edwards (2009a); Edwards (2009b)]. The profiles in Figure 2.9, for increasing H, may loosely be regarded as corresponding to successive instants of time after sunset. The nocturnal inversion layer provides a rather severe test for the vertical resolution used in radiation calculations [Räisänen (1996); Savijärvi (2006)]. The flux-divergence profile in

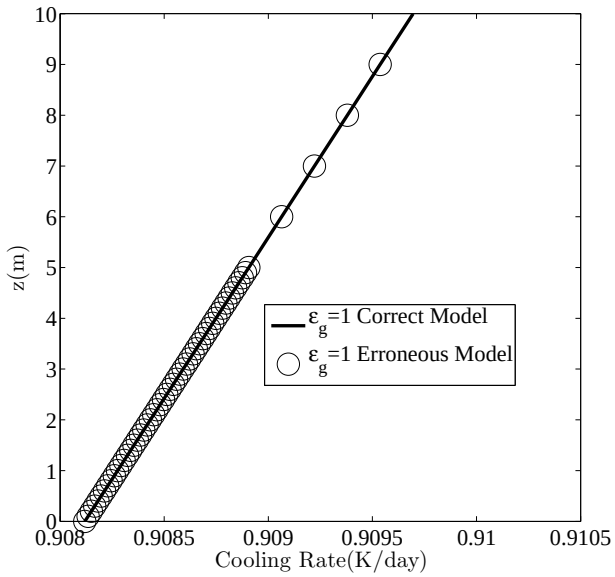

(a) $\epsilon_g = 1$

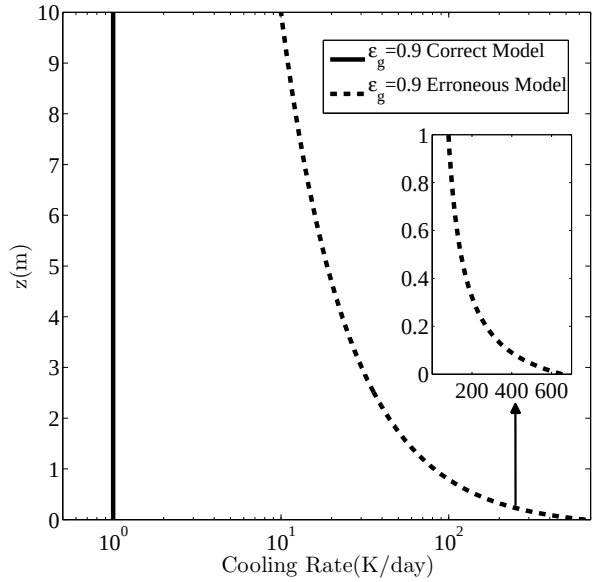

(b) $\epsilon_g = 0.9$

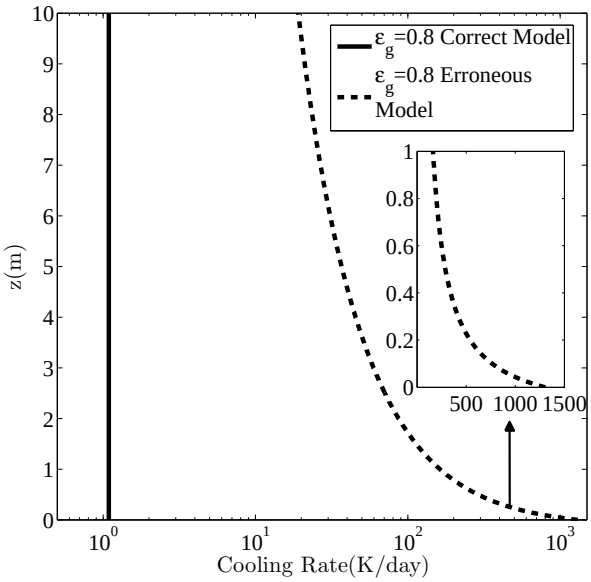

(c) $\epsilon_g = 0.8$

Figure 2.7: Cooling-rate profiles obtained from the correct and erroneous flux-emissivity formulations (using equations (2.47)-(2.50) and (2.13)-(2.16)) for ϵ_g of a)1, b)0.9 and c)0.8, and for an isothermal atmosphere.

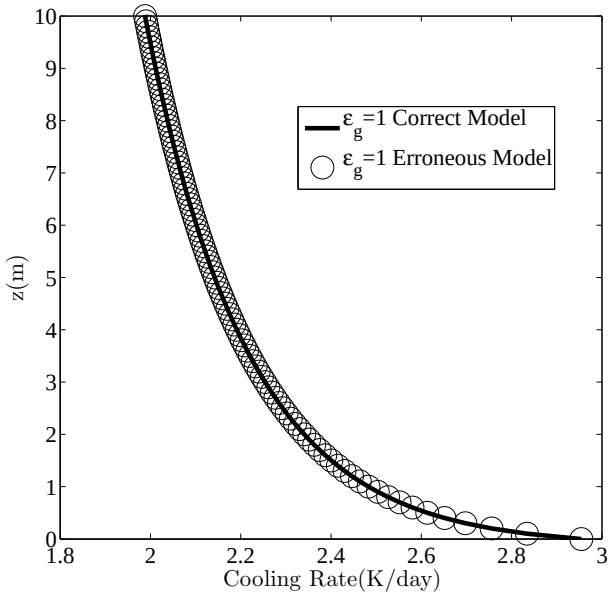

(a) $\epsilon_g = 1$

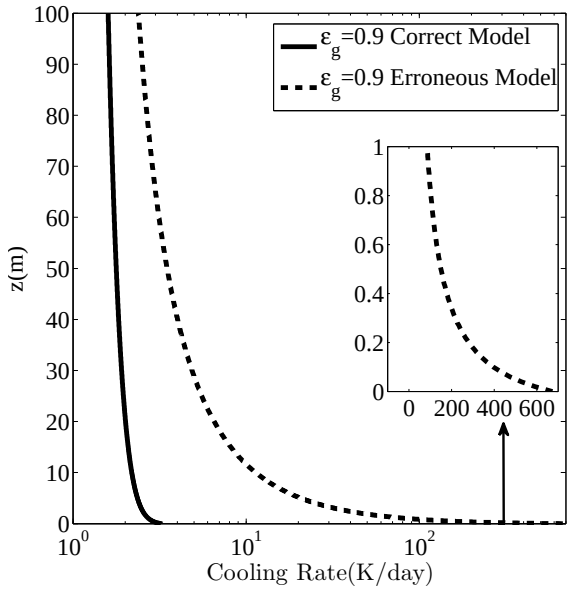

(b) $\epsilon_g = 0.9$

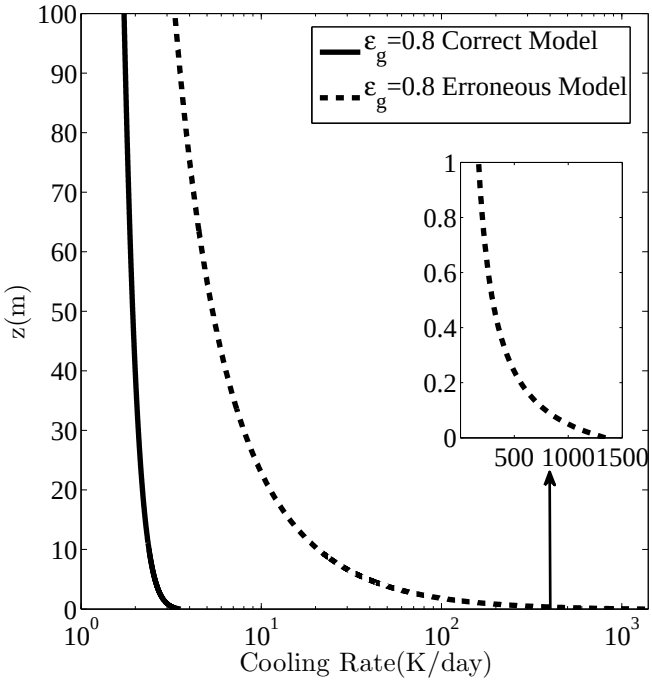

(c) $\epsilon_g = 0.8$

Figure 2.8: Cooling-rate profiles obtained from the correct and erroneous flux-emissivity formulations (using equations (2.47)-(2.50) and (2.13)-(2.16)) for ϵ_g of a)1, b)0.9 and c)0.8, and for a model atmosphere with a constant lapse-rate of $-9.8\,\mathrm{K/km}$ (ground temperature is assumed to be $300\,\mathrm{K}$).

a homogeneous atmosphere includes a shallow warming zone just above ground first predicted by Fleagle (1953) [see table (2.2)]. The warming arises because, for air layers sufficiently close to ground, the cooling-to-space contribution is dominated by opaque-band exchanges with warmer overlying air layers [Fleagle (1955);Edwards (2009a)]. This warming, however, will not be observed in calculations resolved on a scale larger than H, since the region of varying temperature now appears as a slip $(T(0) - T_g)$, and leads to a near-surface cooling instead. The nature of the cooling-rate profile depends on the relative magnitudes of H and a representative photon mean-free-path of $O[(\rho_w(0)\dot{\epsilon}^f(0)]^{-1}$ in the opaque bands. The second plot in Figure 2.9 shows the cooling-rate profiles for various values of the dimensionless parameter $\rho_w(0)\dot{\epsilon}^f(0)H$. The vertical extent of the warming region decreases with decreasing $(\rho_w(0)\dot{\epsilon}^f(0)H)$, approaching the slip regime for $\rho_w(0)\dot{\epsilon}^f(0)H \to 0$.

An estimate for the warming flux-divergence at the surface is obtained on using (2.51) in (2.47)-(2.50). One finds

$$\left(\frac{dF}{du}\right)_{u=0}^{warming} \approx -\frac{\sigma(\Delta T)T_g^3}{\rho_w(0)H}\left[4a_1 e^{\frac{1}{b_1\rho_w(0)H}} E_1\left(\frac{1}{b_1\rho_w(0)H}\right)(2-\epsilon_g)\right], \tag{2.53}$$

where $E_1(z) = \int_z^\infty \frac{e^{-t}}{t}dt$ is the exponential integral [Abramowitz & Stegun (1990)], and the constants a_1 and b_1 have been defined in (2.51). The expression shows that the warming flux-divergence increases with decreasing ϵ_g. As argued by Zdunkowski *et al.* (1966), Lieske & A.Stroschein (1967) and more recently by Edwards (2009a), this is because the reflected flux comprises downward flux contributions from warmer air layers. The spurious cooling contribution, obtained by using (2.51) in equations (2.13) and (2.16) for an isothermal atmosphere, is given by

$$\left(\frac{dF}{du}\right)_{u=0}^{Spurious\,cooling} \approx (\sigma T_g^4)\dot{\epsilon}^f(0)(1-\epsilon_g)(1-\epsilon^f(u_t)), \tag{2.54}$$

where $\dot{\epsilon}^f(0) = a_1 b_1$. The cooling is evidently absent for $\epsilon_g = 1$, but increases sharply with decreasing ϵ_g. This, steep increase has, in several earlier calculations, led to an unphysical exaggeration of the effect of ground emissivity on NBL flux-divergence profiles [Garratt & Brost (1981); Savijärvi (2006)] which is discussed in the following section. One may now obtain $\epsilon_{g-crossover}$, corresponding to a change in sign of the surface flux divergence due to spurious cooling, by equating (2.53) and (2.54), whence

$$\epsilon_{g-crossover} = 1 - \frac{4(\Delta T)}{T_g}\frac{e^{\frac{1}{b_1\rho_w(0)H}} E_1(\frac{1}{b_1\rho_w(0)H})}{(\rho_w(0)a_1b_1H)\left[1 - a_1\ln(1+b_1u_t)\right]}. \tag{2.55}$$

This yields $\epsilon_{g-crossover} \approx 0.99$ and 0.92, respectively, for optically thick $(\rho_w(0)\dot{\epsilon}^f(0)H \to \infty)$ and thin $(\rho_w(0)\dot{\epsilon}^f(0)H \to 0)$ inversion layers. For $\epsilon_g < \epsilon_{g-crossover}$, the error in the prevailing Garratt & Brost (1981) formulation is large enough to change the sign of the surface flux-divergence. The plots in Figure 2.10 illustrate the competing effects of the near-surface warming and spurious cooling for ϵ_g's on either side of $\epsilon_{g-crossover}$, and for different values of $(\rho_w(0)\dot{\epsilon}^f(0)H) \equiv (\rho_w(0)a_1b_1H)$.

Next, we find the height up to which the warming zone exists by equating the radiative cooling rate to zero. The flux divergence, as a function of u, for the assumed inversion profile is given by

$$\begin{aligned}\frac{dF_z}{dz} &= \underbrace{\sigma T^4(u_t)\left[\dot{\epsilon}^f(u_t-u)+(1-\epsilon_g)\dot{\epsilon}^f(u_t+u)\right]}_{\text{Isothermal contribution}}+\frac{\sigma T_g^3\Delta T}{\rho_w(0)H}\Bigg\{4a_1e^{-\frac{(1+b_1\rho_w(0)u)}{\rho_w(0)H}}\\ &\left[Ei\left(\frac{(1+b_1\rho_w(0)u)}{\rho_w(0)H}\right)-Ei\left(\frac{1}{\rho_w(0)H}\right)\right]\\ &-\ 4a_1e^{-\frac{(1-b_1\rho_w(0)u)}{\rho_w(0)H}}\left[E_1\left(\frac{1}{b_1\rho_w(0)H}\right)-E_1\left(\frac{(1+b_1\rho_w(0)(u_t-u))}{\rho_w(0)H}\right)\right]\\ &-\ 4(1-\epsilon_g)a_1e^{-\frac{(1+b_1\rho_w(0)u)}{\rho_w(0)H}}\left[E_1\left(\frac{(1+b_1\rho_w(0)u)}{\rho_w(0)H}\right)-E_1\left(\frac{(1+b_1\rho_w(0)(u_t+u))}{\rho_w(0)H}\right)\right]\Bigg\}\end{aligned} \tag{2.56}$$

where $Ei(u)=\text{pv}\int_{-\infty}^{u}\frac{\mathrm{e}^t}{t}dt$ and $E_1(u)=\int_u^{\infty}\frac{\mathrm{e}^{-t}}{t}dt$ is the exponential integral [Abramowitz & Stegun (1990)]. Since there is no qualitative difference between black and gray surfaces, except for a mild increase in the near-surface warming as discussed above, we will consider only the case of a black surface. Since the radiative warming zone is very close to the ground, one expects $u \ll u_t$ and the cooling-to-space contribution can be neglected, that is, $\dot{\epsilon}^f(z_t)\approx 0$. With this approximation, it can be easily seen that the net heating or cooling of air layers is due to the non-isothermal contribution related to the, exchanges between the air layers in the opaque bands. This is in contrast to the conclusion drawn by Edwards (2009a) where, based on an incorrect governing equation [Edwards (2009a)], he concluded that the flux divergences is dominated by a 'cooling-to-surface' contribution. If one starts from the correct equation (which was subsequently done in an erratum; Edwards (2009a)), the cooling-to-surface term is identically zero, and any radiative cooling or heating during night time, is due to the exchanges between the air layers in the NBL. The equation for the height at which the divergence goes to zero is obtained by equating (2.56) to zero, whence one obtains:

$$Ei\left(\frac{1+b_1\rho_w(0)z}{\rho_w(0)b_1H}\right)-e^{\frac{2}{b_1\rho_w(0)H}}E_1\left(\frac{1}{b_1\rho_w(0)H}\right)-Ei\left(\frac{1}{b_1\rho_w(0)H}\right)=0, \tag{2.57}$$

and depends on the stratification length scale (H) and the smallest length scale in the spectrum $(b_1\rho_w)^{-1}$.This transcendental equation cannot be solved analytically for general values of $b_1\rho_w(0)H$, but one can look at the appropriate asymptotic limits that is, optically thick or thin inversion layers. In the optically thin limit $\rho_w(0)b_1H \ll 1$, the relevant length scale is $O(H)$ and in this limit, the crossover height is $O(H)$. In the optically thick limit, $\rho_w(0)b_1H \gg 1$ (2.57) reduces to

$$Ei\left(\frac{1+b_1\rho_w(0)z}{\rho_w(0)b_1H}\right)=\frac{-2}{\rho_w(0)b_1H}\log\left(\frac{1}{\rho_w(0)b_1H}\right) \tag{2.58}$$

Since the R.H.S is small the problem reduces to finding the zeros of the exponential integral and the value is $z=0.38H$. These results can be shown to be consistent with the numerical values obtained by evaluating the full integral equation for the flux divergence.

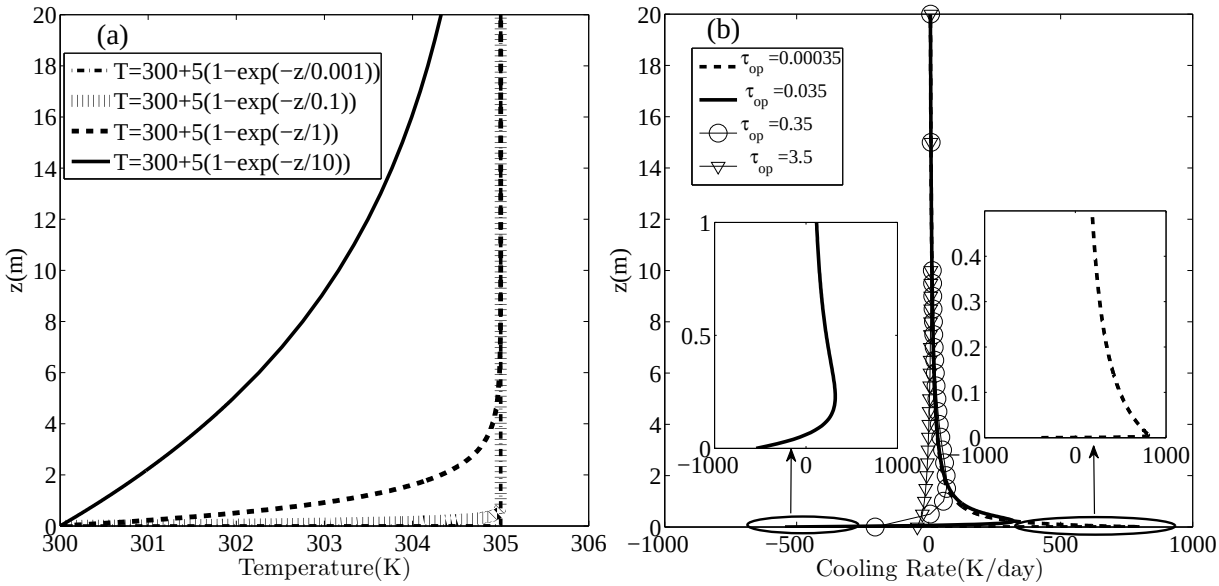

Figure 2.9: (a) Inversion layer temperature profiles for different H. (b) Cooling-rate profiles obtained as a function of $\rho_w(0)\dot{\epsilon}^f(0)H$ (the characteristic optical depth, τ_{op}, of the inversion layer) for $\epsilon_g = 1$.

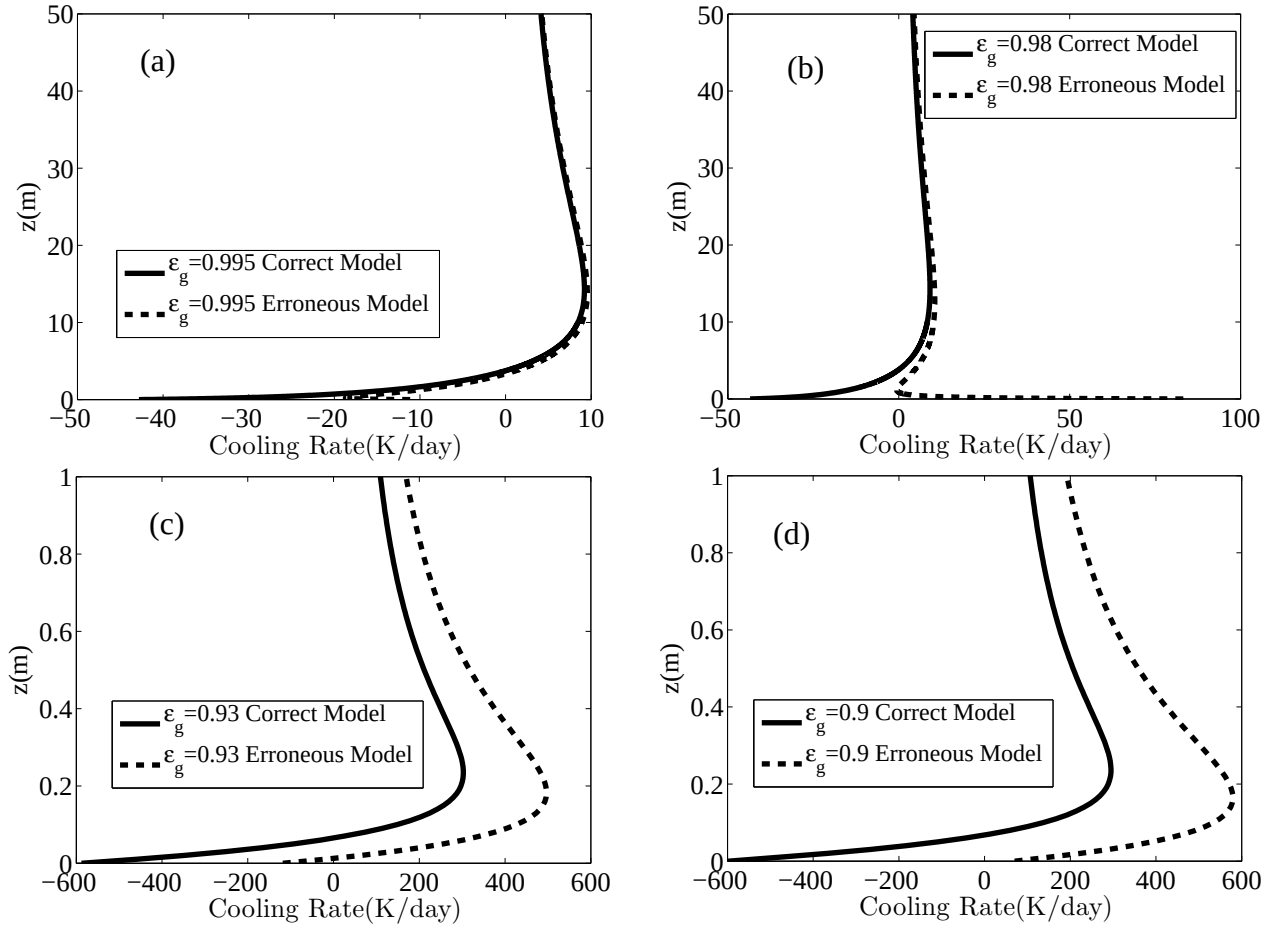

Figure 2.10: The plots compare the flux-divergence profiles, obtained from the correct and erroneous formulations (using equations (2.47)-(2.50) and (2.13)-(2.16)), for ϵ_g's or either side of $\epsilon_{g-crossover}$; figures (a) and (b), and figures (c) and (d), pertain to optically thick ($\tau_{op} = \rho_w(0)\dot{\epsilon}^f(0)H \gg 1$) and thin ($\tau_{op} = \rho_w(0)\dot{\epsilon}^f(0)H \ll 1$) inversion layers, respectively.

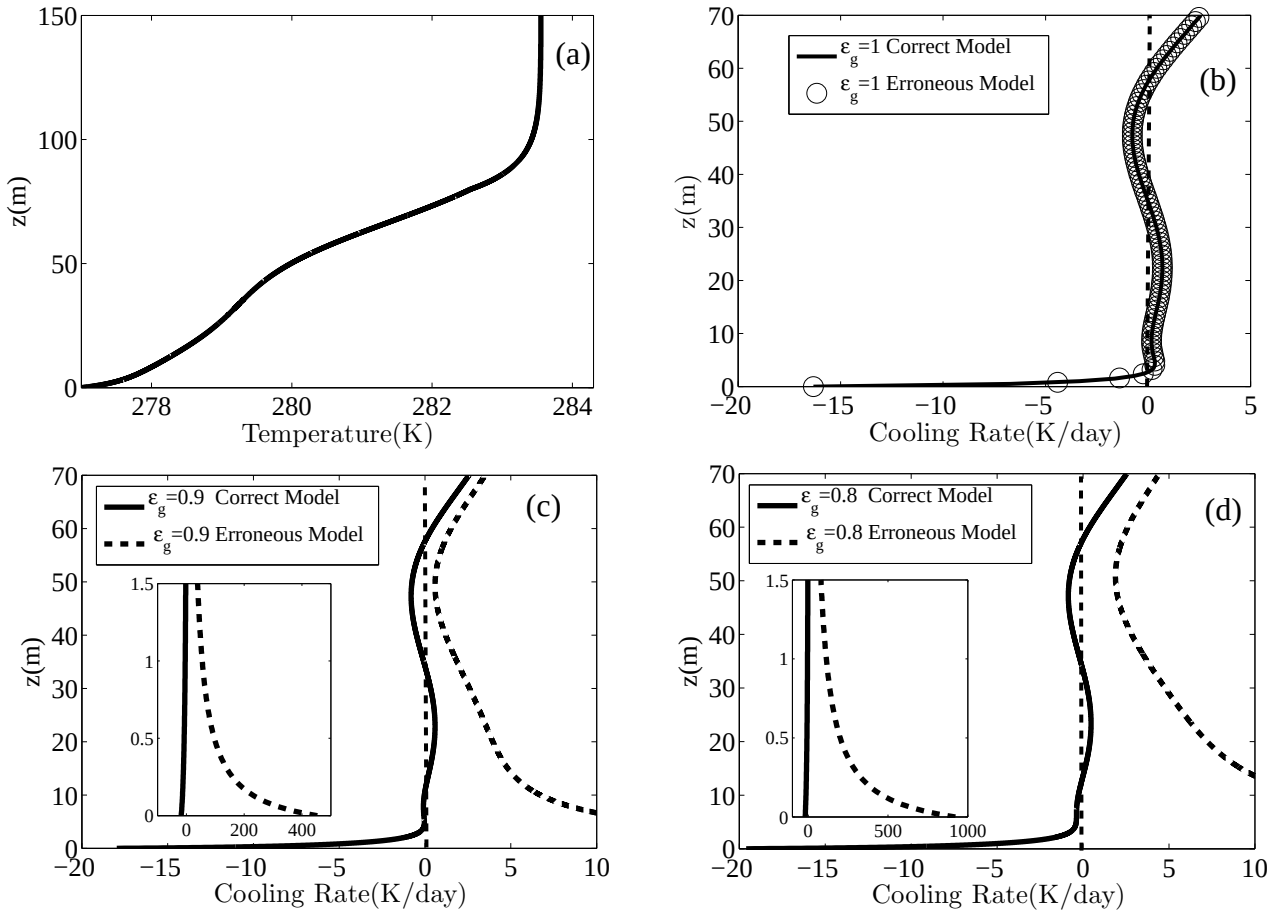

Figure 2.11: For the temperature profile shown in (a), plots (b),(c) and (d) show the cooling-rate profiles, obtained from the erroneous and correct formulations, for $\epsilon_g = 1$, 0.9 and 0.8.

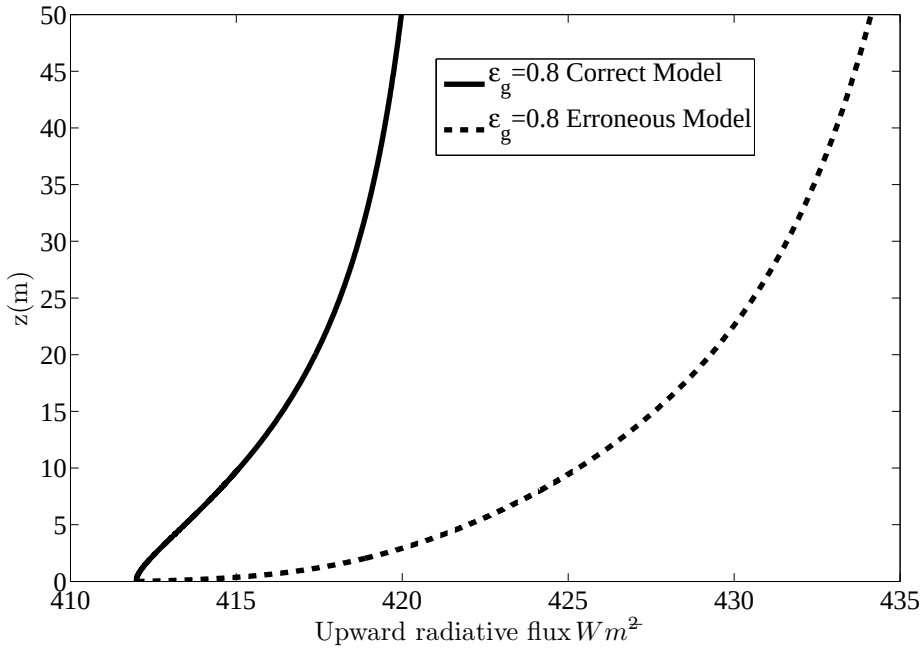

Figure 2.12: The upward radiative fluxes calculated for a inversion layer with a scale height of 10m and $\delta T = 5K$ by both correct formulation and erroneous formulation. The surface emissivity is $\epsilon_g = 0.8$

The spurious cooling error discussed above assumes particular significance for an inversion layer (the simplest model profile for the lowest meters of the NBL) since, as already discussed in section 2.2, the sign of the surface flux-divergence, under stable nocturnal conditions, remains controversial [Funk (1960); Lieske & A.Stroschein (1967); Nkemdirim (1978); Räisänen (1996); Hoch (2005); Edwards (2009a)]. Although the theoretical calculations [Edwards (2009a)] predict a near-surface warming in the NBL for $\epsilon_g = 1$ and a homogeneous atmosphere, the majority of observations support a radiative cooling in the lowest air layers [Funk (1960); Elliott (1963); Nkemdirim (1978); Sun *et al.* (2003)]. To date, there have been only two measurements, those of Lieske and Stroschein (1966) and more recently, those of Hoch (2005), that support a near-surface warming due to an inversion. The reason for this lack of agreement between the different experiments may be clear if one takes a closer look at figure 2.9 which shows the cooling-rate profiles for $\epsilon_g = 1$, together with the asymptotic expressions obtained above for the height of the warming zone. From the analysis, in the optically thin limit, it is clear that the radiative warming zone extends over the same length scale that characterizes the inversion temperature profile. As noted by Edwards (2009a), starting at sunset, this latter length scale increases with time throughout the night. Hence, the time during which the measurements are done, assumes significance. For instance, whether the measurements have been done during the transitional period or a later period of boundary layer development becomes important, since the resolution required to access the region of radiative warming is different in the two cases. For instance, Funk (1960) measured *radiative cooling* in the developing boundary layer where the vertical extent of warming is likely restricted very close to the ground. Lieske & A.Stroschein (1967) measured *radiative warming* over snow where the vertical temperature profile shows a strong and

deep inversion, and the radiative warming is likely spread over larger heights. Hoch (2005) also measured radiative warming over snow. The observation of an increase or decrease in cooling-rate with height depends upon the relative locations of the layers under observation relative to the inversion top [Hoch (2005) Wind speed also plays an important role in determining the vertical distribution of radiative fluxes (figure 2.9 and 2.11). Further, we will see in the later chapters 4 and 6, the possible departure from homogeneity in the lowest air layers [Mukund *et al.* (2010)], can also change the sign of radiative flux divergence near the ground.

Finally, it is worth mentioning that the assumed temperature profiles for the model atmospheres, in the above cooling-rate calculations, are devoid of any slip between the ground and the lowest air layers. The choice is deliberate since invoking a slip, as is done on an ad-hoc basis in many calculations [Ha & Mahrt (2003); Varghese (2003)], would trigger a net radiative exchange between the ground and the air layers in the opaque bands [Zdunkowski *et al.* (1966)]. The resulting cooling flux divergence, however, masks the spurious cooling that arises even for zero slip in the above formulation. The primary focus here has been on the vertical distribution of radiant energy, and thence, on the flux-divergence profiles. The discrepancy in the fluxes, although not small, is not as significant. For instance, for an inversion layer with $\Delta T = 5\,K$ and $H = 10\,\mathrm{m}$, the difference between the upward fluxes, obtained from the two formulations for $\epsilon_g = 0.8$, increases from zero at the surface asymptoting to about $20\,\mathrm{Wm}^{-2}$ at larger heights (see figure 2.12) .

2.5 Structure of the nocturnal boundary layer

The spurious cooling described above, and in earlier sub-sections, has arisen in a number of NBL calculations beginning with Garratt and Brost's attempt [Garratt & Brost (1981)] to examine the roles played by radiation and turbulence in NBL evolution, as a function of ϵ_g, with the radiation being modelled using an emissivity scheme. Subsequent efforts that use the same model, or generalizations thereof, include Andre & Mahrt (1981), Vasudevamurthy *et al.* (1993), Gopalakrishan *et al.* (1997), Koračin *et al.* (1989), Rißmann (1998) Ramakrishna *et al.* (2003), Varghese (2003), Savijärvi (2006), and Siqueira & Katul (2010). In some instances, the model, although stated in its general (and therefore, erroneous) form that is with the reflected flux being given by (2.16), is used only for $\epsilon_g = 1$. The error, when present, varies in magnitude due to differing vertical resolution, emissivity expressions, and varying levels of frequency parameterization (broadband flux-emissivity schemes; narrow-band formulations etc.). A list of earlier work which was affected by the spurious cooling error is tabulated in table **??**.It is shown in the next chapter that this error persists down to frequency intervals of the order of an elementary line width.

Author	**Surface emissivity** ϵ_g	**Cooling rate Kday**$^{-1}$
Garratt & Brost (1981)	1	
NBL	0.8	77 (at 2 m)
Andre & Mahrt (1981)	1	-57.6
NBL	0.965	288

Vasudevamurthy *et al.* (1993) Isothermal	1 0.8	0.3 1728
Varghese (2003) (MLS)	1 0.8	5 38
Savijärvi (2006) (MLS)	1 0.8	4 9.5

Table 2.3: Summary of earlier work in the literature which is affected by cross-talk error.

Based on the relative magnitudes of the turbulent and radiative flux divergences obtained from their simulations for $\epsilon_g = 0.8$, Garratt and Brost (1981) proposed a three-layer structure for the NBL with the top and bottom of this zone being dominated by radiative cooling and the 'bulk' being dominated by turbulence. A similar structure has been found more recently by Gopalakrishnan et al. (1997) and Ramakrishna et al. (2003). The dominance of radiation near the ground in the original simulations is due to spurious cooling. In fact, the exaggerated cooling for the said ϵ_g leads to a spurious peak in the sensible heat flux; and thereby also affects the structure of the turbulent zone. For $\epsilon_g = 1$, Andre and Mahrt (1982) highlight the two-layer NBL structure with a near-surface warming resulting from the inversion profile. This warming region is, however, absent in their calculations for $\epsilon_g = 0.965$ (shown in their appendix), again due to the spurious cooling contribution. As pointed out earlier in section 2.4, a reduced ϵ_g must lead to a relative warming, and the two-layer NBL structure must therefore remain qualitatively unaltered for a reduced ϵ_g.

For an inversion profile with a single-signed curvature (the exponential profile being a specific example), that is a characteristic of weak wind conditions, the flux-divergence profile exhibits a single transition from cooling at greater heights to a near-surface warming. However, in presence of turbulence, the temperature profile exhibits regions of opposite curvature - an additional positive curvature region (expected from the Monin- relations for the stably stratified regime [Turner (1973); Businger *et al.* (1971)] below the original negative curvature zone (see figure 2.11). This leads to a more complicated flux-divergence profile. As shown by Edwards (2009b), the flux divergence, in certain instances, may change sign thrice! An initial change from a cooling contribution at larger heights leads to an intermediate warming zone due to the change in profile curvature. Since the lower part of the profile continues to resemble the original inversion with a single-signed curvature, the flux-divergence changes sign again before finally approaching a near-surface warming. The intermediate warming region is present in earlier calculations including those of Andre and Mahrt (1982) (for the 'mixed layer' temperature profile), Savijärvi (2006), and possibly, even in Steeneveld (2007) (the 'radiation night' profile). In other instances, despite there not being an actual sign change, the cooling-rate profile does go through an intermediate minimum [Gopalakrishan *et al.* (1997); Ramakrishna *et al.* (2003)]. The final transition to a near-surface warming is absent in all these studies either due to coarse resolution or spurious cooling. The profiles in figure 2.11, for the smaller surface emissivities ($\epsilon_g = 0.8, 0.9$), show that the spurious cooling may even eliminate the second elevated region of warming. Since the latter is responsible, in part, for the prevailing notion of a radiative destabilization of the NBL, its

disappearance will evidently affect the overall energy budget. Finally, in many instances, an exaggerated near-surface cooling arises even for a black surface due to an assumed temperature slip at the ground [Räisänen (1996); Duynkerke (1999); Ha & Mahrt (2003); Savijärvi (2006)]: The resulting changes in the NBL structure are the same as those due to spurious cooling.

2.6 Extensions of the flux-emissivity scheme: Non isothermal Flux-Emissivity formulation

An expression for the reflected flux (as part of $F^{\uparrow}(u)$) may also be obtained within the non-isothermal emissivity formulation of Ramanathan and Downey (1986) (henceforth, the RD formulation). The flux expressions in this formulation, obtained from an integration by parts of the original broadband fluxes (see equations (2.13) and (4.3) in section 2.3) are given by

$$F^{\uparrow}(u) = \sigma T_g^4 + \int_0^u A(u,u')\frac{d}{du'}[\sigma T^4(u')]du', \tag{2.59}$$

$$F^{\downarrow}(u) = \sigma T_t^4 \epsilon(u,u_t) - \int_u^{u_t} A(u,u')\frac{d}{du'}[\sigma T^4(u')]du', \tag{2.60}$$

for $\epsilon_g = 1$, where ϵ and A are referred to as the non-isothermal emissivity and absorptivity, respectively. The said authors developed a parameterization for ϵ and A, based on a comparison with narrow-band calculations, in terms of a dependence on both the emitting level temperature and the temperature of the equivalent homogeneous path [Ramanathan & Downey (1986)]. For non-black surfaces, the upward flux takes the form:

$$F^{\uparrow}(z) = \epsilon_g \sigma T_g^4 + \int_0^z A(z,z')\frac{d}{dz'}[\sigma T^4(z')]dz' + (1-\epsilon_g)\left[\sigma T^4(z_t)\hat{\epsilon}(z,z_t) - \int_0^{z_t} \hat{A}(z,z')\frac{d}{dz'}[\sigma T^4(z')]dz'\right], \tag{2.61}$$

where

$$\hat{\epsilon}(z,z') = \frac{\int d\nu\, A_\nu(u_\nu^{\uparrow}, u_\nu'^{\downarrow})B_\nu(z')}{\sigma T^4(z')} \tag{2.62}$$

$$\hat{A}(z,z') = \frac{\int d\nu\, A_\nu(u_\nu^{\uparrow}, u_\nu'^{\downarrow})\frac{dB_\nu}{dT}(z')}{4\sigma T^3(z')}. \tag{2.63}$$

Here, the up and down arrows denote the direction of the trajectory after and before reflection at the ground, respectively. Thus, although the nominal emitting and absorbing levels remain the same, the actual trajectories involved in (2.62-2.63) are bi-directional, having undergone a reflection at the ground; hence, the equivalent path temperature will differ from that used to originally parameterize ϵ and A even for the same z and z'. One therefore needs to define new temperature-dependent functions - in the sense of requiring an independent parameterization. An erroneous generalization of the Ramanathan and Downey (1986) formulation, for an arbitrary ϵ_g, appears in Garand (1983) [Garand (1983)]. Successive versions of the Community Atmosphere Models, originally developed at the National Center for Atmospheric Research (NCAR) as the Community Climate model (CCM), use the Ramanathan and Downey (1986) formulation

and differ only in the parameterization for particular atmospheric gases [Collins *et al.* (2002)]. The spurious cooling error assumes importance since, for $\epsilon_g < 1$, such a contribution will likely negate any marginal improvement from one model version to the next resulting from a more accurate parameterization [Varghese (2003)].

2.7 Conclusions

In this chapter, we have highlighted a fundamental error in the prevailing emissivity scheme for reflective ground originally formulated by Garratt & Brost (1981) together with its consequences for atmospheric cooling rate profiles. The error results from using the same transmissivity for both the surface emission and the reflected fluxes, inspite of their differing spectral content, and leads to a spurious cooling near the surface on the length scale of the order of the photon path-length in the opaque bands of the participating medium. We present a consistent extension of the original scheme, given by (2.47)-(2.50) in section 2.3.2, and repeated here for convenience:

$$F^{\downarrow}(u) = \int_u^{u_t} \sigma T^4(u') \dot{\epsilon}^f(u'-u) du', \tag{2.64}$$

$$F^{\uparrow}(u) = \epsilon_g \sigma T_g^4 \tau^f(u) + \int_0^u \sigma T^4(u',t) \dot{\epsilon}^f(u-u') du' + (1-\epsilon_g) \int_0^{u_t} \sigma T^4(u',t) \dot{\epsilon}^f(u+u') du', \tag{2.65}$$

which is to be used for an atmosphere or more generally, any non-gray participating medium bounded below by a surface (ground for the atmospheric case) with emissivity ϵ_g. Despite the correct broadband reflected flux (as part of (2.65)) having appeared in earlier literature, the error in the formulation of Garrat and Brost (1981) has gone unnoticed. Their flux expressions have since been used by several research groups, primarily for investigations of the NBL, suggesting that the physical implications of the error have not been appreciated. As explained in section 2.3.1 in terms of a two-band model for the water-vapor-laden atmosphere, the error may be interpreted in terms of a band cross-talk in the context of a spectral scheme. Herein, we have explained the error within the framework of a broadband emissivity scheme, allowing us to compare the erroneous and correct schemes on the same footing. Importantly, our study shows that, in contrast to the results of earlier investigations, the cooling-rate profiles are largely insensitive to a departure of the surface from radiatively black behavior.

It is worth emphasizing that the emissivity scheme proposed by Garratt and Brost (1981) for non-black surfaces (and narrow-band formulations such as that of Savijärvi (2006); see chapter 3 for more details with regard to the error in a general frequency-parameterized scheme) suffer from two sources of error. The first is the parameterization error, inherent in any averaged scheme, due to the approximate modelling of the unresolved fine-scale structure [Goody (1964)]. The second source of error is related to spurious cooling, and crucially, arises only for non-black surfaces. The validation of an averaged scheme by comparison with a line by line (LBL) calculation for $\epsilon_g = 1$, as is the norm [Fels *et al.* (1991); Ellingson *et al.* (1991); Savijärvi (2006); Collins *et al.* (2006)], does not prevent the emergence of spurious cooling when the scheme is applied to non-black surfaces. The correct reflected flux, presented above and derived in section 2.3.2 for a broadband emissivity scheme, eliminates the second error component. This ensures that, even with a varying ϵ_g, the discrepancy between an LBL computation and a broadband

emissivity scheme is solely due to the limitations of parameterization.

Chapter 3

Beyond broadband flux-emissivity schemes

A portion of the material in this chapter is reproduced in J.atmos.sci, 70, 278-283, 2013

3.1 Abstract

In this chapter, we extend the correct broadband flux-emissivity scheme formulated in chapter 2, to include multiple reflections between two gray surfaces in a consistent manner, and then, allow for the inclusion of directional characteristics of the medium and boundary emissions which would avoid use of the diffusivity factor approximation in the calculation of radiative divergence. In the previous chapter 2, the prevailing flux-emissivity scheme for non-black surfaces was shown to include an erroneous reflected flux term. The error leads to a spurious cooling within the opaque bands. An expression for the correct broadband reflected flux was given that eliminated this spurious cooling contribution. Herein, it is shown that the error is generic in nature, and is relevant to any frequency-parameterized radiation scheme applied to non-black surfaces. Such schemes continue to be used in longwave radiation budget calculations [Savijärvi (2013)]. The correct reflected flux, previously developed within the framework of a broadband emissivity scheme, is therefore generalized here so as to be applicable to any frequency-parameterized radiation scheme. The error is illustrated by comparing the bandwise fluxes and flux divergences, obtained using the prevailing and correct narrow-band formulations, for a model (tropical) atmosphere. The discrepancy is the smallest for opaque bands within which the participating medium emits like a black body, and largest in frequency intervals where the medium is nearly transparent.

3.2 Flux-emissivity formulation for a cloudy atmosphere with a reflective ground

In the previous chapter, we discussed the flux-emissivity formulation for a reflective ground in a cloud-free night-time atmosphere. In this section, we develop the flux-emissivity formulation in the presence of clouds. The radiative properties of clouds play a significant role in maintaining the earth's energy budget [Freeman & Liou (1979)]. Clouds are the major source of uncertainty in Global Circulation models (GCMs) [Bader *et al.* (2008)]. Thus, it is necessary to model clouds accurately to predict climate change. In this formulation, the cloud cover is assumed to be homogeneous, and of an infinite extent horizontally, so a plane-parallel analysis continues to be valid. As shown by Liou & Wittman (1979), the radiative properties of the cloud layer, both in the solar and infrared range of wavelengths, may be suitably parameterized as a function of

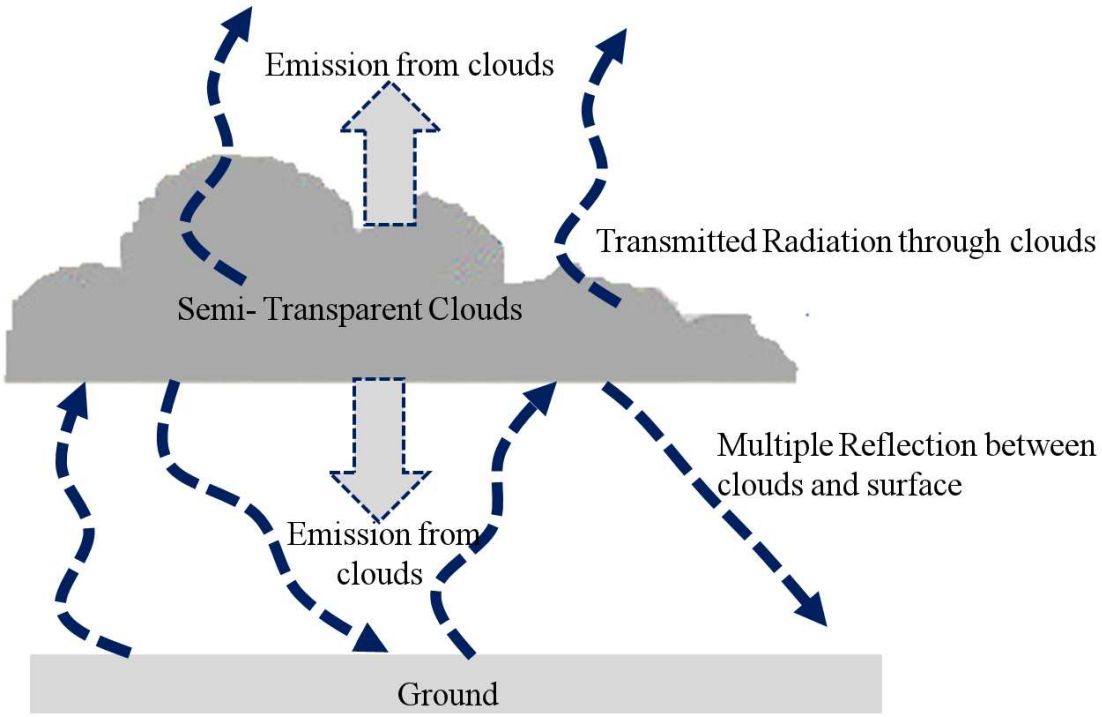

Figure 3.1: Greenhouse effect due to clouds.

the relevant physical variables (droplet size distribution, ice-water content, etc.). Most water clouds, even relatively thin ones (low lying clouds, for instance), are radiatively black in the infrared; the reason is the high droplet number densities and relatively weak scattering intensities due to the small-sized droplets, as a result of which the vapor and liquid phases are in local thermodynamic equilibrium. The flux-emissivity formulation for such a radiatively black cloud layer remains similar to that summarized in (2.47)-(2.50), and one need only account for an additional source of black body (downward) emission due to the cloud layer. The black-body assumption is no longer valid for high cirrus clouds, and the flux-emissivity formulation takes on a more complicated form in having to account for multiple reflections. Cirrus clouds are primarily composed of ice crystals with the optical depth of these clouds being a function of their thickness. They may range from being thin and nearly transparent to being opaque with thicknesses in excess of a kilometer. Thermal equilibrium temperature profiles are known to be very sensitive to cloud height and emissivities, and an increase in cirrus cloudiness may have a significant impact on the radiation balance of the earth-atmosphere system [Freeman & Liou (1979)]. Cirrus clouds reflect solar radiation thereby cooling earth's surface, while on the other hand, the effective absorption of earth's surface emission causes warming (greenhouse effect due to clouds see figure 3.1). As is well known, the fundamental question that needs to be addressed when analyzing cloud radiative forcing is the relative dominance of the solar albedo versus the IR-greenhouse effect [Liou & Wittman (1979)]. The analysis below formulates a consistent broadband flux-emissivity formulation in order to characterize the latter effect while accounting for both cloud and surface reflection.

Before proceeding to determine the radiative cooling-rates for the general case of a semi-transparent cirrus cloud cover above reflective ground, and thereby generalizing Liou & Ou

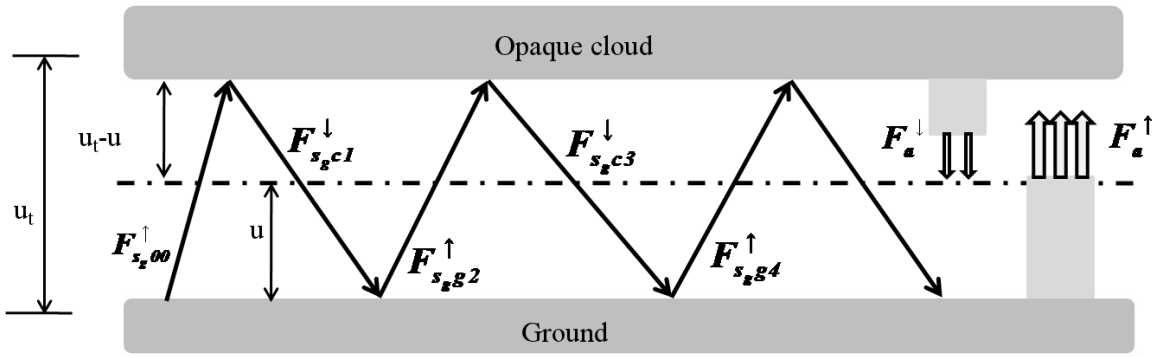

Figure 3.2: Multiple reflection between ground and the cloud base. For simplicity, the surface emission and its subsequent reflection between the cloud and surface is shown. The clouds are assumed to be opaque in the infrared regime.

(1981)'s original formulation to a finite surface reflectivity, we first examine the simpler case of an opaque cloud cover characterized by a reflectivity ρ_c. As expected from the known analysis for a pair of reflecting surfaces in the absence of a participating medium [Sparrow & Cess (1967)], the analysis in sections 3.2.1 and 3.2.2 accounts for infinite hierarchies of fluxes that emerge due to multiple reflections. We begin with an isothermal participating medium wherein the flux-emissivity has a simple interpretation. The generalization to the non-isothermal case is along the same lines as in section 2.3.2 in chapter 2. Section 3.3 discusses the inclusion of an angular dependence of the radiant intensity which avoids the use of a diffusivity factor, and enables one to rigorously account for anisotropic directional characteristics of surface emission and reflection.

3.2.1 An opaque cloud cover

For an opaque cloud cover, the problem reduces to determining the radiative fluxes and flux divergences for a plane-parallel configuration with the participating medium sandwiched between two gray surfaces. As shown in figure 3.2, the emissivities of the lower (ground) and upper (cloud) surfaces are ϵ_g and ϵ_c, respectively, the corresponding reflectivities being given by $\rho_i = 1-\epsilon_i$ ($i \equiv g, c$). One may distinguish four categories with regard to the radiative flux contributions both in the upward ($\uparrow$) and downward ($\downarrow$) directions:

1. Emission from the lower surface (ground) and successive reflection interactions: F_{s_g},
2. Emission from the upper surface (cloud cover) and successive reflection interactions: F_{s_c},
3. Upward emission by the participating air column and successive reflection interactions: $F_{a\uparrow}$,
4. Downward emission by the participating air column and successive reflection interactions: $F_{a\downarrow}$.

In order to keep track of the reflection hierarchy, we notate any flux contribution as $F^{\uparrow/\downarrow}_{op\alpha}$; Here, the first of three subscripts (o) denotes the origin of the contribution; for instance, $o \equiv s_i$ if the flux originally emanated from either of the two surfaces, $o \equiv a\uparrow$ if it arose initially from the

(cumulative) upward emission of the intervening air column, and so on. The second subscript (p) denotes the surface involved in the most recent reflection, while the third (α) denotes the total number of reflections. The particular arrow in the superscript indicates either an upwelling or a downwelling contribution.

Isothermal atmosphere

To begin with, we will assume the participating medium to be at a constant temperature T_0, and the surfaces s_g and s_c to be at different temperatures T_g and T_c, respectively. Considering now the emission from surface s_g, its total contribution to the upward flux at u is given by

$$\begin{aligned} F^{\uparrow}_{s_g}(u) &= F^{\uparrow}_{s_g 00} + F^{\uparrow}_{s_g g2} + F^{\uparrow}_{s_g g4} + \ldots, \\ &= \epsilon_g \sigma T_g^4 [\tau^f(u) + \rho_g \rho_c \tau^f(2u_t + u) + (\rho_g \rho_c)^2 \tau^f(4u_t + u) + \ldots], \qquad (3.1) \\ &= \epsilon_g \sigma T_g^4 \sum_{n=0}^{\infty} (\rho_g \rho_c)^n \tau^f(2nu_t + u), \qquad (3.2) \end{aligned}$$

where $\tau^f(u)$ is, as before, the flux transmissivity, and $F^{\uparrow}_{s_g 00}$ denotes the initial surface emission that has not undergone any reflections. The corresponding contribution to the downward flux at u is given by

$$\begin{aligned} F^{\downarrow}_{s_g}(u) &= F^{\downarrow}_{s_g c1} + F^{\downarrow}_{s_g c3} + F^{\downarrow}_{s_g c5} + \ldots, \\ &= \rho_c \epsilon_g \sigma T_g^4 [\tau^f(2u_t - u) + \rho_g \rho_c \tau^f(4u_t - u) + (\rho_g \rho_c)^2 \tau^f(6u_t - u) + \ldots], \qquad (3.3) \\ &= \rho_c \epsilon_g \sigma T_g^4 \sum_{n=0}^{\infty} (\rho_g \rho_c)^n \tau^f[2(n+1)u_t - u]. \qquad (3.4) \end{aligned}$$

which may be directly obtained from (3.2) by replacing u by $(2u_t - u)$. The contributions of the emission from surface s_c to the upward and downward fluxes at u are similarly given by

$$F^{\uparrow}_{s_c}(u) = \rho_g \epsilon_c \sigma T_c^4 \sum_{n=0}^{\infty} (\rho_g \rho_c)^n \tau^f[(2n+1)u_t + u], \qquad (3.5)$$

$$F^{\downarrow}_{s_c}(u) = \epsilon_c \sigma T_c^4 \sum_{n=0}^{\infty} (\rho_g \rho_c)^n \tau^f[(2n+1)u_t - u]. \qquad (3.6)$$

The remaining two categories are the upward and downward emissions (and successive reflections) of the participating medium. The original upward emission from the air column of height u is given by

$$F^{\uparrow}_{a^{\uparrow}00}(u) = \epsilon^f(u) \sigma T_0^4, \qquad (3.7)$$

where, as before, the zero subscripts imply the absence of any reflection interactions. The fraction of this flux that again contributes to the upward flux at u, after undergoing a pair of reflections at s_g and s_c, is given by

$$F^{\uparrow}_{a^{\uparrow}g2}(u) = \rho_g \rho_c [\epsilon^f(2u_t + u) - \epsilon^f(u_t + u)] \sigma T_0^4, \qquad (3.8)$$

where the difference between the two flux-emissivities isolates photons that have traveled a

distance of at least $(u_t + u)$, and thereby, have undergone two reflections. Extending this to an infinite sequence of reflections, one obtains the required contribution to the upward flux at u from the original upward emission by the air column:

$$F^{\uparrow}_{a^{\uparrow}}(u) = F^{\uparrow}_{a^{\uparrow}00} + F^{\uparrow}_{a^{\uparrow}g2} + F^{\uparrow}_{a^{\uparrow}g4} + \ldots, \tag{3.9}$$

$$= \sigma T_0^4[\epsilon^f(u) + (\rho_g\rho_c)(\epsilon^f(2u_t+u) - \epsilon^f(u_t+u)) + (\rho_g\rho_c)^2(\epsilon^f(4u_t+u) - \epsilon^f(3u_t+u)) + \ldots], \tag{3.10}$$

$$= \sigma T_0^4\{\epsilon^f(u) + \sum_{n=1}^{\infty}(\rho_g\rho_c)^n[\epsilon^f(2nu_t+u) - \epsilon^f((2n-1)u_t+u)]\sigma T_0^4\}. \tag{3.11}$$

The initial upward emission of the air column also contributes to the downward flux at u, and an argument similar to the above yields

$$F^{\downarrow}_{a^{\uparrow}}(u) = \rho_c\sigma T_0^4 \sum_{n=0}^{\infty}(\rho_g\rho_c)^n[\epsilon^f(2(n+1)u_t-u) - \epsilon^f((2n+1)u_t-u)]. \tag{3.12}$$

The corresponding contributions of the original downward air column emission to the upward and downward fluxes, respectively, are given by:

$$F^{\uparrow}_{a^{\downarrow}}(u) = \rho_g\sigma T_0^4 \sum_{n=0}^{\infty}(\rho_g\rho_c)^n[\epsilon^f((2n+1)u_t+u) - \epsilon^f(2nu_t+u)], \tag{3.13}$$

$$F^{\downarrow}_{a^{\downarrow}}(u) = \sigma T_0^4\{\epsilon^f(u_t-u) + \sum_{n=1}^{\infty}(\rho_g\rho_c)^n[\epsilon^f((2n+1)u_t-u) - \epsilon^f(2nu_t-u)]\}. \tag{3.14}$$

In light of the rather cumbersome expressions for the individual flux contributions, it is worth writing them all down at one place. Thus, the expressions for the total upwelling and downwelling fluxes, at a height u within the medium, may be written as:

$$F^{\uparrow}(u) = F^{\uparrow}_{s_g}(u) + F^{\uparrow}_{s_c}(u) + F^{\uparrow}_{a^{\uparrow}}(u) + F^{\uparrow}_{a^{\downarrow}}(u), \tag{3.15}$$

$$F^{\downarrow}(u) = F^{\downarrow}_{s_g}(u) + F^{\downarrow}_{s_c}(u) + F^{\downarrow}_{a^{\uparrow}}(u) + F^{\downarrow}_{a^{\downarrow}}(u), \tag{3.16}$$

where

$$F^{\uparrow}_{s_g}(u) = \epsilon_g\sigma T_g^4 \sum_{n=0}^{\infty}(\rho_g\rho_c)^n\tau^f(2nu_t+u), \tag{3.17}$$

$$F^{\uparrow}_{s_c}(u) = \rho_g\epsilon_c\sigma T_c^4 \sum_{n=0}^{\infty}(\rho_g\rho_c)^n\tau^f[(2n+1)u_t+u], \tag{3.18}$$

$$F^{\uparrow}_{a^{\uparrow}}(u) = \sigma T_0^4\{\epsilon^f(u) + \sum_{n=1}^{\infty}(\rho_g\rho_c)^n[\epsilon^f(2nu_t+u) - \epsilon^f((2n-1)u_t+u)]\}, \tag{3.19}$$

$$F^{\uparrow}_{a^{\downarrow}}(u) = \rho_g\sigma T_0^4 \sum_{n=0}^{\infty}(\rho_g\rho_c)^n[\epsilon^f((2n+1)u_t+u) - \epsilon^f(2nu_t+u)]. \tag{3.20}$$

and

$$F^{\downarrow}_{s_g}(u) = \rho_c\epsilon_g\sigma T_g^4 \sum_{n=0}^{\infty}(\rho_g\rho_c)^n\tau^f[2(n+1)u_t - u], \tag{3.21}$$

$$F^{\downarrow}_{s_c}(u) = \epsilon_c\sigma T_c^4 \sum_{n=0}^{\infty}(\rho_g\rho_c)^n\tau^f[(2n+1)u_t - u], \tag{3.22}$$

$$F^{\downarrow}_{a^{\uparrow}}(u) = \rho_c\sigma T_0^4 \sum_{n=0}^{\infty}(\rho_g\rho_c)^n[\epsilon^f(2(n+1)u_t - u) - \epsilon^f((2n+1)u_t - u)], \tag{3.23}$$

$$F^{\downarrow}_{a^{\downarrow}}(u) = \sigma T_0^4\{\epsilon^f(u_t - u) + \sum_{n=1}^{\infty}(\rho_g\rho_c)^n[\epsilon^f((2n+1)u_t - u) - \epsilon^f(2nu_t - u)]\}. \tag{3.24}$$

The veracity of the above expressions may be checked in different limits. For instance, in the limit of a completely transparent medium ($\epsilon^f(u) = 0, \tau^f(u) = 1$), $F^{\uparrow\,\downarrow}_{a^{\uparrow/\downarrow}}(u) = 0$, and the fluxes that originate from the surfaces, on summing up the geometric series, reduce to a more familiar form [Sparrow & Cess (1967)]:

$$F^{\uparrow}_{s_g} = \frac{\epsilon_g\sigma T_g^4}{(1-\rho_g\rho_c)}, \tag{3.25}$$

$$F^{\uparrow}_{s_c} = \frac{\rho_g\epsilon_c\sigma T_c^4}{(1-\rho_g\rho_c)}, \tag{3.26}$$

$$F^{\downarrow}_{s_g} = \frac{\rho_c\epsilon_g\sigma T_g^4}{(1-\rho_g\rho_c)}, \tag{3.27}$$

$$F^{\downarrow}_{s_c} = \frac{\epsilon_c\sigma T_c^4}{(1-\rho_g\rho_c)}, \tag{3.28}$$

so that

$$F^{\uparrow} = \frac{[\epsilon_g(\sigma T_g^4) + \rho_g\epsilon_c(\sigma T_c^4)]}{(1-\rho_g\rho_c)}, \tag{3.29}$$

$$F^{\downarrow} = \frac{[\epsilon_c(\sigma T_c^4) + \rho_c\epsilon_g(\sigma T_g^4)]}{(1-\rho_g\rho_c)}, \tag{3.30}$$

where we have omitted the dependence on u since the intervening medium is transparent. For $T_g = T_c$, it is readily verified that $F^{\uparrow} = F^{\downarrow}$, regardless of ϵ_g and ϵ_c. This must be the case, since no radiation escapes the configuration which may therefore be regarded as a one-dimensional analog of the Kirchhoff cavity; thermodynamic equilibrium implies that the radiant flux must be isotropic within the cavity which, for one dimension, implies the equality of the upwelling and downwelling contributions. The analogy of a Kirchhoff cavity, and the implied absence of a non-trivial flux divergence at equilibrium continues to be true in the presence of a participating medium. Thus, setting $T_g = T_c = T_0$ in the original expressions viz. (3.17)-(3.20) and (3.21)-(3.24) yields $\dfrac{dF}{du} = 0$, independent of the detailed expression for the flux-emissivity. Although the spectral energy distribution of the 'virgin' emission, comprising the attenuated surface emission and the cumulative medium emission, does not follow a Planck function, the photons corresponding to the deficient transparent bands are precisely the ones that dominate the subsequent hierarchy of reflected fluxes; these latter contributions compensate for the defi-

ciency in the original emission, and the total radiant fluxes involved in the exchanges correspond to those of a black body; as they must be for the equilibrium case. The above argument already illustrates the crucial role of clouds in altering the radiative cooling-rate. As seen in chapter 2 for an isothermal atmosphere, there is a weak cooling near the ground $[O(1Kday^{-1})]$ and the cooling-rate increases with height. The presence of clouds and its multiple reflections on the other hand relatively warms up the air layers, thus ensuring a zero flux divergence, and thence, consistency with thermodynamic equilibrium. It will be seen below, that multiple reflections continue to play a crucial role in determining the flux divergence for non-equilibrium configurations.

As a final check for the isothermal case, we examine the limit of a radiatively black cloud layer ($\rho_c = 0$) at $T_c = 0$. This constraint ensures a vanishing cloud emission ($F^{\uparrow}_{s_c} = F^{\downarrow}_{s_c} = 0$), and the problem reduces to that of a clear atmosphere with a reflective ground. From (3.17)-(3.20), the total upwelling flux is given by

$$F^{\uparrow}(u) = F^{\uparrow}_{s_g}(u) + F^{\uparrow}_{a^{\uparrow}}(u) + F^{\uparrow}_{a^{\downarrow}}(u), \tag{3.31}$$

$$= \epsilon_g(\sigma T_1^4)\tau^f(u) + \epsilon^f(u)(\sigma T_0^4) + \rho_g(\sigma T_0^4)[\epsilon^f(u_t + u) - \epsilon^f(u)], \tag{3.32}$$

and the corresponding downwelling flux is

$$F^{\downarrow}(u) = F^{\downarrow}_{a^{\downarrow}}(u), \tag{3.33}$$

$$= (\sigma T_0^4)\epsilon^f(u_t - u), \tag{3.34}$$

both of which are readily seen to be identical to the expressions obtained earlier in section 2.3.2 for an isothermal atmosphere with reflective ground (see equation (2.34)-(2.37)) at the same temperature T_0.

Non-isothermal atmosphere

We now generalize the expressions, (3.17)-(3.20), (3.21)-(3.24), for the upwelling and downwelling fluxes, respectively, to a non-isothermal atmosphere. The surface emission contributions remain unaltered, of course, and the combined expressions for $F^{\uparrow}(u)$ and $F^{\downarrow}(u)$, including the non-isothermal generalizations of the contributions to the air column emissions, are therefore given

by

$$
\begin{aligned}
F^{\uparrow}(u) = &\epsilon_g \sigma T_g^4 \sum_{n=0}^{\infty} (\rho_g \rho_c)^n \tau^f(2nu_t + u) + \rho_g \epsilon_c \sigma T_c^4 \sum_{n=0}^{\infty} (\rho_g \rho_c)^n \tau^f[(2n+1)u_t + u] \\
&- \int_0^u \sigma T^4(u') \frac{d\epsilon^f}{du'}(u - u')du' - \sum_{n=1}^{\infty} (\rho_g \rho_c)^n \int_0^{u_c} \sigma T^4(u') \frac{d\epsilon^f}{du'}(2nu_t + u - u')du' \\
&+ \rho_g \sum_{n=0}^{\infty} (\rho_g \rho_c)^n \int_0^{u_t} \sigma T^4(u') \frac{d\epsilon^f}{du'}(2nu_t + u + u')du', \qquad (3.35) \\
F^{\downarrow}(u) = &\epsilon_c \sigma T_c^4 \sum_{n=0}^{\infty} (\rho_g \rho_c)^n \tau^f((2n+1)u_t - u) + \rho_c \epsilon_g \sigma T_g^4 \sum_{n=0}^{\infty} (\rho_g \rho_c)^n \tau^f[2(n+1)u_t - u] \\
&+ \int_{u_t}^u \sigma T^4(u') \frac{d\epsilon^f}{du'}(u' - u)du' + \sum_{n=1}^{\infty} (\rho_g \rho_c)^n \int_0^{u_t} \sigma T^4(u') \frac{d\epsilon^f}{du'}(2nu_t + u' - u)du' \\
&+ \rho_c \sum_{n=0}^{\infty} (\rho_g \rho_c)^n \int_0^{u_t} \sigma T^4(u') \frac{d\epsilon^f}{du'}(2(n+1)u_t - u - u')du', \qquad (3.36)
\end{aligned}
$$

where the expression for $F^{\downarrow}(u)$ may directly be obtained from $F^{\uparrow}(u)$ using $\epsilon_c \leftrightarrow \epsilon_g$, $\rho_c \leftrightarrow \rho_g$ and $u, u' \leftrightarrow (u_t - u), (u_t - u')$. The configuration considered above, that is, an infinite hierarchy of multiple reflections between two opaque reflective surfaces, is a commonly encountered situation under laboratory conditions, where the main goal is to study the interaction of radiative forcing of the participating medium sandwiched between two parallel gray plates and its interaction with other heat transfer mechanisms. A similar expression was first obtained by Gille & Goody (1964) in the context of examining the role of radiation in stabilizing Rayleigh Benard convection. The authors obtained the above expressions from the monochromatic radiative balance (as done in section 2.3.2 in chapter 2) and then integrated over a frequency interval of a few inter-line spacing to obtain the narrowband formulation. The expressions above have been arrived at solely based on the physical interpretation of the broadband emissivity given in chapter 2. If one carries out an integration by parts of the above equations (3.35)-(3.36), the resulting expressions are similar to the ones obtained by Schimmel (1969) and Hutchison & Richards (1999). The main concern of these studies was to understand the role of CO_2 in delaying the onset of Rayleigh Benard convection.

For purposes of comparison, we write down the expressions for the radiative fluxes if one naively extends the hierarchy of multiple reflections along the lines of Garratt & Brost (1981). The upward and downward fluxes are then given by

$$
\begin{aligned}
F^{\uparrow}(u) = \; & G\left[\epsilon_g \sigma T_g^4 \tau^f(u) + \rho_g \epsilon_c \sigma T_c^4 \tau^f(u_t)\tau^f(u) + \rho_g \rho_c F_a^{\uparrow}(u_t)\tau^f(u_t)\tau^f(u) + \rho_g F_a^{\downarrow}(0)\tau^f(u)\right] \\
& - \int_0^u \sigma T^4(u') \frac{d\epsilon(u - u')}{du'} du', \qquad (3.37) \\
F^{\downarrow}(u) = \; & G[\epsilon_c \sigma T_c^4 \tau^f(u_t - u) + \rho_c \epsilon_g \sigma T_g^4 \tau^f(u_t)\tau^f(u_t - u) + \rho_c F_a^{\uparrow}(u_t)\tau^f(u_t - u) \\
& + \rho_g \rho_c F_a^{\downarrow}(0)\tau^f(u_t)\tau^f(u_t - u)] + \int_u^{u_t} \sigma T^4(u') \frac{d\epsilon(u' - u)}{du'} du', \qquad (3.38)
\end{aligned}
$$

where

$$G = \frac{1}{1 - \rho_g \rho_c (\tau^f(u_t))^2}. \tag{3.39}$$

As was done in Chapter 2, we now examine the cooling-rate profiles, in the presence of an opaque cloud cover, obtained from both the correct scheme (3.35) - (3.36) and the erroneous formulation (3.37) - (3.38). For simplicity, we assume a lapse-rate atmosphere (where the lapse-rate is chosen to be $6\,\mathrm{Kkm}^{-1}$ corresponding to the moist atmosphere with a height of 5 km). The ground emissivity is taken to be $\epsilon_g = 0.8$ [Garratt & Brost (1981)], the cloud emissivity to be $\epsilon_c = 0.5$ [Liou & Wittman (1979)]. and the reflectivities are $\rho_i = 1 - \epsilon_i$ where i stands for g or c. In figure 3.3, from the cooling-rate profile calculated from (3.35)-(3.36), the presence of clouds is seen to heat up the air layers near the ground (compared to a clear atmosphere. For instance, for a cloud-free atmosphere with the same lapse-rate profile, the predicted cooling rate at the ground is $2.6\,\mathrm{Kday}^{-1}$, and with a cloud cover, the estimated cooling-rate is $1.75\,\mathrm{Kday}^{-1}$ (a 32% increase in warming). There is an additional warming near the cloud base (see figure 3.4) due to the radiative exchanges of air layers with warmer ground and low-lying warmer air layers. Figure 3.5 shows if one doesn't treat the multiple reflections properly, a spurious cooling can occur near the ground and a spurious warming near the cloud base. This spurious warming near the cloud base arises due to the same reason as the cooling. It is due to the incorrect transmissivity to attenuate the warmer ground radiation and the emission from the warmer air layers reflected from the cloud base. Figures 3.3 and 3.4 also help highlight the effect of multiple reflections on the cooling-rate profile obtained from the correct formulation. The cooling-rate profile with multiple reflection is obtained by truncating the summation in (3.35)-(3.36) at $n = 50$.

Further, to examine the effect of the surface emissivities on the cooling-rate, we obtain the cooling rate profiles for different combinations of surface (ground) and cloud emissivities. The results are shown in figure 3.6. When the ground emissivity is reduced the cooling rates of air layers throughout the atmosphere increase with the maximum change occurring close to the ground. The later is due to the fact that the reflected component now comprises of downwelling colder radiation from the uppermost air layers and clouds. The weak cooling throughout the atmosphere is due to weaker surface emission. This is similar to the increase in warming (discussed in chapter 2) when the surface emissivity is reduced in the context of a nocturnal inversion layer where the downwelling radiation is from the overlying warmer air layers.

It is worth noting that the treatment of solar radiation in a cloudy atmosphere would follow those of the surface emission contributions in (3.35) and (3.36). Such an analysis, with the inclusion of multiple reflections between the cloud layer and the surface, has been attempted earlier [Liou & Ou (1983)]. However, the hierarchy of reflection interactions has been modelled using successive products of the transmissivity function (τ^f) therein (similar to the equation (3.39). This is, in essence, the same error as the one committed by Garrat and Brost (1981) in the context of infrared radiation, since product of the monochromatic transmissivities does not translate to product of the corresponding frequency-averaged quantities. Owing to the absence of a source function in the fundamental transfer equation, in the solar range of wavelengths (neglecting scattering effects), the multiplication of broadband transmissivities would lead to the appearance of spurious energy in the opaque bands instead. In turn, this would lead

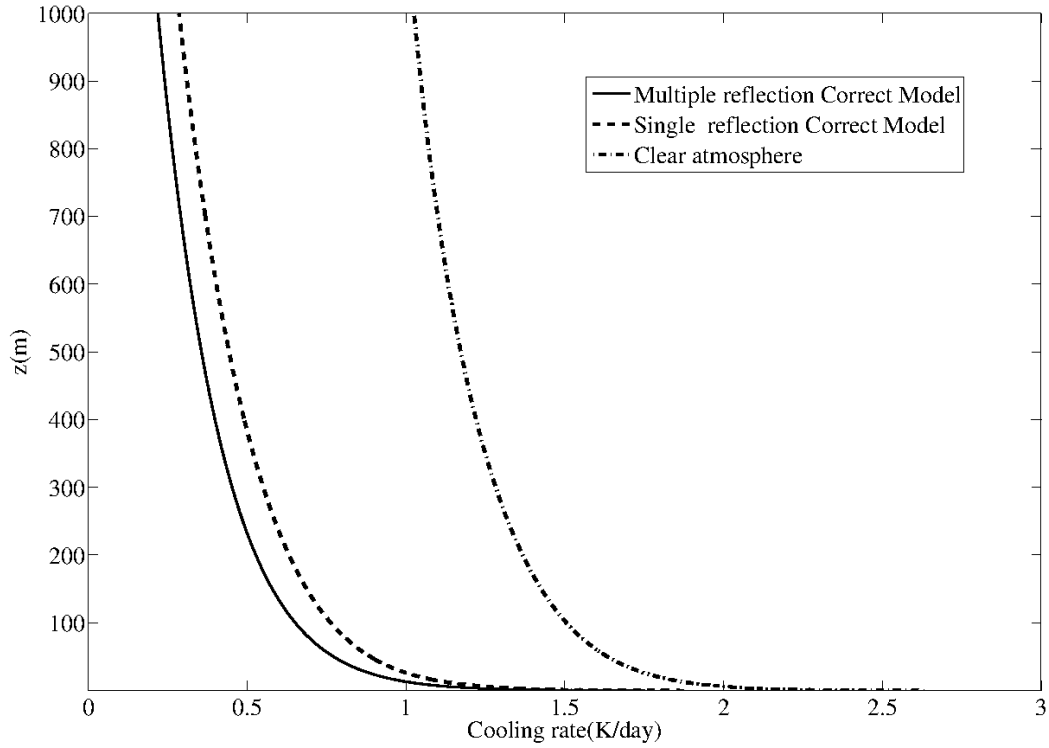

Figure 3.3: Cooling rate profile obtained using the correct formulation ((3.35) - (3.36)) for an assumed moist atmosphere with a lapse rate of $6\,Kkm^{-1}$. The surface emissivity is assumed to be 0.8 and the cloud emissivity is taken to be 0.5.

to a localized heating rate in the immediate vicinity of the reflecting surfaces.

3.2.2 Semi-transparent cloud cover

Herein, we derive the flux-emissivity formulation for a reflective ground with an overlying semi-transparent cloud cover. In reality, this may correspond to a relatively thin cirrus cloud layer. The cloud thickness being small in relation to the other distances involved (cloud height, for instance, which for cirrus clouds is of the order of a kilometer or more), the analysis below assumes the semi-transparent layer to have a zero thickness as shown in figure 3.7. Following section 3.2.1, the radiative properties of this layer are specified *apriori*. Thus, the layer is assumed to have a transmittivity t_c and a reflectivity ρ_c. Further, accounting for the possibly significant temperature gradient across even the thin cloud layer, we assume different emissivities in the upward ($\epsilon_c^{\uparrow}$) and downward ($\epsilon_c^{\downarrow}$) directions [Liou & Wittman (1979)]. As discussed by Liou & Wittman (1979) and Liou & Ou (1981) the cirrus layer is not in thermodynamic- equilibrium due to the strong temperature gradients that exist across the cloud layer and the anisotropic scattering by ice crystals. Hence, the transmissivity, reflectivity and emissivity need not add upto unity as in the case for a system in thermodynamic equilibrium. For the semi-transparent cloud layer, one needs to consider the radiative balances separately below and above the cloud layer (at a temperature T_c) located at $u = u_c$. Here, we directly consider the case of a non-isothermal atmosphere.

Radiative flux balance below the cloud layer ($0 < u < u_c$):

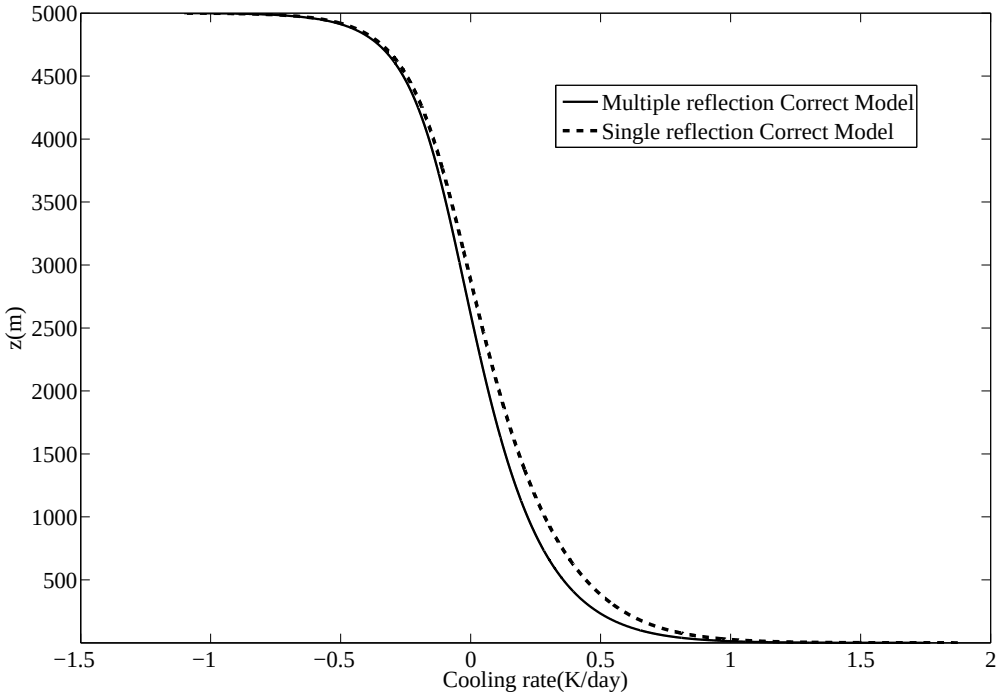

Figure 3.4: Cooling-rate profile, over the lowest kilometer, obtained using the correct formulation ((3.35) - (3.36)) with and without multiple reflection (n=50) for an assumed moist atmosphere with a lapse rate of $6\,Kkm^{-1}$. The surface emissivity is assumed to be 0.8 and the opaque cloud emissivity is taken to be 0.5. The dash-dotted line shows the cooling-rate profile calculated, in the absence of a cloud cover, for ground with the same emissivity.

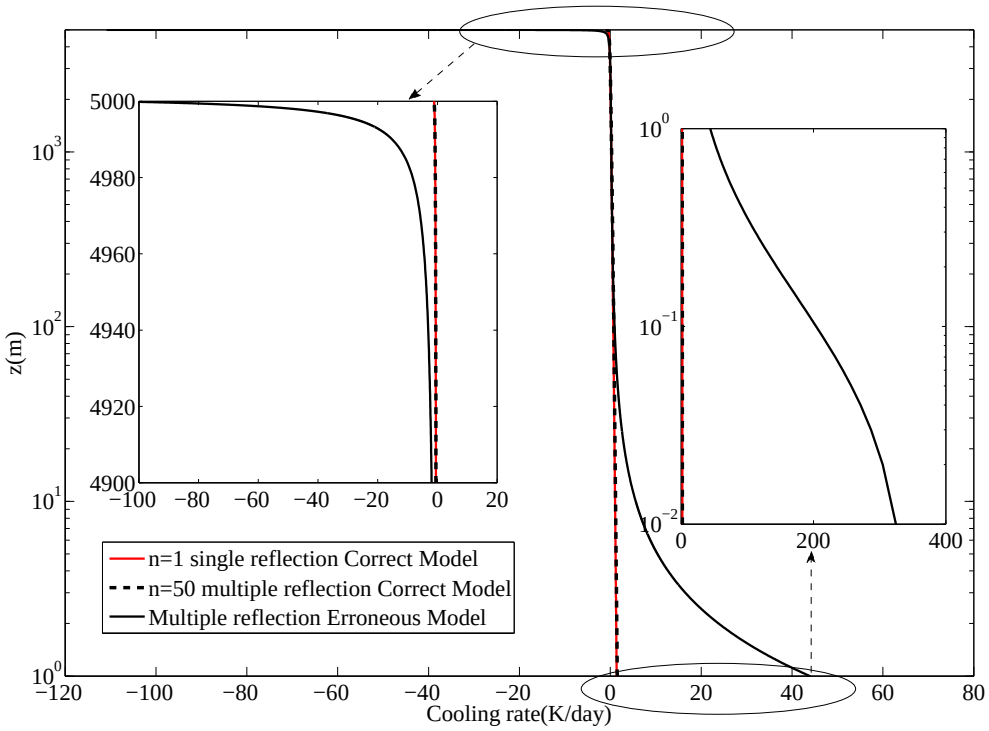

Figure 3.5: Cooling-rate profile obtained using the correct formulation, (3.35 - 3.36), and the existing erroneous scheme, (3.37) - (3.38) for an assumed moist atmosphere with a lapse rate of $6\,Kkm^{-1}$. The surface emissivity is assumed to be 0.8 and the opaque cloud emissivity is taken to be 0.5.

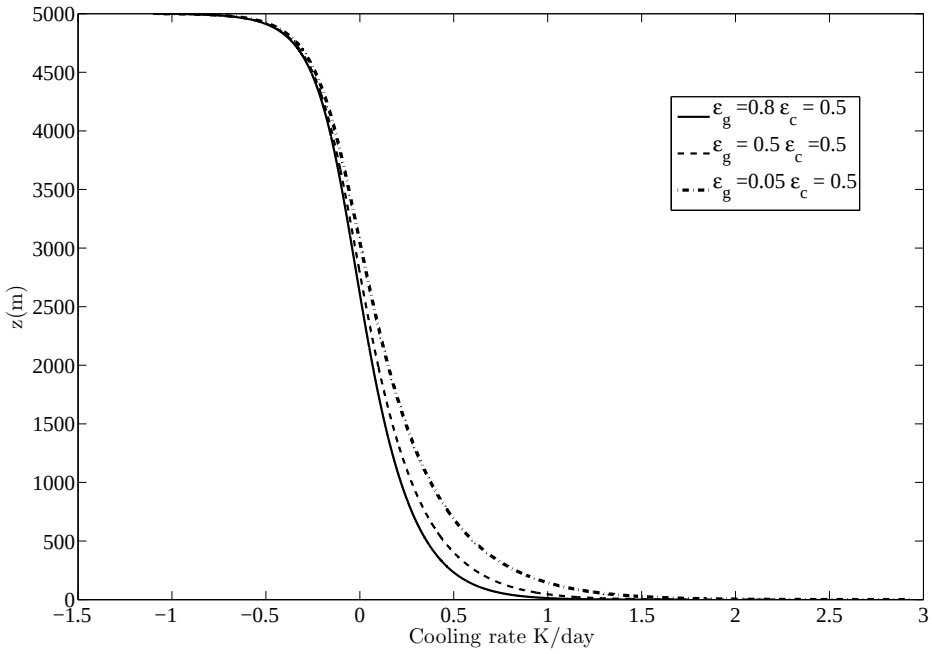

Figure 3.6: Cooling-rate profile obtained using the correct formulation ((3.35) - (3.36)), with and without multiple reflection (n=50) for an assumed moist atmosphere with a lapse rate of $6\,Kkm^{-1}$. The cloud emissivity is assumed to be 0.5 and the surface emissivity is varied.

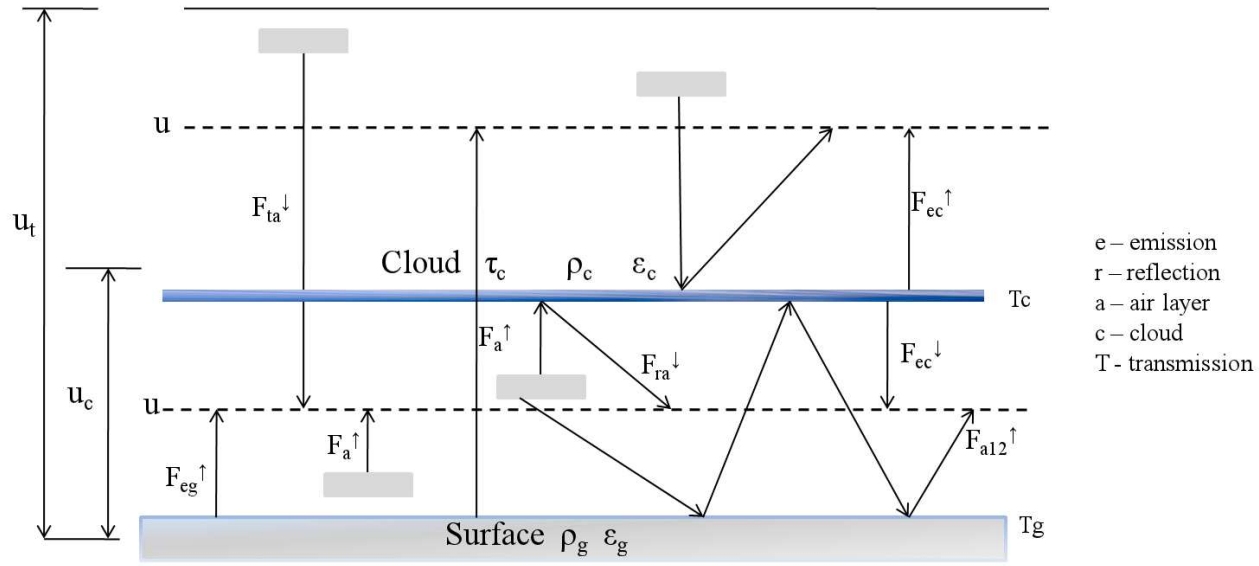

Figure 3.7: Schematic shows various components of radiative fluxes that reaches any level u below and above the cloud .

The contributions to the fluxes, $F^{\uparrow}(u)$ and $F^{\downarrow}(u)$, from the (downward) cloud and ground emissions, and due to the emission of the intervening water-vapor-laden air layers, remain identical to those derived in section 3.2.1 with $\epsilon_c^{\downarrow}$ replacing ϵ_c; see (3.35) and (3.36). There are additional contributions, however, originating from the emissions of the air layers above the cloud layer, that are transmitted through the cloud layer, and thereby, contribute to the fluxes in the region $0 < u < u_c$. Their contributions to the upward and downward fluxes may be written in the form:

$$F^{\uparrow}_{a'\downarrow}(u) = \rho_g t_c \sum_{n=0}^{\infty} (\rho_g \rho_c)^n \int_{u_c}^{u_t} \sigma T^4(u') \frac{d\epsilon^f}{du'} (2nu_t + u + u') du', \tag{3.40}$$

$$F^{\downarrow}_{a'\downarrow}(u) = t_c \sum_{n=0}^{\infty} (\rho_g \rho_c)^n \int_{u_c}^{u_t} \sigma T^4(u') \frac{d\epsilon^f}{du'} (2nu_c + u' - u) du', \tag{3.41}$$

where a' denotes the air column above the cloud layer. The integrals in (3.40) and (3.41) include transmitted photons that have traveled minimum distances of $(u_c + u)$ (with one reflection at the ground) and $(u_c - u)$, respectively, and are evidently proportional to t_c. The expressions for

the total upwelling and downwelling fluxes in the region $0 < u < u_c$ are given by

$$F^{\uparrow}_{u<u_c}(u) = F^{\uparrow}_{s_g}(u) + F^{\uparrow}_{s_c}(u) + F^{\uparrow}_{a^{\uparrow}}(u) + F^{\uparrow}_{a'^{\downarrow}}(u) + F^{\uparrow}_{a^{\downarrow}}(u), \tag{3.42}$$

$$\begin{aligned}
&= \epsilon_g \sigma T_g^4 \sum_{n=0}^{\infty} (\rho_g \rho_c)^n \tau^f (2nu_c + u) + \rho_g \epsilon_c^{\downarrow} \sigma T_c^4 \sum_{n=0}^{\infty} (\rho_g \rho_c)^n \tau^f [(2n+1)u_c + u] \\
&\quad - \int_0^u \sigma T^4(u') \frac{d\epsilon^f}{du'}(u - u')du' - \sum_{n=1}^{\infty} (\rho_g \rho_c)^n \int_0^{u_c} \sigma T^4(u') \frac{d\epsilon^f}{du'}(2nu_c + u - u')du' \\
&\quad + \rho_g t_c \sum_{n=0}^{\infty} (\rho_g \rho_c)^n \int_{u_c}^{u_t} \sigma T^4(u') \frac{d\epsilon^f}{du'}(2nu_c + u + u')du' \\
&\quad + \rho_g \sum_{n=0}^{\infty} (\rho_g \rho_c)^n \int_0^{u_c} \sigma T^4(u') \frac{d\epsilon^f}{du'}(2nu_c + u + u')du',
\end{aligned} \tag{3.43}$$

$$F^{\downarrow}_{u<u_c}(u) = F^{\downarrow}_{s_g}(u) + F^{\downarrow}_{s_c}(u) + F^{\downarrow}_{a^{\uparrow}}(u) + F^{\downarrow}_{a'^{\downarrow}}(u) + F^{\downarrow}_{a^{\downarrow}}(u), \tag{3.44}$$

$$\begin{aligned}
&= \epsilon_c^{\downarrow} \sigma T_c^4 \sum_{n=0}^{\infty} (\rho_g \rho_c)^n \tau^f ((2n+1)u_c - u) + \rho_c \epsilon_g \sigma T_g^4 \sum_{n=0}^{\infty} (\rho_g \rho_c)^n \tau^f [2(n+1)u_c - u] \\
&\quad + \int_{u_t}^{u} \sigma T^4(u') \frac{d\epsilon^f}{du'}(u' - u)du' + \sum_{n=1}^{\infty} (\rho_g \rho_c)^n \int_0^{u_c} \sigma T^4(u') \frac{d\epsilon^f}{du'}(2nu_c + u' - u)du' \\
&\quad + t_c \sum_{n=0}^{\infty} (\rho_g \rho_c)^n \int_{u_c}^{u_t} \sigma T^4(u') \frac{d\epsilon^f}{du'}(2nu_c + u' - u)du' \\
&\quad + \rho_c \sum_{n=0}^{\infty} (\rho_g \rho_c)^n \int_0^{u_c} \sigma T^4(u') \frac{d\epsilon^f}{du'}(2(n+1)u_c - u - u')du'.
\end{aligned} \tag{3.45}$$

For an isothermal atmosphere of temperature (T_0) the above expressions reduce to

$$\begin{aligned}
F^{\uparrow}_{u<u_c}(u) = \sigma T_0^4 \Bigg[& 1 - \rho_g t_c \sum_{n=0}^{\infty} (\rho_g \rho_c)^n \tau (2nu_c + u_t + u) + (\rho_g \epsilon_c^{\downarrow} - \rho_g + \rho_g t_c) \sum_{n=0}^{\infty} (\rho_g \rho_c)^n \tau^f ((2n+1)u_c + u) \\
& + \sum_{n=1}^{\infty} (\rho_g \rho_c)^n \tau^f ((2n-1)u_c + u) \Bigg],
\end{aligned} \tag{3.46}$$

$$F^{\downarrow}_{u<u_c}(u) = \sigma T_0^4 \left[1 - t_c \sum_{n=0}^{\infty} (\rho_g \rho_c)^n \tau (2nu_c + u_t - u) + (\epsilon_c^{\downarrow} + \rho_g + t_c - 1) \sum_{n=0}^{\infty} (\rho_g \rho_c)^n \tau^f ((2n+1)u_c - u) \right]. \tag{3.47}$$

For an opaque cloud cover $t_c = 0$ and considering the system in thermodynamic equilibrium where the cloud emissivity, reflectivity and transmissivity add upto one, the above expression reduces to $F^{\uparrow} = F^{\downarrow}$ as discussed in 3.2.1. Since some amount of radiation can escape via the transparent cloud, unlike an opaque cloud cover there will be cooling below the cloud.

Radiative flux balance above the cloud layer ($u_c < u < u_t$):

The radiative balance above the cloud, particularly the expression for the upwelling flux, is more involved. The expression for $F^{\uparrow}_{u_c<u<u_t}(u)$ includes the contributions already present for the opaque cloud cover (see (3.35) in section 3.2.1), now mediated by the transmissivity t_c, and in addition, new contributions that originate from the upward emission of the cloud and the

cumulative emissions of the air layers above the cloud. Thus,

$$
\begin{aligned}
F^{\uparrow}_{u_c<u<u_t}(u) = t_c\Bigg[&\epsilon_g\sigma T_g^4\sum_{n=0}^{\infty}(\rho_g\rho_c)^n\tau^f(2nu_t+u)+\rho_g\epsilon_c^{\downarrow}\sigma T_c^4\sum_{n=0}^{\infty}(\rho_g\rho_c)^n\tau^f[(2n+1)u_t+u]\\
&-\int_0^{u_c}\sigma T^4(u')\frac{d\epsilon^f}{du'}(u-u')du'-\sum_{n=1}^{\infty}(\rho_g\rho_c)^n\int_0^{u_c}\sigma T^4(u')\frac{d\epsilon^f}{du'}(2nu_c+u-u')du'\\
&+\rho_g\sum_{n=0}^{\infty}(\rho_g\rho_c)^n\int_0^{u_c}\sigma T^4(u')\frac{d\epsilon^f}{du'}(2nu_c+u+u')du'\Bigg]\\
&+\rho_c t_c^2\sum_{n=0}^{\infty}(\rho_g\rho_c)^n\int_{u_c}^{u_t}\sigma T^4(u')\frac{d\epsilon^f}{du'}(2nu_c+u+u')du'+\epsilon_c^{\uparrow}\sigma T_c^4\tau^f(u-u_c)\\
&+\int_u^{u_c}\sigma T^4(u')\frac{d\epsilon^f}{du'}(u-u')du'+\rho_g\int_{u_c}^{u_t}\sigma T^4(u')\frac{d\epsilon^f}{du'}(u'+u-2u_c)du'. \qquad (3.48)
\end{aligned}
$$

The expression for the downwelling flux is much simpler due to the absence of any overlying surface emission, and is simply given by

$$
F^{\downarrow}_{u_c<u<u_t}(u) = \int_u^{u_t}\sigma T^4(u')\frac{d\epsilon^f}{du'}(u'-u)du'. \qquad (3.49)
$$

Similarly for an isothermal atmosphere, one can obtain the net upward and downward flux as

$$
\begin{aligned}
F^{\uparrow}_{u_c<u<u_t}(u) =\sigma T_0^4\Bigg[&(\rho_g\tau_c\epsilon_c^{\downarrow}-\rho_g t_c+\rho_g t_c^2)\sum_{n=0}^{\infty}(\rho_g\rho_c)^n\tau^f((2n+1)u_c+u)\\
&+(\epsilon_c^{\uparrow}+t_c+\rho_c-1)\tau^f(u-u_c)\\
&+t\sum_{n=1}^{\infty}(\rho_g\rho_c)^n\tau^f((2n-1)u_c+u)+1\\
&-\rho_g t_c^2\sum_{n=0}^{\infty}(\rho_g\rho_c)^n\tau^f(2nu_c+u_t+u)-\rho_c\tau^f(u_t+u-2u_c)\Bigg], \qquad (3.50)\\
F^{\downarrow}_{u_c<u<u_t}(u) =&\sigma T_0^4(1-\tau(u_t-u)), \qquad (3.51)
\end{aligned}
$$

3.3 Generalized flux-emissivity formulation incorporating for directional characteristics of surface emission

3.3.1 Directional flux-emissivity formulation

In this section, we devise a broadband emissivity scheme in order to account for the directional characteristics of surface emission and reflection. It is well known that the emissivities ($\epsilon_g(\Omega,\nu,T)$; where $\Omega =\equiv (\theta,\phi)$ denotes the emission direction) of many familiar, naturally occurring surfaces, including sandy soil and ice, exhibit a pronounced spectral variation in the infrared [Wang *et al.* (2009)]. In addition, both the emissivity ($\epsilon_g(\Omega,\nu,T)$) and the bi-directional reflectivity where ($\rho_g(\Omega,\Omega',\nu,T)$, Ω and Ω' denote the directions corresponding to the reflected and incident pencil of rays.) of ideal smooth surfaces (as calculable, from classical electromagnetic theory [Siegel & Howell (2002)]) and real surfaces exhibit a dependence on zenith angle

[Garcia *et al.* (2009),José & Cuenca (1999)]. Although not as pronounced as the spectral variation, this angular variation remains important since it is believed that even a 1% error in ϵ_g leads to an error of $0.5\,K$ in the land surface temperature, and typical angular emissivity variations may therefore lead to temperature errors unacceptable for climate studies [Running *et al.* (1994)]. Incorporating directional characteristics of the reflectivity is important with regard to remote sensing applications, particularly for remote-sensing satellites that operate in a multi-angular mode [José & Cuenca (1999)]. The angular variations in ρ_g are, in fact, more pronounced than those of ϵ_g with prominent peaks in the vicinity of the forward and backward-scattering directions relative to a diffuse background [Running *et al.* (1994)]. The resulting deviation from Lambertian surface behavior also brings into question the diffusivity factor approximation employed commonly in the framework of a plane-parallel approximation [Liou (2002)].

Unlike the emissivity or absorptivity, it is difficult to characterize $\rho_g(\nu, \Omega', \Omega, T)$ because of its dependence on both incident and reflected angles. Conventionally, $\rho_g(\nu, \Omega', \Omega, T)$ is defined as:

$$\rho_{g\Omega'\rightarrow\Omega}(\nu, \Omega', \Omega, T) = \frac{i_{\nu,r}(\nu, \Omega', \Omega)}{i_{\nu,i}(\nu, \Omega')cos\theta d\Omega'}, \tag{3.52}$$

where $i_{\nu,i}$ and $i_{\nu,r}$ are the incident and reflected intensities respectively. The two special types of reflection, often employed in the literature because they correspond to opposite extremes, are diffuse and specular reflection. For a diffuse surface, the reflected intensity is uniform over all the reflected directions. In other words, a diffuse surface viewed from any angle appears equally bright, which is true for microscopically irregular surfaces [Siegel & Howell (2002)] like sand and snow. The other type of reflection is specular reflection, which occurs over optically smooth surfaces [1], and obeys Snell's law. Thus, for incident radiation from a single direction, the reflected radiation will be of the same intensity at precisely the same angle from the surface normal as the incident intensity vector, with the intensity vectors (both incident and reflected) and the surface normal lying in the same plane. An example of a specular surface is window glass when reflecting solar radiation. In performing radiative transfer calculations with other transfer mechanisms the surface emission is usually assumed to be diffuse, an assumption is strictly true only for blackbody emission.

From the expressions for the monochromatic fluxes given in Chapter 1 (see (1.8) and (1.9), the angular dependence of the radiant intensity, in the flux expressions, is seen to occur in the form of the following integral of the monochromatic transmittance function - $\int_0^1 \mu e^{-\frac{z}{\mu}} d\mu$; the corresponding integral in the expression for the flux divergence is $\int_0^1 e^{-\frac{z}{\mu}} d\mu$. These integrals may be expressed in terms of the general exponential integral, defined as $E_n(z) = \int_0^1 \mu^{n-2} e^{-\frac{z}{\mu}} d\mu$ [Abramowitz & Stegun (1990); Sparrow & Cess (1967)], as $E_3(z)$ and $E_2(z)$, respectively. The normal procedure to simplify this angular dependence is to devise an accurate approximation of the exponential integral by an exponential function. For instance, in the engineering literature, one writes $E_2(t) \approx ae^{-bt}$ where the constants a and b are obtained such that the zeroth and first moments of both functions (exponential and exponential integral) are equal. This leads to $E_2(z) \approx \frac{3}{4}e^{-\frac{3z}{2}}$ and $E_3(z) \approx \frac{1}{2}e^{-\frac{3z}{2}}$ [Sparrow & Cess (1967)]. In the atmospheric context, a

[1] Any surface can be classified as optically smooth or rough based on σ_o and λ where σ_o is the root-mean-square roughness scale and λ is the wavelength of the incident photons. For a smooth surface $\sigma_o << \lambda$. Hence, a surface which is optically smooth for long wavelengths can be optically rough at shorter wavelengths.

similar approximation, known as the diffusivity factor approximation is used when the angular integral over photon trajectories in all directions is replaced by the attenuation over an equivalent trajectory at an inclination of $\cos^{-1}(1/\beta)$, where β is the diffusivity factor, $\beta \approx 1.66$.

Thus, the diffusivity factor approximation relies on the accurate approximation of a single exponential integral by an exponential function. In presence of a reflective surface, the dependence on angle, of the reflected flux, is no longer in the form of a single exponential integral. This presents no difficulty at the monochromatic level where the dependence may be written as the product of two exponential integrals, for a diffuse (Lambertian) surface, each of which may still be approximated by an exponential as indicated above. This is no longer the case, after frequency integration, and thus, the angular dependence of the reflected flux that occurs in a frequency-parameterized scheme involves a double integral over polar angles (θ and θ') of an integrand that no longer exhibit a separable dependence on μ and μ', and therefore, cannot, in general be written as the product of exponential integrals. This is, of course, because the broadband transmissivity (or, for that matter, any coarse-grained transmittance; see section 3.5) does not obey the functional relation $\tau^f(x+y) = \tau^f(x)\tau^(y)$. Note that, non-separability is always the case even at the monochromatic level if the surface radiative properties (ρ_g) exhibits non-trivial angular dependencies. Thus applying the diffusivity-factor approximation for radiative transfer in an atmosphere bounded by a gray surface (even a Lambertian one) introduces an error due to the failure of the multiplicative property of the transmissivity, and this is over and above the (small) error involved in the diffusivity-factor approximation. Thus, the whole idea of formulating a directional flux-emissivity scheme for non-black surfaces, in this section is so that the error even for non-black surfaces, is restricted to that arising from the frequency parameterization (that is, formulation in terms of a gray flux-emissivity). This then is the same spirit as the derivation of a consistent frequency-parameterized scheme for non-black surfaces (see chapter 2 and section 3.5).

To start with, we consider the consequence of including the directional characteristics, of the radiant intensity, for a participating medium over a single reflecting surface, and within the framework of a broadband emissivity scheme; although, the flux expressions finally obtained are readily generalizable to any frequency-parameterized radiation scheme. This is intended to mimic the reflection from gray ground in a clear atmosphere where we have neglected the presence of particulate scattering and absorbing agents like aerosols. We will write down the broadband fluxes in a plane-parallel formulation without the aid of a diffusivity-factor, taking explicit account of both the differences in path-lengths of the reflected photons arising from the differing inclinations of their trajectories to the vertical, and any additional anisotropy induced by interaction with a non-Lambertian surface. Having done this, we compare the cooling-rate profiles to those obtained from the diffusivity factor approximation. As done in previous sections, we start with an isothermal atmosphere.

3.3.2 Single reflective ground

In the analysis below, we continue to retain the same definition of the flux-emissivity as in previous sections. Thus, the flux-emissivity continues to denote the inefficiency of an isothermal column emission relative to σT_0^4, although the isothermal column is not vertical as it was in the

earlier, angularly averaged, plane-parallel formulation; instead, it denotes an isothermal pencil of radiation oriented along an arbitrary direction on the unit sphere. The rationale behind using the same emissivity expression is that each infinitesimal element of the medium emits radiation equally in all the directions (isotropic), and the distance along an arbitrary oriented trajectory can again be treated as a effective path length the photon travels. The advantage of the present formulation is that, it doesn't require one to assume any angular dependence for the downwelling radiation. This is in contrast to Edwards (2009a) who examined the effect of including the directional characteristics of the medium and the surface, on the evolution of nocturnal boundary layer, and formulated the problem in terms of differential and isotropic weighted reflectivity. In order to achieve this, however, he had to split the directional characteristics of the medium into an isotropic emission and the deviation from the isotropic emission assumed to be proportional to $cos\theta$. This is equivalent in taking only the first two terms of P_N-approximation as discussed in chapter 1.

As in section 2.3.2, the generalization of the flux-emissivity scheme to include a non-trivial angular dependence of the radiant intensity is best introduced in the context of an isothermal atmosphere at temperature T_0, this being the same as the temperature of the reflective ground. The lone contribution to the radiant flux in the bottom hemisphere is due to the overlying atmospheric column, and is given by

$$i_a^{i\downarrow}(u,\Omega) = \epsilon^f(\frac{u_t-u}{\mu})\frac{\sigma T_0^4}{\pi}, \tag{3.53}$$

where $i_a^{i\downarrow}$ is the downwelling intensity at any height u, $\Omega \equiv (\theta,\phi)$, $\mu = \cos\theta$ and $(\sigma T_0^4/\pi)$ is the isotropic black-body intensity per unit solid angle. Thus, the cumulative downward flux $(dF_a^{i\downarrow}(u))$ due to emission at the level u, and in a differential solid angle $d\Omega$, is given by

$$dF_a^{i\downarrow}(u,\Omega) = \epsilon^f(\frac{u_t-u}{\mu})\frac{\sigma T_0^4}{\pi}\mu\, d\Omega, \tag{3.54}$$

where the factor μ accounts for the dependence of the projected area on θ. The three contributions to the radiant flux in the top hemisphere are

1. the attenuated ground emission within $d\Omega$, and at a height u, given by

$$dF_{eg}^{i\uparrow}(u,\Omega) = \epsilon_{g\Omega}\frac{\sigma T_0^4}{\pi}\tau^f(\frac{u}{\mu})\mu\, d\Omega, \tag{3.55}$$

   where $\epsilon_{g\Omega}$ denotes the total directional surface emissivity.

2. the directional cumulative emission from a pencil of air, within $d\Omega$, given by

$$dF_a^{i\uparrow} = \epsilon^f(\frac{u}{\mu})\frac{\sigma T^4}{\pi}\mu\, d\Omega. \tag{3.56}$$

3. the upwelling reflected flux within $d\Omega$. To determine this, we first write down the expression

for the downwelling flux at the surface, within $d\Omega'$, using (3.54):

$$dF_a^{i\downarrow}(0,\Omega') = \epsilon^f(\frac{u_t}{\mu'})\frac{\sigma T_0^4}{\pi}\mu'\,d\Omega', \tag{3.57}$$

so that the reflected flux at the surface within $d\Omega$ is given by

$$d^2F_{rg}^{i\uparrow}(0,\Omega,\Omega') = [\rho_{g\Omega'\to\Omega}\mu\,d\Omega]\epsilon^f(\frac{u_t}{\mu'})\frac{\sigma T_0^4}{\pi}\mu'\,d\Omega', \tag{3.58}$$

where $\rho_{g\Omega'\to\Omega}$ is the total bi-directional reflectivity, and $d^2F_{rg}^{\uparrow}$ denotes a higher-order differential quantity. The broadband transmissivity, to be used for attenuating $d^2F_{rg}^{\uparrow}$, was obtained in section 2.3.2 for vertical paths. Generalizing this result to angular paths, for inclined upward and downward trajectories having lengths of u/μ and u_t/μ', respectively, the required transmissivity is given by $\dfrac{\tau^f(\frac{u}{\mu}) - \tau^f(\frac{u}{\mu}+\frac{u_t}{\mu'})}{1-\tau^f(\frac{u_t}{\mu'})}$. The expression for the attenuated reflected flux at u, due to downwelling surface fluxes in the entire hemisphere, is then obtained by integration over $d\Omega'$, yielding

$$dF_{rg}^{i\uparrow}(u,\Omega) = \int \frac{[\tau^f(\frac{u}{\mu}) - \tau^f(\frac{u}{\mu}+\frac{u_t}{\mu'})]}{(1-\tau^f(\frac{u_t}{\mu'}))}\,d^2F_{rg}^{i\uparrow}(0,\Omega,\Omega'), \tag{3.59}$$

$$= \mu\,d\Omega\int \mu'\,d\Omega'\rho_{g\Omega'\to\Omega}\left[\tau^f(\frac{u}{\mu}) - \tau^f(\frac{u}{\mu}+\frac{u_t}{\mu'})\right]\frac{\sigma T_0^4}{\pi}. \tag{3.60}$$

Thus, the integrated flux contributions for an isothermal atmosphere, bounded by a non-black ground with directional emissivity $\epsilon_{g\Omega}$ and bi-directional reflectivity $\rho_{\Omega'\to\Omega}$, are given by

$$F_a^{i\downarrow}(u) = \frac{\sigma T_0^4}{\pi}\int \epsilon^f(\frac{u_t-u}{\mu})\mu\,d\Omega, \tag{3.61}$$

$$F_{eg}^{i\uparrow}(u) = \frac{\sigma T_0^4}{\pi}\int \epsilon_{g\Omega}\tau^f(\frac{u}{\mu})\mu\,d\Omega, \tag{3.62}$$

$$F_a^{i\uparrow}(u) = \frac{\sigma T^4}{\pi}\int \epsilon^f(\frac{u}{\mu})\mu\,d\Omega, \tag{3.63}$$

$$F_{rg}^{i\uparrow}(u) = \frac{\sigma T_0^4}{\pi}\int \mu\,d\Omega\int \mu'\,d\Omega'\rho_{g\Omega'\to\Omega}\left[\epsilon^f(\frac{u}{\mu}+\frac{u_t}{\mu'}) - \epsilon^f(\frac{u}{\mu})\right], \tag{3.64}$$

and the radiative flux divergence evaluated using (3.61)-(3.64) is:

$$\frac{dF}{du} = \frac{\sigma T_0^4}{\pi}\int \mu d\Omega\left[\dot\epsilon^f(\frac{u_t-u}{\mu}) + (1-\epsilon_{g\Omega})\dot\epsilon^f(\frac{u}{\mu}) + \int d\Omega'\mu'\rho_{g\Omega'\to\Omega}\left[\dot\epsilon^f(\frac{u}{\mu}+\frac{u_t}{\mu'}) - \dot\epsilon^f(\frac{u}{\mu})\right]\right]. \tag{3.65}$$

For a Lambertian surface, with isotropic emission and reflection properties, that is, with $\epsilon_{g\Omega} = \epsilon_g$, $\pi\rho_{g\Omega'\to\Omega} = (1-\epsilon_g)$ [Siegel & Howell (2002)], the above expression for the flux divergence simplifies to

$$(\frac{dF}{du})_{Lambertian} = 2(\sigma T_0^4)\int_0^1 \mu d\mu\left[\dot\epsilon^f(\frac{u_t-u}{\mu}) + 2(1-\epsilon_g)\int_0^1 \mu' d\mu'\dot\epsilon^f(\frac{u}{\mu}+\frac{u_t}{\mu'})\right]. \tag{3.66}$$

and, with the aid of the diffusivity factor approximation mentioned earlier (see (1.12)), the resulting expression is given by

$$(\frac{dF}{du})_{Lambertian/diff} = \sigma T_0^4 \left[\dot{\epsilon}^f(\frac{u_t - u}{1/\beta}) + (1-\epsilon_g)\dot{\epsilon}^f(\frac{u+u_t}{1/\beta}) \right]. \tag{3.67}$$

A comparison of (3.66) and (3.67) clearly shows that, strictly speaking, the diffusivity factor approximation, within the broadband emissivity scheme, is accurate only for black surfaces where $\dot{\epsilon}^f(\frac{z}{\beta} \approx \int_0^1 \mu\dot{\epsilon}d\mu$ for $\beta = 1.66$ even when the surface is Lambertian in character (Here Lambertian behavior is due to the isotropy of th emission). The reflected flux contribution would not be amenable to this approximation since, it involves a double integral over the directional coordinates of the flux-emissivity, and as already emphasized several times, the flux-emissivity does not satisfy the functional relation $\epsilon^f(x+y) = \epsilon(z/\mu)^f(x)\epsilon^f(y)$. In fact, as shown later in section 3.5, such a functional dependence is already violated for spectral intervals greater than a fraction of an elementary line width. In any case, as pointed out earlier, the approximation is rendered invalid whenever ρ_g exhibits a non-trivial angular dependence.

Figure 3.8 shows the difference between the cooling-rates obtained from the exact formulation which treats the directional characteristics explicitly (see equation (3.66)), and those obtained with the diffusivity factor approximation (see equation (3.67)), for an isothermal atmosphere over a Lambertian surface. It can be seen that the diffusivity factor approximation underestimates the cooling-rate this being equivalent to a spurious warming contribution. The error although presented is that smallest for $\epsilon_g = 1$. The additional error incurred with decreasing ϵ_g is because the diffusivity factor approximation is designed for an isotropic intensity. The downwelling flux at the surface, which is subsequently reflected and attenuated, however, exhibits a dependence on the angular coordinate because there is a greater amount of energy in the more inclined pencils of radiation, than the vertical ones, by virtue of them being longer. The greater energy arises from more energy contained in the transparent bands. After interaction with a diffuse surface, the resulting angular re-distribution of radiant energy implies that the transparent band energy in these nearly horizontal pencils of radiation appears in the vertical ones, and thus in turn implies an attenuation that is weaker than that assumed in the diffusivity factor approximation. This stronger attenuation in the diffusivity-factor approximation leads to a spurious warming contribution for the same reason that the weaker attenuation in the Garratt & Brost (1981) formulation led to a spurious cooling contribution.

The Lambertian surface above is the extreme case of totally diffuse reflection. The opposite extreme is a specularly reflecting, in which case the angle of reflection (the zenith angle θ) is same as that of angle of incidence (θ') and the azimuthal angle is given by $\phi = \phi' + \pi$. Mathematically, this implies that $\rho_g(\Omega', \Omega = \rho_s\delta(\mu - \mu')\delta(\phi - \phi' - \pi)$ and one can write down the resultant reflected radiation is follows:

$$F_{rg}^{i\uparrow}(u) = \frac{\sigma T_0^4}{\pi} \int \mu \, d\Omega \rho_s \left[\epsilon^f(\frac{u}{\mu} + \frac{u_t}{\mu}) - \epsilon^f(\frac{u}{\mu}) \right] \tag{3.68}$$

which, not withstanding the difference in arguments, involves the same underlying exponential integral as for black surfaces. Thus, in this case, the diffusivity factor continues to be a very good approximation; as good an approximation as for black surfaces.

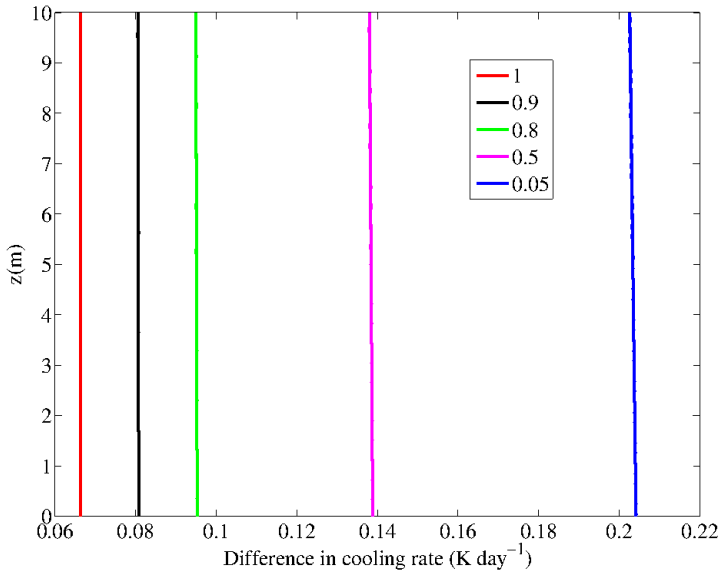

Figure 3.8: The plot shows the difference in cooling-rate, $\left(\frac{dF}{du}\right)_{Lambertian} - \left(\frac{dF}{du}\right)_{Lambertian/diff}$ as a function of z. $\left(\frac{dF}{du}{}_{Lambertian}\right) - \left(\frac{dF}{du}\right)_{Lambertian/diff}$ is the difference between the exact formulation (which deals with the directional characteristics of the medium explicitly), and the one where the diffusivity factor approximation is used for an isothermal atmosphere and a Lambertian surface.

Experiments show that some materials possess the characteristics of both diffuse and specular reflection [Siegel & Howell (2002)] and the bi-directional reflectivity can, in these cases, be written in mixed form:

$$\rho_{\Omega' \to \Omega}) = \frac{\rho_d}{\pi} + \rho_s \delta(\mu' - \mu)\delta(\phi - \phi' - \pi). \tag{3.69}$$

Here, ρ_d and ρ_s signify the diffuse and specular reflectivities, respectively. The reflected component is given by

$$F^{\uparrow}_{rg} = \frac{4\pi^2 \rho_d}{\pi} \frac{\sigma T_0^4}{\pi} \int_{\Omega} \mu d\mu \int_{\Omega'} \mu' d\mu' \left[\epsilon^f(\frac{u_t}{\mu'} + \frac{u}{\mu}) - \epsilon^f(\frac{u}{\mu})\right] + 2\pi\rho_s \frac{\sigma T_0^4}{\pi} \int \mu d\mu \left[\epsilon^f(\frac{u+u_t}{\mu}) - \epsilon^f(\frac{u}{\mu})\right] \tag{3.70}$$

On the other hand, one can also obtain an expression, with the aid of the diffusivity-factor approximation, as follows:

$$F^{\uparrow}_{rg} = (\rho_d + \rho_s)\sigma T_0^4 \left[\epsilon^f\left(\frac{u_t + u}{1/\beta}\right) - \epsilon^f\left(\frac{u}{1/\beta}\right)\right] \tag{3.71}$$

The cooling-rate can now be calculated based on equation (3.70) and the difference in the cooling-rates between equation (3.70) and (3.71) is plotted in figures 3.9 and 3.10. As expected, the error is minimum when the specularly reflecting component is dominant. The surface emission is assumed to be diffuse in all the cases discussed above.

As in section 2.3.2, the formulation, (3.61)-(3.64), may be generalized to the case of a non-

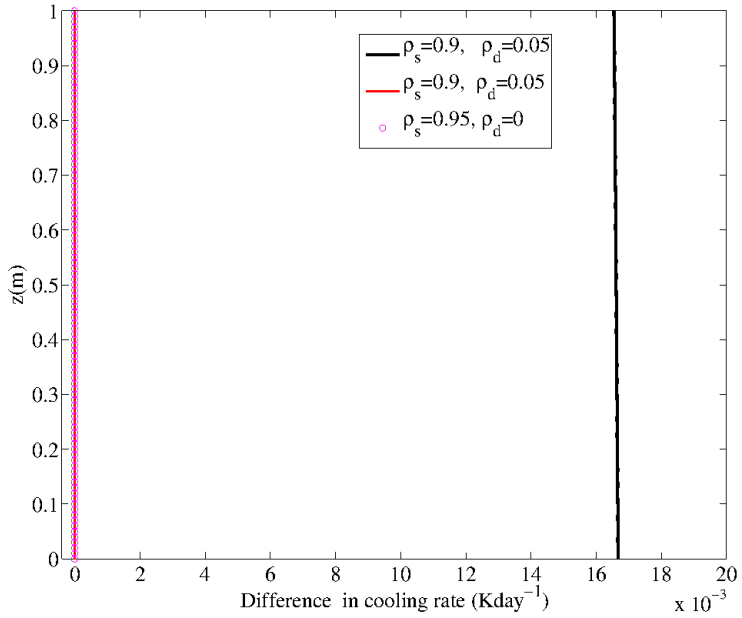

Figure 3.9: The plot shows the difference in cooling-rate, $\left(\frac{dF}{du}\right)_{Lambertian} - \left(\frac{dF}{du}\right)_{Lambertian/diff}$ as a function of z. $\left(\frac{dF}{du}\right)_{Lambertian} - \left(\frac{dF}{du}\right)_{Lambertian/diff}$ is the difference between the exact formulation (which deals with the directional characteristics of the medium explicitly), and the one where the diffusivity factor approximation is used for an isothermal atmosphere. The reflectivity is modeled as a combination of diffuse and specular component (3.69). The specular reflectivity is fixed to be 0.9 and the diffuse part is varied.

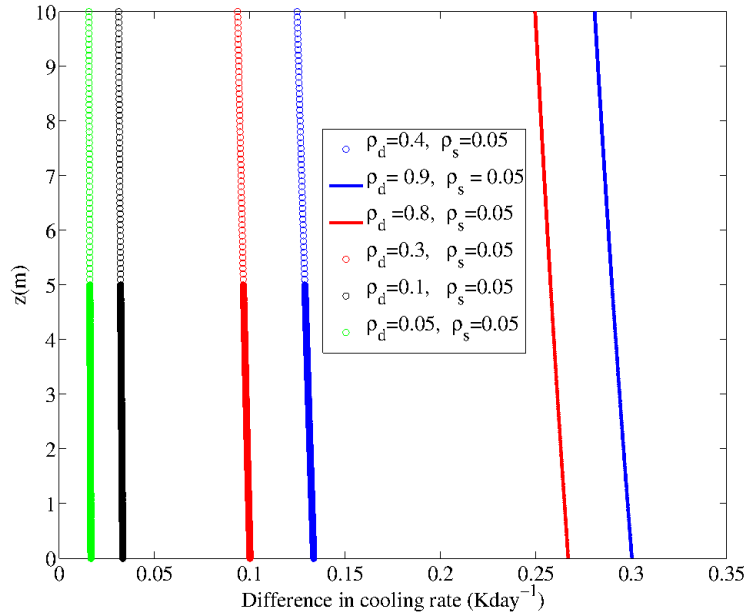

Figure 3.10: The plot shows the difference in cooling-rate, $\left(\frac{dF}{du}\right)_{Lambertian} - \left(\frac{dF}{du}\right)_{Lambertian/diff}$ as a function of z. $\left(\frac{dF}{du}\right)_{Lambertian} - \left(\frac{dF}{du}\right)_{Lambertian/diff}$ is the difference between the exact formulation (which deals with the directional characteristics of the medium explicitly), and the one where the diffusivity factor approximation is used for an isothermal atmosphere. The reflectivity is modeled as a combination of diffuse and specular component (3.69). The specular reflectivity is fixed to be 0.05 and the diffuse part is varied.

isothermal atmosphere and one obtains the following expressions for the different contributions:

$$F_a^{\downarrow}(u) = \frac{1}{\pi}\int \mu\, d\Omega \int_u^{u_t} \sigma T^4(u')\frac{d\epsilon^f}{du'}(\frac{u'-u}{\mu})du', \tag{3.72}$$

$$F_{eg}^{\uparrow}(u) = \frac{1}{\pi}\int \mu\, d\Omega \epsilon_{g\Omega}\sigma T^4(u')(1-\epsilon^f(\frac{u}{\mu})), \tag{3.73}$$

$$F_a^{\uparrow}(u) = -\frac{1}{\pi}\int \mu\, d\Omega \int_0^{u} \sigma T^4(u')\frac{d\epsilon^f}{du'}(\frac{u-u'}{\mu})du', \tag{3.74}$$

$$F_{rg}^{\uparrow}(u) = \frac{1}{\pi}\int \mu\, d\Omega \int \mu'\, d\Omega' \rho_{g\Omega'\rightarrow\Omega}\int_0^{u_t} \sigma T^4(u')\frac{d\epsilon^f}{du'}(\frac{u'}{\mu'}+\frac{u}{\mu})du', \tag{3.75}$$

which may now be used for an arbitrary atmospheric temperature profile.

3.4 Frequency parameterized radiation schemes : Narrow band Models

3.4.1 Introduction

In the interests of computational efficiency, one resorts to frequency parameterization in radiation calculations. At the coarsest level of frequency resolution, this leads to flux-emissivity schemes discussed in detail in chapter 2. At the next level in frequency resolution, of the order of a few inter-line spacings, this leads to narrow-band formulations that are typically used in calculations involving the longwave radiation budget [Goody (1964);Liou (2002)]. The fluxes in such a formulation are obtained by integrating the monochromatic fluxes over a frequency interval much larger than the average inter-line spacing but smaller than the length scale of variation of the Planck function, and are given by [Liou (2002)]:

$$F_j^{\uparrow}(u) = \pi B_j(T_g)\tau_j^f(u) - \int_0^u \pi B_j[T(u')]\dot{\tau}_j^f(u-u')du', \tag{3.76}$$

$$F_j^{\downarrow}(u) = -\int_u^{u_t} \pi B_j[(T(u'))]\dot{\tau}_j^f(u'-u)du', \tag{3.77}$$

for an atmosphere of height u_t above black ground which corresponds to $u = 0$ (by black ground, it is implied that $\epsilon_{g\nu} = 1\ \forall\ \nu$ i.e unity in all bands). Here, B_j is the (approximately constant) Planck function in band j and the overdot denotes differentiation with respect to the argument. The net flux is $F(u) = \sum_{j=1}^{M}(F_j^{\uparrow}(u) - F_j^{\downarrow}(u))$, with M being the number of bands. The diffuse transmission function in (3.76) and (3.77), $\tau_j^f(u)$, is a band-averaged quantity that, with the aid of regular or statistical band models, is expressible in terms of averaged line characteristics [Goody (1964)].

The idea often employed to determine the averaged line characteristics is based upon replacing the actual absorption band with a hypothetical infinite array of absorption lines of uniform statistical properties. Then, the properties of this array are tuned to obtain for instance, the average transmission of the real band [Goody (1964)]. The band models differ in their assumed distributions of line spacing, shape and intensity [Siegel & Howell (2002)] and the distribution

depends in turn on the type of molecule under consideration. For instance, the spectra of linear molecules (for instance, the Q-branch of the 15 μm band of CO_2) show that a single line may repeat itself periodically. This led to the idea of regular band models, in which case, the band consists of an infinite array of lines of equal intensity and spacing [Goody (1964)]. One can analytically find a band averaged transmittance for a Lorentz line shape, in which case the band model as referred to as the Elsasser model. On the other hand, the rotational band of the water vapor spectrum suggests that the only common feature of the 25 cm^{-1} range is the apparently random line positions this is related to the underlying asymmetry of the water molecule (the resulting distinct values of the moments of inertia about the three principal axes leads to a complicated spectral distribution of lines arising from rotational transitions). To account for this feature, one can invoke a band model where the strength of the lines and the spacing between them is randomly distributed .

Earlier studies have employed narrowband formulations to study the evolution of both diurnal [Savijärvi (2006)] nocturnal and planetary boundary layers [Savijärvi (2013);Duynkerke (1999);Savijärvi (2009)]. The formulation is sometimes used as a benchmark to test the validity of simpler models [Rodgers & Walshaw (1966); Ramanathan & Downey (1986)]. In this chapter, we show the fundamental inconsistency that arises when extending (3.76)-(3.77), over a non-black surface (ground), in a manner analogous to assigning an emissivity to a gray solid surface. The error is due to an incorrect reflected flux, and arises from not discriminating between the spectral content of ground emission and the atmospheric column emission reflected from the ground. As was the case for the flux-emissivity schemes, it manifests as an intense cooling close to ground, and the cooling intensity is a function of the vertical resolution used in a given calculation. We present in section 3.5 the correct reflected flux that removes this spurious cooling in a narrow-band formulation. Thereafter, the discrepancy in the bandwise fluxes and the flux divergences, calculated using the erroneous and correct formulations, is determined for a standard tropical atmosphere. Section 3.6 summarizes the main points of the analysis and highlights the inherent superiority of the correlated-k methods in this regard.

3.5 The narrow-band formulation for reflective ground

The existing generalization of (3.76) for ground with an emissivity ϵ_{gj} in the j^{th} band is given by [Savijärvi (2006)]:

$$F_j^{\uparrow}(u) \quad = \quad [\epsilon_{gj}(\pi B_j(T_g)) + (1-\epsilon_{gj})F_j^{\downarrow}(0)]\tau_j^f(u) - \int_0^u \pi B_j[T(u')]\dot{\tau}_j^f(u-u')du'. \qquad (3.78)$$

As argued in the previous chapter 2, in the context of flux-emissivity schemes, an error arises in using the same transmissivity (in this case, the band transmittance) $\tau_j^f(u)$ in (3.78) to attenuate both ground emission $(\epsilon_{gj}(\pi B_j(T_g)))$ and the reflected flux $((1-\epsilon_{gj})F_j^{\downarrow}(0))$ despite the sharp contrast in the respective spectral energy contents. As for the broadband case, The use of $\tau_j^f(u)$ for the reflected flux, despite the non-Planckian spectral energy distribution of $F_j^{\downarrow}(0)$, leads to a spurious deficiency of radiant energy in the opaque bands, and thereby, an intense cooling close to ground.

Before deriving the correct narrow-band formulation, let us consider the results obtained for

the broadband case from a different perspective - that of comparing the erroneous and correct expressions for the reflected flux. The incorrect ($F^{\uparrow}_{rgw}$) and correct ($F^{\uparrow}_{rgc}$) reflected flux derived in the broadband case, are given by;

$$F^{\uparrow}_{rgw}(u) = (1-\epsilon_g)F^{\downarrow}(0)\tau^f(u); \tag{3.79}$$

$$F^{\uparrow}_{rgc}(u) = (1-\epsilon_g)\int_0^{u_t}\sigma T^4(u')\dot{\tau}^f(u+u')du', \tag{3.80}$$

for gray ground with emissivity ϵ_g, and with $F^{\downarrow}(0) = -\int_0^{u_t}\sigma T^4(u')\dot{\tau}^f(u')du'$. Here, $\tau^f(u)$ is the diffuse broadband transmissivity used (incorrectly) to attenuate both ground emission and the reflected flux. The transmissivity appropriate for the reflected flux is:

$$\tau^f_r(u) = -\frac{\int_0^{u_t}\sigma T^4(u')\dot{\tau}^f(u+u')du'}{F^{\downarrow}(0)}, \tag{3.81}$$

and not $\tau^f(u)$. From (3.79) and (3.80), we now obtain the condition under which the erroneous broadband reflected flux equals the correct one. As will be seen, the resulting constraint clearly points to the generic nature of the error, and thence, its relevance to any frequency-parameterized radiation scheme including narrow-band formulations considered here. Equating the reflected fluxes in (3.79) (3.80) one finds that the relation

$$\int_0^{u_t} du'\, T^4(u')\Big[\tau^f(u)\dot{\tau}^f(u') - \dot{\tau}^f(u+u')\Big] = 0, \tag{3.82}$$

must hold for the spurious cooling error to be absent. Since the temperature profile in (3.82) is arbitrary, one must have

$$\frac{d}{du'}\Big[\tau^f(u)\tau^f(u') - \tau^f(u+u')\Big] = 0 \tag{3.83}$$

$$\Rightarrow \tau^f(u)\tau^f(u') - \tau^f(u+u') = G(u), \tag{3.84}$$

with $G(u)$ being an arbitrary function of u. Using $u' = 0$ in (3.84), one concludes that G is identically zero. Hence,

$$\tau^f(u+u') = \tau^f(u)\tau^f(u'). \qquad \forall \quad u, u'. \tag{3.85}$$

The only non-trivial continuous solution of this functional equation is an exponential. For the transmissivity function, this must mean an exponential decay. Thus, for the spurious cooling error to be absent, regardless of the particular (atmospheric) temperature profile, the participating medium must be gray implying an exponentially decaying broadband transmissivity function; that is, $\tau^f(u) = \mathrm{e}^{-\alpha u}$ where α^{-1} is the photon mean free path that, by definition is independent of the particular frequency interval under consideration. It may be seen from (3.81) that $\tau^f_r(u) = \tau^f(u)$ in this case. Note that a similar constraint was arrived at in chapter 2, but this was for the restricted case of an isothermal atmosphere.

The water-vapor-laden atmosphere (water vapor is the principal participating component in a cloud-free troposphere) is, however, pronouncedly non-gray due to the enormous wavelength

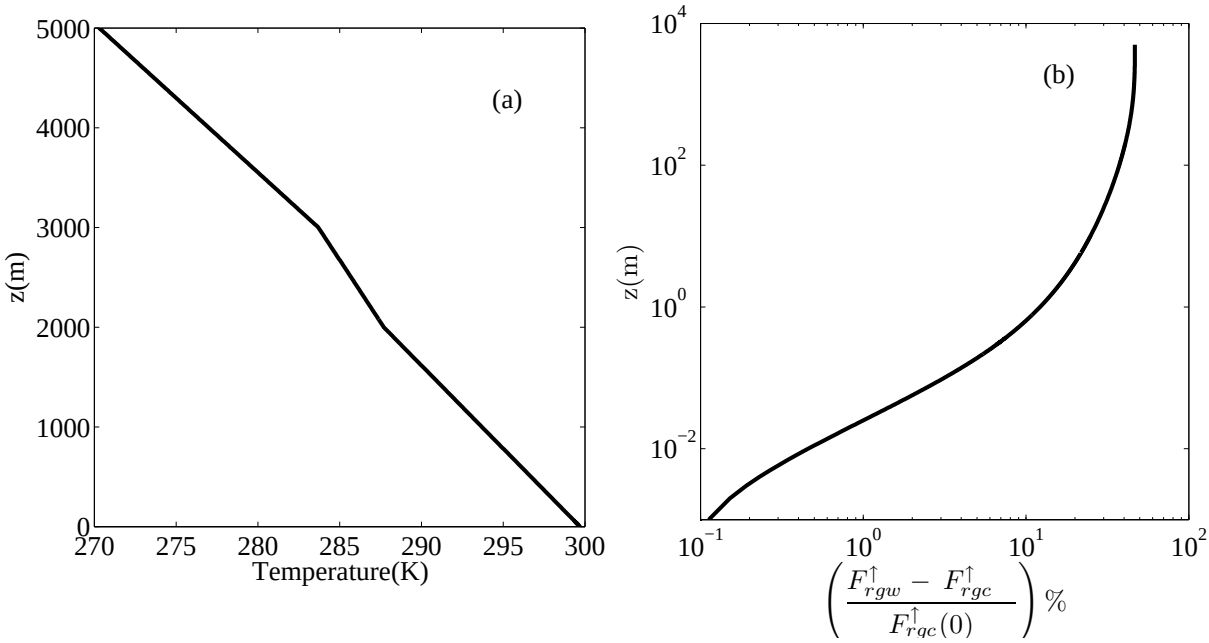

Figure 3.11: The plot in (a) shows the temperature profile for a standard tropical atmosphere, while (b) shows the corresponding difference between the erroneous $(F^{\uparrow}_{rgw})$ and correct $(F^{\uparrow}_{rgc})$ broadband reflected fluxes, (normalized by $F^{\uparrow}_{rgc}(0)$) as a function of z.

sensitivity of the water vapor absorption in the infrared and the resulting disparity in photon path-lengths even within small spectral intervals. Thus, $\tau^f(u)$ for water vapor departs significantly from a decaying exponential (see Figures 2.2b, 2.4). One therefore expects the erroneous reflected flux to lead to a spurious cooling error in any atmospheric calculation with non-black bounding surfaces and with radiation modelled using an emissivity scheme. An unlikely scenario may arise if (3.82) holds despite the broadband transmissivity not being an exponential; in which case, $T(u')$ would have to closely approximate the null-eigenfunction of (3.82) (a Fredholm integral equation of the first kind). Rather than attempt to calculate this eigenfunction, it is easier to verify if such an exception occurs for typical atmospheric profiles. In other words, is the typical atmospheric profile an eigenfunction of (3.82)? Figure 3.11 shows this not to be the case. Since the flux difference for a model tropical atmosphere [2] remains comparable to the individual fluxes. The normalized flux divergences plotted in figure 3.12 again emphasize the large error (close to 80%) that can occur close to the ground, if the reflected flux is attenuated by the wrong transmittivity. In summary, a necessary and sufficient condition for the spurious cooling error to arise in a broadband emissivity scheme is for $\tau^f(u)$ to deviate from an exponentially decaying function of the path length.

We now generalize the expressions for the reflected flux given by (3.80) to a smaller frequency interval: that corresponding to the j^{th} band in a narrow-band formulation. Accounting for the non-Planckian energy distribution of the downwelling surface flux, in the same manner as in (3.80), one obtains the following expression for the upward bandwise flux to be used in a

[2]The temperature profile for the tropical atmosphere is taken from McClatchey *et al.* (1972) which specifies the lapse-rate as a function of height. In the lower 2 kilometers the lapse-rate is 6 Kkm^{-1} and then changes to a lapse-rate of 4 Kkm^{-1} from 2-3 km. Then, again, the lapse-rate changes to 7 Kkm^{-1} up to 5 km. The corresponding density, moisture profiles are also tabulated.

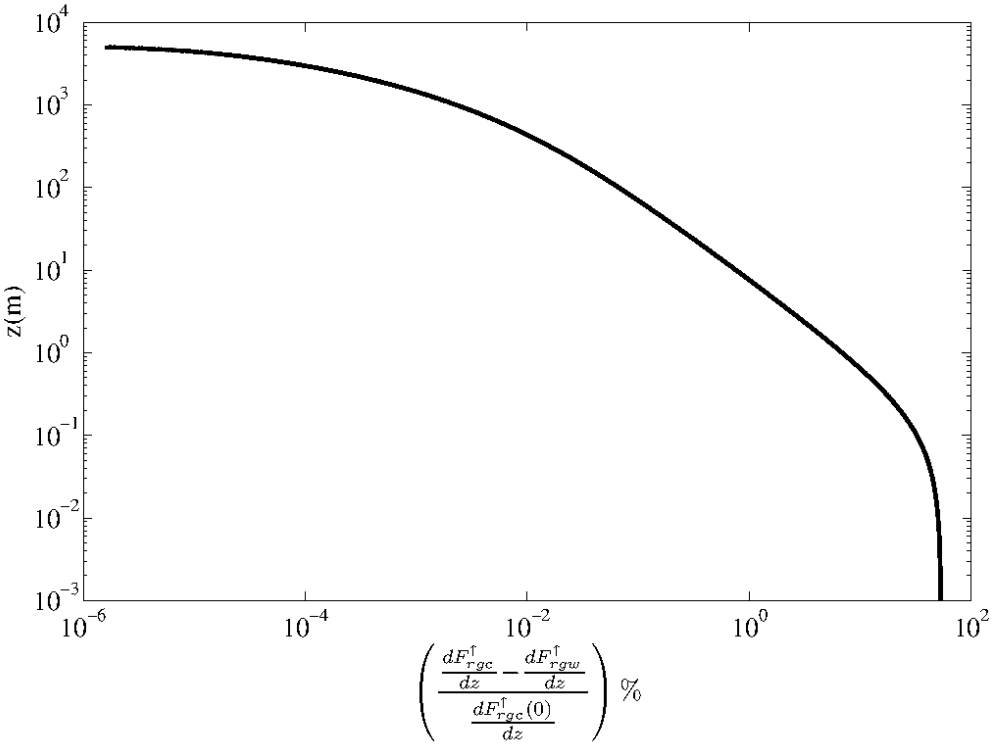

Figure 3.12: The plot show the differences in the divergences of the erroneous $(\frac{dF^{\uparrow}_{rgw}}{dz})$ and correct $(\frac{dF^{\uparrow}_{rgc}}{dz})$ reflected fluxes normalized by the correct reflected flux divergence at the surface $(\frac{dF^{\uparrow}_{rgc}(0)}{dz})$for a standard tropical atmosphere.

narrow-band formulation for an atmosphere with reflective ground:

$$F_j^{\uparrow}(u) = \epsilon_{gj}\pi B_j(T_g)\tau_j^f(u) - \int_0^u \pi B_j[T(u')]\dot{\tau}_j^f(u-u')du' - (1-\epsilon_{gj})\int_0^{u_t} \pi B_j[T(u')]\dot{\tau}_j^f(u+u')du' \quad (3.86)$$

Equating (3.86) and (3.78), one obtains that

$$\int_0^{u_t} du'\, B_j[T(u')]\Big[\tau_j^f(u)\dot{\tau}_j^f(u') - \dot{\tau}_j^f(u+u')\Big] = 0, \quad (3.87)$$

for the spurious cooling error to be absent in a narrow-band calculation. For an arbitrary temperature profile, (3.87) implies a condition analogous to (3.85) but one involving $\tau_j^f(u)$ instead. Thus, similar to the emissivity scheme above, an error will arise in a narrow-band formulation if and only if the band-averaged transmittance departs from an exponential. As mentioned in section 3.4.1, $\tau_j^f(u)$ typically involves an average over a frequency interval much larger than the inter-line spacing, and may be obtained in terms of effective line characteristics using statistical band models, in which case it turns out not to be a simple exponential function. For instance, a band model with identical Lorentzian profiles and random line positions [Goody (1964);Rodgers & Walshaw (1966)] yields

$$\tau_j^f(u) = \exp\left[\frac{-Su}{\delta}\left(1+\frac{Su}{\pi\alpha_L}\right)^{-\frac{1}{2}}\right], \quad (3.88)$$

where δ is the average line spacing, S is the mean line intensity and α_L denotes the Lorentzian half-width. As is well known [Goody (1964)], (3.88) exhibits three asymptotic regimes - the weak-line approximation when $(1-\tau_j^f) \propto u$ (for $Su \ll \pi\alpha_L$), the strong-line approximation with $(1-\tau_j^f) \propto u^{\frac{1}{2}}$ (for $\pi\alpha_L \ll Su \ll \delta^2/(\pi\alpha_L)$) when the line-centers are strongly absorbed with additional absorption occurring in the wings, and subsequent saturation ($\tau_j^f \to 0$) once the path length exceeds the mean inter-line spacing ($Su \gg \delta$). An exponentially decaying transmittance is only realized in the heavily overlapping limit ($\delta \ll \pi\alpha_L$) when there is a direct transition from a linear decrease for small u to an exponential one for large u. Thus, the existence of a sensible strong-line regime is direct evidence of fine structure in the absorption spectrum and the related significance of 'wing' contributions. The resulting departure of $\tau_j^f(u)$ from an exponential implies the appearance of a spurious cooling contribution on use of (3.78) in place of (3.86) [Varghese (2003); Savijärvi (2006)].

Figure 3.13 shows the bandwise flux discrepancy, (3.87), normalized by the correct reflected flux at the surface($(1-\epsilon_g)F_j^{\downarrow}(0)$), plotted against the height (z) for a water-vapor-laden tropical atmosphere. The assumed temperature profile for the tropical atmosphere is the same as that for figure 3.11. The plots are for both an opaque ($1550 - 1650\,\mathrm{cm}^{-1}$: the $6.3\,\mu$m vibration-rotation band) and a transparent band ($720 - 800\,\mathrm{cm}^{-1}$) with $\tau_j^f(u)$ given by (3.88) and the band parameters taken from Rodgers & Walshaw (1966). The discrepancy between the two reflected fluxes is smaller in the opaque band because the atmosphere is essentially infinite in extent in this interval. This is best seen from comparing the actual transmittance for the

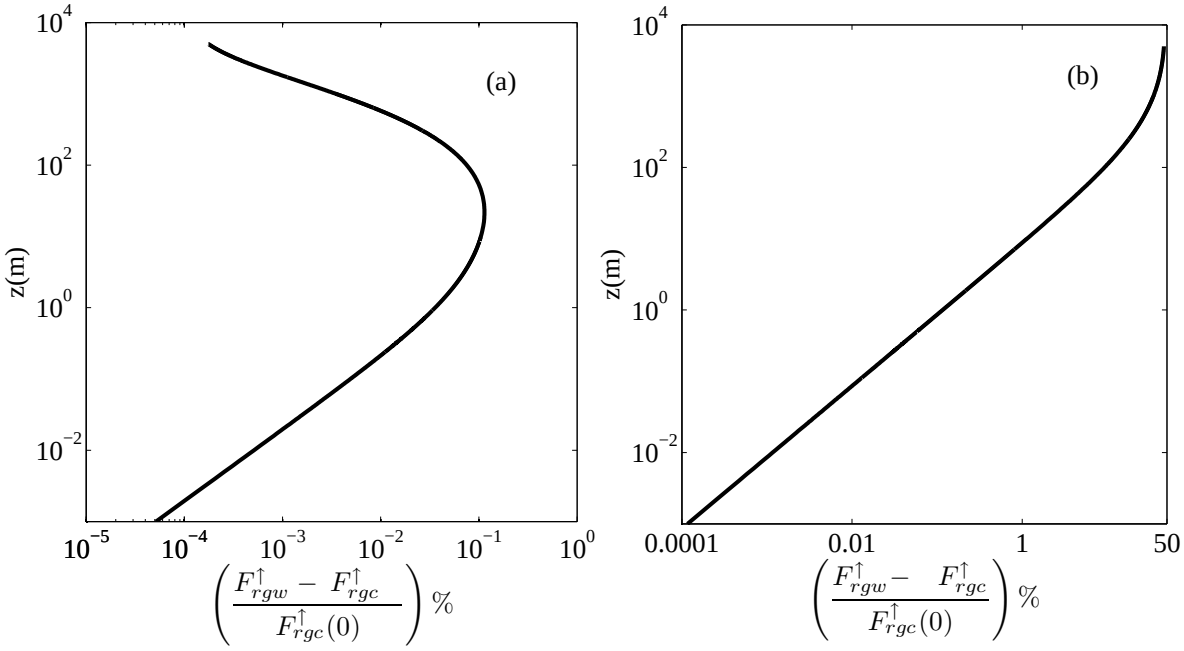

Figure 3.13: The two plots show the differences in the erroneous $(F^{\uparrow}_{rgw})$ and correct $(F^{\uparrow}_{rgc})$ reflected fluxes (normalized by the reflected flux at the surface in the particular band) for a tropical atmosphere and for the frequency ranges $720 - 800\,\mathrm{cm}^{-1}$ and $1550 - 1650\,\mathrm{cm}^{-1}$ (the 6.3 μm vibration-rotation band); the band-averaged transmittance, τ^f_j, is given by (3.88) with the band parameters taken from Rodgers & Walshaw (1966).

bandwise reflected flux in an isothermal atmosphere,

$$\tau^{fi}_{rj}(u) = \frac{(\tau^f_j(u) - \tau^f_j(u+u_t))}{(1-\tau^f_j(u_t))}, \tag{3.89}$$

with the erroneous one, $\tau^f_j(u)$. Both equal each other for an infinite atmosphere since $\tau^{fi}_{rj}(u+u_t)$ and $\tau^{fi}_{rj}(u_t) \to 0$ for $u_t \to \infty$. A comparison of the normalized flux divergences (flux divergence predicted by the wrong and correct formulation normalized by the correct flux divergence at the surface) is shown in figure 3.14 for both opaque and transparent bands. As expected, the error is minimum for opaque bands and a large error occurs in transparent bands, again reinforcing the fact that the error is minimum when the medium is infinite, since the reflected flux now corresponds to that of a blackbody.

The mention of a near-surface spurious cooling error in the above discussion implicitly assumes that the reflected-flux-transmittance, $\tau^{fi}_{rj}(u)$, given by (3.89), is always smaller than $\tau^f_j(u)$. This assumption is reinforced by figures 3.11 and 3.13 where the erroneous reflected flux is always seen to be greater than the actual one. It is of interest to enquire if there is the possibility of a spurious heating. In other words, restricting our consideration to an isothermal atmosphere (a reasonable approximation for the small length scales that characterize the erroneous flux divergence), are there conditions where the actual transmittance, $\tau^{fi}_{rj}(u)$, is greater than $\tau^{fi}_j(u)$?

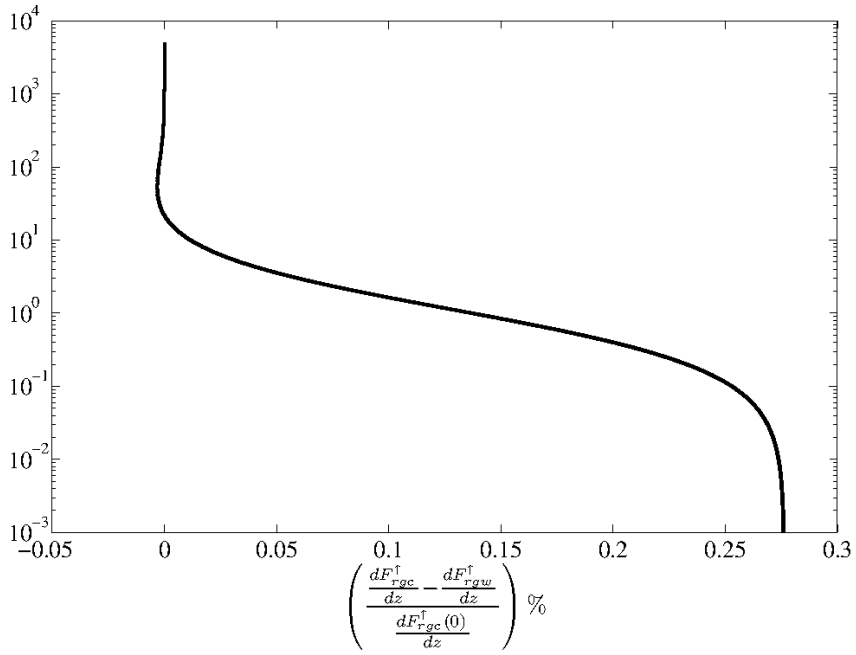

(a) Normalized flux divergence in opaque band

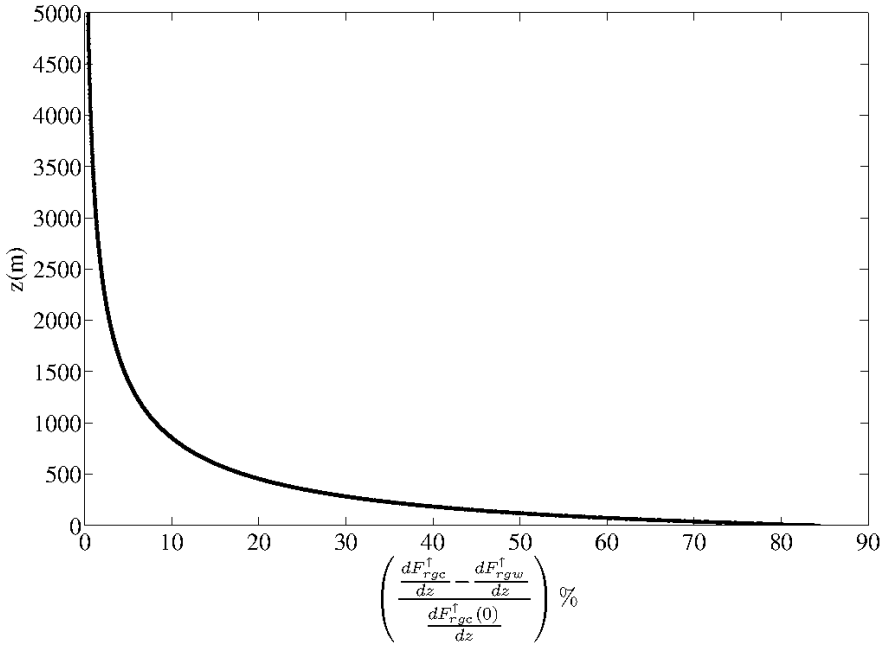

(b) Normalized flux divergence in window band

Figure 3.14: The two plots show the differences in the correct ($F^{\uparrow}_{rgc}$) reflected and erroneous ($F^{\uparrow}_{rgw}$) flux divergences and (normalized by the reflected flux divergence at the surface in the particular band) for a tropical atmosphere and for the frequency ranges $720 - 800\,\mathrm{cm}^{-1}$ and $1550 - 1650\,\mathrm{cm}^{-1}$ (the 6.3 μm vibration-rotation band); the band-averaged transmittance, τ^f_j, is given by (3.88) with the band parameters taken from Rodgers & Walshaw (1966).

For this purpose, (3.89) may be rewritten in the following alternate form:

$$(\tau_j^{fi}(u) - \tau_{rj}^{fi}(u))(1 - \tau_j^{fi}(u_t)) = \tau_j^{fi}(u + u_t) - \tau_j^{fi}(u)\tau_j^{fi}(u_t) \tag{3.90}$$

The RHS of (3.90) must be negative for a spurious heating contribution. Writing $\tau_j^{fi}(u) = \exp[-f(u)]$, this translates to the condition $f(u + u_t) > f(u) + f(u_t)$. Now, with the equality sign, this relation is the Cauchy functional equation, satisfied by $f(u) \propto u$, which corresponds, of course, to a gray atmosphere. The above inequality is satisfied when $f(u)$ varies more rapidly than a linear function, say, $f(u) \propto u^x$ (with $x > 1$); a transmittance of the form $\exp[-u^x]$ would therefore lead to a spurious heating contribution. Although a mathematical possibility, such a functional form appears to not be relevant to tropospheric heat exchanges with pressure-broadened spectra. This is clearly evident from the form of the transmittance in the strong-line regime, in which case $f(u) \propto u^{\frac{1}{2}}$ [Goody (1964)], and therefore, $f(u + u_t) < f(u) + f(u_t)$, implying that $\tau_j^{fi}(u) > \tau_{rj}^{fi}(u)$.

The arguments above show that the deviation of the band-averaged transmittance from an exponential is directly linked to the existence of a strong-line regime, and that the nature of this deviation is such as to lead to a spurious cooling contribution. It is therefore worth emphasizing that typical infrared spectra of atmospheric gases, at moderate pressures characteristics of atmospheric conditions have pressure-broadened line widths $[O(0.01 - 0.1\ \text{cm}^{-1})]$ smaller than the smallest inter-line spacing $[O(1\,\text{cm}^{-1})]$ due to rotation transitions: In other words, atmospheric radiative exchanges correspond largely to the strong-line regime [Goody (1964)]. Indeed, the importance of the atmospheric window implies that radiative cooling in the lower troposphere is dominated by wing contributions; the weak window attenuation, modelled as the water vapor continuum, is thought to arise from cumulative far-wing contributions [Bignell (1970);Clough *et al.* (1989), although the additional role of water-vapor dimers continues to be debated [Ptashnik *et al.* (2011)]]. The significance of the strong-line regime is also evident in emissivity parameterizations used for NBL modelling [Siqueira & Katul (2010);Garratt & Brost (1981);Rodgers (1967)] wherein the emissivity, for small u, being expressed in terms of $u^{\frac{1}{2}}$ (strong-line regime), rather than u (weak-line regime). Scaling approaches for an inhomogeneous atmosphere have again been based on the strong-line approximation [Cess (1974);Ramanathan (1976);Chou & Arking (1980)]. Clearly, one therefore expects a spurious cooling contribution in typical narrow-band formulations. To the extent that the frequency interval used in a narrow-band formulation is arbitrary [Ramanathan & Downey (1986)], a spurious cooling error is expected in any frequency-parameterized scheme with the parameterization applied to intervals larger than an elementary line width: The error, of course, arises only when such a scheme is applied to reflective ground. The calculations of Andre & Mahrt (1981), Schaller (1977), and more recently, Savijärvi (2006), are examples in this regard. Due to the spurious cooling error, the cooling-rate profiles obtained by Savijärvi (2006), using a narrow-band formulation, are very sensitive to a departure of ϵ_g from unity. Reducing ϵ_g from 1 to 0.8, for a mid-latitude summer (MLS) atmosphere led to perceptible cooling-rate differences at heights of upto a kilometer; the cooling-rate at 0.1 m, in particular, changed from 3.8 K/day for $\epsilon_g = 1$ to 9.5 K/day for $\epsilon_g = 0.8$. In contrast, the actual cooling-rate profiles for the (dry) lapse-rate atmosphere have been shown to be fairly insensitive to ϵ_g [see figure 2.8 in chapter 2]. Morcrette's original narrow-band cal-

culation [Morcrette (1977)], extended by Andre & Mahrt (1981) to model NBL over a non-black ground, highlights the incorrect effect of ϵ_g on the cooling-rates. In contrast to the enhancement with decreasing ϵ_g, expected on physical arguments, for a nocturnal inversion [Lieske & A.Stroschein (1967);Edwards (2009a)], the warming layer is already lost for $\epsilon_g = 0.965$.

3.6 Conclusions

In this chapter, we extend the flux-emissivity formulation to include multiple reflections between the ground and an opaque or semi-transparent cloud cover. This is particularly important when one has to predict the climate change accurately. Clouds are the major source of uncertainty in modeling climate change. It has been shown that, for a model atmosphere, not including multiple reflections can produce error an upto 7%. We then generalize the flux-emissivity formulation to include the directional characteristics of the medium which avoids the use of the diffusivity factor approximation. For a specular surface, the use of this approximation produces the minimum error while the maximum error, occurs for a Lambertian surface.

Further, we have highlighted the generic nature of the spurious cooling error in the context of frequency-parameterized radiation schemes when applied to reflective surfaces. A necessary and sufficient condition for this error, in the form of an intense near-surface cooling, to occur is the deviation of the appropriate frequency-averaged transmissivity function from a simple exponential decay. This deviation results from the multiplicity of photon path-lengths in the relevant frequency interval. The latter is almost always true for atmospheric radiative exchanges. The infrared spectra of most atmospheric gases is dominated by vibration-rotation bands, and the specificity of the underlying (discrete) transitions renders the photon mean free path an extremely sensitive function of frequency. Thus, any frequency-parameterized radiation scheme that does not resolve intervals comparable to or smaller than an elementary line width will suffer from a spurious cooling error. We have presented the corrected scheme that removes the error.

The spurious cooling error inherent in a frequency-parameterized radiation scheme highlights the superiority of the k-distribution method, and its extension (the correlated-k method) to an inhomogeneous atmosphere [Liou (2002)]. The method is based on the grouping of absorption coefficient (k_ν) values. Thus, the frequency integrals in the expressions for the monochromatic fluxes are replaced by integrals over k weighted by the cumulative probability distribution of photon path-lengths $g(k)$. The smooth variation of g with k, in sharp contrast to the rapid variation of k with ν, leads to an immediate computational advantage. In the present context, forming contiguous intervals based on k_ν values naturally negates the error in the reflected flux, since the error arises due to the disparity in photon path-lengths over small frequency intervals. Finally, it is worth mentioning that several calculations have been based on an exponential-sum fitting of the narrow-band transmittances [Liou & Sasamori (1975); Stephens (1978)], this being a discrete representation of the k-space integral with each decaying exponential corresponding to a gray sub-band. Importantly, the flux-divergence in this must be calculated as a sum of sub-band contributions. Not conforming to this procedure will lead to an error due to the huge disparity in the sub-band photon path-lengths, within a single band, as is the case in Varghese et al. (2003) [Varghese *et al.* (2003b)]. Similar to Savijärvi (2006), the predicted flux-divergence

profiles (for an MLS atmosphere [3])remain sensitive to a small deviation of ϵ_g from unity even at heights of the order of a kilometer; the surface cooling rate changes from 4.5 K/day for $\epsilon_g = 1$ to 37.5 K/day for $\epsilon_g = 0.8$.

[3]The temperature profile for the mid-latitude summer atmosphere is taken from McClatchey *et al.* (1972) which specifies the lapse-rate as a function of height. In the lowest kilometer, the lapse-rate is 4 Kkm^{-1} and then changes to a lapse-rate of 5 Kkm^{-1} upto 2 km. After that, there is a constant lapse-rate of 4 Kkm^{-1} up to 4 km. The corresponding density, moisture profiles are also tabulated.

Chapter 4

The Ramdas layer

A portion of material in this chapter is reproduced in JNCASR report JNCASR/EMU/2009-1

4.1 Abstract

We demonstrate here that a relatively recent theory proposed by Narasimha and co-workers, termed as VSN model, (outlined in Vasudevamurthy *et al.* (1993); Narasimha (1994); Narasimha & Vasudevamurthy (1995)), which purports to explain the origin of the Ramdas layer or the lifted temperature minimum (LTM), first observed by Ramdas and co-workers in the 1930's (Ramdas & Atmanathan (1932)), is erroneous. The theory is based on radiative transfer processes in a homogeneous water-vapor-laden atmosphere, and predicts the lifted temperature minimum to occur only when the ground emissivity decreases below unity. However, the exaggerated effect of the reduced ground emissivity on the near-surface radiative cooling rates (infrared flux divergences) predicted by the theory, and that leads to the LTM, is spurious, and the result of a what we call a 'band cross-talk'. The error arises from an incorrect treatment of the reflected radiation within an broadband flux-emissivity scheme and serves as a canonical illustration of the spurious cooling discussed in chapter 2. The inevitable conclusion from our analysis in this chapter is that radiative processes, acting in a homogeneous isothermal atmosphere, will not lead to a preferential cooling of the air layers near the ground, and thence, to an LTM. The origin of the LTM must therefore lie in a night-time atmosphere that is heterogeneous on the same length scales. We discuss the role of aerosols as a likely candidate for this heterogeneity.

4.2 Introduction

This chapter focusses on the origin of a well-known micrometeorological paradox variously termed as the Ramdas layer, the lifted temperature minimum (LTM), the elevated minimum etc [Ramdas & Atmanathan (1932); Lettau (1979);Oke (1970);Geiger (1995)]. Originally observed by Ramdas and co-workers in the 1930's, the Ramdas paradox concerns the occurrence of a minimum in the night-time temperature profile a few tens of centimeters above the ground on calm clear nights. A typical LTM profile, along with the typical daytime profile and the expected inversion profile is shown in figure 4.1. The phenomenon was initially thought to be restricted to the tropics. However, it has since been shown to be quite robust, having been observed all over the world over varied surfaces including rough soil, bare soil, Aluminum and concrete surfaces etc. under relatively calm cloudless conditions [Albani (1951); Brawand & Kohnke (1952); Lake (1956); Oke (1970); Raschke (1957); Mukund *et al.* (2010)]. The phenomenon is characterized by two parameters: the height and the intensity of the temperature minimum, and these are

illustrated in figure 4.2. The height (measured from the ground) at which the minimum temperature occurs ranges from 20 cm - 50 cm, and the intensity of the minimum, defined as the temperature difference between ground and the minimum value, ranges from 2-7 K. Despite its robustness, the phenomenon remains counter-intuitive in more ways than one.

- First, solid surfaces are far more effective radiators compared to gases. Efficient absorption of short-wave radiation leads to the ground heating up rapidly during the day, and likewise, emission in the infra-red range to outer space via the transparent bands in the water vapor spectrum is expected to lead to a rapid cooling at night. Thus, conventional wisdom suggests a nocturnal inversion layer with ground, and not the air layers above it, being the coldest at night [Sutton (1953);Stull (1988)]. Figure 4.1 shows a schematic of the familiar day-time profile, the expected night-time inversion temperature profile together with a night-time temperature profile exhibiting an LTM.

- Secondly, as already pointed out earlier [Narasimha (1991)], the relevance of a length scale of the order of decimeters in an atmosphere that is apparently homogeneous on length scales of the order of a kilometer (the water vapor scale height $u_t \approx 2.7\,km$) is far from obvious. That there are photon path lengths of this order, in the opaque bands, is known, but their manifestation only in the region close to the ground remains counter-intuitive.

- Thirdly, the Rayleigh number calculated based on the height and intensity of the LTM is $O(10^6)$, a factor of 1000 greater than the familiar critical threshold one would estimate based on the usual balance of conduction and convection [Chandrasekhar (1981)]. The apparent persistence of the LTM through the night, with no perceptible indication of an overturning instability, is again perplexing. It is thought that the stabilizing effects of cooling due to long-wave radiation may play a role, although there exists no quantitative prediction in this regard [1].

Assuming a homogeneous atmosphere[2], however, the most puzzling aspect of the LTM, is the existence of a cold layer of air in the immediate neighborhood of warmer ground and warmer layers of air above. Since any cooling below the ground temperature can only arise on account of radiation to outer space, the occurrence of the LTM implies that layers of air closest to the ground radiate most efficiently to outer space (here, we use the term 'outer space' to denote the upper reaches of the atmosphere where the temperature, on account of the adiabatic lapse-rate, $\sim 10\,\mathrm{Kkm}^{-1}$, has dropped to a level significantly below the ground temperature). This is difficult to explain, since radiant heat exchange, although a strongly non-local process in certain regions of the infra-red spectrum, is still a decaying function of the distance between participating elements in a homogeneous medium; for instance, the transmissivity function monotonically decreases with the height see figure 2.2b in chapter 2 of a homogeneous water-vapor-laden air column.

[1] Recent experiments by Singh (2013), [personal communication] suggest that the lowest air layers are not entirely quiescent, and that there is strong evidence of an overturning instability in the region below the temperature minimum. There is also, however, a clear indication of radiation-enhanced stability, and the elevated minimum does persist despite the aforementioned convective overturning.

[2] This is the central assumption in the VSN model to be discussed later. The only relevant length scale in the theory, indicative of an inhomogeneous atmosphere, is the water vapor scale height. The latter is about 2.7 km, a factor of $O(10^4)$ greater than the length scales relevant to the LTM, and therefore, irrelevant to its existence.

Thus, initial observations of the LTM were variously attributed to instrumentation error, advection of horizontal inhomogeneities (cold air from the environs), etc. However, more definitive experiments by Raschke (1957), and very recently by Mukund *et al.* (2010), have established that radiation plays a key role in the phenomenon. The Ramdas layer highlights in general the important but subtle role played by radiative processes in the stable atmospheric surface layer. Apart from its fundamental significance, the need to accurately resolve the temperature variation in the lowest meters of the atmosphere is also of particular importance in agricultural meteorology (the occurrence of frost and its adverse effect on crops [Lake (1956)], radiation fog and remote sensing (determination of true surface temperatures and emissivities [Snyder *et al.* (1998)]

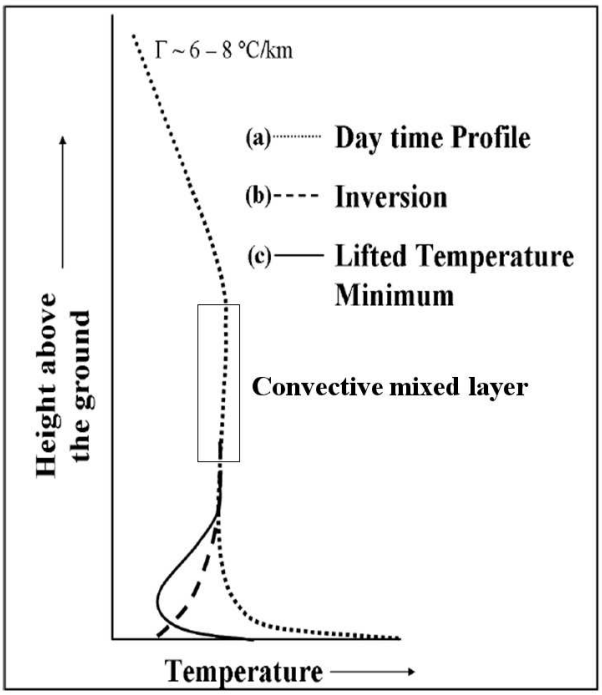

Figure 4.1: The figure shows three temperature profiles typically encountered in the lowest meters of the atmosphere. The dotted and dashed lines denote the expected day-time and night-time temperature profiles, the latter characteristic of a near-surface inversion layer. The solid line denotes the non-monotonic variation of temperature very near the ground leading to the emergence of an elevated minimum.

4.3 Earlier studies - Observations

The initial observations were made by Ramdas & Atmanathan (1932) and his co-workers in 1932 in Pune. It was suggested that, the warming up of the ground is greater in the tropics (due to higher solar insolation) and the ground cooling after sunset is not so rapid as to bring the surface temperature below that of the air layers. This is the reason for the initial skepticism that this phenomenon is restricted only to tropics. Further, the initial observational site was in a low-lying area and the drainage of air from the neighboring slopes could have affected the measured temperature profile. However, later measurements by other researchers confirmed that

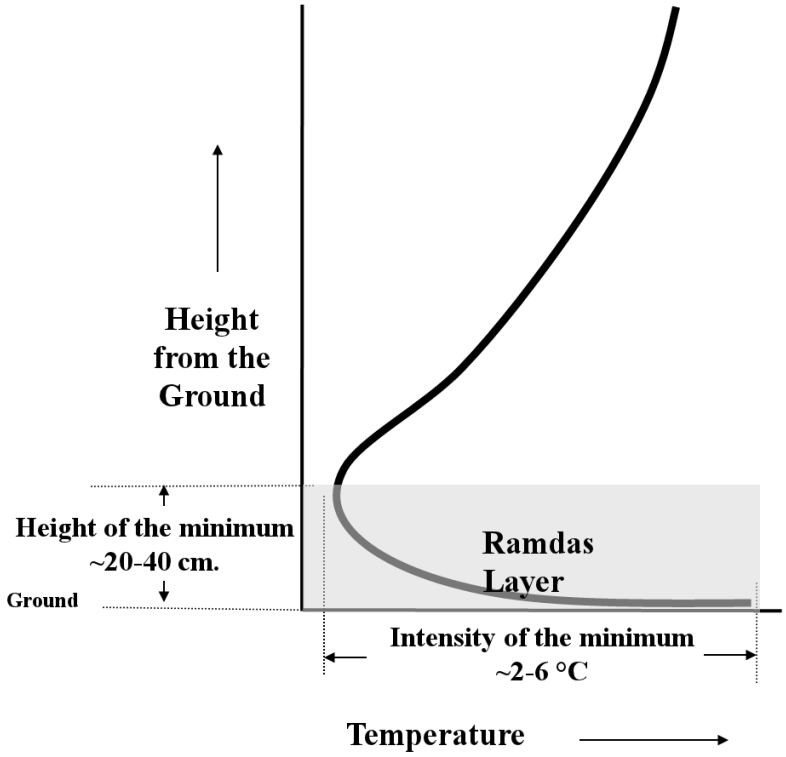

Figure 4.2: The figure shows the definition of intensity and height of minima which characterizes the LTM phenomenon.

this phenomenon is not restricted to tropics alone and measurements over large fetch-to-height ratio sites showed the presence of LTM-type profiles. The suggestion was that radiation could play a role in determining the temperature profile.

Later, Lake (1956) established the presence of this phenomenon over bare soil using thermometers and thermistors. The author put forward the mechanism for the occurrence of this phenomenon: "*the air on a clear night must lose heat by some mechanism other than convection and conduction to the surface; radiation exchange may provide a mechanism for such a loss. In this case, the air would continue to lose heat by radiation until it reached radiative equilibrium with its surroundings and this process might be retarded or assisted by other heat transfer processes such as conduction and eddy diffusion*". The author further surmised that the periodic fluctuations in the inversion layer could be due to a breakdown of the Ramdas layer.

Experiments by Raschke (1957) confirmed the existence of this phenomenon beyond any doubt. Based on careful measurements, the author classified the nocturnal temperature profile into three types; (i) the advection type profile with minimum at some height above the ground, (ii) LTM-type profiles with minimum at some height above the surface and (iii) inversion profiles. The role of turbulence and wind speed on LTM characteristics were studied carefully. The observations indicated, when wind speeds increase, the intensities of the minima decrease, and occasionally, the LTM-type profiles were replaced by inversion profiles. Further, LTM was vulnerable to turbulence. When the turbulence levels increased the minima disappeared but reappeared in a few minutes once the turbulence level came down.

Oke (1970) reported observations over bare soil, rough soil, snow and grass close to the

ground, on calm, clear nights, with sensitive instruments, and on a site where advective influence was small (fetch is around 180 m). The observations showed strong minima over bare soil (LTM intensity was 3^oC and height of minima was around 50 cm), and minima with weaker intensities over rough surface (LTM intensity being 0.3^oC). The striking feature of these observations was the occurrence of minima over snow (which has a high emissivity in the IR spectrum, and is an insulator), in contrast to previous experiments by Lütze (1960) didn't observe LTM over snow. Over grass, the minimum in temperature occurred over the grass tip (there is a clear distinction between the grass tip minimum and the LTM-type profile; the grass tip minima is where the minimum temperature occurs at the tip of the blade instead of the root). In the case of the LTM, the grass tip should be considered as the 'true active surface' and the measurements done over that surface must help discriminate between an inversion or LTM. Further, the role of clouds was also studied. The intensity of minimum was found to decrease during the passage of a cloud cover. A special type of the minimum was observed when an altostratus cloud layer covered the sky and this was attributed to the warming of ground by the cloud.

Recently, Mukund (2008) carried out very careful experiments to study the effect of thermo-physical and radiative properties of the surface on the characteristics of the LTM-type profile. The experiments were carried over concrete (high emissivity, high thermal inertia), concrete + aluminum (low emissivity, high thermal inertia), foam (high emissivity, low thermal inertia) and foam + aluminum (low emissivity, low thermal inertia) [Mukund *et al.* (2013)]. Unlike the previous field observations, the temperature profile was resolved near the surface over a finer vertical scale. The observed temperature, temperature gradient and radiative flux divergence profiles are shown in figures 4.3, and 4.4 (see Mukund (2008); Mukund *et al.* (2010) for more details). The figure shows that the intensity of minimum was higher over the low emissivity high thermal inertia surface (concrete + aluminum) and that the LTM-type profile was replaced by an inversion profile over the high emissivity, low thermal inertia surface (foam). Even over the foam surface, if the emissivity of the surface was reduced or at low wind speeds, LTM-type profiles were observed. Further, in line with the previous observations, when the wind speeds or turbulence levels increase the intensity of minima decrease. The passage of clouds again leads to a decrease in the LTM intensity. The observed temperature gradients were O(1000 Km^{-1}), values that are much higher than those reported in previous observations, and are, in fact, comparable to typical day-time temperature gradients. Further, the observed radiative flux divergence were O($1Ks^{-1}$). The higher values are due to the higher resolution near the surface (see figure 4.4)

A chronological description of the observational studies is given in table 4.1. The gist of the observational studies may be summarized as follows:

- The LTM phenomenon is real and robust.
- Wind speed and turbulence levels affect the intensity of the minimum, and may even modify the profile from an LTM-type profile to an inversion.
- The response of the near-surface air layers to the passing clouds suggest that the phenomenon is radiative in origin, and that there is a strong interaction of low-lying air layers

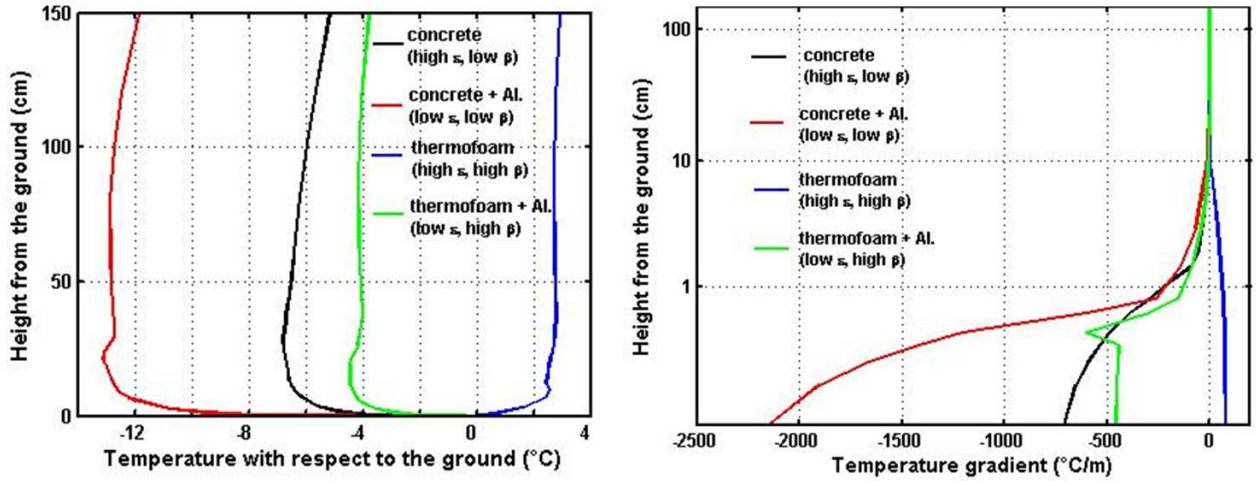

Figure 4.3: The figure shows the vertical variation of the measured temperature and surface gradient in Mukund (2008).

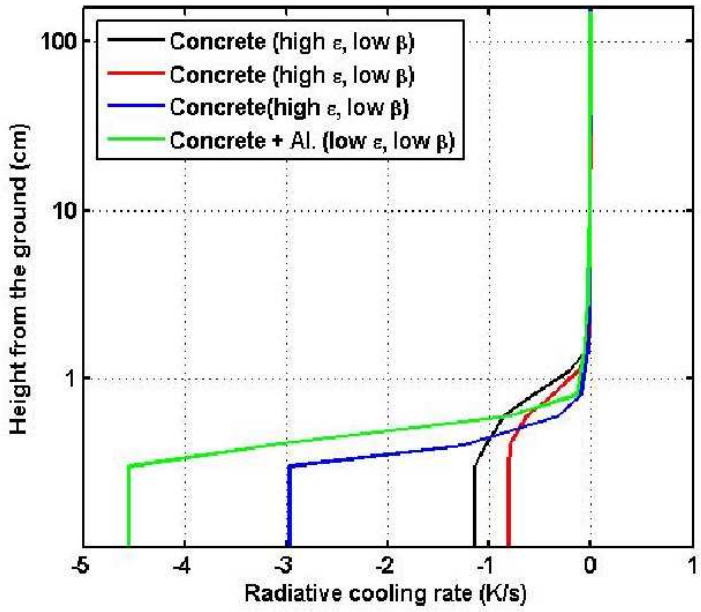

Figure 4.4: The figure shows the vertical variation of the measured infra-red flux divergences in Mukund (2008); the flux divergences may also be interpreted as radiative cooling rates.

and the uppermost air layers. This suggest that there is a mechanism of effective interaction through the window band in the water vapor spectrum(the photon mean-free path in this wavelength interval is of the order of kilometers).

- The intensity and the height of the minimum are a strong functions of the surface emissivity and the thermophysical properties of the surface.
- Values of the observed radiative flux divergence and the temperature gradient, close to the ground, are much higher than the values recorded in other observations, and those observed in the boundary layer. For instance, Funk (1960), from the observation inferred a cooling rate of $300\,K day^{-1}$ based on the difference in net fluxes measured at 0.5 and 1.5 m. On the other hand, Mukund (2008) measured a cooling rate of O(1 Ks^{-1} which is 86400 $K day^{-1}$) based on a much finer vertical resolution.

Reference	**Surface**	**Resolution near the ground**	**Intensity**	**Height of minima**
Ramanathan & Ramdas (1935)	Dry ground (Poona and Agra). Surface temperature - Ordinary thermometer	2.5 cm, 7.6cm, 15.2 cm, 25.4cm, 50.8 cm, 101 cm, 152 cm and 254 cm	3.2 K	25 cm
Lake (1956)	bare soil (Silsoe). Surface temperature - mean of two thermometer readings at the surface	2.5 mm, 1.2 cm, 6.4 cm, 9 cm and 1.3 m	3.2 K	25 cm
Raschke (1957)	bare soil(Poona)	1 mm, 1 cm, 10 cm, 1 m, 10m	6.3 K	10 cm
Oke (1970)	bare soil (Ontario), rough soil, snow and grass. Surface temperature - unshielded and non-aspirated thermocouple	1, 2.5, 5, 7.5, 10, 15, 20, 25, 50 and 100 cm.	bare soil - 3 K rough soil-0.2 K snow - 2 K	50 cm 2.5 cm 10 cm 7.5 cm above grass tip
Mukund (2008)	Concrete (high emissivity and high thermal inertia) Concrete+ Al (low emissivity and high thermal inertia) Foam (high emissivity and low thermal inertia) Foam + Al (low emissivity	1, 2, 3, 4, 6, 8, 15, 30, 50, 70,90, 115, 143, 166, 190, 212, 240, 260, 292, 310, 340, 400, 800, 1000, 1250, 1500 mm	Concrete 2-7 K concrete+Al 7-13 K Foam - 0 K Foam + Al 2-5 K	20 cm 20 cm 0 (Inversion) 20 cm

	and low thermal inertia)			

Table 4.1: Summary of observations which have studied the preferential cooling of the near-surface air layers leading to the LTM.

Any theory which is developed to address the origin of this phenomenon should be able to reproduce the above mentioned features. In the following section, we will revisit the broadband flux-emissivity scheme (discussed extensively in Chapter 2), that forms the basis of the VSN model, since the existing erroneous explanation for the origin of this phenomenon arises from the incorrect extension of this model for non-black surfaces. Further, based on the correct formulation, we will argue that preferential cooling near the ground cannot occur in a compositionally homogeneous atmosphere. We hypothesise an inhomogeneity on the length scale of the Ramdas layer as being necessary to explain the origin of this layer. Results from recent laboratory measurements [Mukund *et al.* (2013)] which have verified the above hypothesis are discussed briefly as a motivation to study the radiative forcing of inhomogeneity here, and later in chapters 5 and 6. In section 4.6, we present some preliminary theoretical results in support of the hypothesis.

4.4 The VSN model

The currently accepted theoretical explanation for the origin of the LTM is the so-called VSN model proposed in 1993 [Vasudevamurthy *et al.* (1993)]. More detailed accounts of various aspects of the original theoretical formulation, and with the inclusion of additional factors such as turbulence, have since appeared elsewhere in a series of later papers [Narasimha (1994); Narasimha & Vasudevamurthy (1995); Ragothaman *et al.* (2001); Vasudevamurthy *et al.* (2005)]. The theory is essentially an application of the well-known flux-emissivity scheme for radiative heat transfer [Liou (2002)], in the form proposed by Garratt & Brost (1981) for ground with emissivity ϵ_g, to a water-vapor-laden atmosphere. For convenience, the governing equations described in chapter 2 have been repeated here

$$F^{\uparrow}_{eg}(u) = \epsilon_g \sigma T_g^4 \tau^f(u), \tag{4.1}$$

$$F^{\uparrow}_{a}(u) = \int_0^u \sigma T^4(u',t)\dot{\epsilon}^f(u-u')du', \tag{4.2}$$

$$F^{\downarrow}_{a}(u) = \int_u^{u_t} \sigma T^4(u',t)\dot{\epsilon}^f(u'-u)du', \tag{4.3}$$

$$F^{\uparrow}_{rg}(u) = (1-\epsilon_g)F^{\downarrow}_{a}(0)\tau^f(u). \tag{4.4}$$

The flux-emissivity $\epsilon^f(u)$ is determined from an experimental fit down to length scales (of the order of tens of centimeters) relevant to the LTM. Unlike earlier theories [Zdunkowski (1966a)] which invoked the presence of a haze layer near the ground in order to explain the LTM [3], the

[3] The earlier calculation by Zdunkowski (1966a), although based on an inhomogeneous atmosphere, had to assume an unphysically low value of the molecular conductivity of air to explain the origin of this phenomenon. Hence, this method is not accepted in the literature. Although the author claims that, with the correct thermal conductivity, the model continues to predict an LTM, the results haven't been published. Further, later field observational studies (those that are aware of Zdunkowski (1966a) theory) do not show any haze layer near the ground [Oke (1970)].

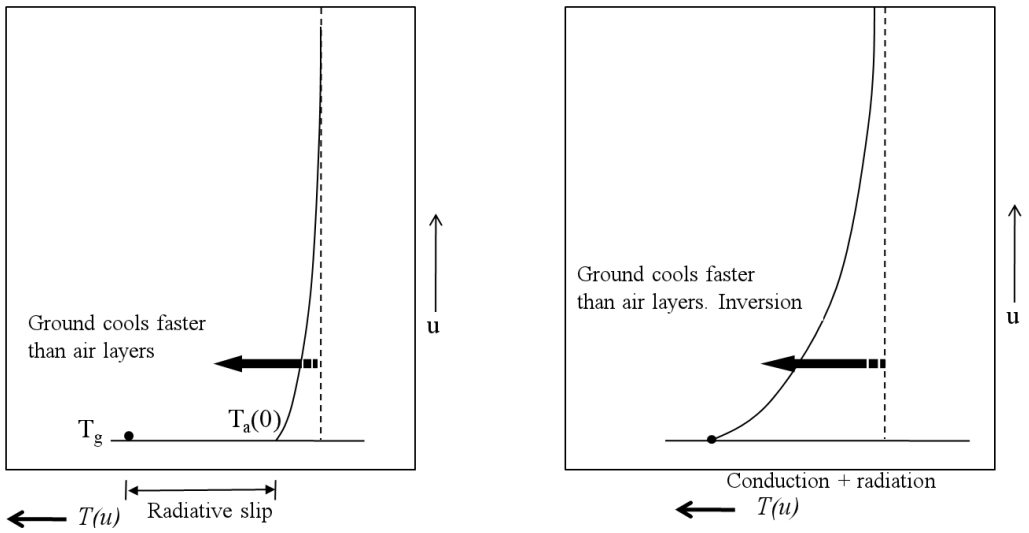

Figure 4.5: The temperature profiles predicted by the VSN model over a black surface. In the absence of conduction, ground cools faster than the air layers (the radiative cooling by water vapor is small see 4.5); conduction cools the layers further, and the resultant temperature profile is an inversion.

VSN model predicts a minimum in temperature at a height of a few tens of centimeters in a compositionally homogeneous night-time atmosphere.

The prediction of an LTM by the VSN model hinges on the generation of a radiative slip ($T_g - T_a(0^+, t) > 0$) in an initially homogeneous isothermal atmosphere [Vasudevamurthy *et al.* (2005); see figure 4.6]. The slip is the result of a radiative flux-divergence profile that peaks at the ground and decays thereafter over a length scale of the order of meters. The latter length scale corresponds to the photon mean-free-path in the strongly absorbing bands of the water vapor spectrum (α_{nw}^{-1}, see discussion on the two-band model in chapter 2). The resulting layer of radiatively cooled air immediately above warmer ground has been termed the 'emissivity sub-layer' [Vasudevamurthy *et al.* (1993);Narasimha & Vasudevamurthy (1995)]. With the inclusion of conduction, this discontinuity in temperature is smoothed into a boundary layer that now exhibits a non-monotonic temperature dependence - the LTM. This is in contrast to the model's prediction of an inversion layer over a black surface using the flux-emissivity scheme and the existing notion of inversion layer where the ground cools faster than the air layers. Over a black surface, in the absence of conduction, the surface, cools faster than the air layers via the transparent bands of the spectrum (see figure 4.5), and this results in a positive slip (the lowermost air layer is at a higher temperature than the ground). Conduction smoothens the slip and into a monotonic increase characteristic of an inversion temperature profile.

The initial radiative slip, due to a preferential cooling of the near-surface air layers in an isothermal homogeneous atmosphere, is thus crucial to the prediction of the LTM. Further, such a sub-layer is predicted to occur only for a non-black surface. Both the cooling in the emissivity sub-layer and the resulting temperature minimum in presence of conduction are spurious effects resulting from a "band cross-talk". The latter error was discussed in detail in chapter 2 and refers to, a physically incorrect coupling between the most opaque and most transparent bands in the water vapor emission-spectrum due to the use of an erroneous broadband transmissivity

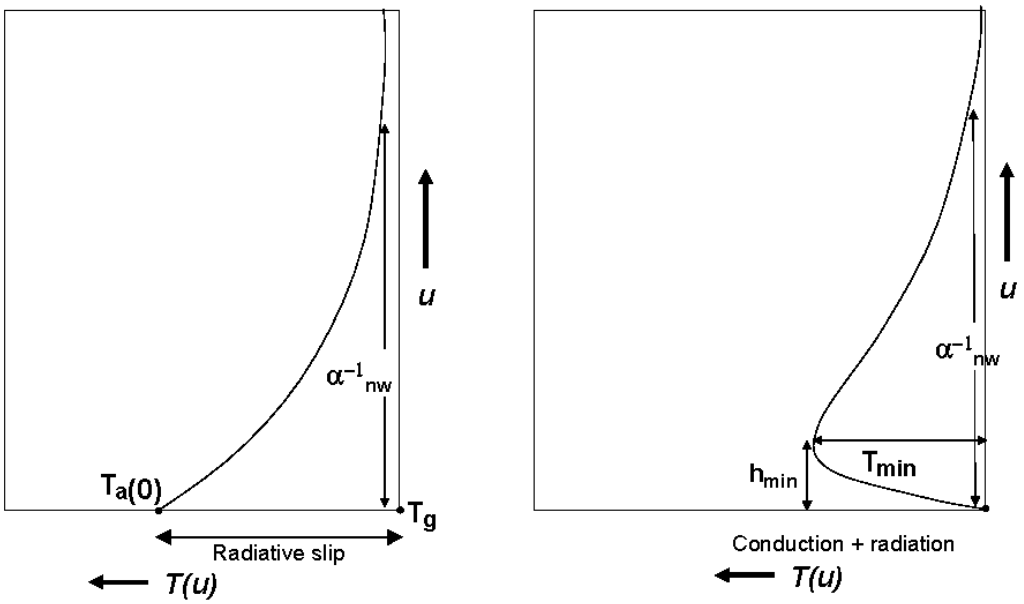

Figure 4.6: The temperature profiles predicted by the VSN model. In the absence of conduction, the model predicts a layer of cold air of height α_{nw}^{-1} (in the present notation) with an associated slip at the ground; conduction smoothens the radiative slip into a temperature profile exhibiting an LTM.

for the reflected radiation. The emissivity sub-layer, in the context of the VSN model, is merely a boundary layer where the spurious cooling caused by the cross-talk term is the most significant.

The occurrence of the aforementioned cooling can be easily seen by examining the radiative flux divergence for an isothermal atmosphere as calculated from (4.1)-(4.4)

$$\frac{dF}{du} = \sigma T_0^4[\dot{\epsilon}^f(u_t - u) + \dot{\epsilon}^f(u)(1-\epsilon_g)(1-\epsilon^f(u_t))], \tag{4.5}$$

In the above expression, the term $(1-\epsilon^f(u_t))$ denotes the transparency of the atmosphere which is due to the presence of weakly absorbing lines corresponding to photon path-lengths comparable to or greater than the height of the atmospheric column. The initial rapid increase in $\epsilon^f(u)$ is due to the strongly absorbing lines (see figure 2.2b in chapter 2). Hence, in the above formulation, it appears as if the reflection interaction, changes the spectrum from being initially restricted to the opaque bands, (as in $F_a^{\downarrow}(0)$), to having a significant fraction of its energy in the window band in the up-welling reflected radiation. This is, of course, incorrect since the reflection interaction must leave the spectrum of the incident radiation unaltered. It is the apparent unavailability of this warming reflected component that leads to the preferential cooling near the ground.

A comparison of the Vasudevamurthy et al. (1993) and Garrat and Brost (1981) predictions also reveals the singular nature of the energy density that drives the spurious cooling. The former differs only in that the flux-emissivity is determined from an experimental fit down to much smaller scales relevant to the LTM. As a result, for a decrease in ϵ_g from unity to 0.8, the near-surface cooling rate predicted by Garrat and Brost (1981) increases from about 17 K/day to 77 K/day, while that predicted by the Vasudevamurthy et al. (1993) model shoots up from

a mere 0.3 K/day to 1728 K/day! This scale-dependent sensitivity to ϵ_g becomes obvious on examining the flux divergence for an isothermal atmosphere using (4.5). The factor $(1-\epsilon^f(u_t))$ which denotes the overall medium transparency, is insensitive to an increased resolution of the opaque bands. In contrast, $\dot{\epsilon}^f(0)$ scales as the inverse of the smallest photon path-length resolved, and is directly responsible for the enhanced cooling in the Vasudevamurthy et al. (1993) model. With the addition of increasingly opaque bands, the portion of the reflected energy that is (incorrectly) attributed to the transparent bands corresponds to shorter photon path-lengths; the resulting deficiency in warming flux is felt closer to the surface, leading to an increasingly large cooling flux-density. Thus, an attempt to refine a given prediction by a careful synthesis of the flux-emissivity function leads one further away from the correct answer (close to the surface). It is worth noting that although the Vasudevamurthy et al. (1993) surface cooling-rate prediction for $\epsilon_g = 0.8$ is exaggerated, the cooling rate predicted by the model at 1 m is about 125 K/day [Varghese *et al.* (2003b)], this being comparable to the Garrat and Brost prediction at 2 m (the lowest level used in the calculation), again emphasizing the resolution-dependent magnitude of the spurious cooling error.

The flux divergence predicted using the correct formulation (see equation (2.34)-(2.37) in chapter 2) is given by (see also equation (2.22))

$$\frac{dF}{du} = \sigma T_0^4[\dot{\epsilon}^f(u_t-u) + (1-\epsilon_g)\dot{\epsilon}^f(u+u_t))]. \tag{4.6}$$

Unlike the VSN model, the correct formulation predicts a much weaker cooling, close to ground, proportional to the much smaller gradient of ϵ^f for u comparable to u_t and more importantly, the cooling rate to *increase* with height. This suggests that no *preferential* cooling can occur near the ground. Further, reducing ϵ_g doesn't change the qualitative nature of the flux divergence profile. Thus, the main conclusion is that LTM *cannot* occur in a homogeneous atmosphere. As will be demonstrated in later chapters, neither the simplification to an isothermal atmosphere nor the restriction to a static equilibrium scenario (a time-independent ground temperature) changes the essential physical arguments.

4.5 The origin of the Ramdas layer

Having established that the explanation put forth by the VSN model for the existence of an LTM is wrong, we return to the question of what actually causes the LTM. We first examine the possibility that the LTM may simply be a remnant of the day-time temperature profile. The ground, especially in the tropics, is left considerably hotter than the lower layers of air by the absorption of solar radiation during the day and the temperature gradient at the ground may exceed the nominal adiabatic lapse-rate by three or four orders of magnitude. It was therefore suggested by Ramdas & Atmanathan (1932) that this characteristic of the evening temperature profile might persist through the night even as the ground starts to cool by emission of long-wave radiation. The night-time profile with an LTM is not merely a displaced late-evening temperature profile, however. This is seen in figure 4.7 which highlights the qualitative difference between the two profiles. Although the ground is warmer in both cases, the evening temperature profile exhibits a monotonic variation with the hottest layers of air closest to the warmest surface (ground).

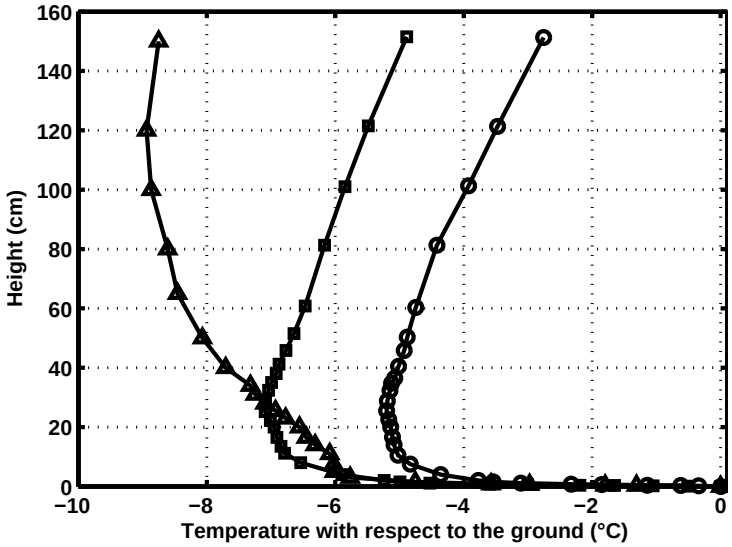

Figure 4.7: The figure compares a typical day-time temperature profile (triangles) with two typical night-time profiles (squares and circles) exhibiting an LTM in order to highlight the qualitative difference between the two cases. The LTM profiles represent observations by Mukund (2008).

This is in contrast to the counter-intuitive non-monotonic temperature dependence in an LTM profile, already discussed in section 4.2.

A couple of other points reinforce the existence of an intrinsic cooling mechanism giving rise to the LTM, rather than it being the result of an imprint left at sunset. Figure 4.8 shows the recent observations by Mukund (2008), where the response of air layers to a change in the wind speed and turbulence levels is presented. The corresponding change in the intensity of the minimum is also plotted in the lower panel. It can be seen, the wind speed remains constant the initial 30 minutes. and turbulence levels started decreasing after this interval. The temperature trace shows the ground cooling-rate is unaffected by the change in turbulence level but the air layers, up to a height of $150\,cm$, started cooling *faster* than the ground. This results in an increase in the intensity of the minimum. This is again seen in figure 4.9 which includes scatter plots of the ground cooling rate against the air cooling rate for the various surfaces used in the observational study of [Mukund *et al.* (2013)]. The plot shows a pronounced tilt towards the air cooling rate axis implying that air in fact, cools faster than the ground. Note that, although the instantaneous cooling rate shows that the lowermost air layers cool faster than the surface, the mean cooling rates of the surface and air layers, when averaged over longer periods, remain comparable [Mukund *et al.* (2013)]. This is because the surface inertia prevents the runaway cooling of air layers.

The relative magnitudes of the cooling rates above are crucial since one has an inherently unsteady scenario with the ground starting to cool at sunset by emission of long-wave radiation, and thereby, 'dragging' the overlying layers of air along with it. Since the ground is warmest at sunset, one would normally expect the near-surface air layers to heat up to the ground on account of radiative exchanges in the opaque bands. This radiative heating would lead to a decreasing temperature difference between the air layers and ground even as the respective absolute temperatures continue to decrease after sunset. This is, however, in direct opposition

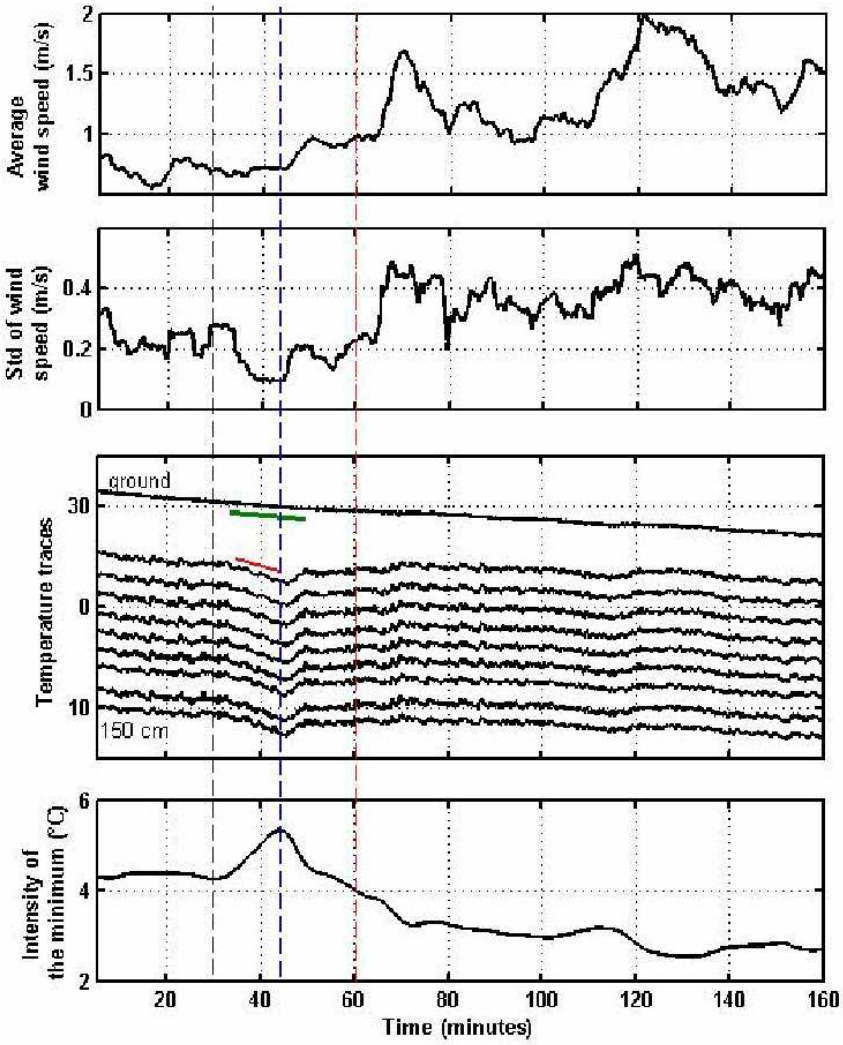

Figure 4.8: The observed cooling rates of the lowest air layers and that of the ground in relation to the prevailing mean wind speed and fluctuations (Mukund (2008)). The different temperature traces have been displaced vertically for clarity. The faster cooling of the air layers leads to an increase in the intensity of the LTM when the wind the turbulence level decreases around 25-45 minutes.

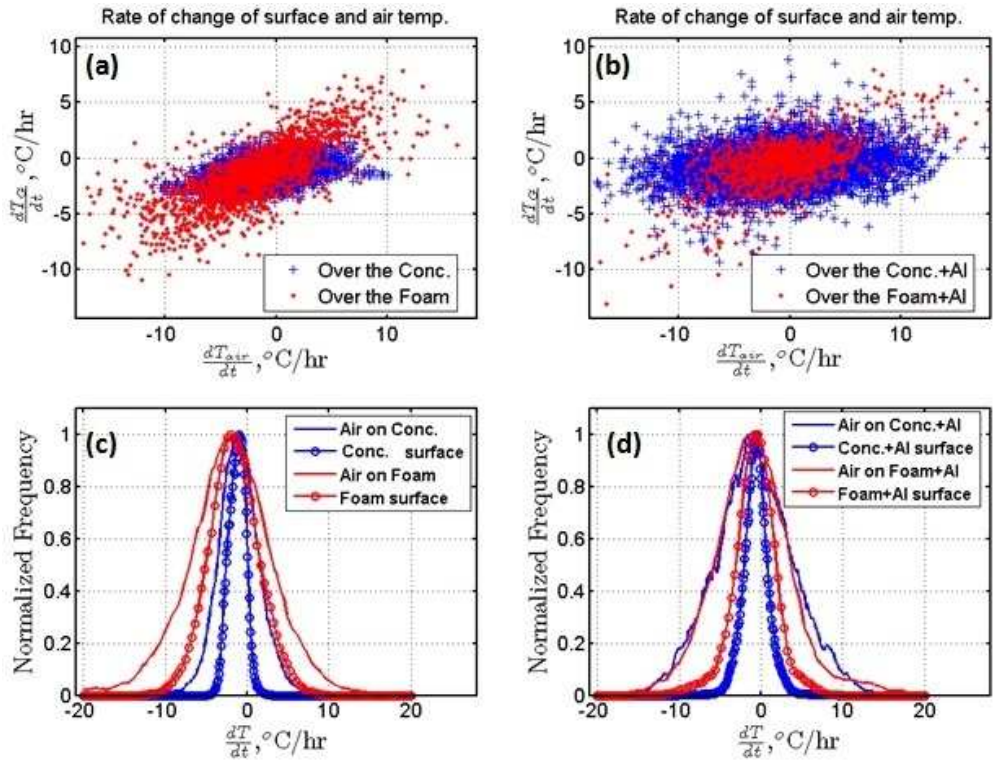

Figure 4.9: Top panels denote the scatter plots of the window-averaged, instantaneous rate of change of surface temperature against those for air layers close to the ground over different surfaces Mukund *et al.* (2013). Bottom panels represent the normalized histograms. Left and right panels correspond to high- and low-emissivity surfaces respectively. Blue color is data over concrete surface (high thermal inertia) and red is data over foam surface (low thermal inertia).

to the experimental observations above. Thus, the cooling of the air-layers relative to the ground can only occur due to radiative exchanges with the upper layers of the atmosphere which are at a temperature substantially lower than either. But, the importance of a 'cooling-to-outer-space' contribution for the air layers implies that the dynamics in the transparent window band must play a crucial role in the underlying radiative balance; a role that is unlike the usual one where the ground leads the window-band driven cooling process. Further, that the radiative exchange involving the layers of air just above the ground and outer space is most efficient can only imply that the constitution of these layers of air must differ from the warmer layers of air above; in other words, *a night-time atmosphere that is heterogeneous in the lowest meters*. The heterogeneity must then be responsible for enhancing the radiative efficiency, the enhancement made possible by an increased emission in the window band [4]. The existence of a heterogeneity also helps clarify the counter-intuitive nature of the LTM - the existence of cold air in warmer surroundings.

A detail concerns the role of the rapid temperature variation (the 'slip layer'), in the late-evening temperature profile, in determining the observed cooling rates (see figure 4.7). The varying temperature itself implies a thermally inhomogeneous atmosphere, and it is known that with such a variation, it is possible for the calculated radiative flux divergence to change sign very close to the ground [see Edwards (2009a)]. Indeed, approximating the late-evening temperature profile by an exponential with an explicit length scale to denote the height of the 'slip layer', it is easy to show that the radiative flux divergence in a gray medium, changes sign in this slip layer. The situation, is in fact, complementary to the case of an inversion profile in that the temperature in the transitional layer decreases with height (rather than increase as is the case for an inversion). Thus, based on the cooling-rate profile for an inversion layer (see section 2.4 in chapter 2), one expects, a transition from radiative heating at greater heights to cooling near the surface. This is again because the lowest layers of air in the region of rapid temperature variation, with temperatures close to T_g, begin to cool to the colder layers of air above. This change in sign may already be seen for a gray medium. For a slip layer of height H, (that is, with the transitional temperature profile being given by $T(z) = T_g - \Delta T(1 - \mathrm{e}^{\frac{-z}{H}})$ and a gray medium with absorption coefficient α, the flux divergence at the ground is given by $\dfrac{dF}{du} = 4\alpha(\sigma T_g^3)\dfrac{(\Delta T)}{(1+\alpha H)}$, and the corresponding cooling rate is $4\alpha(\sigma T_g^3)\dfrac{(\Delta T)}{\rho C_p(1+\alpha H)}$; here, ΔT denotes the (constant) temperature deficit of the air layers above the slip layer relative to the ground and ρC_p is the heat capacity of air. Figure 4.7 shows that $H \approx 10\,cm$ and $\Delta T \approx 5K$; The radiative cooling at the surface for a water-vapor-laden atmosphere can be obtained immediately by changing the sign of ΔT in the expression (2.53) (given in chapter 2) obtained for the inversion layer. The resulting cooling rate for ΔT $5\,K$ and $H = 10$ cm is around 600 K day^{-1} which is very small compared to the observed cooling rate which is 1 Ks^{-1} . Thus, any possible cooling due to the temperature variation in the slip layer is minuscule in comparison to observed values quoted above, implying that the observed cooling rates even in the air layers just above ground are unrelated to any near-surface non-isothermality, It is also worth emphasizing that, although the temperature variation very close to the ground leads to

[4] Since the heterogeneity may be in the form of microscopic solid particles or water droplets, its emission spectrum, like most solids, is expected to be a relatively smooth function of wavelength. The requirement of an efficient emission in the window band is thus hardly a restrictive one.

a small radiative cooling contribution, it doesn't explain the continued cooling of the air layers above the slip layer. Most importantly, such cooling can never lead to the lowest layers of air attaining a lower temperature than those above them. Thus, the strong non-isothermality of the late-evening atmosphere in the lowest meter is but a detail when it comes to explaining the LTM, and it makes sense to look for an explanation, at least an initial one, in the simplified theoretical construct of an initially isothermal atmosphere.

To sum up, experimental observations clearly show that the origin of the LTM lies in an intrinsic cooling mechanism of the lowest layers of air. Both with regard to the LTM, and in a more general context, the conclusion that emerges from the analysis in section 4.4 and experimental observations [Mukund (2008);Mukund *et al.* (2010);Mukund *et al.* (2013)] is that there can exist no preferential radiative cooling or heating mechanism in an atmosphere homogeneous on the relevant length scales (a few decimeters). The occurrence of the LTM in particular must therefore be a reflection of an atmosphere that is inhomogeneous on the same length scales as the temperature minimum. The near-surface layers of air, on account of the suspended heterogeneity, a likely efficient emitter in the atmospheric window band, manage to cool more efficiently to outer space than their immediate surroundings. The aerosol particles which are suspended in the air could be a plausible candidate for this heterogeneity. The inhomogeneity arises due to a balance between sedimentation and turbulent/laminar diffusion (depending upon the wind speed), and it is this balance that determines the detailed functional form of the aerosol concentration profile. For instance, a balance between sedimentation and the laminar diffusion leads to an exponentially decaying concentration profile with height; turbulent diffusion, on the other hand, leads to an algebraically decaying (Rouse) concentration profile.

4.6 The Aerosol hypothesis

Figure 4.10 shows a typical aerosol concentration profile over the lowest kilometers under nocturnal conditions obtained from $LIDAR$ measurements [Devara & Raj (1993)]. There is the clear suggestion of a rapid rise in concentration with approach towards the ground. Unfortunately, the lowest data point is at $50\,m$- about two orders of magnitude greater than the scales relevant to the LTM! Thus, although the variation in aerosol concentration is consistent with the above hypothesis, it is by no means quantitative.

The origin and stability of the LTM on laboratory scales has been studied extensively by Mukund (2008), and very recently by Singh (2013). The laboratory set-up helps examine the LTM under controlled conditions and eliminates the vagaries of weather and advection effects. The detailed experimental set-up and procedures have been discussed in Mukund (2008);Mukund *et al.* (2010), and here, we focus only on the essential idea underlying the basic configuration. In order to achieve the LTM-type profiles under laboratory conditions, the conditions prevalent in the night-time atmosphere have to be established. In the atmospheric context, the conductive and radiative fluxes incident on a fluid element close to ground are different in the sense that the temperature corresponding to the downwelling radiative flux differs from the governing local conductive or convective heat transfer. The temperature boundary condition for the local heat transfer mechanisms like conduction or convection is fixed by length scales of the order of the height of the nocturnal boundary layer, while the effective temperature of the radiative flux

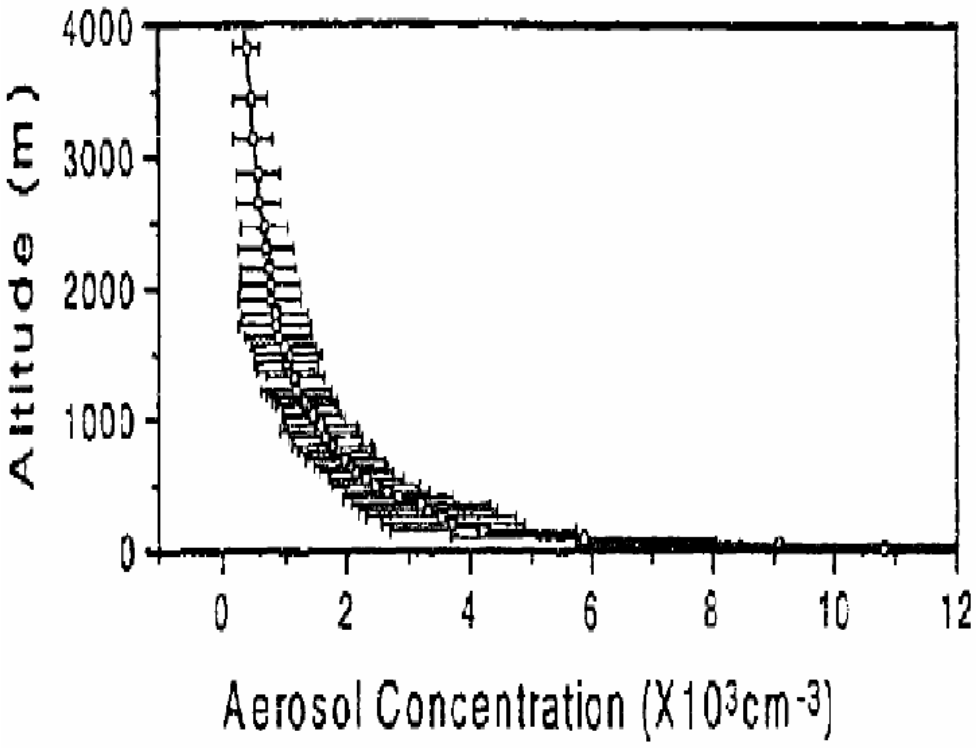

Figure 4.10: The figure shows the variation of aerosol concentration in the lowest meters of the atmosphere under nocturnal conditions as measured by Devara & Raj (1993).

is determined by much larger length scales of the order of the length scale of the atmospheric column itself. This decoupling is due to the following reason. The great height of the atmospheric column, and the fact that it can support a lapse-rate profile, implies that the uppermost air layers are much colder than those close to the ground. Next, the transparency of the atmospheric column in the infra-red enables the lowermost air layers to interact with the uppermost cold layers, making the effective temperature of the cold 'radiative sink' entirely different from that corresponding to the local heat transfer processes. This de-coupling should be established on the laboratory length scales to obtain LTM-type profiles. This has been achieved in an ingenious manner in the laboratory by having the upper plate in the form of a transparent polythene sheet, with the cold radiative sink being mimicked by using ice bath which acts as a surrogate for the upper atmosphere. Experiments with unfiltered air as the participating medium, and interacting with the ice bath, led to LTM-type profiles. Experiments in this set-up have since been carried out to validate the aerosol hypothesis put forth in the previous section. Towards this end, a HEPA (High Efficiency Particulate Air) filter was used to progressively filter out the aerosol particles of size greater than 0.3 μm. Experiments with different durations of filtering, and the corresponding equilibrium temperature profiles are shown in figure 4.11. It can be seen that the intensity of the minima decrease with an increase in the duration of filtering which is expected to lead to a decrease in the particle number density. For a filtering duration of 60 min, the temperature variation follows a linear conduction profile, with there no longer being an elevated minimum; under these conditions the particle number density is presumably, low enough for the associated radiative fluxes to be negligible.

Motivated by the above experimental results, we have theoretically studied the role of the participating medium inhomogeneity in modifying the temperature profile. The detailed modeling of the laboratory experiments, described briefly above, will be discussed chapter in 6. In this chapter we emphasize the role of the aerosol radiative forcing, in the context of the field observations. out in the following simplistic scenario. To begin with, in section 4.6.1 we will estimate the particle number density needed to obtain the near-surface observed cooling rate of $O(1Ks^{-1})$ reported in Mukund *et al.* (2013) for the case of an isothermal atmosphere. Then, we will obtain the final equilibrium temperature profile considering the water vapor spectrum to consist of only two bands (along lines discussed in section 2.3.1 in chapter 2). The analysis for the equilibrium profile is carried out in the limit of small aerosol concentrations when the radiative forcing due to the aerosol particles is restricted to the window, that is, the weakly absorbing part of the spectrum. Water vapor dominates the radiative exchanges in the strongly absorbing part of the spectrum. Such a demarcation can be naturally arrived from the full form of the governing equation for the flux divergence for the small values of a dimensionless parameter that measures the relative magnitudes of the water- vapor and aerosol-driven cooling.

4.6.1 Initial cooling-rate

Herein, we will estimate the aerosol forcing needed to reproduce the near-surface cooling rates in Mukund (2008) observations. Since the arguments in section 4.4 show that the non-isothermality of the evening transitional profile is a minor consideration, we will restrict our attention to an inhomogeneous but isothermal atmosphere, the inhomogeneity being a dilute optically thin layer of aerosol particles close to ground. We begin by considering the radiative balance of an isolated aerosol particle interacting with the sky and the ground. The emission from a gray ground at temperature T_0 and emissivity ϵ_g is $\epsilon_g \sigma T_0^4$, and the emission from the cold sink at temperature T_{sky} is σT_{sky}^4, where T_{sky} is the effective temperature that corresponds to the emission from the entire atmosphere (both upward an downward); note that T_{sky} is much lower than T_0, even for an isothermal atmosphere, since the atmospheric column emission does not resemble a black body. The reflected component from the ground is given by $(1-\epsilon_g)\sigma T_{sky}^4$ and the emission from the aerosol particle, initially at a temperature T_0, is $2\sigma T_0^4$. The net heating/cooling rate for the aerosol particle equals the radiation from sky+ground - emission of the particle. Hence, the initial cooling of an isolated aerosol particle is given by

$$m^{aero} C_p^{aero} \left(\frac{\partial T}{\partial t}\right)_{t=0} = Q_{ext} A \left[\sigma(2-\epsilon_g)(T_0^4 - T_{sky}^4)\right], \tag{4.7}$$

where $m_p^{aero} C_p^{aero}$ is the heat capacity of the aerosol particle, Q_{ext} is the extinction efficiency (derivable from Mie theory; see Stephens (1961); Zdunkowski *et al.* (1966); in case of a spherical particle this can be interpreted as the emissivity of the particle [Bohren & Clothiaux (2006)]), and an expression for T_{sky}, the effective outer-space temperature, is given below (see (4.19)). The above expression gives the net cooling of a single particle. Since we are considering the dilute limit, the net cooling rate of aerosol-laden-atmosphere is obtained by multiplying with the number density, and is given by

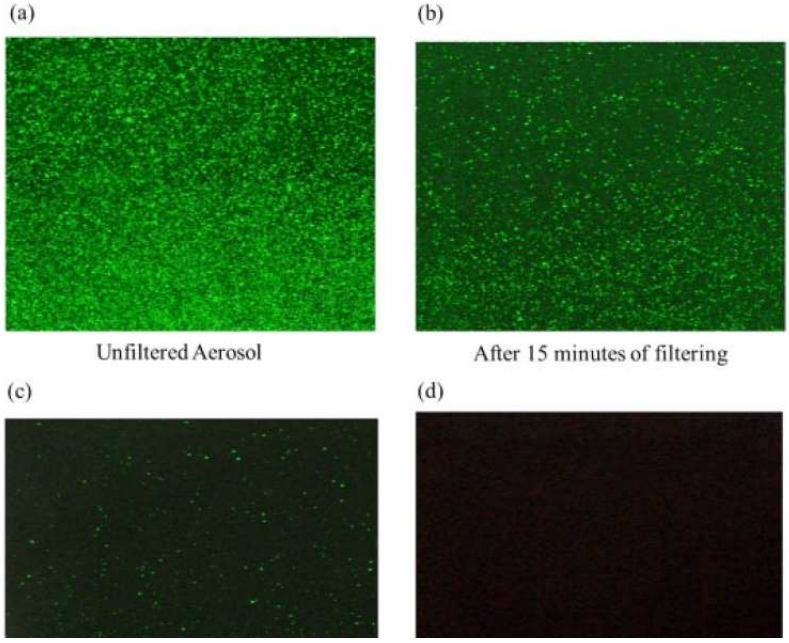

(a) Aerosol number density as a function of duration of filtering

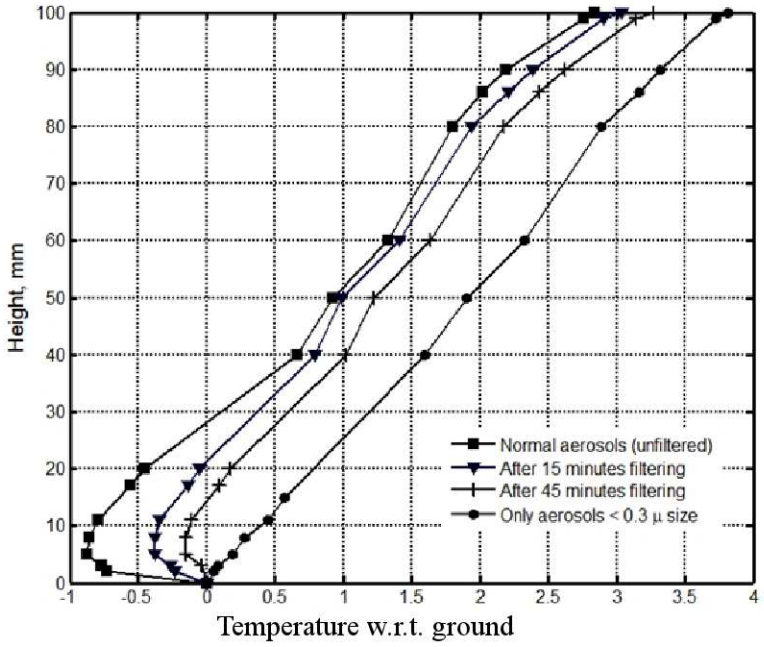

(b) Aerosol number density as a function of duration of filtering

Figure 4.11: Temperature profiles with a low emissivity surface ($\epsilon_g \approx 0.05$) for unfiltered air (normal aerosols) and for a duration of 60 min of filtering using a High Efficiency Particulate Air (HEPA) filter Mukund *et al.* (2013). With filtering, intensity of the lifted temperature minimum progressively decreases, and eventually the elevated minimum completely disappears, with the profile transitioning to a linear conduction profile.

$$\left(\frac{\partial T}{\partial t}\right)_{t=0} = \frac{\sigma(T_0^4 - T_{sky}^4)(2-\epsilon_g)AQ_{ext}n(u)}{[n(u)V^{aero}\varrho^{aero}C_p^{aero} + \varrho^{air}C_p^{air}]}. \tag{4.8}$$

$n(u)$ is the aerosol concentration, nA and nV^{aero} are the specific interfacial area and volume fraction, respectively, $\rho C_p = n(u)V^{aero}\varrho^{aero}C_p^{aero} + \varrho^{air}C_p^{air}$ is the heat capacity of the aerosol-air mixture, The small diffusion time scale of $O(n^{-\frac{2}{3}}/\kappa)$, κ being the thermal diffusivity of air, implies that air is conductively coupled to the aerosols necessitating a weighted heat capacity in (4.8). The cooling time scale then increases from that for an isolated particle, $\tau_{rad}^p \approx \frac{a\varrho^{aero}C_p^{aero}}{12\sigma T_g^3}$, where a is the particle diameter to $\tau_{rad} = \frac{[n(u)V^{aero}\varrho^{aero}C_p^{aero} + \varrho^{air}C_p^{air}]}{8\sigma T_g^3 An(u)Q_{ext}}$. For a monotonically decreasing $n(u)$, (4.8) decreases with height since higher aerosol concentrations drive a faster cooling in the lower air layers; any additional water-vapor-induced cooling is negligible in comparison. Equating (4.8) to $O(1\,K\mathrm{s}^{-1})$, a typical measured value by Mukund *et al.* (2013), yields $n(0) \approx 10^{12} - 10^{13}\,m^{-3}$. This is about two to three orders of magnitude higher than typical atmospheric boundary layer concentrations [Welch & Zdunkowski (1976); Devara & Raj (1993); Hess *et al.* (1998); Corrigan *et al.* (2008)], and mirrors a similar discrepancy in cooling rates [for instance, the highest near-surface cooling rates reported in the literature are those by Funk (1960), and are $O(300\,K\mathrm{day}^{-1})$; see table 2.1 in chapter 2]. However, typical temperature and 'flux-difference' measurements only extend down to about a meter and aerosol concentration measurements range from heights of $O(20-50\,m)$ (the measured number density at $20\,m$ is of $O(10^{10}\,m^{-3})$; see [Raj *et al.* (2001)] to length scales of $O(1\,km)$ [Hess *et al.* (1998) quote an average number density of $O(10^{11}m^{-3})$ for an urban polluted environment). This is in sharp contrast to the centimeter-scale resolution relevant to the LTM.

After estimating the particle number density required to produce the observed cooling-rates close to the ground, we will now examine the effect of heterogeneity on the vertical distribution of the radiative flux divergence. We will formulate the problem in an approximate manner within the framework of a flux-emissivity formulation for an inhomogeneous atmosphere. The flux-emissivity formulation in its full form will be considered in chapter 5, and here, we only consider the balance within the window band since a near-surface atmospheric inhomogeneity cannot interact with outer space via opaque bands. Denoting the absorption coefficient of a single element of heterogeneity (a single aerosol particle) as Q_{ext}, the transmissivity of an atmospheric column of height u may be written as $\tau(u) = \mathrm{e}^{-\int_0^u \alpha(u')du'}$ with $\alpha(u) = \alpha_w + A\,n(u)Q_{ext}$. Here, α_w is the combined absorption coefficient, accounting for the contributions, in the window band of all atmospheric gases relevant to the lowest meters of the atmosphere. This will be a constant on length scales pertaining to the LTM since the relevant density-scale heights are of the order of kilometers. The second term, $An(u)Q_{ext}$, is the appropriately weighted contribution of the heterogeneity to the transmissivity, where $n(u)$ is the local number density of the heterogeneity, and $An(u)$ is a measure of the specific interfacial area (relevant to emission). The various contributions to the total radiant flux may again be written in a manner similar to section 2.3.1 (see chapter 2 for the detailed expressions). Since it has already been pointed out that there is no qualitative difference between black and non-black surfaces, we consider only

$\epsilon_g = 1$, in which case, $F^{\uparrow}_{rg} = 0$, and the contributions from $F^{\uparrow}_{eg}$ and $F^{\uparrow}_{a}$ cancel. Thus, for an isothermal atmosphere bounded below by black ground, the only remaining contribution is due to the down-welling flux $F^{\downarrow}_{a}(u)$. The down-welling flux is given by

$$F^{\downarrow}_{a}(u) \;=\; f_w \sigma T_0^4 \left(1 - \mathrm{e}^{-[\alpha_w(u_t-u)+AQ_{ext}\int_u^{u_t} n(u')du']}\right), \tag{4.9}$$

The radiative flux divergence representative of the aerosol-driven cooling is:

$$\begin{aligned} \frac{dF}{du} &= \frac{dF_w}{du} = \frac{dF^{\downarrow}}{du} \\ &= f_w(\sigma T_0^4)\mathrm{e}^{-[\alpha_w(u_t-u)+AQ_{ext}\int_u^{u_t} n(u')du']}[\alpha_w + An(u)Q_{ext}], \end{aligned} \tag{4.10}$$

and the corresponding cooling rate is given by:

$$\frac{\partial T}{\partial t}(u) = -\frac{f_w(\sigma T_0^4)\mathrm{e}^{-[\alpha_w(u_t-u)+AQ_{ext}\int_u^{u_t} n(u')du']}[\alpha_w + An(u)Q_{ext}]}{[n(u)V^{aero}\varrho^{aero}C_p^{aero} + \varrho^{air}C_p^{air}]}. \tag{4.11}$$

The requirement of the heterogeneity being an efficient emitter translates to $An(u)Q_{ext} \gg \alpha_w$, so the expression for the cooling rate simplifies to:

$$\frac{\partial T}{\partial t}(u) = \frac{f_w(\sigma T_0^4)}{[n(u)V^{aero}\varrho^{aero}C_p^{aero} + \varrho^{air}C_p^{air}]}\,\mathrm{e}^{-AQ_{ext}\int_u^{u_t} n(u')du'} AQ_{ext}n(u). \tag{4.12}$$

The expression (4.12) is the same as that obtained earlier from physical arguments based on a microscopic picture of an aerosol particle interacting with the ground and a distant cold sink at T_{sky} (see equation (4.8)). This may be seen by noting that σT_{sky}^4 is the cumulative emission from the entire atmosphere which has contributions from both opaque and window bands (see the definition of T_{sky} in expression (4.19)), whence one obtains:

$$\begin{aligned} \sigma T_{sky}^4 &= f_{nw}\sigma T_0^4 + f_w \sigma T_0^4 \left[1 - \mathrm{e}^{-[\alpha_w(u_t)+AQ_{ext}\int_0^{u_t} n(u')du']}\right] \\ f_w \sigma T_0^4 \left[\mathrm{e}^{-[\alpha_w(u_t)+AQ_{ext}\int_0^{u_t} n(u')du']}\right] &= \sigma\left[T_0^4 - T_{sky}^4\right] \end{aligned} \tag{4.13}$$

Since $An(u)Q_{ext} \gg \alpha_w$, the cooling rate is much larger in magnitude than that for the homogeneous atmosphere. On the other hand, $AQ_{ext}\int_0^{u_t} n(u')du'$ is small enough that the entire heterogeneous atmosphere continues to be transparent in the window band. The rapidly decaying concentration field, however, reverses the profile for the radiative flux divergence. The cooling rate over the lowest meters now peaks at the ground and decreases with increasing height, as is required for the formation of an LTM. This is seen from the vertical derivative of the cooling rate:

$$\frac{\partial}{\partial u}\left(\frac{\partial T}{\partial t}\right) = \frac{f_w(\sigma T_0^4)\mathrm{e}^{-AQ_{ext}\int_u^{u_t} n(u')du'}}{[n(u)V^{aero}\varrho^{aero}C_p^{aero} + \varrho^{air}C_p^{air}]}\left(\{A^2 n(u)\}^2 Q_{ext}^2 + AQ_{ext}\frac{dn}{du}\right), \tag{4.14}$$

where the second term in brackets arises only for a heterogeneous atmosphere. The radiative cooling rate will decrease starting from the ground only if $(\frac{1}{n_0}\frac{dn_0}{du})^{-1} \ll (An_0Q_{ext})^{-1}$; here, the subscript '0' denotes quantities evaluated at $u = 0$. The physical interpretation is that, for

preferential cooling of the near-surface air layers to occur, the length scale characterizing the inhomogeneity must be smaller than the path-length in an atmosphere with a uniform number density n_0 of the relevant heterogeneity. Thus, the above analysis shows that a sufficiently steep variation of aerosol content will lead to a decrease rather than an increase in the radiative cooling rate with height consistent with the intuitive notion of the lowest layers of air being able to 'see' outer space better.

The cooling predicted in (4.8) and the equivalent form predicted by the flux-emissivity formulation (see equation (4.12)), at all heights, is only true for the initial isothermal state. The non-isothermality at shorter times will trigger warming exchanges in the opaque bands as characterized by $\frac{dF_{nw}}{du}$, and a diffusive flux from (warmer) ground. These contributions will eventually be in balance, and in what follows, we first analyze the equilibrium temperature profile when opaque-band exchanges are dominant, that is to say, the effect of aerosol is dominant only in the window bands, being overwhelmed by water vapor in the opaque bands. This analysis has been carried out for a fixed ground temperature T_g. In the next chapter, we discuss the air-soil coupled problem where the surface temperature is determined as a function of time by considering the conductive heat exchange with air and soil.

4.6.2 Equilibrium temperature profiles and LTM evolution

In the previous section, we examined the role of heterogeneity in determining the nature of the cooling-rate profile associated with an isothermal atmosphere. At the initial instant, the cooling is entirely in the window band, and the contributions due to opaque-band exchanges is identically zero. Once the lowermost air layers are at a lower temperature, there arise additional warming contributions due to conductive flux from the warmer ground and due to opaque-band exchanges with the overlying warmer air layers. In this section, we will analyze the steady state temperature profile obtained from a balance between conduction, radiative window-band cooling and opaque-band exchanges between adjacent air layers. A general analysis of this problem, is of course, not possible, and here, we restrict ourselves to the case where the aerosol-driven cooling is weak. This limit translates to small values of a dimensionless parameter ζ_0 that is defined below, and that measures the relative magnitudes of the aerosol-driven cooling and the water-vapor-driven warming in the opaque bands. The analysis is shown in detail for $\epsilon_g = 1$ although, in light of the observations over modified surfaces (see Mukund (2008)), we also quote the final result for an arbitrary ϵ_g.

To determine the flux-divergences for the opaque bands (nw) and the atmospheric window (w), the following emissivities are used:

$$\epsilon^f_{nw}(u) = 1 - \left[1 - \frac{\epsilon^f(u)}{\epsilon^f(u_t)}\right] e^{-\int_0^u An(u')\frac{Q_{ext}}{\rho_w(0)}du'}, \tag{4.15}$$

$$\epsilon^f_{w}(u) = 1 - e^{-\left[\alpha_w u + \int_0^u An(u')\frac{Q_{ext}}{\rho_w(0)}du'\right]}, \tag{4.16}$$

where α_w characterizes the weak water vapor absorption in the atmospheric window. Note that $\epsilon^f_{nw} \to 1$ once $\epsilon^f(u) \to \epsilon^f(u_t)$, and the latter happens on the length scale of the opaque bands. Thus (4.15) is an approximate representation of the flux-emissivity in the opaque-bands

of the water vapor spectrum. For small aerosol optical depths ($\alpha_w u_t \gg \int_0^{u_t} An(u')\frac{Q_{ext}}{\rho_w(0)}du'$), the flux-divergences in the two regimes of the spectrum are:

$$\frac{dF_{nw}}{du} = -(1-f_w)\left[\dot{\epsilon}^f_{nw}(u)\sigma[T_g^4 - T^4(0)] - \int_0^{u_t}\frac{d}{du}\left[\epsilon_{nw}(|u-u'|)\right]\frac{d}{du'}(\sigma T^4)du'\right], \quad (4.17)$$

$$\frac{dF_w}{du} = Q_{ext}An(u)(\sigma f_w)\left[2T^4 - T_g^4 - \hat{T}_{sky}^4\right], \quad (4.18)$$

where $f_w = (1-\epsilon^f(u_t))$ is the window energy fraction. For the flux-emissivity used in the calculations here, $f_w \approx 0.5$ (see figure 2.2b). In (4.17), the slip-induced heating contribution from the ground is distinguished from the contribution corresponding to radiative exchanges between air layers. The temperatures T_{sky} (used earlier in (4.8)) and $\hat{T}_{sky}$ in (4.18) (the effective sky temperature seen in the atmospheric window) are given by

$$T_{sky} = \left[\int_0^{u_t} T^4(u')[f_w(AQ_{ext}n(u'))e^{-\alpha_w u'} + (1-f_w)\dot{\epsilon}_{nw}(u')]du'\right]^{\frac{1}{4}}, \quad (4.19)$$

$$\hat{T}_{sky} = \left[\int_0^{u_t} T^4(u')(AQ_{ext}n(u'))e^{-\alpha_w u'}\,du'\right]^{\frac{1}{4}}, \quad (4.20)$$

for dominant aerosol window emission ($AQ_{ext}n(u) \gg \alpha_w$ for $u \to 0$). The flux expressions above, and the expressions for the sky temperatures, can be obtained from the governing integral equation and the derivation is given in appendix A. The cooling driven by $\frac{dF_w}{du}$ alone would yield an isothermal equilibrium, $T_{eq} = [\frac{T_g^4 + \hat{T}_{sky}^4}{2}]^{\frac{1}{4}}$. This is consistent with the microscopic picture where, for small optical depths, every particle eventually attains the same temperature due to interaction with ground and outer space. A non-isothermal equilibrium arises on including opaque-band warming and conduction, in which case the energy equation may be written as:

$$\frac{d^2R}{dz^2} = \chi\rho_w(0)\left(\frac{dF_w}{du} + \frac{dF_{nw}}{du}\right) = \chi\rho_w(0)\frac{dF}{du}, \quad (4.21)$$

where $\chi = \dfrac{\sigma T_g^3}{[\rho_w(0)\dot{\epsilon}^f_{nw}(0)k]}$ is the ratio of the radiative and thermal conductivities, and

$$\frac{dF}{du} = (1-f_w)\left[\zeta(u)(2R^4 - R_1^4 - 1) - \dot{\epsilon}^f_{nw}(u)(1-R^4(0)) + \int_0^{u_t}\frac{d}{du}\left[\epsilon^f_{nw}(|u-u'|)\right]\frac{dR^4}{du'}du'\right]. \quad (4.22)$$

Here, $R = \frac{T}{T_g}$, $R_1 = \frac{\hat{T}_{sky}}{T_g}$, and $\zeta(u) = \zeta_0 N(u)$, $N(u)$ being the dimensionless aerosol concentration profile. The parameter $\zeta_0 = \frac{f_w Q_{ext}An(0)}{[(1-f_w)\rho_w(0)\dot{\epsilon}^f_{nw}(0)]}$ is the ratio of the (radiative) cooling and heating contributions near the ground, and u is now the path length in units of $[\dot{\epsilon}^f_{nw}(0)]^{-1}$. For number densities of $O(10^{12} - 10^{13}m^{-3})$, required to reproduce the cooling rates associated with typical LTM-type profiles, one obtains $\zeta_0 \approx 10 - 100$. However, for purposes of a proof-of-principle calculation, we assume $\zeta_0 \ll 1$. In this limit, using $T = T_g + T'$ ($T' \ll T_g$), and noting that any slip will be smoothed within a boundary layer of thickness $O(\kappa\tau_{rad})^{\frac{1}{2}}$ (for $\tau_{rad} \approx 10s$,

this is about a centimeter), (4.21) takes the form

$$\frac{d^2R}{dz^2} = \chi\left[4\int_0^\infty \frac{d}{du}[\epsilon^f_{nw}(|u-u'|)]\frac{dR}{du'}du' + \zeta_0 N(u)(1-R_1^4)\right]. \tag{4.23}$$

With R_1 fixed and for a given inhomogeneity profile ($N(u)$), the nature of the radiative-conductive equilibrium is governed by the parameters ζ_0 and χ.

Note again that the limit for $\zeta_0 < 1$ corresponds to the case where aerosol emission is dominant in the window while being swamped by water vapor in the opaque bands. Further, assuming the opaque band to be gray ($\epsilon^f_{nw}(u) = 1 - \mathrm{e}^{-\alpha_{nw}u}$) [5] for simplicity, with $\alpha_{nw} = \dot{\epsilon}^f_{nw}(0)$, (4.23) may be differentiated twice to give:

$$\frac{d^4R}{dz^4} = (8\chi+1)\frac{d^2R}{dz^2} + \zeta_0\chi(1-R_1^4)(\frac{d^2N}{dz^2} - N), \tag{4.24}$$

where all terms are now written in terms of z using $u = \rho_w(0)z$ (valid on scales much smaller than the scale height of water vapor). Imposing $R = 1$ both at $z = 0$ and for $z \to \infty$ (due to a vanishingly small aerosol concentration), the equilibrium profile is given by

$$R(z) = \quad 1 + Vh^2\tfrac{(1-H^2)}{(1-p^2H^2)}(e^{-z/H} - e^{-pz}), \tag{4.25}$$

where $V = \chi(1-R_1^4)\zeta_0$, and $p = \sqrt{8\chi+1}$ is the inverse of the conductive boundary layer thickness. Figure 4.12a shows the small-ζ_0 equilibrium temperature profiles, and the corresponding cooling rate profiles, for varying χ (using the thermal conductivity of air, and (2.51) to estimate the opaque-band pathlength (α_{nw}^{-1}), one finds $\chi \approx 100$). The radiative equilibrium, emerging in the limit $\chi \to \infty$ (shown as a dashed line), is:

$$R(z) = \quad 1 + \tfrac{R_1^4-1}{8}\zeta_0 e^{-z/H}, \tag{4.26}$$

with a (negative) slip ($(T-T_g)|_{z=0} = -\zeta_0 T_g \frac{1-R_1^4}{8}$ at the ground;. The flux-divergence profiles, shown in figure 4.12b, decay over the aerosol scale height H - the assumed dimensionless concentration profile is $N(z) = \mathrm{e}^{-z/H}$. Finally, the equilibrium profile for an arbitrary ϵ_g is given by

$$R(z) = \quad 1 + Vh^2(2-\epsilon_g)\tfrac{(1-h^2)}{(1-p^2h^2)}(e^{-z/h} - e^{-pz}), \tag{4.27}$$

where the slip at the ground (for $\chi \to \infty$) may be seen to increase with decreasing ϵ_g. This is consistent with the observations in Mukund (2008) which show a higher LTM intensity over low-emissivity surfaces.

4.7 Conclusion

In this chapter, we have shown that the prevailing explanation for the origin of the Ramdas layer, based on the VSN model, is fundamentally inconsistent. Further, it has been conclusively

[5] This may be a reasonable approximation when the aerosol scale height is smaller than the smallest photon mean-free-path obtained in the flux-emissivity functional.

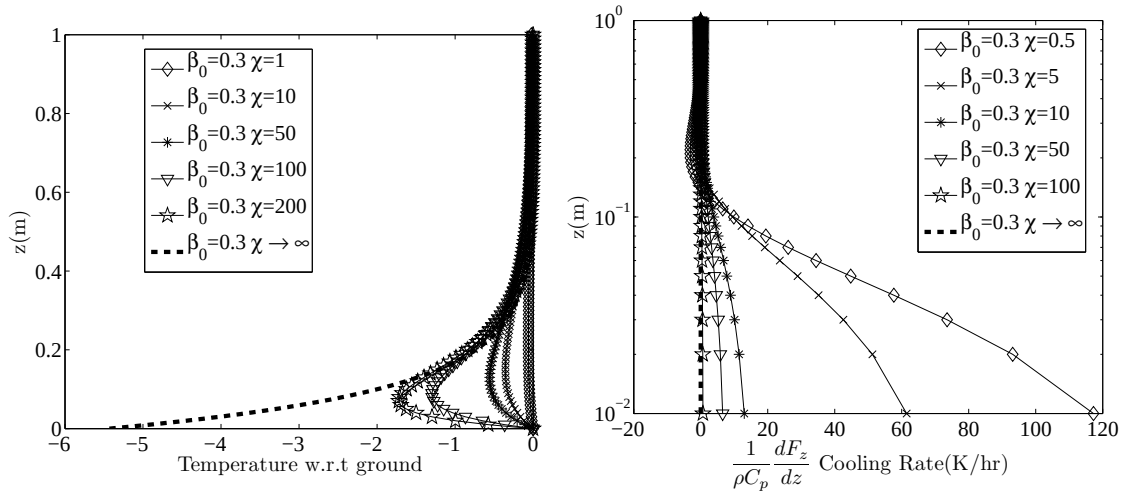

(a) Temperature Profile

(b) Radiative Cooling Rate

Figure 4.12: Radiative-conductive equilibria, in a heterogeneous atmosphere, as a function of χ, for the limit where opaque-band warming is dominant ($\zeta_0 \ll 1$); we have assumed $R_1 = 0.8482$, corresponding to an effective sky temperature of $\hat{T}_{sky} = 254.5K$. The limit, $\chi \to \infty$, denotes an approach to radiative equilibrium, and the limiting profile is shown as a dashed line with a slip of $-5.4K$ at the ground.

proved that preferential cooling cannot occur in a homogeneous atmosphere. The presence of an inhomogeneity, on the scale of the Ramdas layer, is necessary to explain the origin of this phenomenon. This inhomogeneity is likely due to the steep variation in the concentration of aerosol particles near the ground and there appears to be direct visual evidence for this in recent observations by Singh (2013). The indirect evidence of the effect of aerosol forcing in laboratory experiments, both in the two-plate and three-plate (LTM) configurations has already been obtained Mukund *et al.* (2013). Having confirmed the role of aerosols in leading to the laboratory LTM, the role of the aerosol radiative forcing is studied in the atmospheric context in a simplified approximation characterized by small values of a dimensionless parameter which demarcates the importance of aerosol in window and non window band. In this asymptotic regime, it is shown that, in the absence of conduction, the aerosol radiative forcing does lead to a negative radiative slip near the ground with the lowest air layers near the ground being colder than the ground. Conduction acts to smoothen this slip, leading to an elevated minimum at a finite height.

Chapter 5

Numerical studies - Field observation

5.1 Abstract

In this chapter, we present the results of dynamical simulations which demonstrate the origin of the Ramdas layer in an inhomogeneous aerosol-laden atmosphere. In the previous chapter, we discussed the results for an aerosol-laden atmosphere, in a simplified limit, where the atmosphere was assumed isothermal and the bounding surface (ground) was assumed to be at a fixed constant temperature. However, after sunset, efficient emission in the infrared also results in surface cooling, and the inhomogeneous atmosphere is subject to this time-dependent surface temperature boundary condition. Here, we first present a simplified analysis, based on a Newtonian cooling approximation, for the air-soil coupled problem where the ground is allowed to cool by emitting radiation to outer space through the atmospheric window. The analysis introduces a new non-dimensional parameter which we call the Ramdas - Zdunkowski factor (R_f) [1], and that is the ratio of the air cooling rate to the surface cooling rate. This non-dimensional parameter helps in discriminating between the inversion layer and the LTM regimes, with the latter favored for large values of R_f. It is shown that the nature of the temperature profile in the lowest meters of the NBL, under calm clear conditions, can be characterized by two parameters - the surface emissivity and the Ramdas-Zdunkowski factor, although the latter parameter is the more important of the two. Then, we present the results of full dynamic simulations, with both water vapor and aerosols included, to elucidate the origin of the preferential cooling near the ground. The results of these simulations are consistent with the LTM regime emerging above a critical value of R_f.

5.2 Introduction

After sunset, ground being a good emitter in the infrared regime, the temperature of the ground starts to fall. This led to the original presumption that ground cools *faster* than the overlying air layers, and leads the cooling, resulting in an inversion profile [Sutton (1953);Stull (1988)]. But, measurements very close to the ground conclusively prove that it is the near-surface air layers that cool faster than the ground, and thereby, lead the post-sunset cooling process (Mukund *et al.* (2013); see chapter 4). This led to the micrometeorological paradox called the Ramdas layer or LTM which was introduced in the previous chapter. It has been argued therein that the radiative forcing due to suspended aerosol particles is necessary to explain this phenomenon, and this hypothesis has been conclusively proven using laboratory experiments [Mukund *et al.* (2010);Mukund *et al.* (2013)]. In the analysis presented in the previous chapter, the ground

[1] The name seems appropriate since, the lifted temperature minimum was originally discovered by Ramdas and co-workers in the year 1932 [Ramdas & Atmanathan (1932)] and on the other hand, the role of heterogeneity, in establishing LTM-type profiles, was first incorporated in the theoretical analysis by Zdunkowski (1966a)

temperature is assumed to be constant. However, the rate at which the ground cools depends on its heat capacity and thermal conductivity. For high-thermal-inertia surfaces, the resulting response time is longer than that characterizing the air layers (inverse of the air cooling rate), and one can assume a constant ground temperature. In recent field observations by Mukund *et al.* (2010), the thermal inertia of the surface has been varied by modifying the surface with an overlying layer with different thermophysical and radiative properties. A prominent feature of these observations is that, over low-thermal-inertia surfaces, for instance, ground covered with a layer of thermofoam, there is no LTM. This motivates us to study the effect of ground cooling on LTM evolution. Based on the relative magnitudes of the ground and air cooling rates one can expect to discriminate between the occurrence of an inversion or an LTM in the lowermost meters of the NBL. It is also of interest to obtain a simpler expression for the ground temperature itself, in the presence of an inhomogeneous participating medium, which can serve as a forecast for the minimum ground temperature under calm clear conditions. The surface (ground) plays an important role in NBL development. The effect of ground can be represented in various ways. The simplest thing is to directly specify the ground temperature which does not take explicit account of the surface energy budget [Brunt (1932);Edwards (2009a)]. In some cases, even the surface sensible heat flux is specified, but this works well only for diurnal conditions; during night time this strongly depends on the near-ground turbulence levels, [Mahrt & Vickers (2006)], an aspect that is poorly understood in the context of the nocturnal boundary layer.

5.3 Surface energy balance

In the absence of vegetation, the interface between the surface and atmosphere is relatively well defined. At the interface, the conservation of energy should hold at all times and this requires that

$$F_s - k_a \frac{\partial T_a}{\partial z}\bigg|_{z=0} = G_{z=0} + \lambda E_0. \tag{5.1}$$

where F_s is the net radiative flux from the surface, The second term on the left hand side is the heat flux from the air to surface, k_a being the conductivity of air. On the other side, G is the conductive flux from the soil to the surface, and the second term is the heat flux associated with the flux of water vapor from the surface, due to evaporation or sublimation with λ being the latent heat of vaporization or sublimation. For the dry nocturnal conditions under consideration, we assume that the flux of water vapor is small.

The temperature within the soil is governed by conduction, and assuming Fourier's law for the conductive flux, one obtains, for the soil temperature T_s, the following equation:

$$\frac{\partial T_s}{\partial t} = \frac{k_s}{\rho_s C_{ps}} \frac{\partial^2 T_s}{\partial z^2}. \tag{5.2}$$

In the earlier literature, a 'force-restore method' is used to obtain the conductive flux from soil to the surface. In this method, the heat flux to the surface can be represented in terms of the deep soil temperature (T_D) and the rate of energy storage in the soil $\left(\frac{\partial W_s}{\partial t}\right)$, where $W_s = \rho_s C_{ps} \Delta z' T_s$. For a sinusoidal forcing at the surface, one can obtain the relation between

G and T_D as follows:

$$G_{z=0} = \frac{k_s}{Z_g}\left[\frac{1}{\Omega_d}\frac{\partial T_s}{\partial t} + T_s - T_D\right], \tag{5.3}$$

where Ω_d is the diurnal frequency and Z_g is the penetration depth given by $\sqrt{\left(\frac{2\kappa_s}{\Omega_d}\right)}$, κ_s being the thermal diffusivity of the soil ($\kappa_s = \frac{k_s}{\rho_s C_{ps}}$).

The other more rigorous method is to solve the conductive equation in the soil with the energy budget at the surface providing a boundary condition for all time. An example of this method is the analysis by Brunt (1932) who, for purposes of simplicity, assumed the net radiative flux at the surface to be constant throughout the night, and in addition, neglected the conductive heat flux from air to the surface. One can then obtain the solution for the ground temperature variation with respect to time as

$$T = T_0 - \beta\sqrt{t}. \tag{5.4}$$

where

$$\beta = \frac{2}{\pi}\frac{F_s}{\rho_s C_{ps}\sqrt{\kappa_s}}. \tag{5.5}$$

The parameter β, a 'surrogate' cooling rate, depends on the soil properties and the net flux at the surface. Although it provides a good approximation for some natural surfaces, this method is not very useful for surfaces with low thermal conductivity, for instance insulators, like ice.

In this chapter, we will solve the entire air-soil coupled problem for an inhomogeneous radiatively participating medium. We will assume the inhomogeneity as being due to a concentrated aerosol layer near the ground that is, nevertheless, in the optically thin limit. To begin with, in section 5.4.1, the analysis is carried out in the pure radiation limit where conduction between air layers is neglected. The radiative forcing of the suspended aerosol particles is modelled using a Newtonian cooling approximation appropriate for the optically-thin limit. It is shown, in this limit, that the slip at the ground is well described by two parameters - the surface emissivity (ϵ_g) and the Ramdas-Zdunkowski factor (R_f). Note that, in the pure radiation limit, it is the sign of this temperature slip (defined as the temperature difference between the soil and the lowermost air layer) that differentiates between the LTM (positive slip) and inversion (negative slip) regimes. Then, in section 5.4.2, we include the effects of conduction between adjacent air layers that smears out the radiative slip. Finally, we carry out full dynamical simulations to study the role of water vapor alone in section 5.5.1, and together with aerosol particles in section 5.5.2. The focus is on developing an understanding of the parameters that control the LTM regime.

5.4 The Ramdas-Zdunkowski factor

To begin with, we obtain, via scaling arguments, an expression for the Ramdas-Zdunkowski factor (R_f), defined as the ratio of the cooling rates of the near-surface air layers to that of the ground. Assuming the primary mechanism of cooling under calm conditions to be of a radiative character, the air cooling rate can be written as $\frac{\Delta T}{\tau_{rad}}$, where ΔT is a measure of the driving force, that is, the temperature difference between the initial isothermal state and the radiative

equilibrium temperature, over length-scales relevant to the LTM. Here, $\Delta T = T - T_{rad}$, T_{rad} being the hypothetical radiative equilibrium state and τ_{rad} being the radiative time scale for the near-surface air layers. Accounting for the thermal penetration depth of $O(\sqrt{\kappa_s \tau_{rad}})$ within the surface, the surface cooling rate is given $\frac{F_s}{\rho_s C_{ps} \sqrt{\kappa_s \tau_{rad}}}$, where F_s, as before, is the net upward radiative flux from the surface; The ratio between these cooling rates leads to the required expression for the Ramdas-Zdunkowski factor:

$$R_f = \frac{\Delta T}{F_s} \rho_s C_{ps} \sqrt{\frac{\kappa_s}{\tau_{rad}}}. \tag{5.6}$$

We now solve the equations governing the temperature profiles both in the near-surface air layers, and within the ground, and show that the Ramdas-Zdunkowski factor (R_f) is the relevant dimensionless parameter that governs the NBL temperature profile, and emerges naturally from the governing equations under conditions where conductive processes in air may be neglected. The dimensional energy equation for the air layers can be written as

$$\frac{\partial T(z,t)}{\partial t} = \frac{k_a}{\rho_a C_{pa}} \frac{\partial^2 T}{\partial z^2} - \frac{\partial F_z}{\partial z}, \tag{5.7}$$

where the radiative flux divergence can be written as

$$\frac{\partial F_z}{\partial z} = A Q_{ext} n(z) \sigma \left[2T^4(z,t) - T_s^4(0,t) - T_{sky}^4 \right]. \tag{5.8}$$

The above equations are non-dimensionalized using the characteristic time scale as the radiative relaxation time at the ground ($\tau_{rad}(0)$); in terms of aerosol characteristics, the dimensional time-scale characterizing the approach towards a radiative equilibrium is given by $\tau_{rad}(z) = \frac{\rho_a C_{pa}}{4A\alpha n(z) \sigma T_{g0}^3}$, where *n(z)* is the aerosol number density profile. The relevant length scale is H, the length scale characterizing the aerosol concentration profile, the characteristic temperature scale is the initial temperature T_{g0}, and σT_{g0}^4 is used as the scale for the radiative flux. The resulting non-dimensional energy equation for the air layers is given by:

$$\frac{\partial \theta_a(z,t)}{\partial t} = \mu_1 \frac{\partial^2 \theta_a}{\partial z^2} - \frac{\partial F_z}{\partial z} \qquad z > 0, \tag{5.9}$$

where

$$\frac{\partial F_z}{\partial z} = \frac{1}{\hat{\tau}_{rad}(z)} \left[2\theta(z,t) - \theta_s(0,t) - \Delta T_1 \right]. \tag{5.10}$$

In (5.9), F_z is the dimensionless radiative flux in air, and the non-dimensional function $\hat{\tau}_{rad} = \frac{\tau_{rad}(z)}{\tau_{rad}(0)}$ in (5.34), characterizes the vertical profile of radiative relaxation times. Further, $\theta(z,t) = \frac{[T(z,t) - T_{g0}]}{T_{g0}}$; $\Delta T_1 = \frac{[T_{sky} - T_{g0}]}{T_{g0}}$; $\mu_1 = \frac{\tau_{rad}(0)}{\frac{\rho_a C_{pa} H^2}{k_a}}$. Here *T(z,t)*, denotes the dimensional temperature profile in air, T_{g0} is the temperature of the initial isothermal atmosphere, and the parameter μ_1 is the ratio of the radiative timescale to the conductive timescale (based on the scale height H) in air. Finally, T_{sky} is the temperature of the radiative sink, which drives the cooling process from the initial isothermal state. As explained earlier, the radiative transfer

in the participating heterogeneous (aerosol-laden) medium has been modelled in (5.9) using a Newtonian cooling approximation Since the aerosol concentration decrease as a function of height, $\tau_{rad}(z)$ is an increasing function of z, and hence, the lowest air layers relax most rapidly.

Within the ground, the heat transfer is governed by the diffusion equation already discussed in section 5.3. Using the above characteristic scale, the corresponding non-dimensional equation is:

$$\frac{\partial \theta_s}{\partial t} = \mu \frac{\partial^2 \theta_s}{\partial z^2}, \tag{5.11}$$

where $\theta_s(z,t) = \dfrac{[T_s(z,t) - T_{g0}]}{T_{g0}}$. The parameter $\mu = \dfrac{\tau_{rad}(0)}{\frac{\rho_s C_{ps} H^2}{k_s}}$ is the ratio of the radiative time-scale to the conduction time-scale in the soil, and is the analog of μ for the soil. The initial and boundary conditions are as follows:

Dimensional form	**Non-dimensional form**
$T_s(z,0) = T_{g0}$	$\theta_s(z,0) = 0$ (5.12)
$T_s(-\infty,t) = T_{g0}$	$\theta_s(-\infty,t) = 0$ (5.13)
$T_a(0,t) = T_s(0,t)$	$\theta_a(0,t) = \theta_s(0,t)$ (5.14)
The surface energy budget is given by	
$F_s - k_a \left.\dfrac{\partial T_a}{\partial z}\right\|_{z=0} = k_s \left.\dfrac{\partial T_s}{\partial z}\right\|_{z=0}$	$4\big[\theta_s(0,t) - \Delta T_1\big] = -\eta_a \dfrac{\partial \theta_a(0,t}{\partial z} = -\eta_s \dfrac{\partial \theta_s(0,t)}{\partial z}$ (5.15)
	where $\eta_i = \dfrac{\frac{k_i T_{g0}}{H}}{\sigma T_{g0}^4}$, with $i = a$(air) or s(soil)
$T_a(z,0) = T_{g0}$	$\theta_a(z,0) = 0$ (5.16)

$T_a(\infty, t) = T_{g0}$	$\theta_a(\infty, t) = 0$	(5.17)

Table 5.1: The initial and boundary conditions in dimensional and non-dimensional form are listed.

5.4.1 Pure radiation

Given a specific functional form for the aerosol number density profile, the non-dimensional parameters on which the temperature profile depends are η_s, μ, η_a and μ_1. The situation simplifies considerably under conditions where conduction in air may be neglected, in which case $\eta_a = \mu_1 = 0$. This purely radiative limit allows for a slip between the lowest air layer and the ground, and the sign of this temperature slip may then be regarded as discriminating between the LTM and inversion regimes. Although both η_s and μ continue to be relevant dimensionless parameters, the solution of the limiting equations below shows that only the ratio $\frac{\eta_s}{\sqrt{\mu}}$ governs the temperature slip at the ground over a black surface. This ratio is, in fact, proportional to R_f. To write R_f in terms of $\frac{\eta_s}{\sqrt{\mu}}$, the net radiative flux can first be written as $F_s = \epsilon_g \sigma \left[T_{g0}^4 - T_{sky}^4\right]$. One can linearize about the initial temperature T_{g0}, in which case F_s can be written as:

$$F_s = \frac{8\epsilon_g \sigma T_{g0}^3}{2 - \epsilon_g} \Delta T. \tag{5.18}$$

Substituting for $\frac{F_s}{\Delta T}$ from (5.18), and the expression for τ_{rad} given earlier in (5.6), one obtains R_f to be:

$$R_f = \frac{2 - \epsilon_g}{8\epsilon_g \sigma T_{g0}^3} \sqrt{\frac{k_s \rho_s C_{ps}}{\tau_{rad}}},$$

$$R_f = \frac{2 - \epsilon_g}{\epsilon_g} \frac{\eta_s}{8\sqrt{\mu}}. \tag{5.19}$$

For $\epsilon_g = 1$,

$$R_f = \frac{\eta_s}{8\sqrt{\mu}}. \tag{5.20}$$

In the analysis, that follows, we will first consider the bounding surface (ground) to be black. Later, the analysis is generalized to incorporate an arbitrary surface emissivity. The system of governing equations, (5.9) and (5.11) with the initial and boundary conditions given by (5.12 - 5.17) may be solved using the Laplace transform technique. Defining,

$$W(z, s) = \int_0^\infty \theta_s(z, t) \mathrm{e}^{-st} dt, \tag{5.21}$$

one obtains from (5.11) with the initial and boundary conditions (5.17 - 5.13):

$$W(z,s) = \frac{\Delta T_1}{2R_f} \frac{\mathrm{e}^{\frac{z\sqrt{s}}{\sqrt{\mu}}}}{s\left[\sqrt{s} + \frac{1}{2R_f}\right]}. \tag{5.22}$$

When we neglect the conductive processes in air, the equations governing the soil temperature de-couple from those involving the air, since the surface energy budget is the source of such a coupling. As a result, θ_s may be solved for first, and then, θ_a can be calculated. On inversion of (5.22), the normalized temperature profile within the soil is given by

$$\theta_s(z,t) = \Delta T_1 \left[\mathrm{erfc}\left(\frac{z}{2\sqrt{\mu t}}\right) - \mathrm{e}^{\frac{z}{2R_f\sqrt{\mu}}} \mathrm{e}^{\frac{t}{4R_f^2}} \mathrm{erfc}\left(\frac{\sqrt{t}}{2R_f} + \frac{z}{2\sqrt{\mu t}}\right)\right] \text{ for } z < 0, \tag{5.23}$$

Here, $\mathrm{erfc}(x)$ is the complementary error function defined as $\mathrm{erfc}(x) = \frac{2}{\sqrt{\pi}} \int_x^\infty \mathrm{e}^{-\eta^2} d\eta$ [Abramowitz & Stegun (1990)]. The variation of the surface temperature with time is given by setting $z = 0$ in equation (5.23):

$$\theta_s(0,t) = \Delta T_1 \left[1 - \mathrm{e}^{\frac{t}{4R_f^2}} \mathrm{erfc}\left(\frac{\sqrt{t}}{2R_f}\right)\right], \tag{5.24}$$

For small t, the ground temperature is given by

$$\theta_s(0,t) = \Delta T_1 \frac{1}{R_f\sqrt{\pi}} \sqrt{t}, \tag{5.25}$$

which, in the dimensional form, is given by:

$$T_g(0,t) = T_{g0} - \frac{T_{g0} - T_{sky}}{R_f\sqrt{\pi\tau_{rad}}} \sqrt{t}. \tag{5.26}$$

This is similar to the expression obtained by Brunt (1932), where the ground cooling rate was characterized by β (defined earlier in equation (5.5)). On substituting the expression for R_f and τ_{rad}, it can be shown that equations (5.25) and (5.4) are the same, and β can be defined in terms of R_f as

$$\beta = \frac{T_{g0} - T_{sky}}{R_f\sqrt{\pi\tau_{rad}}}. \tag{5.27}$$

The greater complexity of the surface temperature given by (5.24), in relation to that given by Brunt (1932), is due to the variation with time of the net radiative flux (F_s). The net flux from the ground is $4\left[\theta_s(0,t) - \Delta T_1\right]$ (in non-dimensional form) which, for small t is given by $\Delta T_1 \left(1 - \frac{\sqrt{t}}{R_f\sqrt{\pi}}\right)$. This can be considered as a constant up to $t \approx R_f^2$. Hence Brunt (1932)'s analysis is valid over all the surfaces for times up to $t \approx R_f^2$, and serves as a good approximation for large R_f (high-thermal-inertia) surfaces.

For large times, the ground temperature is given by

$$\theta_s(0,t) = \Delta T_1 \left(1 - \frac{2R_f}{\sqrt{\pi t}}\right), \tag{5.28}$$

and when $t \to \infty$, then $\theta_s \to \Delta T_1$ and the ground approaches the cold-source temperature T_{sky}. The initial ground cooling rate, obtained by differentiating (5.24) and taking the limit of small t, is:

$$\frac{\partial \theta_s(0,t)}{\partial t} \approx \frac{\Delta T_1}{2R_f\sqrt{\pi t}}. \tag{5.29}$$

The cooling-rate diverges as $O(\frac{1}{\sqrt{t}})$ for small t, since an $O(1)$ radiative flux drives the cooling of a slab whose thickness, on account of conduction, scales as $O(\sqrt{\frac{k_s t}{\rho_s C_{ps}}})$.

Knowing the ground temperature from (5.24), one may now solve the energy equation for each air layer independently to obtain the following expression for the air temperature profile:

$$\begin{aligned}\theta_a(z,t) =& \Delta T_1\Big[1 - \mathrm{e}^{\frac{-2t}{\hat{\tau}_{rad}(z)}}\Big] - \frac{\Delta T_1}{\hat{\tau}_{rad}(z)\Big(\frac{2}{\hat{\tau}_{rad}(z)} + \frac{1}{4R_f^2}\Big)}\Bigg[- \mathrm{e}^{\frac{-2t}{\hat{\tau}_{rad}(z)}} + \mathrm{e}^{\frac{t}{4R_f^2}}\mathrm{erfc}\Big(\frac{\sqrt{t}}{2R_f}\Big) \\ &+ \mathrm{e}^{\frac{-2t}{\hat{\tau}_{rad}(z)}}\frac{1}{2R_f}\sqrt{\frac{\hat{\tau}_{rad}(z)}{2}}\mathrm{erfi}\Big(\sqrt{\frac{2t}{\hat{\tau}_{rad}(z)}}\Big)\Bigg].\end{aligned} \tag{5.30}$$

Here, erfi(z) is the imaginary error function defined as $\mathrm{erfi}(z) = -i\mathrm{erf}(iz)$ where $\mathrm{erf}(x) = \frac{2}{\sqrt{\pi}}\int_0^x \mathrm{e}^{-\eta^2} d\eta$ [Abramowitz & Stegun (1990)]. For small times the variation of air temperature is given by

$$\theta_a(0,t) \approx 2\Delta T_1 t, \tag{5.31}$$

while, for large times, the air temperature is given by

$$\theta_a(0,t) \approx \Delta T_1 - \frac{\Delta T_1}{2 + \frac{1}{4R_f^2}}\left[\frac{2R_f}{\sqrt{\pi t}} + \frac{1}{2R_f\sqrt{\pi t}}\right]. \tag{5.32}$$

At short times the ground temperature changes as $O(\sqrt{t})$ while air temperature changes like $O(t)$ (corresponding to a finite initial cooling rate dictated by the finite aerosol concentration) which is much smaller for small t. Hence, at short times ground invariably leads the cooling, and there will be always an inversion profile to begin with. For long times, both the ground and the air temperatures approach radiative equilibrium which corresponds to an isothermal state at T_{sky}.

The temperature slip at the ground is defined as, $(\theta_s(0,t) - \theta_a(0,t))$, the difference in temperature between the ground and the lowermost air layer. In the absence of conduction in air, from (5.24) and (5.30), the slip, is seen to be only a function of R_f , and is given by:

$$\theta_s(0,t) - \theta_a(0,t) = \Delta T_1 \mathrm{e}^{-2t}\frac{1+4R_f^2}{1+8R_f^2} - \Delta T_1 \mathrm{e}^{\frac{t}{4R_f^2}}\frac{1+4R_f^2}{1+8R_f^2}\mathrm{erfc}\Big(\frac{\sqrt{(}t)}{2R_f}\Big) + \frac{\Delta T_1 \mathrm{e}^{-2t}\mathrm{erfi}(\sqrt{(}2t)}{2\sqrt{(}2)R_f\big[\frac{1}{4R_f^2} + 2\big]}. \tag{5.33}$$

Equation (5.33) describes the transition of the coupled air-soil system from the initial (T_{g0}) to the final (T_{sky}) isothermal states and equals zero in both these limits. Equating (5.33) to zero determines the cross-over time, t_{cr}, when the lowest air layer first cools to a temperature lower than that of the surface. For large R_f, the transient corresponding to a surface leading

the air layers is very small, and the appropriate limiting form of (5.33) leads to $t_{cr} \approx \frac{1}{R_f^2} \ll 1$. In contrast, for small R_f, the surface leads the air for a prolonged period of time, there being an eventual cross-over with $t_{cr} \approx \log\left(\frac{1}{\sqrt{R_f}}\right) \gg 1$ predicted based on the large-t form of (5.30). The cross-over times predicted by the asymptotic scaling analysis are compared with the numerical solution of (5.33) in Figure 5.1, and both agree very well in the corresponding limits.

The transition from the initial isothermal state at T_{g0} to the final isothermal state T_{sky} is shown for a high R_f surface (concrete) and a low R_f surface (foam) in figures 5.2 and 5.3 respectively. In this calculation, we have used a simple exponential profile with a scale height of $1\,cm$ to model the functional dependence of the radiative relaxation times on the vertical coordinate. The aerosol concentration at the surface is chosen such that the fastest relaxation time, consistent with the estimate in chapter 4, is 10 s. As discussed above, to begin with, for all R_f values, the ground cools faster than the air layers and this leads to an inversion profile. However, as time progresses, the air layers overtake the ground, leading to an eventual transition to an LTM-type profile. This transition occurs faster over a high R_f surface (for instance over concrete with $R_f = 37$, the non- dimensional cross-over time is 1.5×10^{-4}) than over a low R_f surface (for foam with $R_f = 1.4$, the non-dimensional cross-over time is 0.3). For a sufficiently small value of R_f, the cross-over time can be larger than the fastest relaxation time scale in the problem. To show this, we chose a hypothetical surface with $R_f = 0.1$ and the corresponding transition from the initial state to an isothermal radiative equilibrium is shown in figure 5.4. The non-dimensional cross-over time in this case is 1.5 (in units of τ_{rad}).

The above analysis can be easily generalized to the case of an arbitrary surface emissivity (ϵ_g). The surface emissivity enters the formulation via the surface condition (in determining the net radiative flux from the ground), and also affects the net radiative flux-divergence of air layers because there is now an additional reflected component. The governing non-dimensional equation for the air layers, overlying a gray surface, is given by:

$$\frac{\partial F_z}{\partial z} = \frac{1}{\hat{\tau}_{rad}(z)} \left[2\theta(z,t) - \epsilon_g \theta_s(0,t) - (2-\epsilon_g)\Delta T_1\right]. \tag{5.34}$$

The governing system of equations now involves three parameters: R_f, μ and ϵ_g. The temperature profile inside the soil is given by:

$$\theta_s(z,t) = \Delta T_1 \left[\operatorname{erfc}\left(\frac{z}{2\sqrt{\mu t}}\right) - \mathrm{e}^{\frac{(2-\epsilon_g)z}{2R_f\sqrt{\mu}} \frac{(2-\epsilon_g)^2 t}{4R_f^2}} \operatorname{erfc}\left(\frac{(2-\epsilon_g)\sqrt{t}}{2R_f} + \frac{z}{2\sqrt{\mu t}}\right)\right] \text{ for } z < 0, \tag{5.35}$$

Note that R_f here is given by (5.19), and is therefore itself dependent on the surface emissivity.

The temperature profile in the air layers is given by:

$$\begin{aligned}\theta_a(z,t) =&\Delta T_1\left[1-\mathrm{e}^{\frac{-2t}{\hat{\tau}_{rad}(z)}}\right]-\frac{\epsilon_g\Delta T_1}{\hat{\tau}_{rad}(z)\left(\frac{2}{\hat{\tau}_{rad}(z)}+\frac{(2-\epsilon_g)^2}{4R_f^2}\right)}\Bigg[-\mathrm{e}^{\frac{-2t}{\hat{\tau}_{rad}(z)}}\\&+\mathrm{erfc}\Big(\frac{(2-\epsilon_g)\sqrt{t}}{2R_f}\Big)\mathrm{e}^{\frac{(2-\epsilon_g)^2t}{4R_f^2}}\\&+\mathrm{erfi}\Big(\sqrt{\frac{2t}{\hat{\tau}_{rad}(z)}}\Big)\frac{(2-\epsilon_g)}{2R_f}\sqrt{\frac{\hat{\tau}_{rad}(z)}{2}}\mathrm{e}^{\frac{-2t}{\hat{\tau}_{rad}(z)}}\Bigg],\end{aligned}\tag{5.36}$$

From (5.35), the ground temperature at short times is given by $\theta_s(0,t)\approx\frac{\epsilon_g\sqrt{t}}{\sqrt{\pi R_f}}$. Here, the deviation from the initial isothermal state is smaller by a factor of ϵ_g in relation to that for the black surface, and this is due to the reduced upwelling flux from the ground.

The relation defining the cross-over time is given by

$$\mathrm{e}^{-2t_{cr}}-\mathrm{e}^{\frac{(2-\epsilon_g)^2t_{cr}}{4R_f^2}}\mathrm{erfc}\Big(\frac{(2-\epsilon_g)\sqrt{t_{cr}}}{2R_f}\Big)+\frac{\epsilon_g(2-\epsilon_g)\mathrm{e}^{-2t_{cr}}}{2\sqrt{2}R_f}\frac{\mathrm{erfi}(\sqrt{2t_{cr}})}{2-\epsilon_g+\frac{(2-\epsilon_g)^2}{4R_f^2}}=0,\tag{5.37}$$

For high-R_f surface the cross-over time is given by $t_{cr}\approx\frac{1}{R_f^2},\ll 1$, and, similarly, for the low-R_f surface, $t_{cr}\approx\log\left(\frac{R_f}{\sqrt{\pi}}\right)^{-\frac{1}{2}}\gg 1$, The lack of a dependence on ϵ_g in the asymptotic regimes does suggest a decreased sensitivity to ϵ_g even for values of R_f outside these regimes. The sensitivity of the cross-over time to surface emissivity for different $R_f's$ is shown in figures 5.5a and 5.5b. There is a weak dependence of the cross-over time on the surface emissivity even for intermediate R_f surfaces. Thus, it is worth noting that even for a surface with emissivity ϵ_g, R_f continues to be the relevant parameter in determining the cross-over time, at least in the asymptotic limits of high and low R_f values. This of course, means that the surface emissivity enters only via the definition of R_f in the expression for the cross-over time, and not as a separate parameter. If one looks at the definition of R_f, (see (5.19)) the surface emissivity is seen increase the effective R_f value compared to a black surface, and thereby, enables the inversion-LTM transition to occur faster. This is because, when the surface emissivity is reduced, the surface cooling rate is reduced (upwelling flux from the surface is reduced in proportion to the surface emissivity) while the air cooling-rate is moderately increased because of the reflected component (here, the reflection consists of radiation from the cold source that then, increase the air cooling rate).

To summarize, the above analysis which only includes radiation, clearly demonstrates the relevance of the Ramdas-Zdunkowski factor in demarcating the LTM and inversion temperature regimes. In what follows, we will include conduction which smears out the radiative slip, that is predicted by the pure radiation analysis (see (5.33)) and also affects the cross-over time especially for small R_f surfaces.

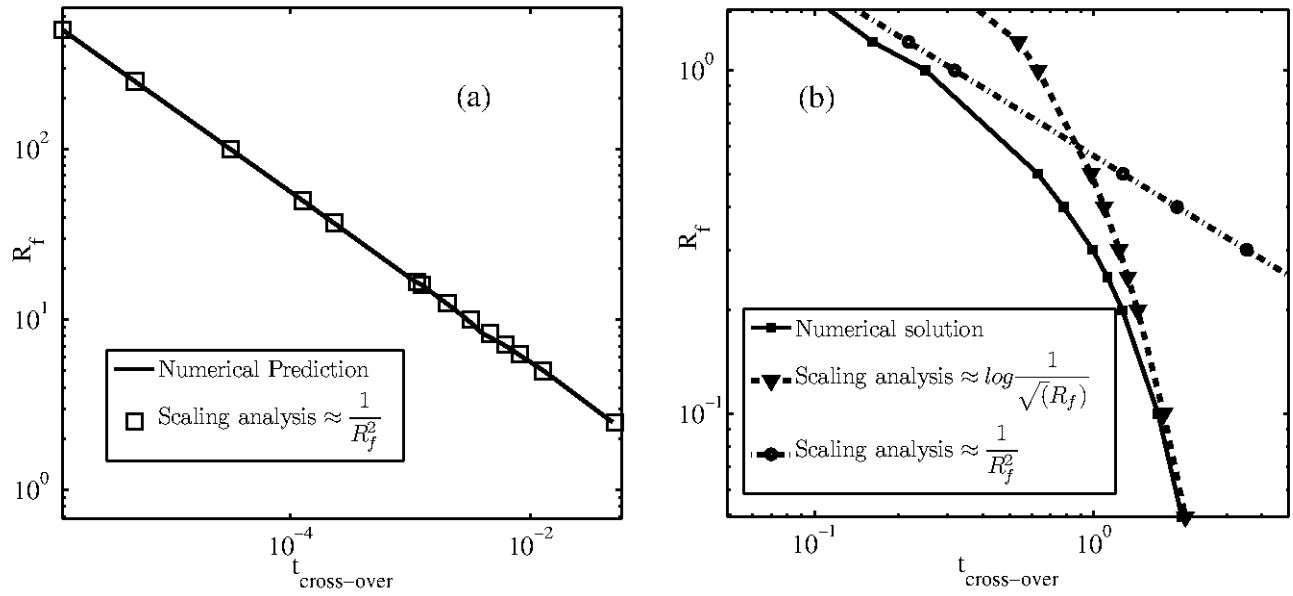

Figure 5.1: Comparison of the cross-over time predicted by scaling analysis and the numerical solution of (5.33): (a) comparison for large R_f and (b) for small R_f.

5.4.2 Effect of conduction

In this section we present the results for the evolution of the temperature profile in the lowest meters of the NBL with the effect of conduction among air layers having been included. The role of conduction in general, is to smear out the slip predicted by the pure radiation analysis, detailed in the previous section. For a positive slip, this results in a lifting up of the minimum temperature above the ground. The energy equation, (5.9), with conduction included is a partial differential equation PDE with variable coefficients, and therefore, cannot be solved analytically although, under certain limits (for instance $\mu_1 \to 0$), a singular perturbation analysis can be carried out to understand the role of conduction. We solved equations (5.9) and (5.11), along with the boundary conditions listed in the previous section, using the Method of lines [Schiesser & Griffiths (2009)]. In this method, the vertical coordinate is discretized using a finite-difference scheme, and the resulting system of ODE's is integrated with respect to time The system of ODE's is stiff, and ODE23s matlab routine is used to carry out the time marching (ODE23s is based on a modified Rosenbrock formula of order 2).

High-R_f surfaces

In this subsection, we will present the results for high-R_f surfaces. A high R_f implies that the surface responds slowly to any forcing, (for instance, a change in the wind speed) compared to the near-surface air layers. Examples of such surfaces include concrete and dry soil whose R_f values, based on the radiative time scale of $O(10\,s)$, are around 37 and 16, respectively. We have used the same simple exponential profile used in the pure radiation limit, with a scale height of $1\,cm$, and a surface concentration that leads to a response time close to ground of around 10 s. For the chosen scale height, the ratio of radiative to conductive time scales in air is $\mu_1 = 2$.

The temperature profiles for concrete, at various time instants, are given in figure 5.6a

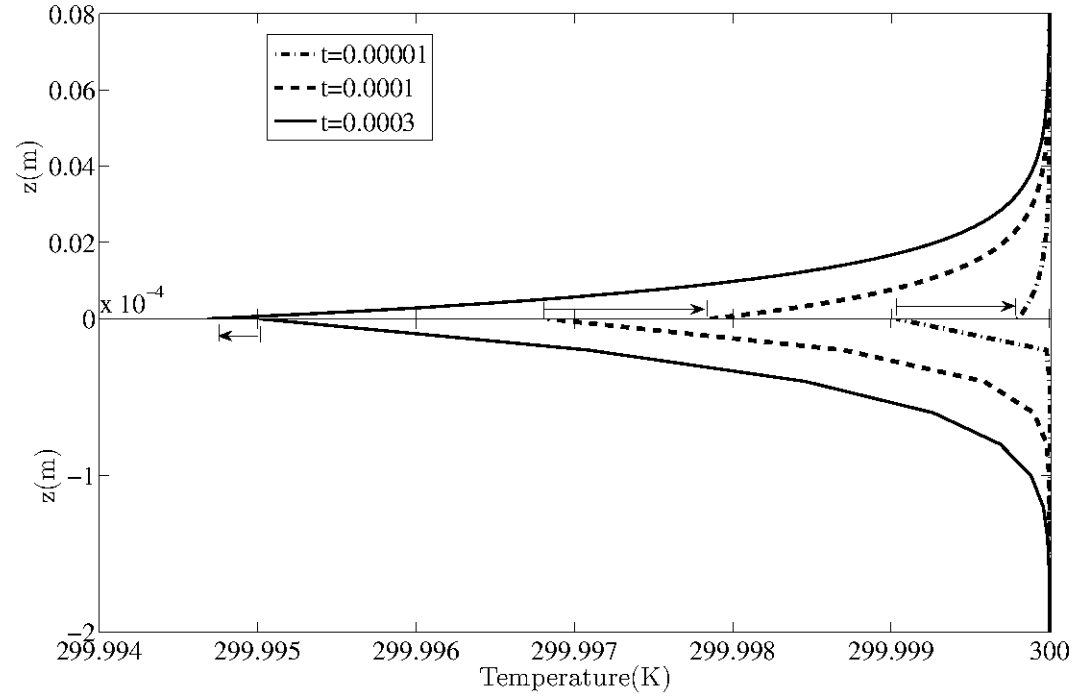

(a) Concrete:short time

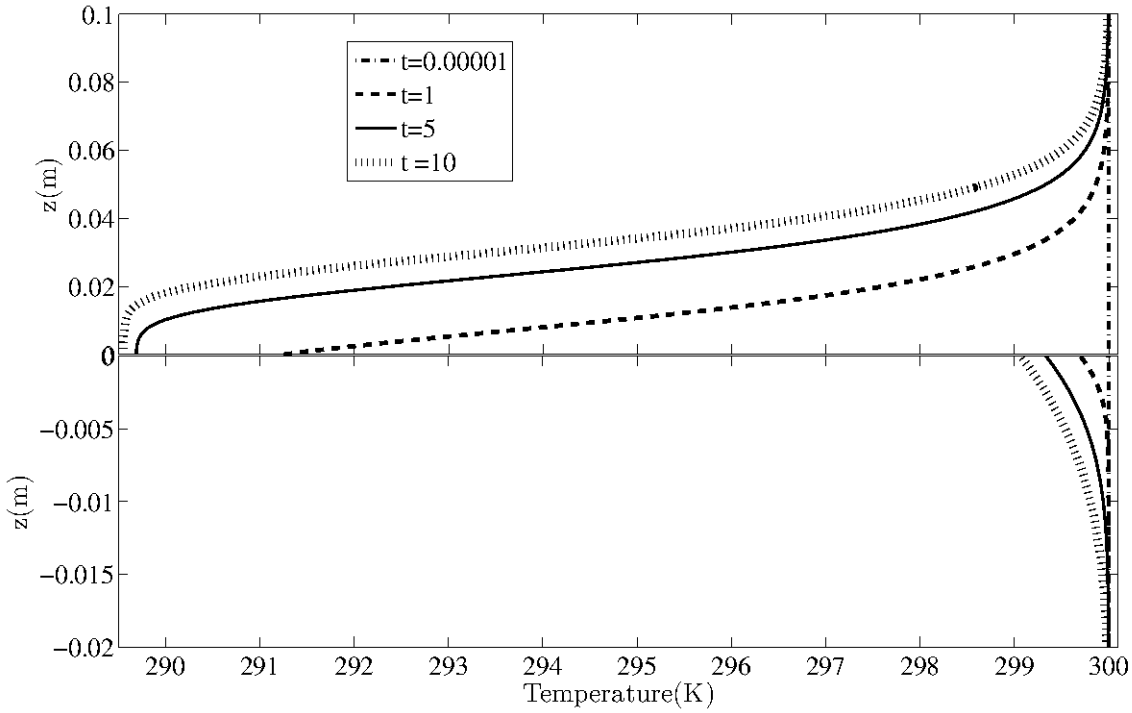

(b) Concrete:long time

Figure 5.2: Evolution of temperature profile over concrete $R_f = 37$. Plot(a) Temperature profile for short time and (b) the temperature profile at long times.

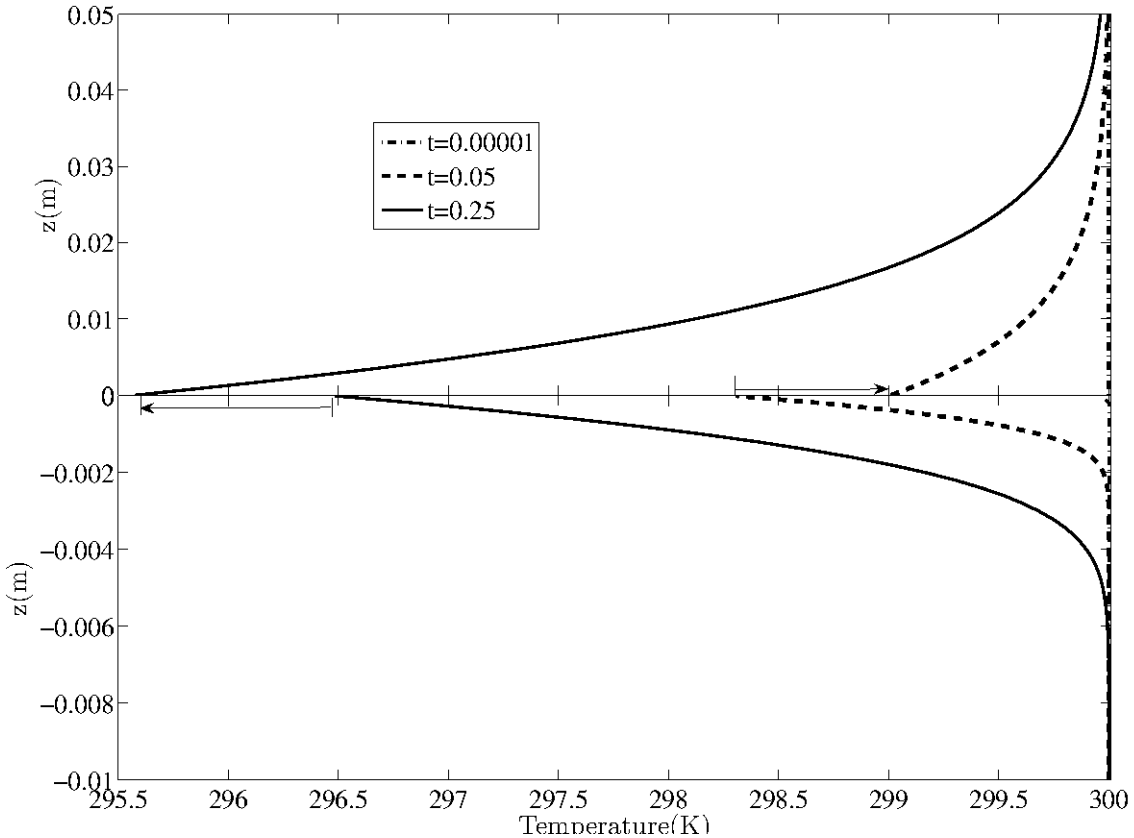

(a) Foam:short time

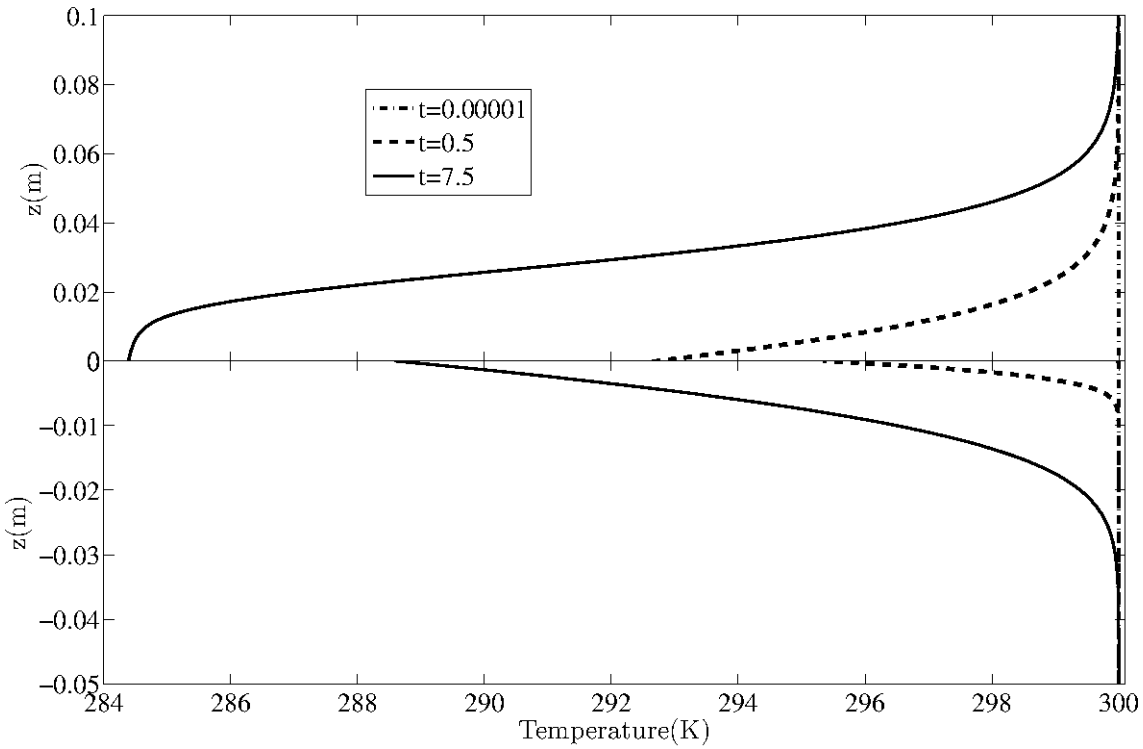

(b) Foam:long time

Figure 5.3: Evolution of temperature profile over foam $R_f = 1.4$. Plot(a) Temperature profile for short time and (b) the temperature profile at long times.

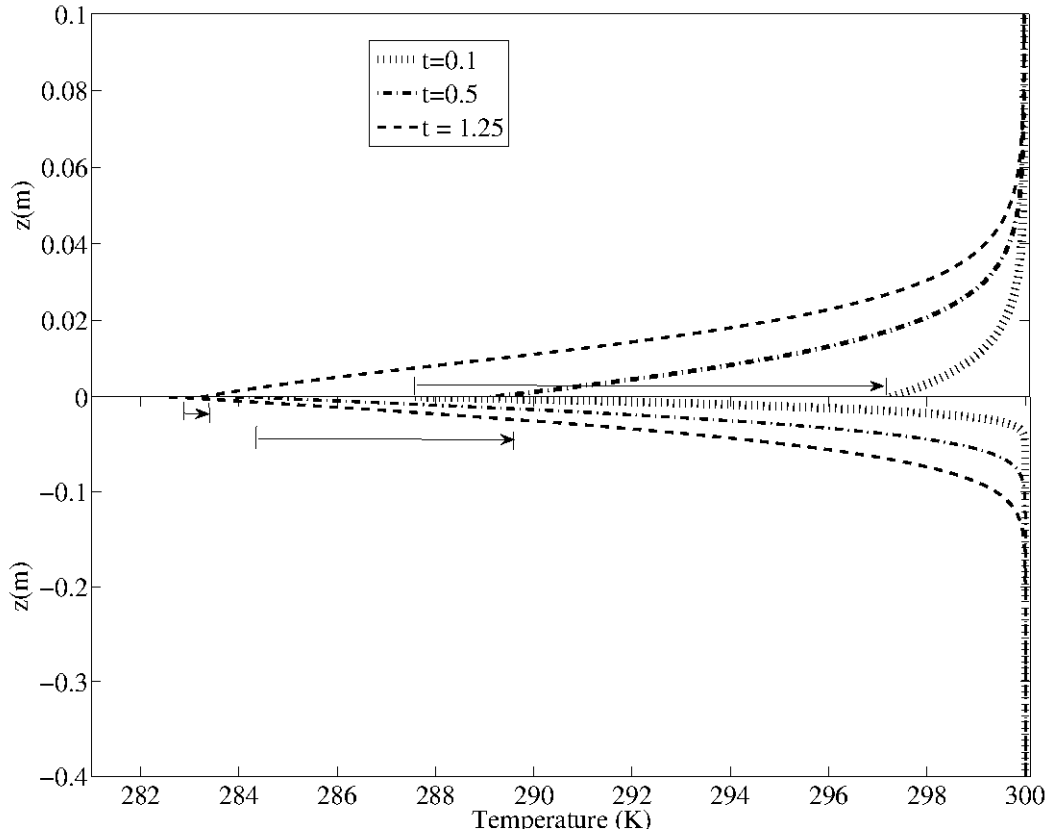

(a) Low-R_f surface:short time

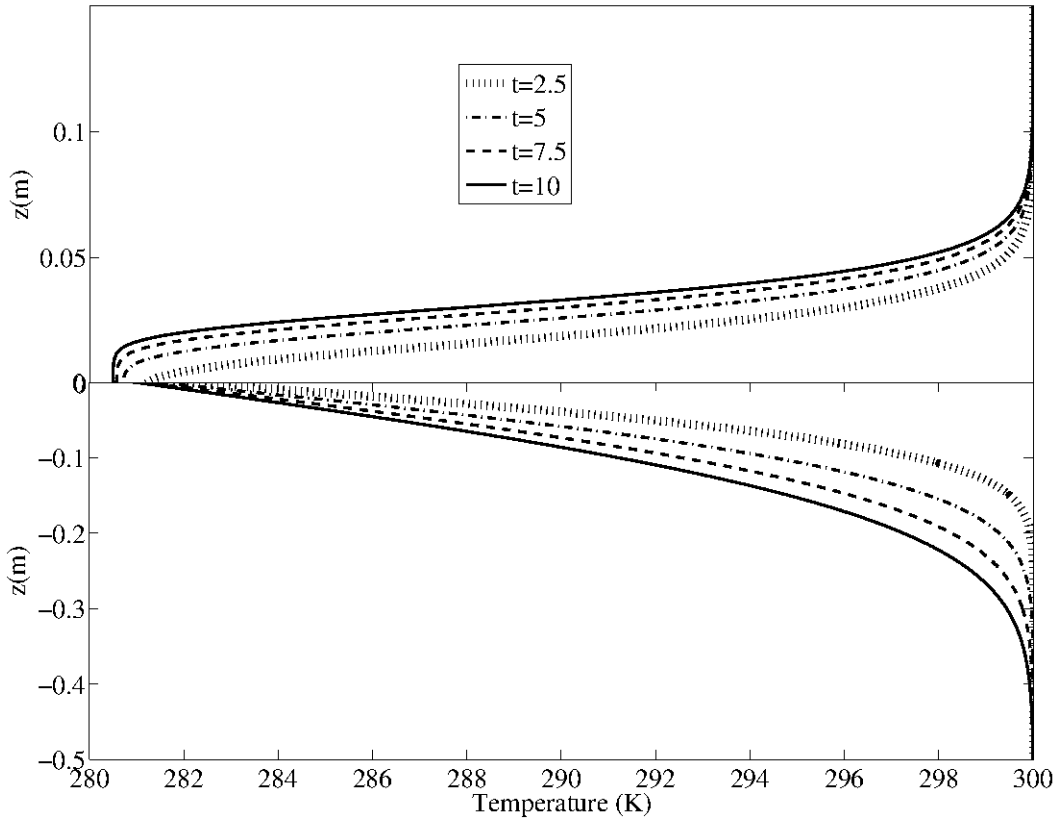

(b) Low-R_f surface: long time

Figure 5.4: Evolution of temperature profile over a low (hypothetical) R_f surface $R_f = 0.1$. Plot(a) Temperature profile for short time and (b) the temperature profile at long times.

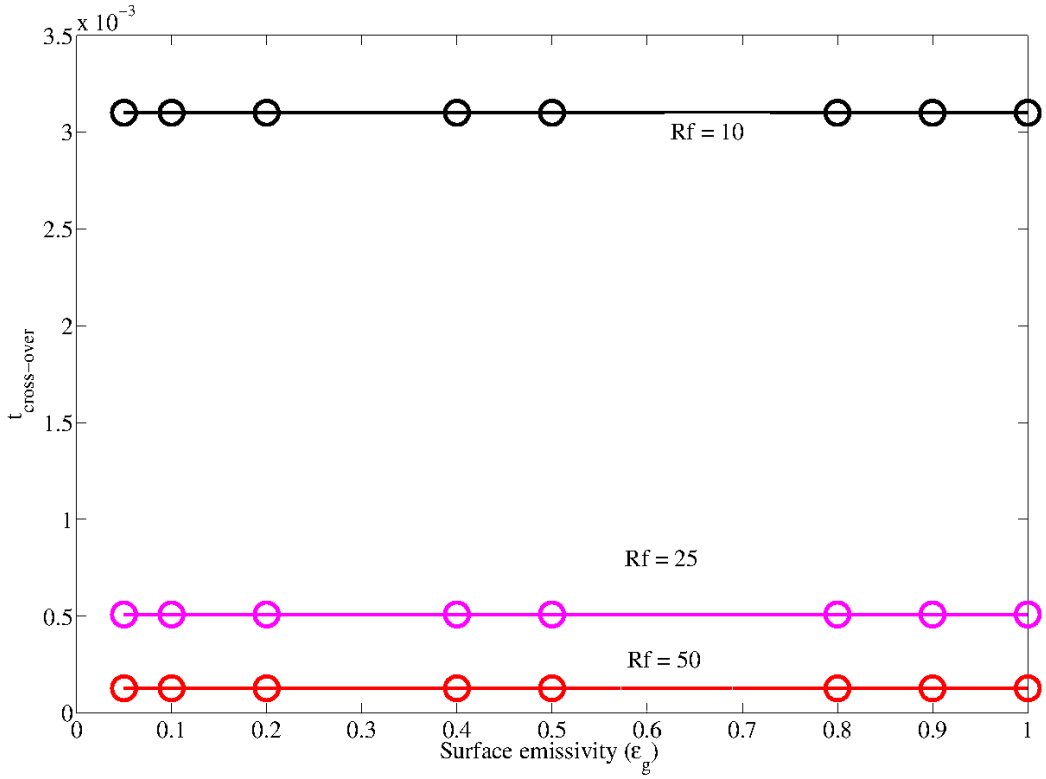

(a) High R_f surface

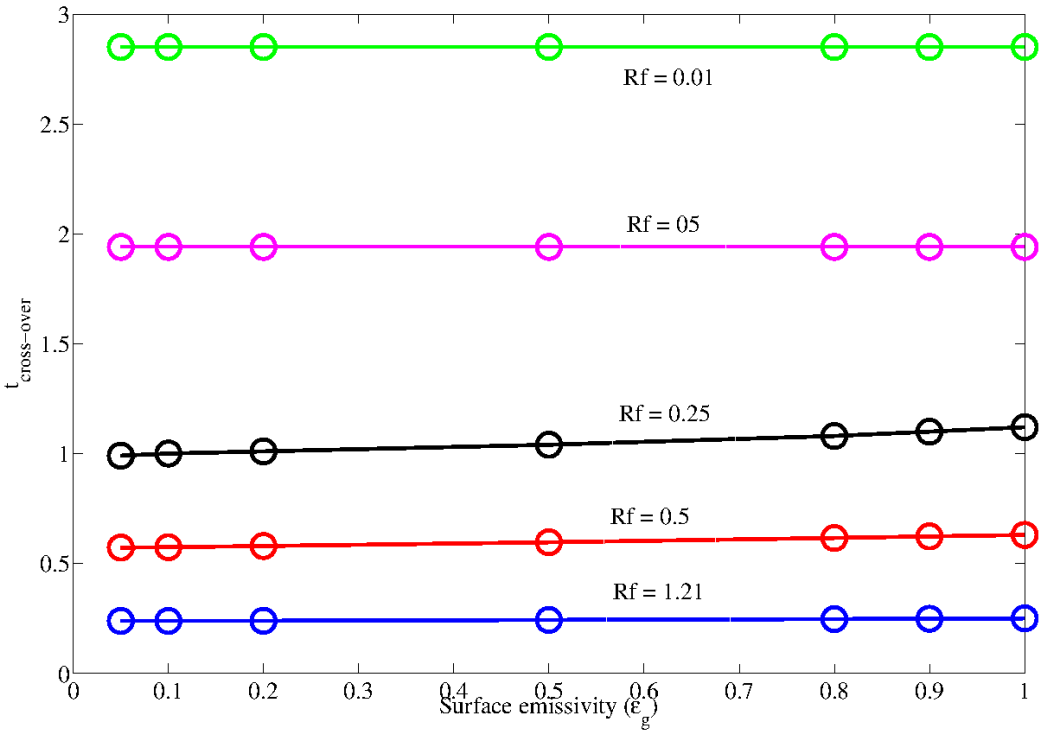

(b) Low R_f surface

Figure 5.5: The inversion-LTM cross-over time predicted as a function of ϵ_g for various R_f values.

and the corresponding vertical profiles of the temperature gradients, conductive cooling rates $\left(\frac{k}{\rho_a C_{pa}}\frac{\partial^2 T}{\partial z^2}\right)$, and radiative cooling rates are shown in figures 5.6b and 5.7, respectively. The profiles are plotted along with those obtained in the earlier section using the pure radiation analysis. It can be seen from the figure 5.6a that, at the initial instant, the ground cools faster than the air layers, and there is always an inversion profile to start with. Unlike the case of the inversion layer in the water-vapor-laden atmosphere, the radiative cooling-rate profile remains single-signed, and this is because the analysis here only includes the contribution due to aerosol particles and the cooling rate decays over a distance of the order of the aerosol scale height. In the inversion profile, for short times, the conductive flux to the ground cools the air layers close to the surface. Thus, the near-surface air layers cool both by radiation (interaction with cold sky) and via conductive cooling to the ground which increases the net cooling of air layers compared to the pure-radiation limit. However, the air layers do not continue to cool conductively for all times. The ground, on account of its inertia, retards the near-surface air layers, as a result of which the conductive contribution changes to a warming, and importantly, this change in sign of the profile curvature precedes the change in temperature gradient. Thus, there is already a conductive warming of the near-surface air layers in an inversion profile. With conduction included, strictly speaking, the cross-over for the inversion-LTM transition time may be defined as the time at which the temperature gradient at the ground reverses sign, since this gradient has opposite signs for the inversion and LTM-type profiles. Based on this criterion, the cross-over time is found to be smaller than the one predicted by the pure radiation limit for $\mu_1 = 2$ (see table 5.2). This acceleration of the transition may be attributed to the initial period of conductive cooling to the ground mentioned above. Subsequent to the transition, the minimum in temperature is slowly lifted up with time as the conductive boundary layer grows. As shown in figure 5.6a outside the conductive boundary layer, the temperatures are identical to those predicted by the pure radiation analysis. Note that, in this outer region, there is always a conductive cooling to the lower air layers. In figure 5.6a, the stars in the x-axis denote the surface temperature, as a function of time, obtained from the pure radiation analysis. It is clear from the coincidence of these stars with the actual surface temperature (with conduction included) that the conductive flux, for $\mu_1 = 2$, is too small to play any role in the surface energy budget.

To examine the effect of conduction we varied μ_1, the ratio of the radiative relaxation time to conductive time scale in the aerosol-laden air layers. For $\mu_1 \ll 1$ ($\mu_1 = 0.002$) when the effect of conduction is important only very close to the ground, the predicted profile of temperature, gradient and cooling-rates are shown in figure 5.8a, 5.8b and 5.9. The cross-over time at which the sign change occurs is now longer than that for $\mu_1 = 2$ (see table 5.2). This is because of the reduced conductive cooling to the ground. In addition, the intensity of minimum is higher and the minimum occurs closer to the ground. This is expected, since conduction lifts up the minimum, and the height of the minimum is therefore closely related to the conductive boundary layer thickness. In the limit $\mu_1 \gg 1$ conduction dominates the radiative transfer within the aerosol-laden air layers (this limit may be regarded as a crude manifestation of vertical transport due to turbulent velocity fluctuations). Physically the parameter μ_1 may also

be written as the ratio of two characteristic length scale,$\mu_1 = \left[\frac{\sqrt{\kappa_a \tau_{rad}}}{H}\right]^2$, and the limit $\mu_1 \gg 1$ therefore corresponds to the thickness of the conductive boundary layer being much greater than the aerosol scale height. Figure 5.10a shows the evolution of the vertical temperature profiles for $\mu_1 = 200$. The corresponding gradient, conductive and radiative cooling rate are shown in figure 5.10b and 5.11. In this limit, the cross-over time predicted is closer to the pure radiation analysis (see table 5.2), and therefore takes longer time than the previous case where $\mu_1 = 2$. This is due to the opposing effects of conductive cooling from ground and the conductive heating from the overlying air layers. Further, it can be seen, after the transition to LTM, the conductive flux warms the layers and the layers are at a temperature higher than the one predicted by pure radiation analysis. For $\mu_1 = 200$, the value of μ_1 is altered by changing the scale height of the aerosol (H = 1 mm) concentration layer keeping the relaxation time scale at the ground fixed.

The temperature profiles for larger times of $O(\tau_{rad})$ and beyond for concrete are shown in figure 5.12. Both the intensity and height of the minimum increase with time. Maximum intensity predicted is around 3 K.

In the above cases, the inversion-LTM cross-over has been defined based on the sign of the temperature gradient at the ground. While this is true in principle, one needs a different criterion from the point of view of experiments. In the latter case, the transition between the two regimes would be sensed by a thermocouple at a fixed height, and the cross-over time becomes a sensitive function of this height. One expects the cross-over time to increase with height, and in addition, the cross-over time at a particular height to converge to the corresponding prediction based on a pure radiation analysis in the limit of vanishing thermal conductivity. It is worth noting that the latter is not true for the criterion based on the surface temperature gradient since the point on the surface is always within the conductive boundary layer. Accordingly, 5.2 also gives the cross-over corresponding to the sign of the temperature slip at a height of 1mm (this corresponds to the lowest thermocouple in the experiments; see Mukund *et al.* (2013)).

Surface	μ_1	$t_{cross-over}$ (in units of τ_{rad})	
		5×10^{-3} mm (ground)	1 mm
Concrete	0 (pure radiation limit)	2.39×10^{-4}	2.8×10^{-4}
($R_f = 37$)	2	1.5×10^{-4}	2.8×10^{-4}
	0.002	1.8×10^{-4}	2.8×10^{-4}
	200	2.05×10^{-4}	1.5×10^{-3}
Foam	0 (pure radiation limit)	0.16	0.19
($R_f = 1.4$)	2	0.19	0.38
	0.002	0.19	0.19
	200	∞	∞

Table 5.2: Cross-over time predicted by the pure radiation analysis and with conduction at different locations for different ratio of radiative to conductive time scales. $\mu_1 = 0$ corresponds to pure radiation limit. In the numerical simulation 5×10^{-3} mm is the first grid point and in the recent experiments by Mukund *et al.* (2013), the first thermocouple is located at 1mm.

5.4.3 Low-R_f surfaces

In this subsection, we present the results for a low R_f surface such as foam. Observations by Mukund *et al.* (2013) show that over a foam surface (low-thermal-inertia, high emissivity), an LTM-type profile is replaced by an inversion profile. Although, under weak wind conditions, there is a weak minimum at a height of a few millimeters. We have simulated the evolution over such a low thermal inertia surface ($R_f = 1.4$) and the resulting temperature profiles are given in figure 5.13a for $\mu_1 = 2$. The corresponding vertical profiles of the temperature gradients, conductive and radiative cooling-rates are shown in figure 5.13b and 5.14. Figure 5.13a shows a weak minimum very close to the ground. Unlike the high R_f surface considered previously, the cross-over time predicted is higher than that predicted by the pure radiation analysis (see table 5.2), and this delay in the inversion-LTM transition is due to conductive warming from overlying air layers. As seen for the $R_f = 37$ case, although the ground initially cools the lowermost-air layers, conductive warming from the overlying air layers dominates at later times. It is the competition between these two conductive contributions(of opposite signs) that determines the cross-over time in relation to that predicted by the pure radiation analysis. For high R_f surfaces, the conductive warming at later times is unable to overcome the effects of the initial cooling, but this is no longer the case for low R_f surfaces. Note that even in the low R_f case, the conductive flux from the air layers contributes an insignificant factor, and the variation in surface temperature with time remains close to that predicted by the pure radiation analysis. For $\mu_1 \ll 1$, $\mu_1 = 0.002$ the predicted temperature, gradient and cooling-rate profiles are shown in 5.15a, 5.15b and 5.16. As expected, the predicted minimum has a greater intensity, occurs closer to the ground. For an increased value of $\mu_1 = 200$ (the aerosol layer now being within the thick conductive boundary layer), and find there to be no LTM! The temperature, gradient, conductive and radiative cooling-rate profiles are shown in figures 5.17a, 5.17b and 5.18, where it is also evident that the conductive flux now constitutes a significant portion of the energy budget, and thereby causes a pronounced deviation of the surface temperature from the prediction of the pure radiation analysis.

The above analysis captures the essential features needed to explain the origin of the Ramdas layer. The gist of the theory is that there is a steeply varying concentration of aerosol particles near the ground which interacts effectively with the cold sky, and thereby, cools the lowermost air layers. Conduction acts to move the minimum temperature upward leading to an LTM-type profile, and this explains the origin of the Ramdas layer. However, in chapter 4, in section 4.6.2, we showed the results for aerosol-driven cooling in the window along with a water-vapor-driven contribution in the opaque bands. The radiative cooling-rate profile (plotted in figure 4.12b) associated with the equilibrium temperature profile shows there is a transition from a

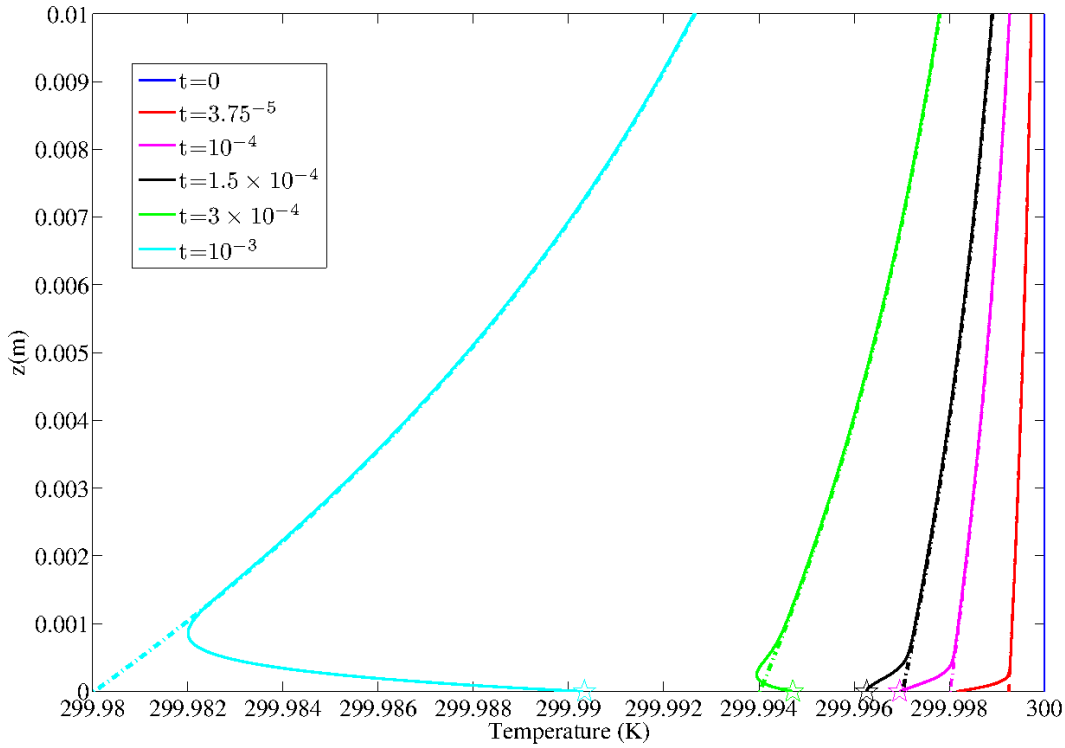

(a) Temperature profile

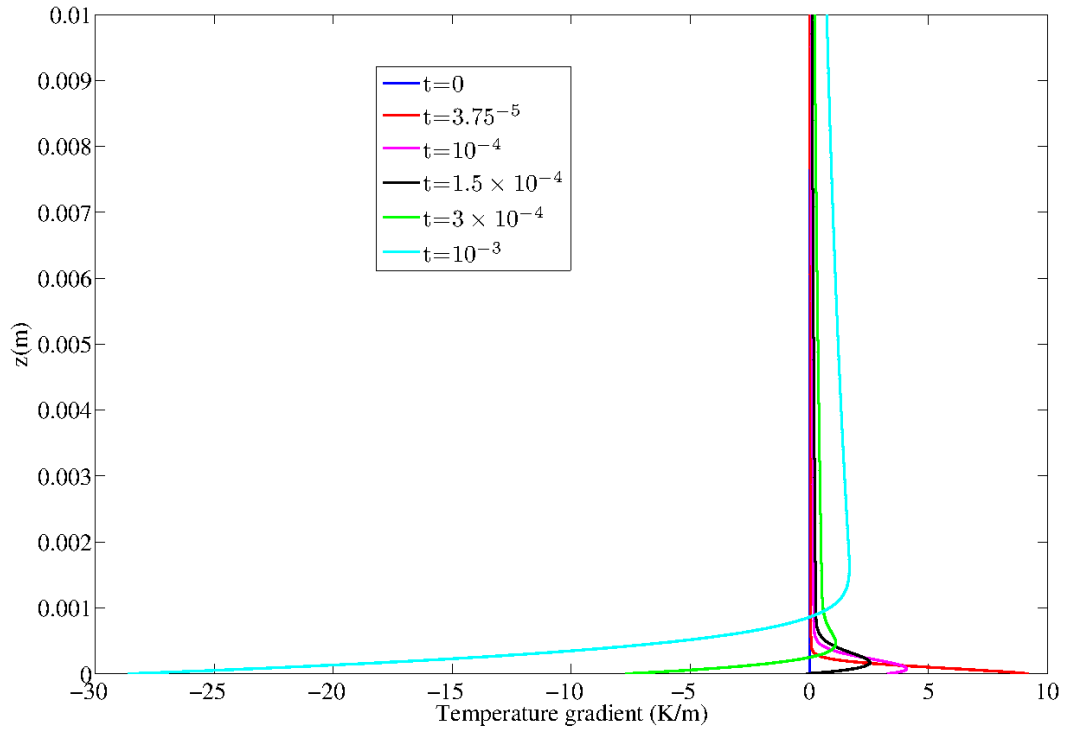

(b) Temperature gradient

Figure 5.6: Evolution of the vertical temperature profile over concrete ($R_f = 37$, $\mu_1 = 2$). The distribution of relaxation times is assumed to be a simple exponential with a scale height of 1 cm, and the fastest relaxation time at the ground is assumed to be 10 s. Plot(a) shows the temperature profiles before and after the cross-over time (which is $t_{cross-over} = 1.5 \times 10^{-4}\, \tau_{rad}$); plot (b) shows the corresponding temperature gradient profile. The symbol $\star$ and the dashed line in (a) correspond to the surface temperature and the temperature profile predicted by the pure radiation analysis.

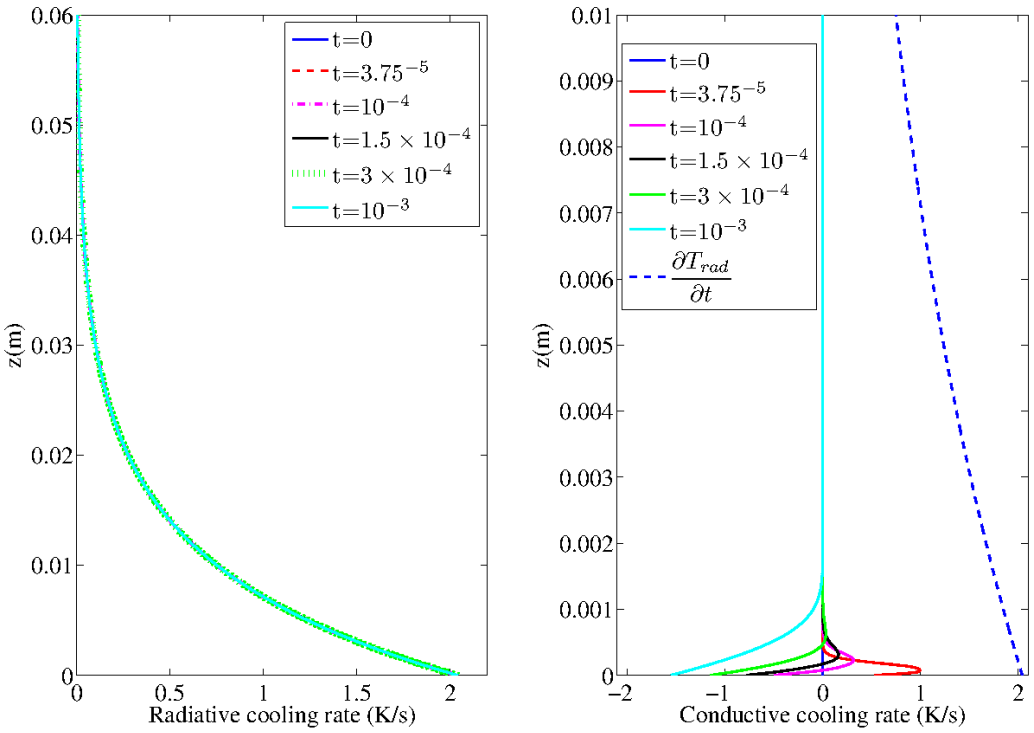

Figure 5.7: The radiative and conductive cooling-rate profiles over concrete ($R_f = 37$, $\mu_1 = 2$). The distribution of relaxation times is assumed to be a simple exponential with a scale height of 1 cm, and the fastest relaxation time at the ground is assumed to be 10 s. The dashed line is the predicted radiative cooling-rate at the initial instant due to aerosol particle interaction with cold sink.

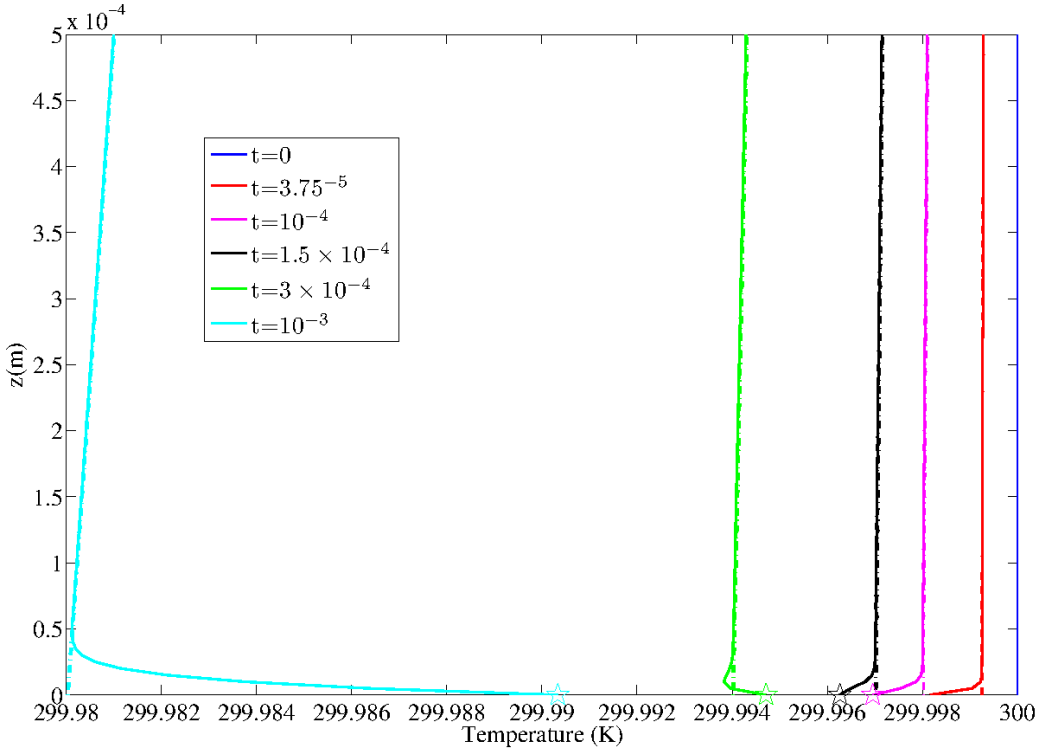

(a) Temperature profile

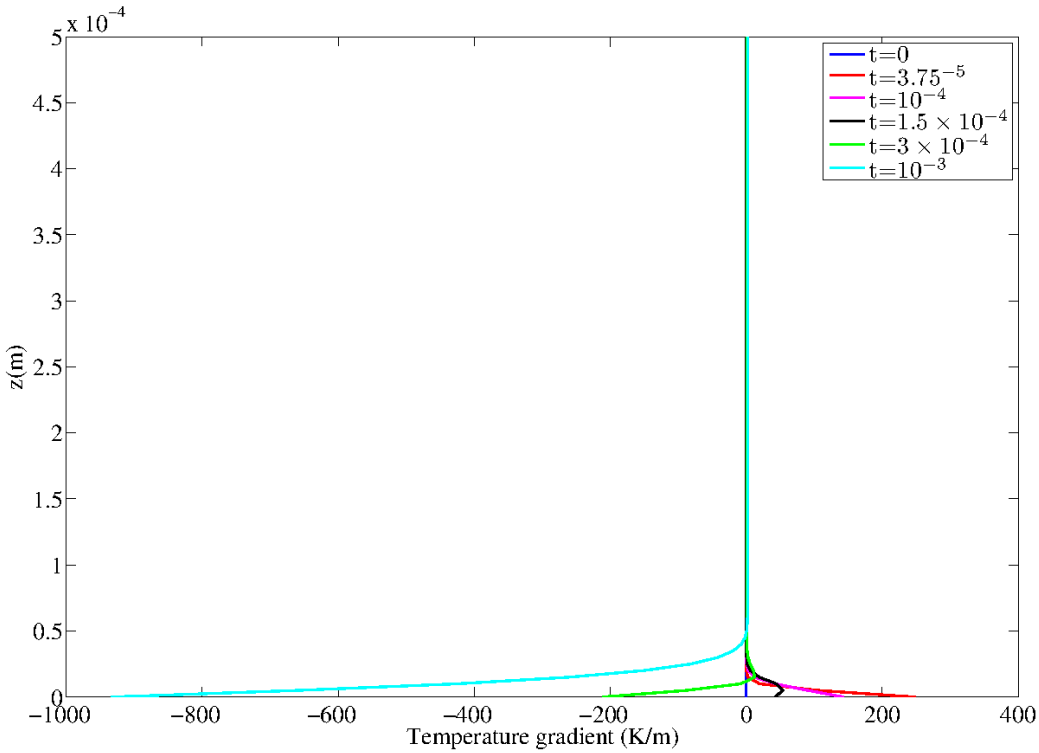

(b) Temperature gradient

Figure 5.8: Evolution of the vertical temperature profile over concrete ($R_f = 37$, $\mu_1 = 0.002$). The distribution of relaxation times is assumed to be a simple exponential with a scale height of 1 cm, and the fastest relaxation time at the ground is assumed to be 10 s. Plot(a) shows the temperature profile before and after the cross-over time (which is $t_{cross-over} = 1.8 \times 10^{-4}\,\tau_{rad}$); and plot (b) shows the corresponding temperature gradient profile. The symbol * and the dashed line in (a) correspond to the surface temperature and the temperature profile predicted by pure radiation analysis.

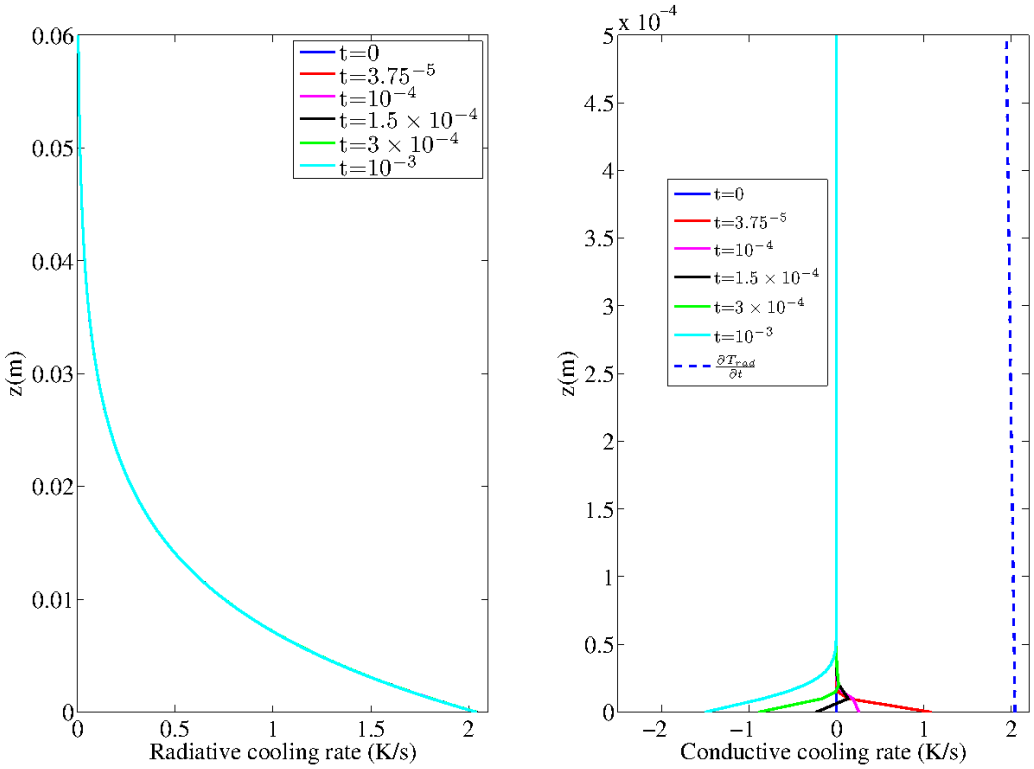

Figure 5.9: The radiative and conductive cooling-rate profiles over concrete ($R_f = 37$, $\mu_1 = 0.002$). The distribution of relaxation times is assumed to be a simple exponential with a scale height of 1 cm, and the fastest relaxation time at the ground is assumed to be 10 s. The dashed line is the predicted radiative cooling-rate at the initial instant due to aerosol particle interaction with cold sink.

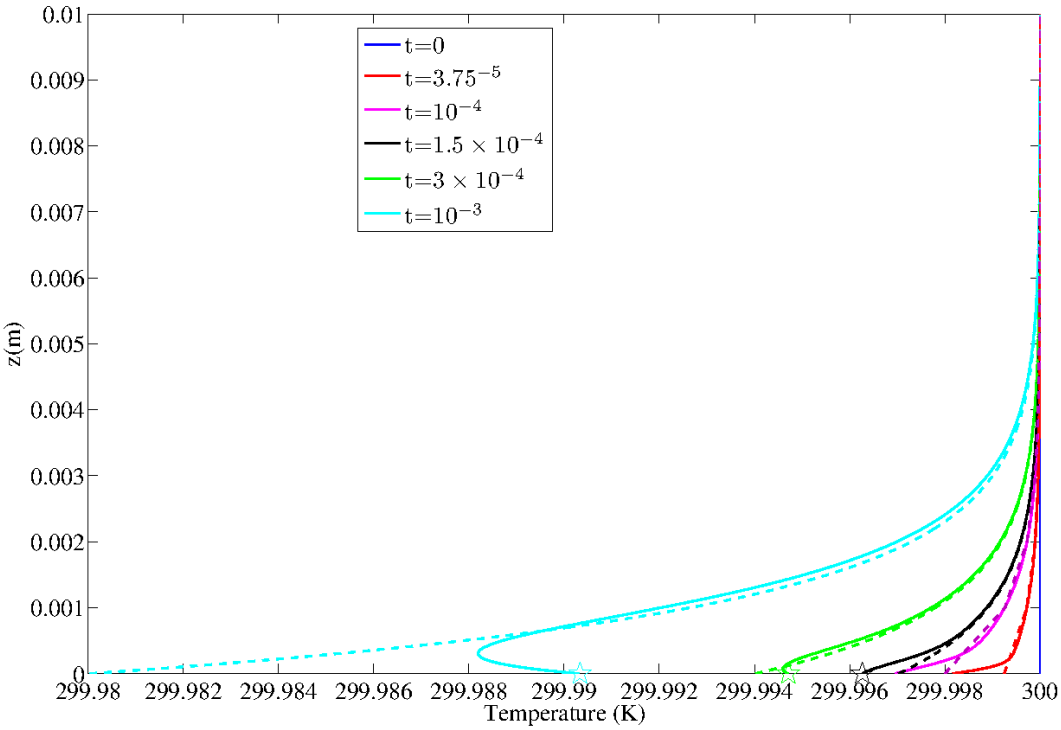

(a) Temperature profile

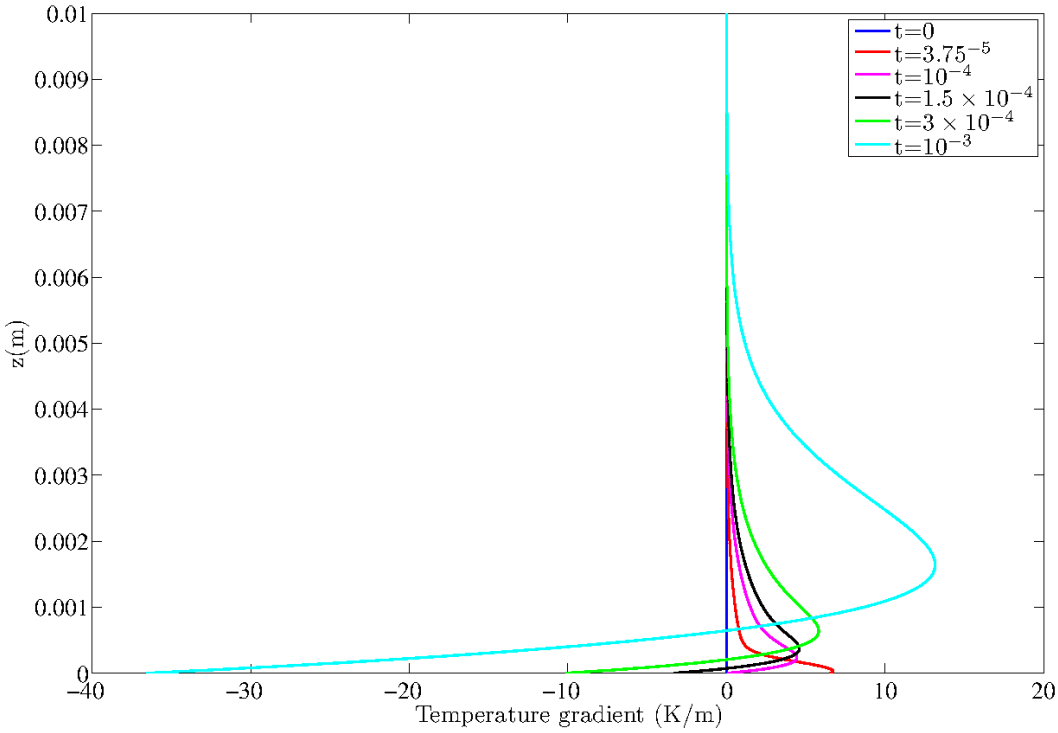

(b) Temperature gradient

Figure 5.10: Evolution of the vertical temperature profile over concrete ($R_f = 37$, $\mu_1 = 200$). The distribution of relaxation is assumed to be a simple exponential with a scale height of 1 mm, and the fastest relaxation times at the ground is assumed to be 10 s. Plot(a) shows the temperature profile before and after the cross-over time (which is $t_{cross-over} = 2.05 \times 10^{-4}\, \tau_{rad}$); and plot (b) shows the temperature gradient profile. The symbol * and the dashed line in (a) correspond to the surface temperature and the temperature profile predicted by pure radiation analysis.

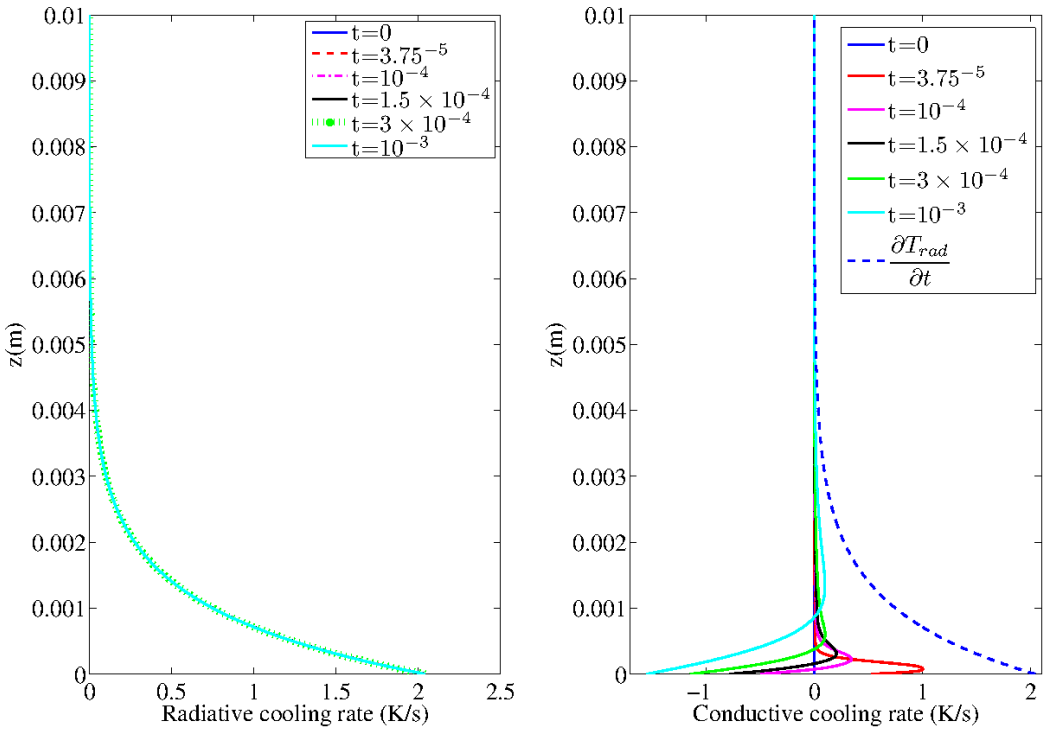

Figure 5.11: The radiative and conductive cooling-rate profiles over concrete ($R_f = 37$, $\mu_1 = 200$). The distribution of relaxation times is assumed to be a simple exponential with a scale height of 1 mm and the fastest relaxation time at the ground is assumed to be 10 s. The dashed line is the predicted radiative cooling-rate at initial instant due to aerosol particle interaction with cold sink.

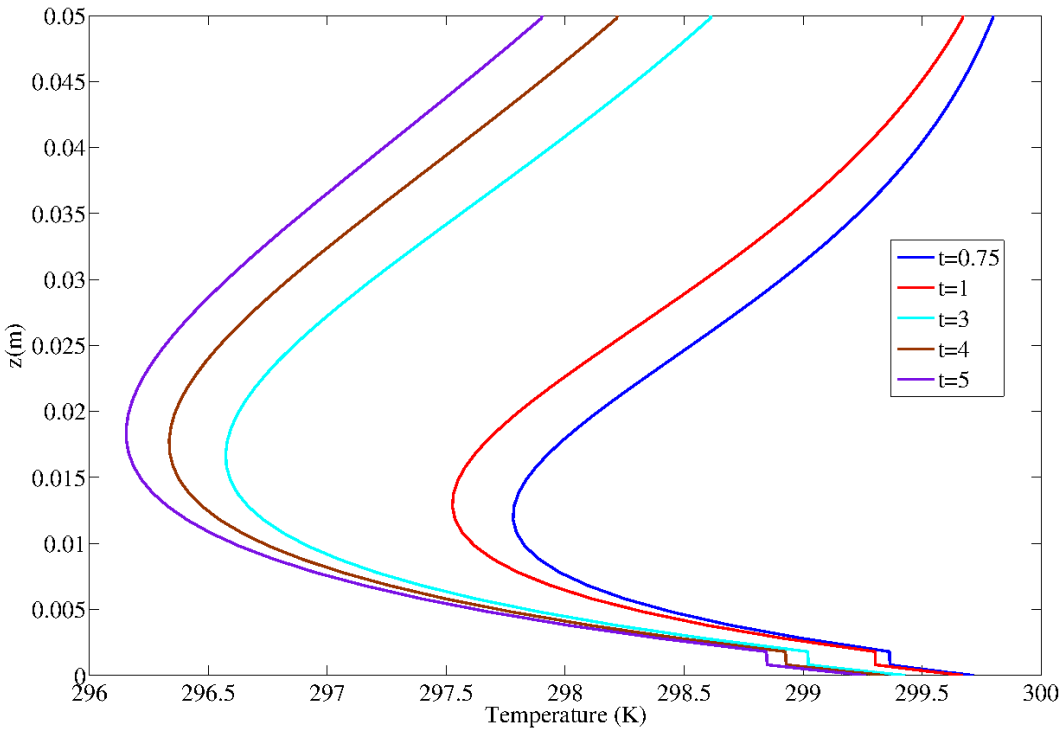

Figure 5.12: Evolution of temperature profile at larger times over concrete $R_f = 37$. The kink in the above profiles are due to a jump in the step size (the numerical scheme uses a step size of 5×10^{-3} mm in the range 0 to 1 mm, a step size of 1 mm from 1 mm to 1 m).

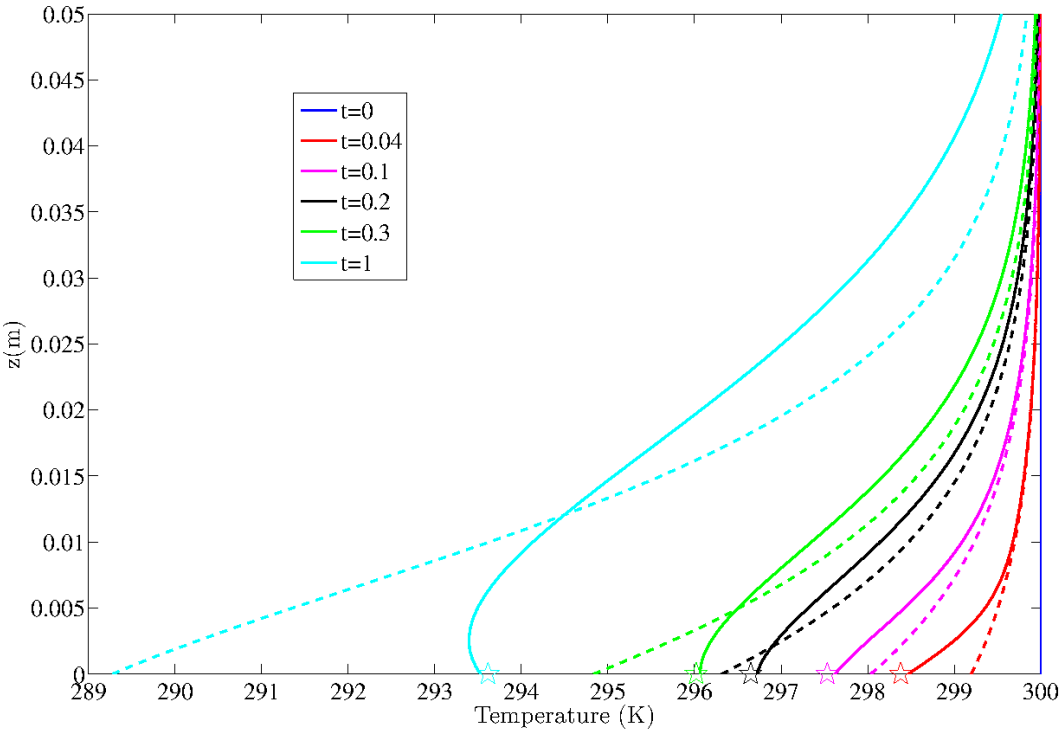

(a) Temperature profile

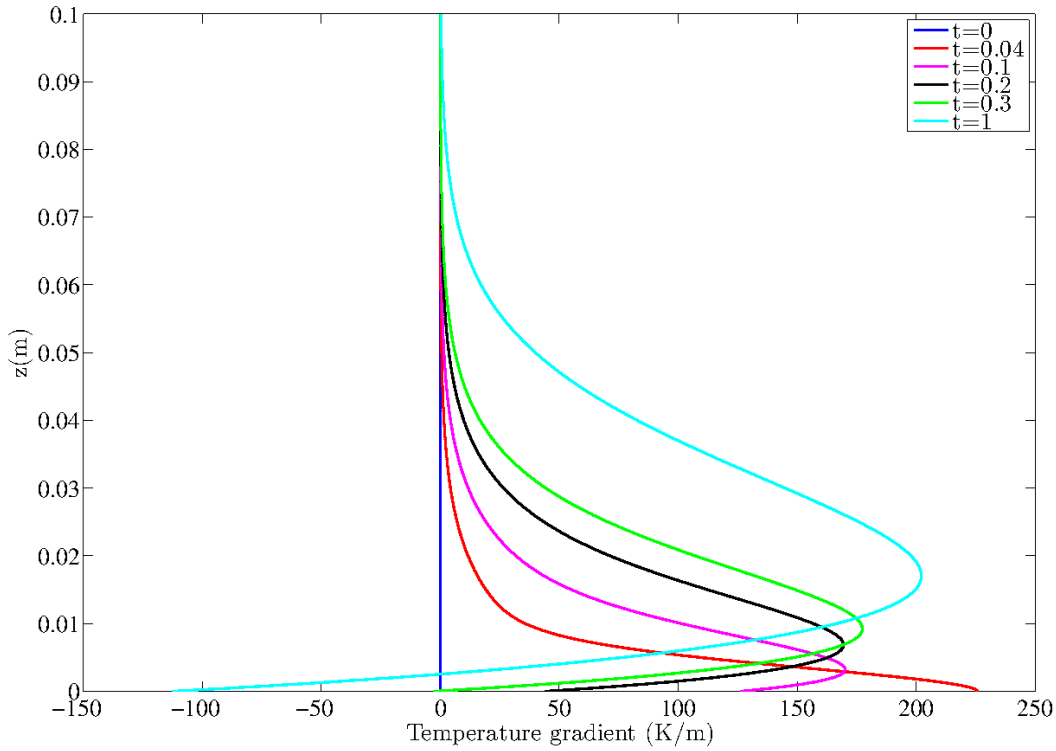

(b) Temperature gradient

Figure 5.13: Evolution of the vertical temperature profile over foam ($R_f = 1.4$, $\mu_1 = 2$). The distribution of relaxation times is assumed to be a simple exponential with a scale height of 1 cm, and the fastest relaxation time at the ground is assumed to be 10 s. Plot(a) shows the temperature profile before and after the cross-over time which is (which is $t_{cross-over} = 0.16\tau_{rad}$); plot (b) shows the corresponding temperature gradient profile. The symbol $\star$ and the dashed line in (a) correspond to the surface temperature and the temperature profile predicted by pure radiation analysis.

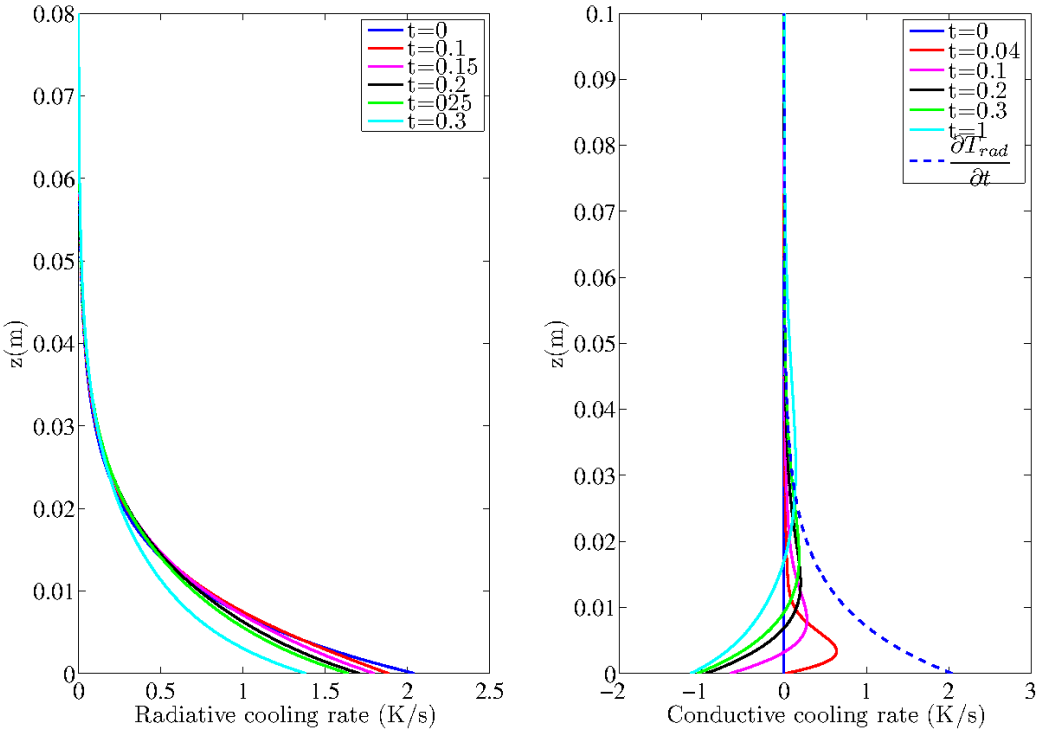

Figure 5.14: The radiative and conductive cooling-rate profiles over foam ($R_f = 1.4$, $\mu_1 = 2$). The distribution of relaxation times is assumed to be a simple exponential with a scale height of 1 cm and the fastest relaxation time at the ground is assumed to be 10 s. The dashed line is the predicted radiative cooling-rate at initial instant due to aerosol particle interaction with cold sink.

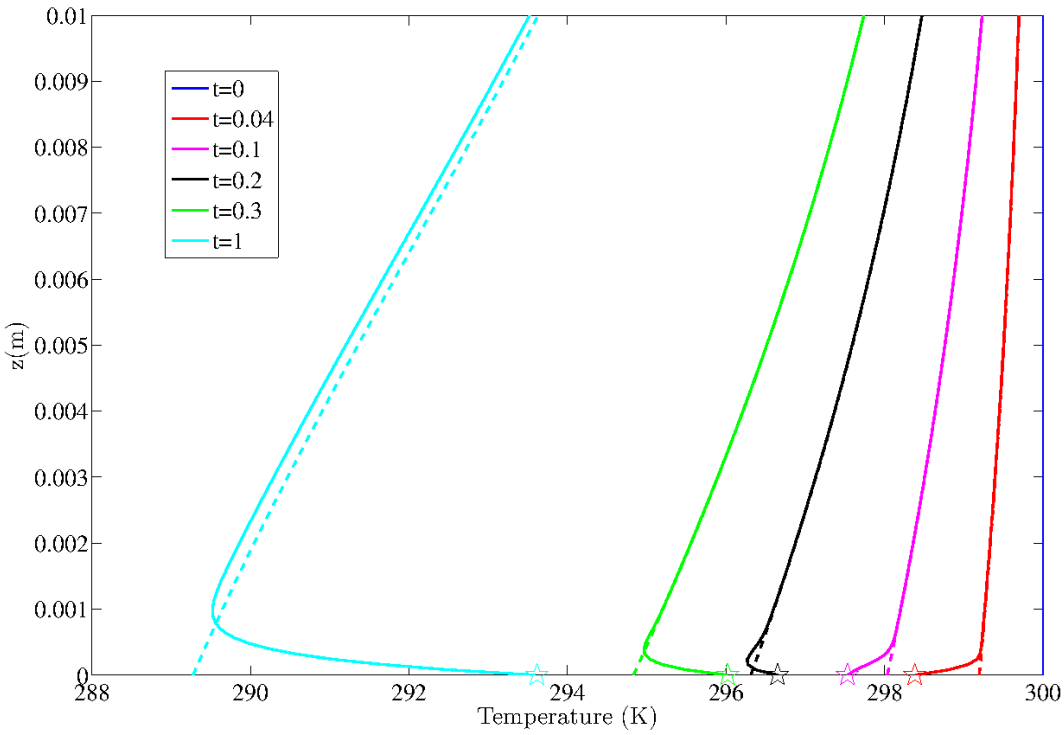

(a) Temperature profile

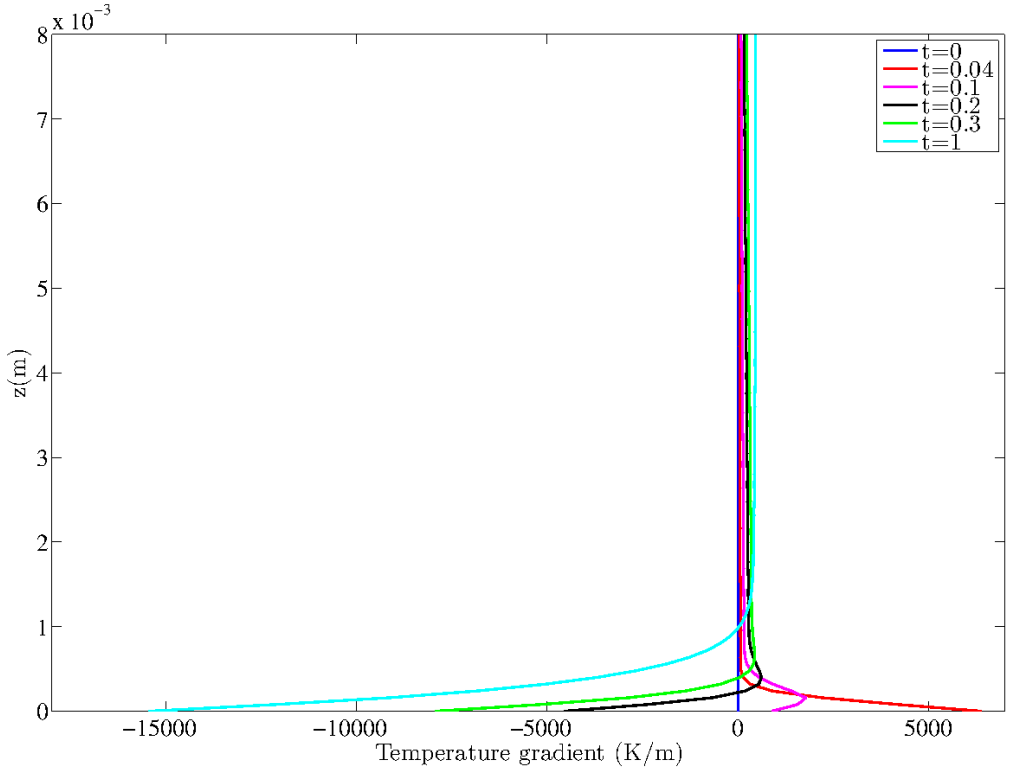

(b) Temperature gradient

Figure 5.15: Evolution of the vertical temperature profile over foam ($R_f = 1.4$, $\mu_1 = 0.002$). The distribution of relaxation times is assumed to be a simple exponential with a scale height of 1 cm, and the fastest relaxation time at the ground is assumed to be 10 s. Plot(a) shows the temperature profile before and after the cross-over time (which is $t_{cross-over} = 0.19\tau_{rad}$); plot (b) shows corresponding temperature gradient profile. The symbol * and the dashed line in (a) correspond to the surface temperature and the temperature profile predicted by pure radiation analysis.

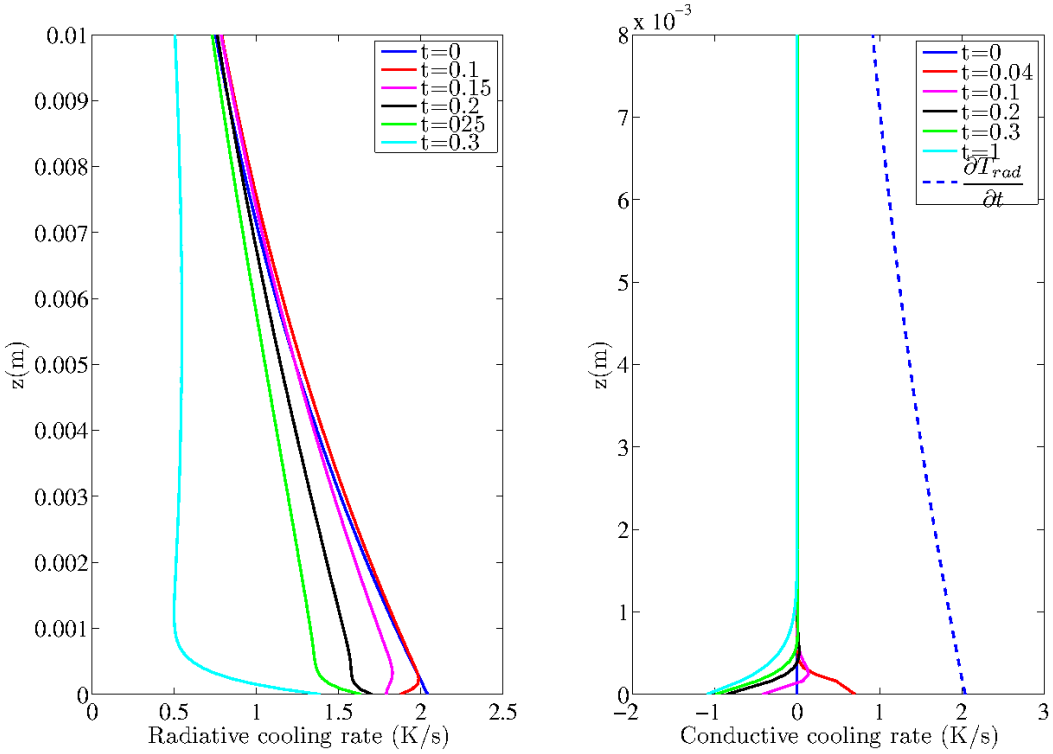

Figure 5.16: The radiative and conductive cooling-rate profiles over foam $R_f = 1.4$, $\mu_1 = 0.002$. The distribution of relaxation times is assumed to be a simple exponential with a scale height of 1 cm, and the fastest relaxation time at the ground is assumed to be 10 s. The dashed line is the predicted radiative cooling-rate at initial instant due to aerosol particle interaction with cold sink.

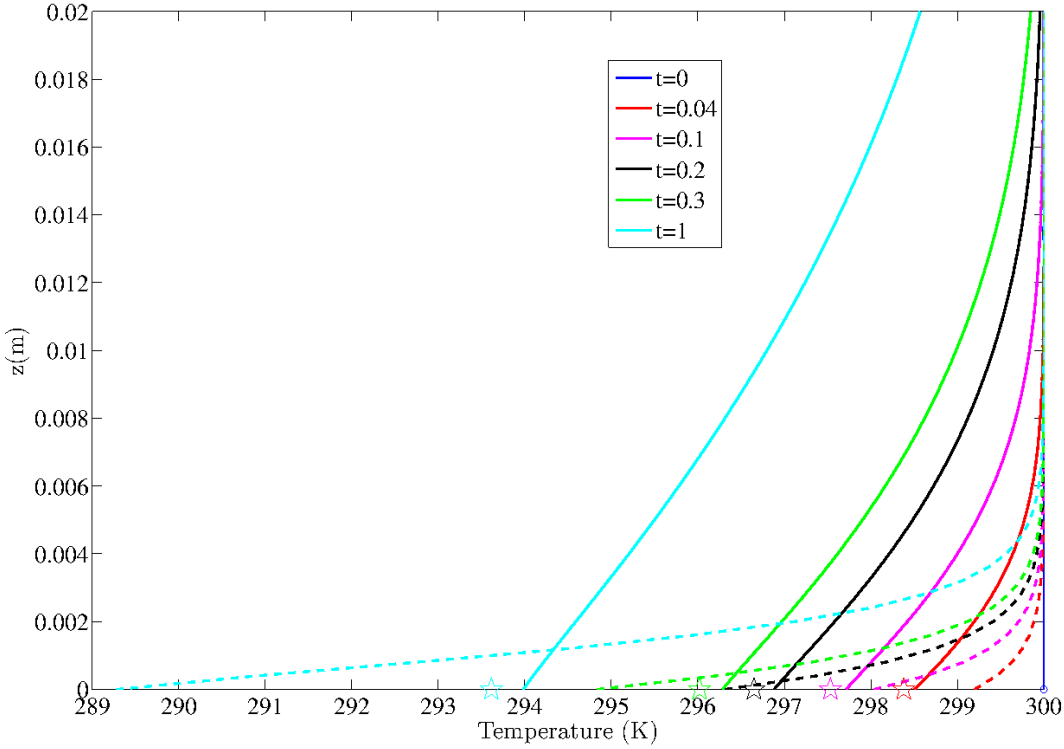

(a) Conductive cooling-rate

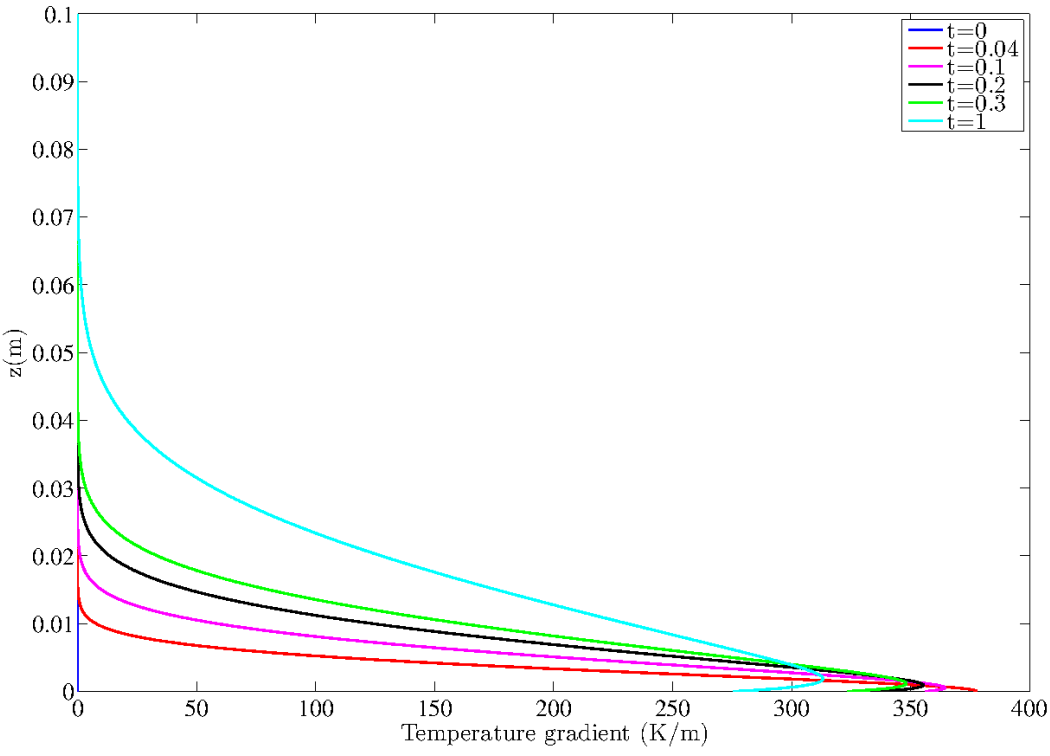

(b) Radiative cooling-rate

Figure 5.17: Evolution of the vertical temperature profile over foam ($R_f = 1.4$, $\mu_1 = 200$). The distribution of relaxation times is assumed to be a simple exponential with a scale height of 1 mm, and the fastest relaxation time at the ground is assumed to be 10 s. Plot(a) shows the temperature profile and there is no transition from inversion to LTM regime and plot (b) shows the corresponding temperature gradient profiles.

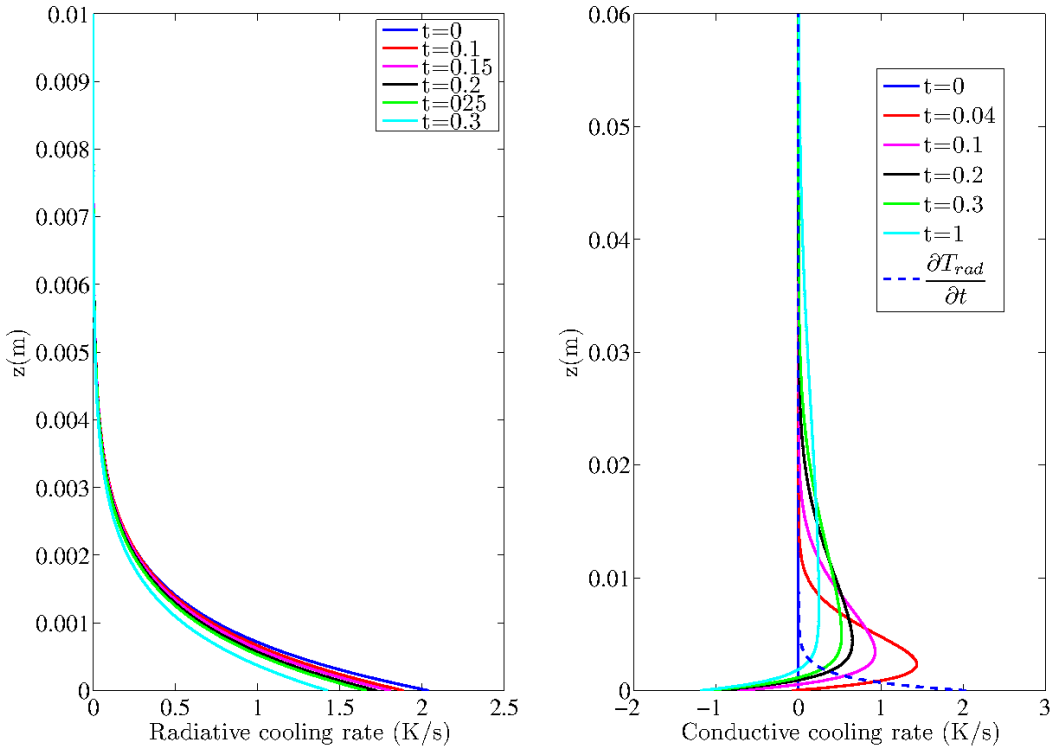

Figure 5.18: The corresponding radiative and cooling rates over foam $R_f = 1.4$, $\mu_1 = 200$. The distribution of relaxation time is assumed to be a simple exponential with a scale height of 1 mm and the fastest relaxation time at the ground is assumed to be 10 s. The dashed line is the predicted radiative cooling-rate at initial instant due to aerosol particle interaction with cold sink.

near-surface radiative cooling (which is maximum at the ground and decays with height) to a radiative warming at greater heights. The latter is due to the radiative exchange of the near-surface air layers with the overlying warmer layers through the opaque bands of the water vapor spectrum, cannot be captured by the present model which only includes aerosol particles as the radiatively participating component and further, the aerosol layer is assumed to be in the optically thin limit. In this limit, the aerosol particles directly interact with the cold sky and ground but not with the neighboring layers. Although water vapor is not crucial to explain the origin of the Ramdas layer, if one wants to conduct a quantitative study of the evolution of the nocturnal boundary layer, then one has to also include the radiative contribution of water vapor. In the following section we will include the role of water vapor along with aerosol particles to study NBL evolution. Before going into the detailed results for an inhomogeneous, aerosol-laden atmosphere, we present the results for water-vapor-laden-atmosphere, free of particulate aerosols, so as to establish the evolution of the post-sunset inversion layer during night which has been studied well in the literature [Fleagle (1955);Edwards (2009a);Savijärvi (2013)].

5.5 Thermal structure of the inhomogeneous NBL (water vapor and aerosols)

In this section, we examine, via numerical simulations, the role of both water vapor and aerosols in determining the vertical temperature profile over the lowest meters of the NBL, and the associated vertical distribution of radiative flux divergence. In section 5.4.1, we have already determined the role of aerosol-driven cooling alone in a simplified framework, and the simulations here help clarify the validity of the Newtonian cooling approximation, and the additional role played by water vapor. The full numerical solution is based on the flux-emissivity formulation introduced in chapter 2, and includes the radiative effect of both water vapor and suspended aerosol particles. The role of water vapor is again modeled using a flux-emissivity scheme and emissivity expressions are taken from Zdunkowski and Johnson (1965). As already discussed in chapter 2, the emissivity, being defined in a piecewise manner, results in an undesired discontinuity in the cooling-rate profile. In order to avoid this, we combine both expressions in the original Zdunkowski and Johnson (1965) parameterization (see (2.51) and (2.52) in chapter 2 into one, valid for all path lengths, and that reduces to the original expressions in the respective ranges. The combined expression can be written as:

$$\epsilon^f_{wv}(u) = a_1 \log(1 + b_1 u) \left(1 - \tanh\left(\frac{u}{0.01}\right)\right) + a_2 \log(1 + b_2 u) \tanh\left(\frac{u}{0.01}\right), \tag{5.38}$$

which is now, being a smooth function of the path length. At the monochromatic level, the transmissivity of the water-vapor-aerosol mixture in an inhomogeneous night-time atmosphere can be written as the product of the individual transmissivities. Such a relation is valid even at the narrow-band level when the components are not interacting, and has been shown experimentally to be valid for regular and random band models for overlapping gases [Goody (1964)]. However, it is not obvious that the same holds even at the broadband flux-emissivity level. As discussed in chapter 2 whenever a product of broadband-flux transmssivities is involved, there is the possibility of a 'band cross-talk' where the energy from one band is attenuated by the

absorption coefficient of another band. In this chapter, we will assume the spectrum of aerosol particles to be gray. This is a reasonable approximation for solid particle, as their spectrum is relatively smooth function of the wavelength when compared to the gases and the approximation becomes progressively better for mixtures of differently sized particles (since the average over the particle size distribution further smoothens the wavelength dependence). With this assumption, it can be shown that the transmssivity of the mixture is the product of component transmissivities even at the broadband level. One may therefore write the broadband transmissivity in an aerosol cum water-vapor-laden atmosphere as

$$\tau^f(u) = \tau^f_{wv}(u)\tau_{aerosol}(u) \tag{5.39}$$

Having done this, one can write down the flux divergence for a black surface as follows:

$$\frac{dF(u)}{du} = -\int_0^u \frac{d\tau^f(u-u'))}{du'}\frac{d}{du'}[\sigma T^4(u')]du' + \sigma T^4(u_t)\frac{d\tau^f(u_t-u)}{du} - \int_u^{u_t}\frac{d\tau^f(u'-u)}{du'}\frac{d}{du'}[\sigma T^4(u')]du', \tag{5.40}$$

Here, $\epsilon^f(u)$ includes the contributions of both water vapor and aerosol. The derivative of the flux-emissivity may be obtained using $\frac{d\epsilon^f(u)}{du} = -\frac{d\tau^f(u)}{du}$:

$$\frac{d\tau^f(u)}{du} = \tau_{aerosol}(z)\frac{d\tau^f_{wv}(u)}{du} + \tau^f_{wv}(u)\frac{d\tau^f(z)_{aerosol}}{dz}, \tag{5.41}$$

with $\tau_{aerosol}(z) = \mathrm{e}^{-\int_0^z \alpha(z')dz'} = \mathrm{e}^{-\int_0^z A\alpha_h n(z')dz'}$ In terms of water vapor emissivity, the above equation can be written as:

$$\frac{d\epsilon^f(u)}{du} = \tau_{aerosol}(z)\frac{d\epsilon^f_{wv}(u)}{du} - (1-\epsilon^f_{wv}(u))\frac{d\tau^f_{aerosol}(z)}{dz}, \tag{5.42}$$

The above can be written as

$$\frac{d\epsilon^f(u)}{du} = \tau_{aerosol}(z)\frac{d\epsilon^f_{wv}(u)}{du} + \alpha(z)\tau_{aerosol}(z)(1-\epsilon_{wv}(u)), \tag{5.43}$$

which can be reduced to

$$\frac{d\epsilon^f(u)}{du} = \tau_{aerosol}(z)\dot{\epsilon}(0)\left[\frac{d\hat{\hat{\epsilon}}^f_{wv}(u)}{du} + \zeta_0\hat{\alpha}(z)(1-\epsilon_{wv}(u))\right], \tag{5.44}$$

where ζ_0 is the dimensional parameter defined earlier in the context of obtaining the equilibrium LTM profile in chapter 4 and given by $\zeta_0 = \frac{f_w Q_{ext} A n(0)}{[(1-f_w)\rho_w(0)\dot{\epsilon}^f_{nw}(0)]}$. The non dimensional energy equation is

$$\frac{\partial\theta}{\partial t} = \mu_1\frac{\partial^2\theta}{\partial z^2} - \frac{1}{4A\alpha_h n(0)H}\frac{\partial F_z}{\partial z}. \tag{5.45}$$

The relevant non dimensional parameters that govern NBL evolution are the Ramdas-Zdunkowski (R_f), ζ_0 (which measures the relative magnitude of aerosol cooling and heating by water vapor), μ_1 (ratio of the radiative to conductive time scales in air) and the optical thickness of the concentrated aerosol layer ($A\alpha n(0)H$). The analog μ_1 for the surface does not

enter the formulation here, since the ground temperature is specified as a function of time.

The initial and boundary conditions for the simulation are given by:

1. The temperature profile is assumed to be an adiabatic lapse-rate profile at the initial instant of time. Hence, $T(z,0) = T_{g0} - \Gamma z$ where Γ is the specified lapse-rate, and here, it is assumed to be $9.8\,Kkm^{-1}$, corresponding to the dry adiabatic lapse-rate. The non-dimensional form is $\theta(z,0) = -\frac{\Gamma T_{g0}}{H}$. Since the specified lapse-rate is small in relation to typical near-surface temperature gradients [Mukund *et al.* (2013)], on the scale of the Ramdas layer, the initial state is virtually isothermal. As argued before, since there is an intrinsic cooling mechanism associated with the lowermost air layers, one should nevertheless be able to predict the emergence of an LTM-type profile

2. The variation of ground temperature with time is specified as $T_g(0,t) = T_{g0} - \beta\sqrt{t}$. The non-dimensional form is $\theta(0,t) = \frac{R_f T_g}{\Delta T_1}\sqrt{t}$. To begin with, we simulate the temperature profiles over high R_f surfaces. In the previous section, it was shown that the above simplified boundary condition remains a good approximation for times of $O(R_f^2)$. For instance over concrete, with $R_f = 37$, and for a radiative time scale of 10 s, the approximation is valid up to $2\frac{1}{2}$ hours; the β value for concrete $1.5\,\mathrm{hr}^{\frac{-1}{2}}$. Then, to simulate the evolution of the temperature profile over other surfaces with smaller values of R_f we specify the ground temperature obtained using the Newtonian cooling approximation in section 5.4. Although it doesn't include the radiative role of water vapor, it serves as a better estimate than specifying β, since it includes the variation of net radiative flux as a function of time, and more importantly, the conduction among air layers. The full air-soil coupled problem, with both the heterogeneous aerosol medium and water vapor, is beyond the scope of the study presented here.

3. The temperature gradient at the top of the domain (in the present simulation the height of the domain h is fixed at 5 km) is specified to be the adiabatic lapse-rate, that is, $\frac{\partial T(h,t)}{\partial z} = -\Gamma$ and the non dimensional form is $\frac{\partial T(\frac{h}{H},t)}{\partial z} = -\frac{\Gamma T_{g0}}{H}$

The integro-differential equation, resulting from using the flux-emissivity formulation to calculate the radiative flux divergence in the energy equation, is solved numerically using the Method of lines which was described earlier. In the following section, we first present the role of water vapor alone (which is uniformly distributed on the relevant length scales) in establishing the structure of the NBL in the lowest meters. Then, in section 5.5.2 we include the role of aerosols.

5.5.1 The homogeneous NBL - Role of Water vapor

In this section, we present the results for a homogeneous water-vapor-laden atmosphere. As will be seen below, the cooling rate of a water-vapor-laden atmosphere is small, and hence, the ground cools faster than the air layers, leading to an inversion profile. The emissivity of the water-vapor-laden atmosphere is obtained from that for an aerosol-laden-atmosphere given earlier with $\tau_{aerosol} = 1$. To validate the code, initial simulations were done with water vapor alone over a black surface. These are compared with earlier results obtained using the VSN

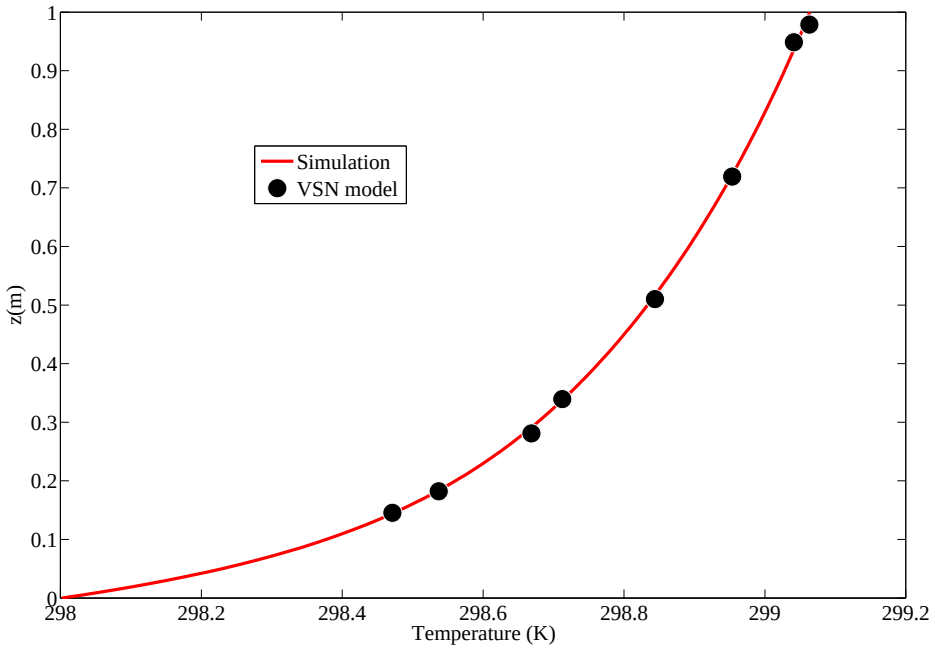

Figure 5.19: Comparison of the temperature profile predicted by our code with that obtained from simulation of the VSN model [Narasimha & Vasudevamurthy (1995)] for the physical parameters $\epsilon_g = 1$, $\beta = 2\,K\mathrm{hr}^{\frac{-1}{2}}$ and the water vapor mixing ratio is $q = 0.005$, at time t = 1 hr.

model described in chapters 2 and 4. The comparison is restricted to the temperature profile over a black surface, in which case there won't be any cross-talk error and the associated spurious cooling contribution. The comparison is for the following parameters: $\epsilon_g = 1$, $\beta = 2\,K\mathrm{hr}^{\frac{-1}{2}}$ and the water vapor mixing ratio $q = 0.005\,kgkg^{-1}$ [2]. The comparison of the temperature profiles is shown in figure 5.19 at a post-sunset time of 1 hour. There is clearly good agreement between the results obtained from the present code and those of Narasimha & Vasudevamurthy (1995).

We now study the role of water vapor on NBL evolution with the intent to understand the role of different parameters like β and ϵ_g on the temperature and cooling-rate profiles. First, for the set of parameters chosen above, the results of a simulation for a 9-hour period are shown. The temperature profiles appear in figure 5.20a and the corresponding radiative cooling-rate profiles are shown in figure 5.20b. In this case, the surface cools faster than the air layers and there is always an inversion profile. The radiative cooling-rate profile indicates, at the initial instant that there is a cooling at all levels and this is associated with the radiative exchanges between the lowermost air layer with the overlying colder air layers. Then, as the ground cools faster than the air layers, an inversion layer emerges, and there is a transition from a cooling at greater heights to a radiative warming in the lowest centimeters arising from the radiative exchanges in the opaque bands of the water vapor spectrum [Fleagle (1955), Edwards (2009a); see discussion in chapter 2]. Both the height corresponding to this transition, and that corresponding to

[2] The inhomogeneity due to variation of water vapor density is included via the definition of u. As discussed in chapter 2 the variation of water vapor density is assumed to be an exponential with a scale height of 2.7 km. The water vapor mixing ratio at the surface is assumed to be $q = 0.005\,kgkg^{-1}$

the maximum cooling rate, increase with time. The qualitative nature of the above results is consistent with the recent numerical simulations of the NBL by Edwards (2009a).

Role of surface emissivity(ϵ_g)

As discussed in chapter 2, a few studies which have attempted to study the role of surface emissivity, using a broadband flux-emissivity model, have (erroneously) exaggerated its effect on the cooling-rate profile near the ground (Garratt & Brost (1981);Savijärvi (2006)). Physical arguments show that, for an inversion layer profile, when the surface emissivity is reduced, there should be a moderate increase in the radiative warming [Edwards (2009a) and see chapter 2]. Based on the correct reflected flux obtained in chapter 2, we carried out the simulation for the NBL development over a gray surface. The ground cooling rate is again fixed at $\beta = 2\,K\mathrm{hr}^{\frac{-1}{2}}$ and the surface emissivity is taken to be 0.9. Fixing the ground temperature allows one to isolate the effect of surface emissivity on the temperature of the air layers without additional complications arising due to its indirect role via the surface energy budget. The temperature profiles and the corresponding radiative cooling-rates are shown in figures 5.21a and 5.21b, and show a warming trend with decreasing surface emissivity. This confirms our previous analysis in chapter 2 where this warming trend was obtained for the case of an inversion characterized by a simple exponential inversion profile over ground at a fixed temperature, and also agrees with the findings of Edwards (2009a) and Hoch (2005).

Role of the (surrogate) surface cooling-rate (β)

We now present the results for the surface at a fixed temperature. When the ground temperature is fixed ($\beta = 0$) the air layers can cool to space (that is, the upward emission from the fluid element is not compensated by the downward emission of the overlying atmospheric column). The results of a simulation, with $\beta = 0$, starting from an initial lapse-rate profile, are shown in figures 5.22a and 5.23a for $\epsilon_g = 1$ and 0.8, respectively. It may be seen that the temperature decreases with height in contrast to the cases already considered. The temperature change at 1 m, after 9 hours of simulation, is only around 0.2 K! The corresponding radiative cooling-rate profiles are shown in figures 5.22b and 5.23b. The near-surface cooling-rates that result are $O(10^4)$ times smaller than the cooling-rate of $O(1\,Ks^{-1})$ observed by Mukund *et al.* (2013). The cooling-rate profiles resemble the mirror images of the profiles obtained for an inversion layer (where the temperature increases with height) with there being a transition from warming at greater heights to cooling near the ground. Most importantly, there is no preferential cooling near the ground for any value of the surface emissivity, with the higher layers of air always cooling at a faster rate consistent with the cooling-rate profiles obtained. A decrease in ϵ_g increases the cooling rate at all levels (due to downwelling radiation from overlying colder layers forming a part of the reflected flux) although there is no qualitative change in either the temperature or cooling-rate profiles.

In conclusion, a preferential cooling of the air layers cannot occur in a homogeneous water-vapor-laden atmosphere regardless of the surface emissivity or surface cooling-rate. The above results are consistent with physical arguments given in chapters 2 and 4 for a time independent scenario. The role of the suspended aerosol particles, in the origin of the Ramdas layer is discussed in the next section.

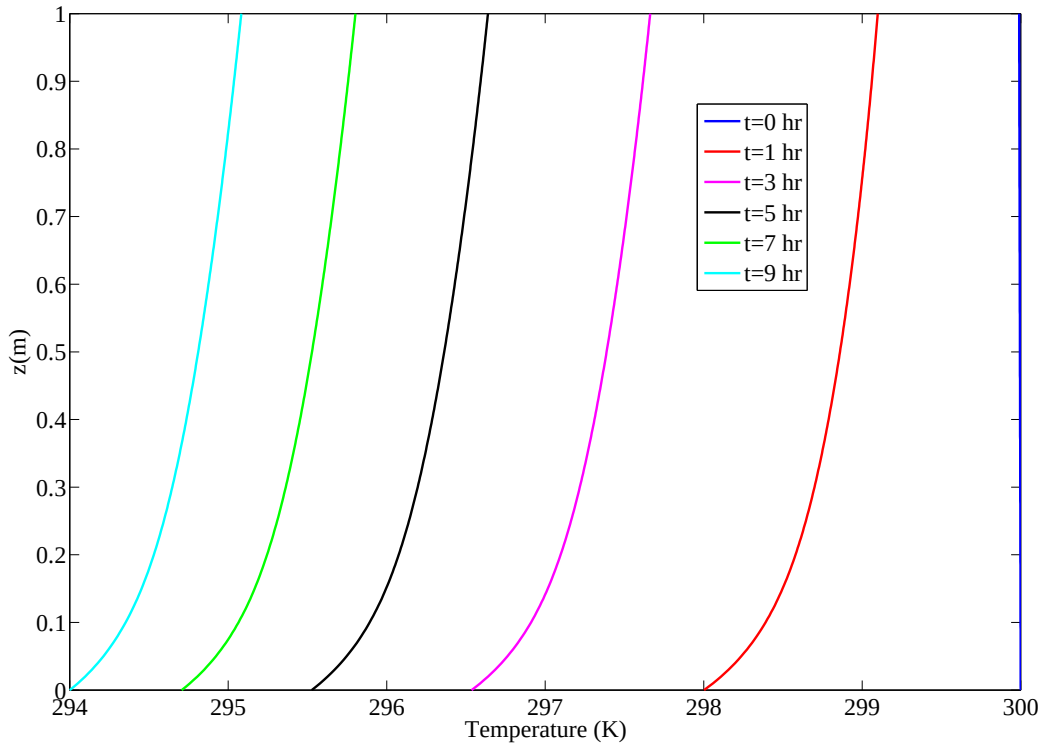

(a) Temperature profile

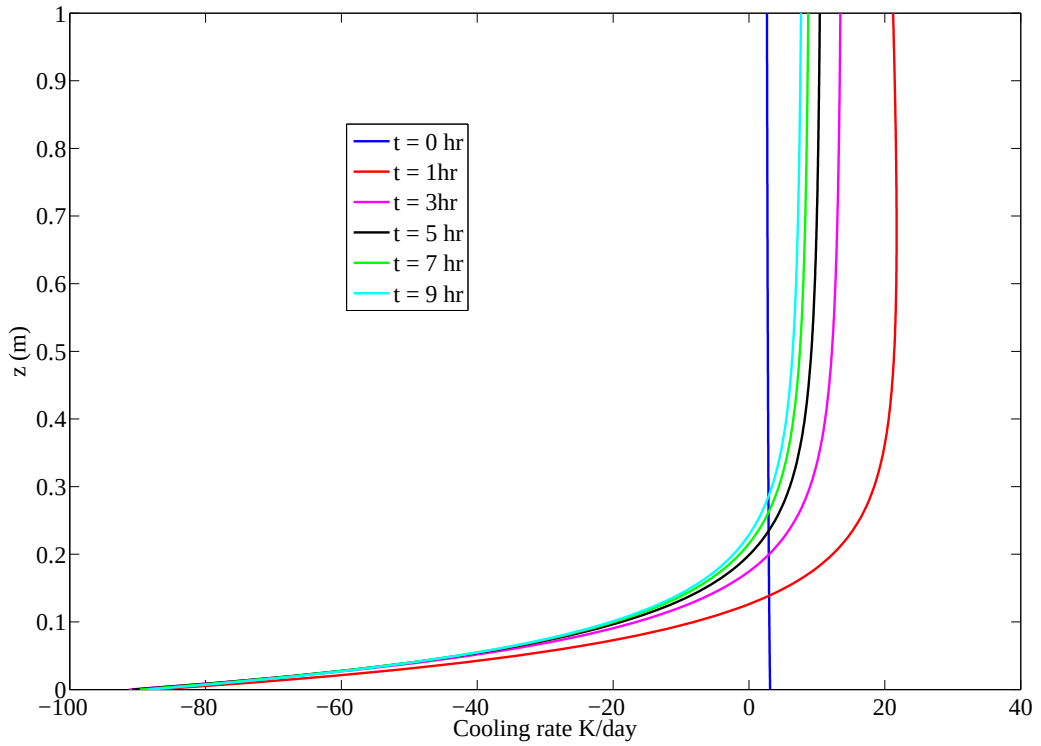

(b) Radiative cooling rate

Figure 5.20: The evolution of the lowest meter of the stable NBL starting from an adiabatic lapse-rate profile. Plot (a) shows the temperature profiles at different instants, and plot (b) shows the corresponding radiative cooling-rate profiles for $\epsilon_g = 1$, $\beta = 2\,K\mathrm{hr}^{\frac{-1}{2}}$ and the water vapor mixing ratio specified to be $q = 0.005$.

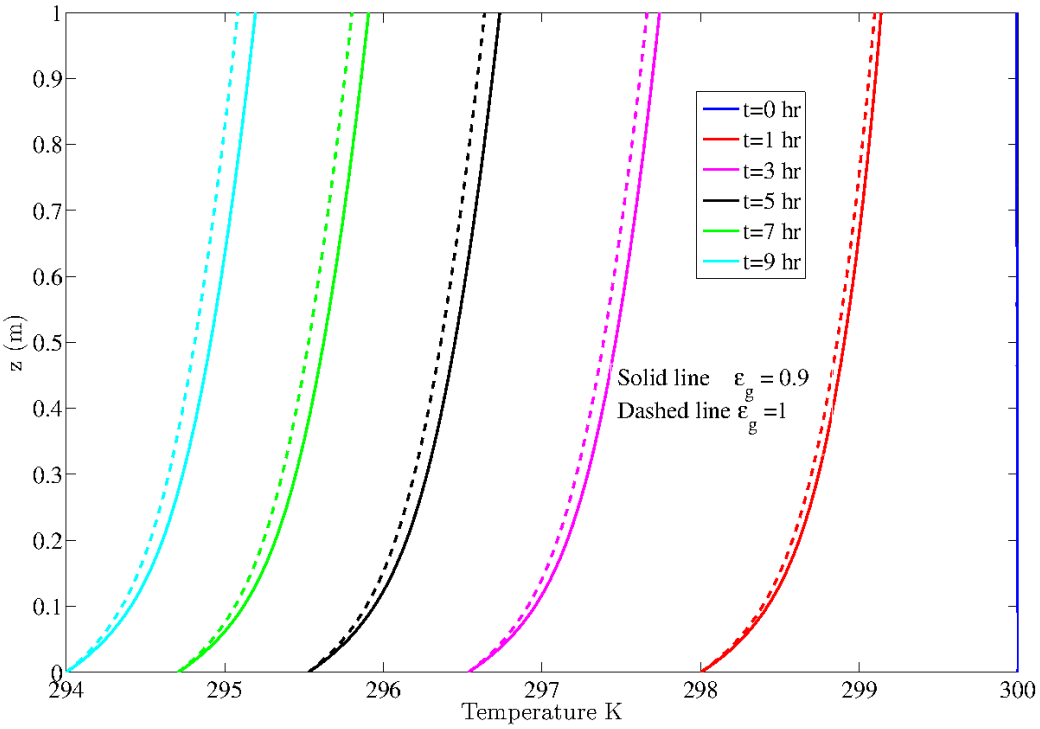

(a) Temperature profile

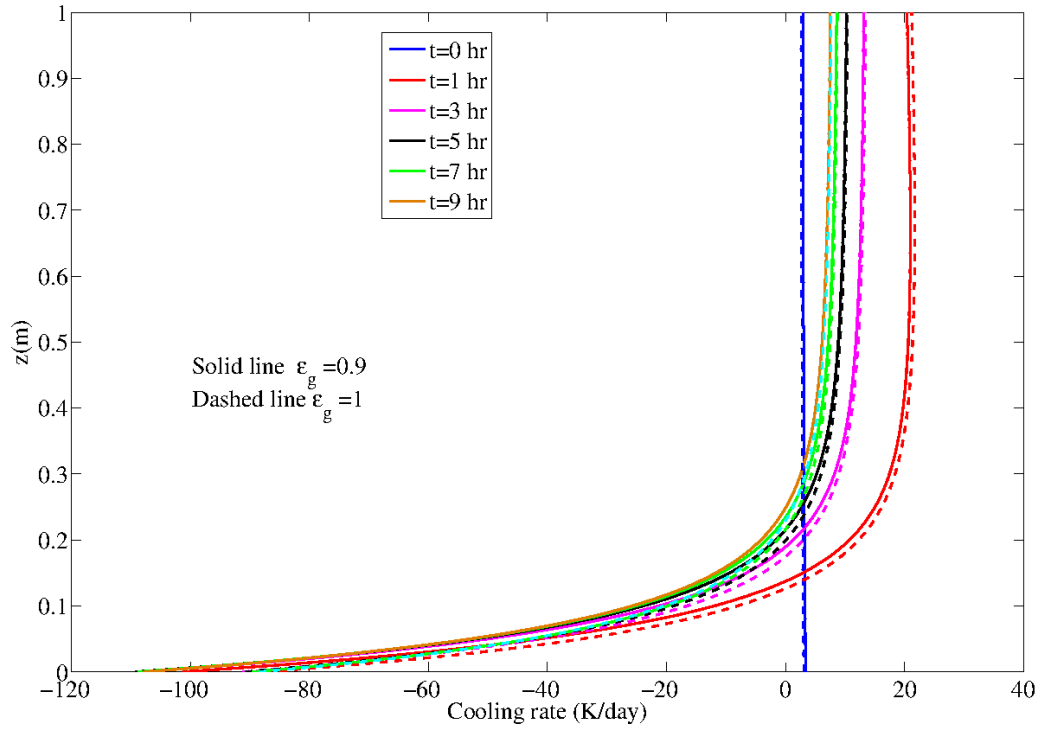

(b) Radiative cooling rate

Figure 5.21: The evolution of the lowest meter of the stable NBL starting from an adiabatic lapse-rate profile for a gray surface with emissivity $\epsilon_g = 0.9$, and ground cooling-rate taken to be 2 $\text{Khr}^{\frac{-1}{2}}$. Plot (a) shows the temperature profiles at different instants of time, and the corresponding radiative cooling-rate profiles are shown in plot (b). The dashed lines correspond to that of the black surface.

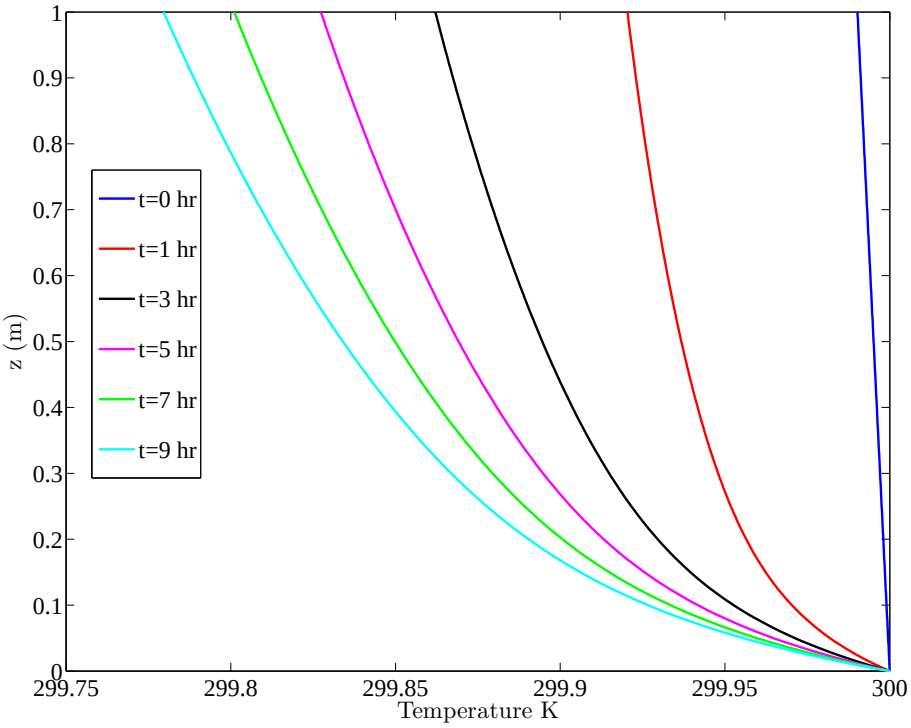

(a) Temperature profile

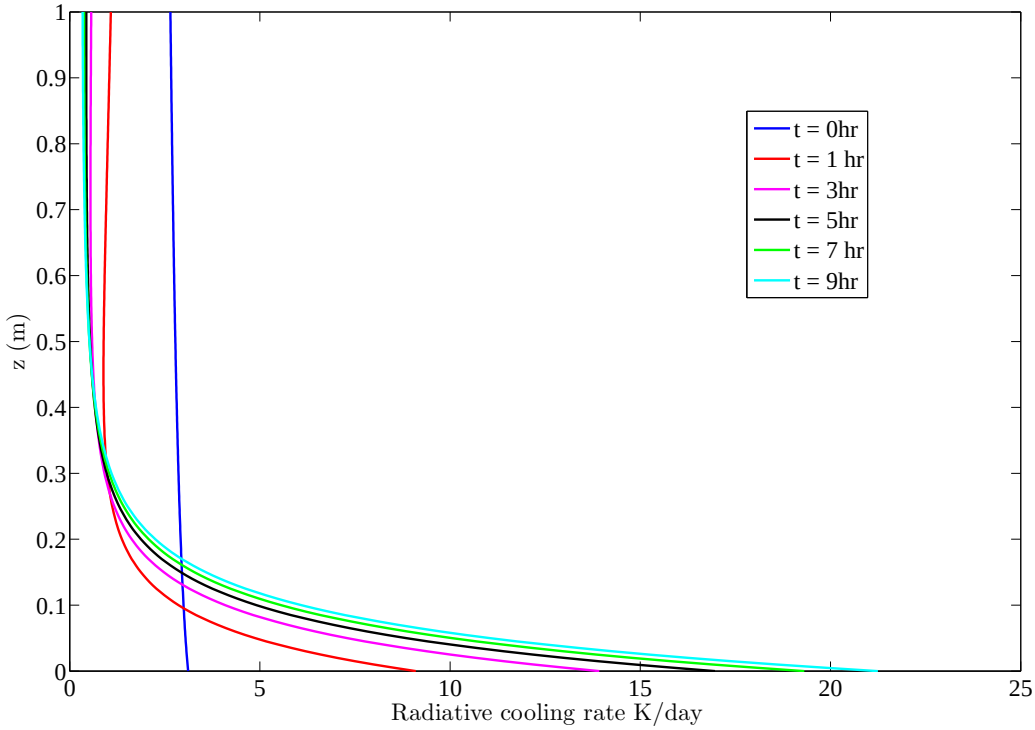

(b) Radiative cooling rate

Figure 5.22: The evolution of the lowest meter of the stable nocturnal boundary layer starting from an adiabatic lapse-rate profile. Plot (a) shows the temperature profiles at different instants, and plot (b) shows the corresponding radiative cooling-rate profiles for $\epsilon_g = 1$, $\beta = 0\,K\mathrm{hr}^{\frac{-1}{2}}$ (fixed ground temperature) and the water vapor mixing ratio specified to be $q = 0.005$.

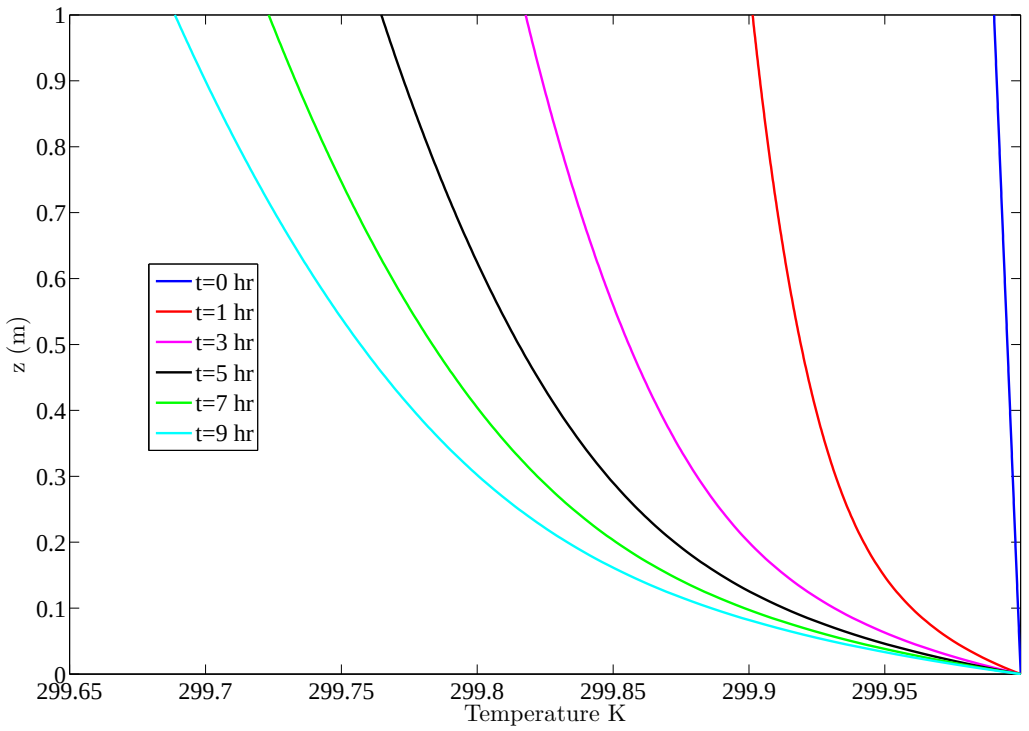

(a) Temperature profile

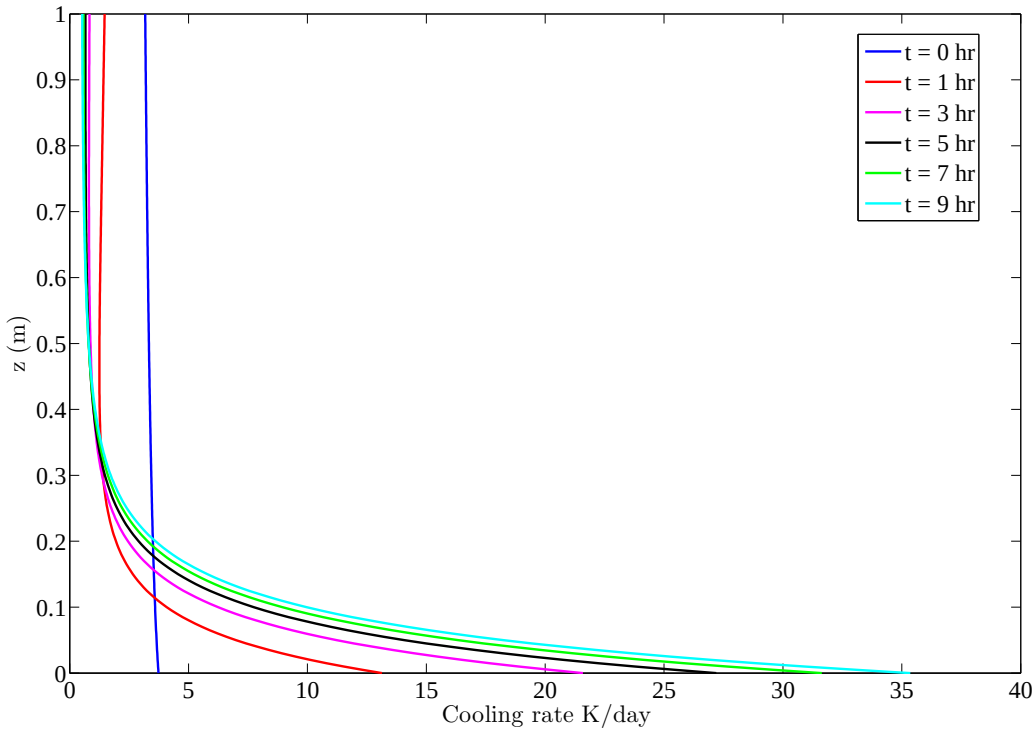

(b) Radiative cooling rate

Figure 5.23: The evolution of the lowest meter of the stable nocturnal boundary layer starting from an adiabatic lapse-rate profile. Plot (a) shows the temperature profiles at different instants, and plot (b) shows the corresponding radiative cooling-rate profiles for $\epsilon_g = 0.8$, $\beta = 0\,K\mathrm{hr}^{\frac{-1}{2}}$ (fixed ground temperature) and the water vapor mixing ratio specified to be $q = 0.005$.

5.5.2 Role of the heterogeneity (aerosols)

In the previous section, we have shown that water vapor alone cannot produce an LTM in a night-time atmosphere, and that aerosol particles are therefore necessary to explain the origin of the Ramdas layer. In this section, we present simulations including the radiative forcing of the aerosol heterogeneity, and show that an LTM-type profile emerges above a critical aerosol concentration (corresponding to a threshold value of $R_f \approx 8$). Here, the ground cooling-rate is taken to be 1.5 $\text{Khr}^{\frac{-1}{2}}$ and the water vapor mixing ratio is taken to be 0.005 in all the simulations. Further, the surface emissivity is taken to be unity (black surface) to begin with. For the proof-of-principle calculations presented here, we use a simple exponential to model the aerosol number density profile with the scale-height being fixed at 2 cm, and only the concentration of the particles at the ground being varied. This is equivalent to varying the fastest radiative relaxation time, and thereby, changing the near-surface air cooling-rate which then alters the Ramdas-Zdunkowski factor (ground cooling rate is fixed for most of the results presented here; for purposes of comparison with the small-ζ_0 theory in chapter 4, a few results will be given for ground at a fixed temperature). Relevant physical parameters like the aerosol concentration at the ground, the corresponding relaxation time scale of the lowermost air layer, the optical thickness based on the scale-height, are tabulated in table 5.3 for the different cases considered.

Optical thickness	τ_{rad} (s)	**Number density at ground** (particles m^{-3})	R_f
2×10^{-5}	183813	3×10^{8}	0.8
2×10^{-3}	1838	3×10^{10}	8
2×10^{-2}	183	3×10^{11}	25

Table 5.3: The aerosol-related parameters which are used in the simulations

When the medium is transparent, that is, for an optical thickness is $\approx 10^{-5}$, $R_f = 0.8$ the effect of aerosol particles in determining the temperature profile is very small as shown in figure 5.24a. But, one can see their effect in the radiative cooling-rate profiles in figure 5.24b. Aerosol particles cool the air layers throughout the domain leading to displaced cooling-rate profiles in relation to those for a water-vapor-laden medium.

Next, the concentration of the particles is increased corresponding to an aerosol layer with an optical thickness of 2×10^{-3}, $R_f = 8$. The corresponding temperature profiles in figure 5.25a show the emergence of a weak minimum. The radiative cooling-rate profiles, plotted in figure 5.25b, show a large cooling near the ground due to the dominance of the aerosol contribution (the water vapor contribution remains similar in magnitude to that in figure 5.24b). The initial development demonstrating the inversion-LTM transition is shown in figure 5.26. The figure clearly shows that the aerosol layers cool faster than the ground resulting in an isothermal layer at around 2 s; further cooling results in an LTM-type profile. It should be emphasized here that there arises an LTM-type profile even over a black surface in sharp contrast to the prediction

of the VSN model for a homogeneous water-vapor-laden atmosphere. A further increase in the aerosol concentration (optical thickness) increases the intensity of the minimum. This is seen in the temperature and radiative cooling-rate profiles in figure 5.27a and 5.27b which correspond to an optical thickness of 0.02 and an $R_f \approx 25$. The short-time evolution of the temperature profile in figure 5.28 shows that the LTM occurs earlier and this is consistent with the above results obtained earlier using Newtonian cooling approximation (high R_f corresponding to shorter crossover time).

Role of ground cooling rate

In this section, as done before in section 5.5.1, we fix the ground temperature and allow the aerosol and water-vapor-laden atmosphere to evolve starting from an initial lapse-rate profile (thus $R_f = \infty$ for these calculations). The resulting temperature profiles are shown in figure 5.29a. There is a preferential cooling near the ground and an LTM-type profile with an intensity of 2 K occurs after 9 hours. The corresponding radiative cooling-rate profiles are shown in figure 5.29b. The reason for the LTM intensity being small is the conductive warming to the ground which acts as a brake to the cooling mechanism. It is of interest to compare these temperature profiles to the approximate theory developed in chapter 4 for the equilibrium LTM-profile, with ground at a fixed temperature. The profile in figure 5.29a correspond to $\zeta_0 \gg 1$, however. Thus, in the interests of a comparison, we carry out simulations with T_g fixed and for a much smaller aerosol concentration. Now, the small ζ_0 theory analysis requires the cumulative emission from the atmosphere (modeled via T_{sky}) as an input is obtained, for the aerosol concentration profile under consideration. The value of T_{sky} is obtained from the temperature profiles in the simulations by calculating the surface downwelling flux corresponding to each of these profiles. The change in the downwelling radiation with time is small, and thus T_{sky} is quite insensitive to the precise choice of this time instant. In figure 5.30 a comparison is given between a simulated temperature profile at 1 hour (starting from an isothermal atmosphere) and the corresponding prediction of the small-ζ_0 theory. The choice of time for the simulated profile is 1 hour because, for these times, the near-surface portion of the temperature profile appears to have relaxed to a quasi-equilibrium (note that this is not a true equilibrium, since the steady-state NBL would exhibit a monotonic variation of temperature with height). The simplistic theory predicts the general shape of the temperature profile, but there is a discrepancy in the intensity of the minima. This is because of modeling the opaque band emissivity $\epsilon^f_{nw}(u)$ as a simple exponential, which eliminates the radiative cooling contribution in the opaque bands at greater heights of $O(1)$ m.

Role of surface emissivity

Next, we varied the surface emissivity to see its effect on the temperature profile and the radiative cooling-rate. The optical thickness is taken to be 0.02 and $R_f = 25$. The temperature profiles and the corresponding cooling-rate profiles are shown in figures 5.31a and 5.31b. The reduction in surface emissivity leads to an increase in the intensity of the minima. This is consistent with the observation by Mukund *et al.* (2013) where an Aluminum foil was used to reduce the surface emissivity of concrete. Figure 5.31b shows an increase in the cooling-rate near the ground for a decrease in $\epsilon_g = 0.8$. This is due to the reflected component which consists of downwelling colder radiation from the overlying colder layers. There is a transition to radiative warming at

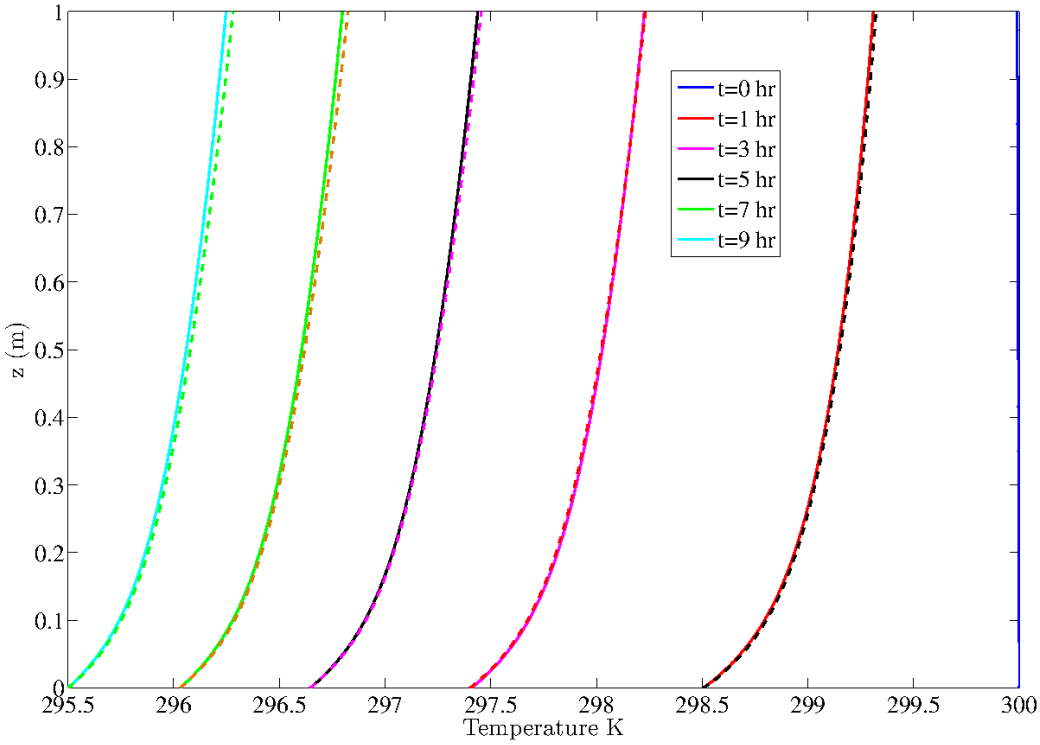

(a) Temperature profile

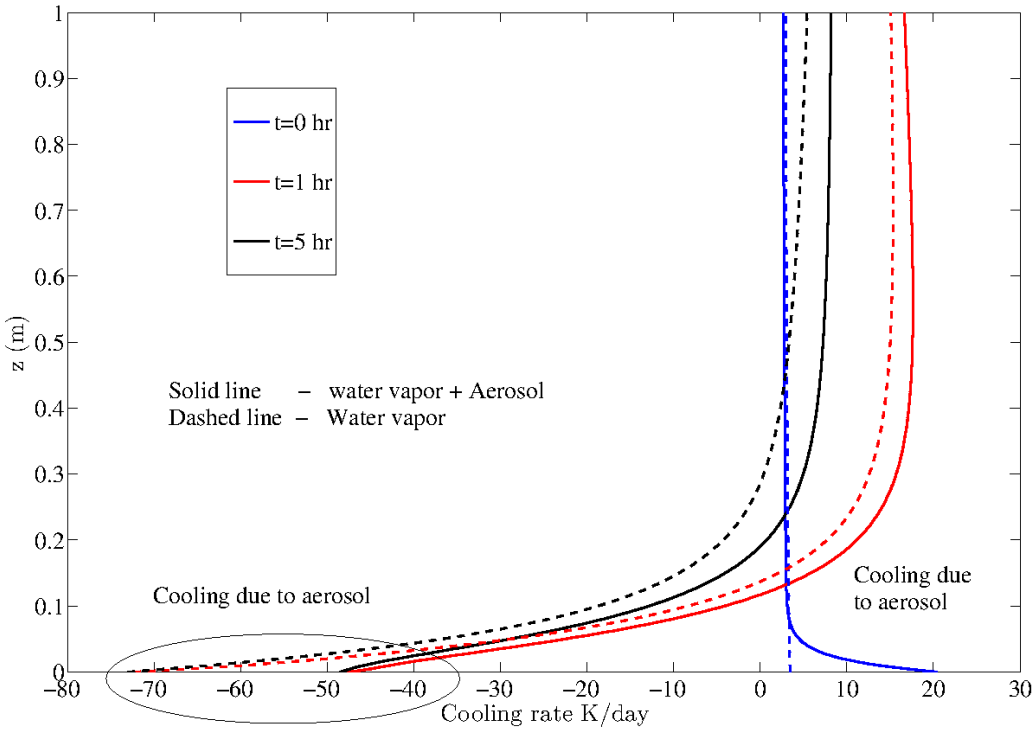

(b) Radiative cooling rate

Figure 5.24: The evolution of an LTM-type starting from an adiabatic lapse-rate profile for a surface emissivity $\epsilon_g = 1$, a ground cooling rate of $\beta = 1.5\,K\mathrm{hr}^{\frac{-1}{2}}$ and a water-vapor mixing ratio specified to be $q = 0.005$. The aerosol optical thickness is 0.00002, radiative relaxation time scale is 183813 s and $R_f = 0.8$. Plot (a) shows the temperature profiles at different instants, and plot (b) shows the corresponding radiative cooling-rate profiles. The dashed lines are the profiles obtained with water vapor alone as the participating medium.

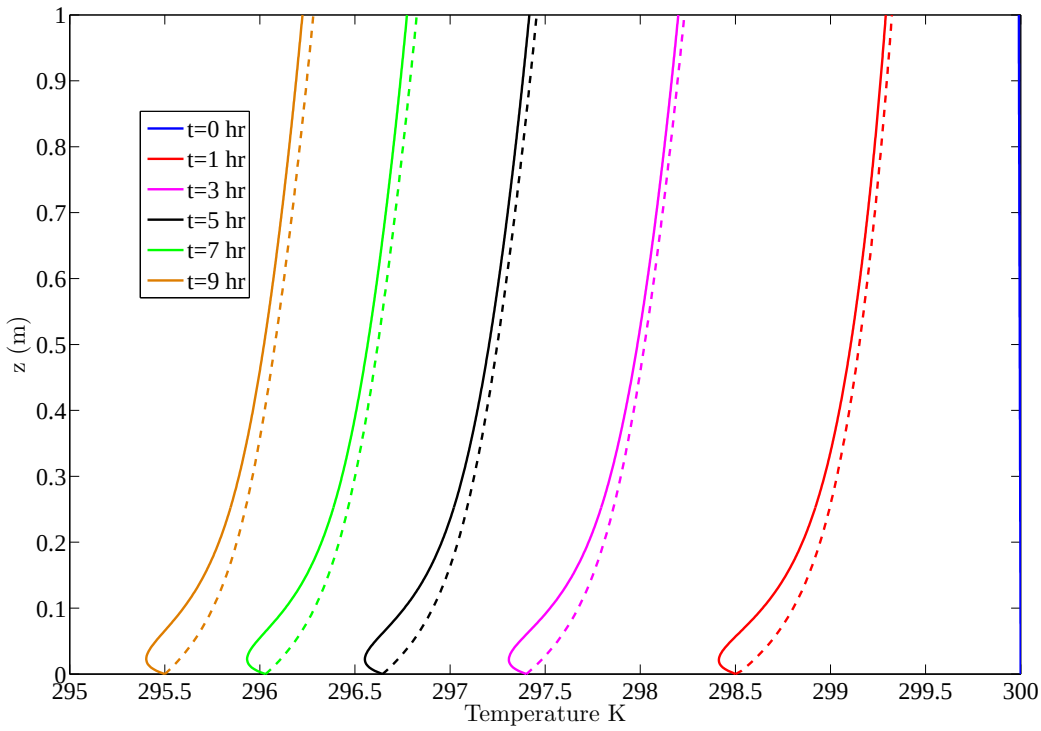

(a) Temperature profile

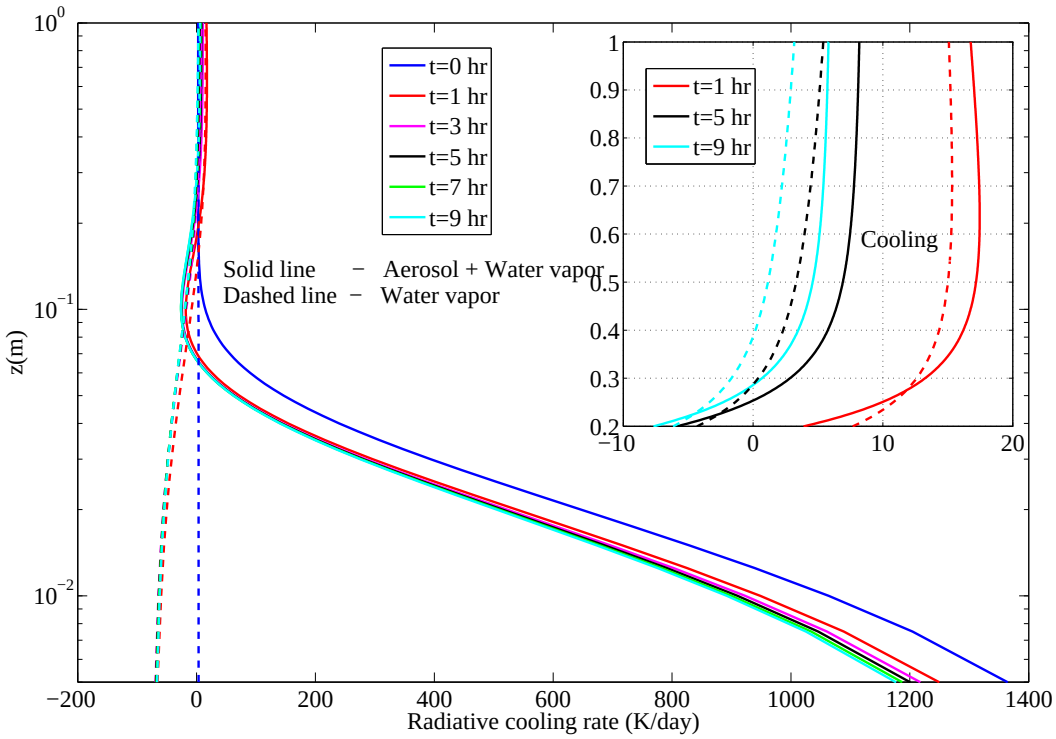

(b) Radiative cooling rate

Figure 5.25: The evolution of an LTM-type profile starting from an adiabatic lapse-rate profile for a surface emissivity $\epsilon_g = 1$, a ground cooling rate of $\beta = 1.5\,K\mathrm{hr}^{\frac{-1}{2}}$ and a water-vapor mixing ratio specified to be $q = 0.005$. The aerosol optical thickness is 0.002 and radiative relaxation time scale is 1838 s and $R_f = 8$. Plot (a) shows the temperature profiles at different instants, and plot (b) shows the corresponding radiative cooling-rate profiles. The dashed lines are the profiles obtained with water vapor alone as the participating medium.

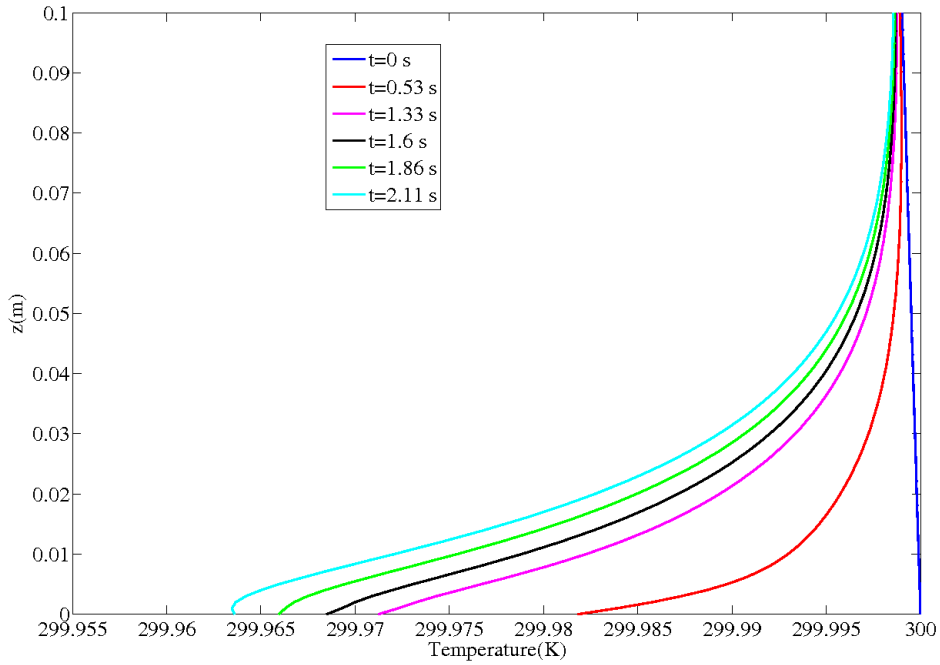

Figure 5.26: The short-time evolution leading to an LTM-type profile starting from an adiabatic lapse-rate profile for a surface emissivity $\epsilon_g = 1$, a ground cooling rate of $\beta = 1.5\,K\mathrm{hr}^{\frac{-1}{2}}$ and a water vapor mixing ratio specified to be $q = 0.005$. The aerosol optical thickness is 0.002 and radiative relaxation time scale is 1838 s and $R_f = 8$. The plot shows the transition from an initial inversion profile to an LTM-type profile.

greater heights due to opaque-band exchanges of the water vapor spectrum. The reduction in surface emissivity increases this radiative warming which is consistent with the previous results for the water-vapor-laden atmosphere.

5.6 Effect of water vapor on the evolution of temperature profile obtained using Newtonian cooling approximation

In this section, we present results, including the radiative forcing of suspended aerosol particles along with water vapor, but the surface temperature is now taken from the analysis in section 5.4.2, that uses the Newtonian cooling approximation for the aerosol-driven cooling, while including both the conductive exchanges between air layers and the variation of the net radiative flux with time. To get the ground temperature, we have to specify the brightness temperature of the entire atmosphere. The value T_{sky} is taken to correspond to the initial isothermal atmosphere. The ground temperature obtained in the above manner is specified as a boundary condition at the ground in the full simulation [3]. The simulation results are given for two R_f values, 16 and 1.4, which correspond to dry soil and foam respectively. The resultant temperature profile along with the Newtonian cooling approximation is presented in figure 5.32a and 5.32b.

[3]Though the absorption and emission by water-vapor-laden atmosphere is taken into analysis, the effect of water vapor on changing the surface atmosphere has been neglected. It is important to note that in the previous analysis using Newtonian cooling approximation (see 5.4.1), the downwelling radiation is assumed to be independent of time. However, this varies on account of the evolution of NBL.This effect may be rigorously incorporated via a fully coupled air-soil formulation.

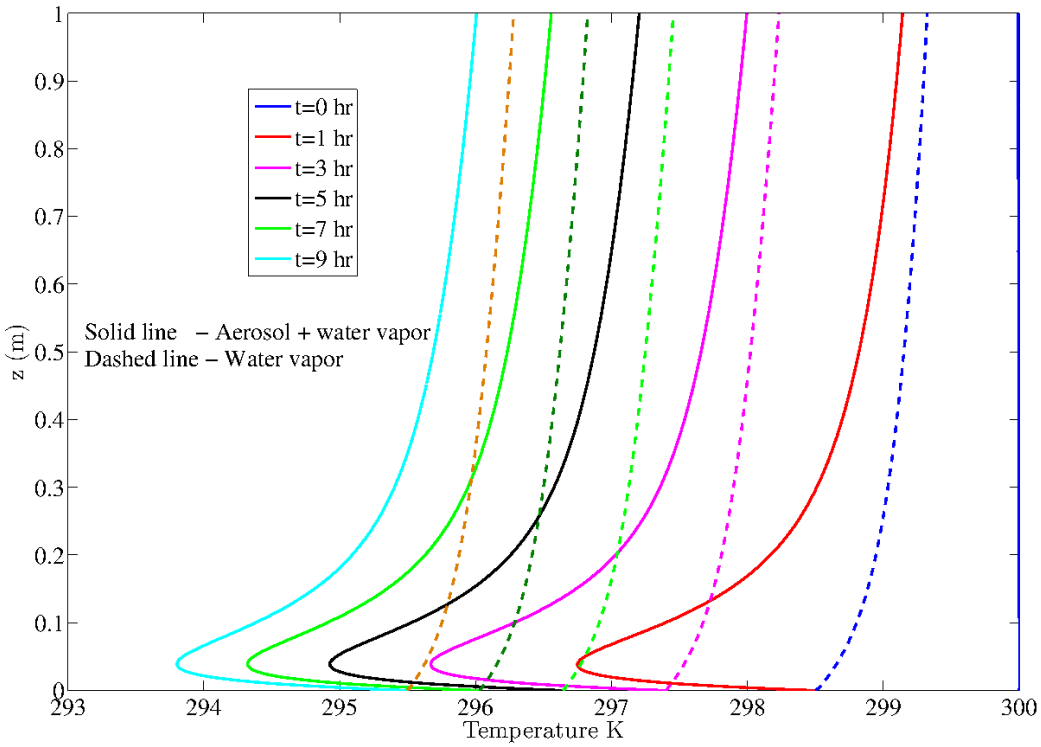

(a) Temperature profile

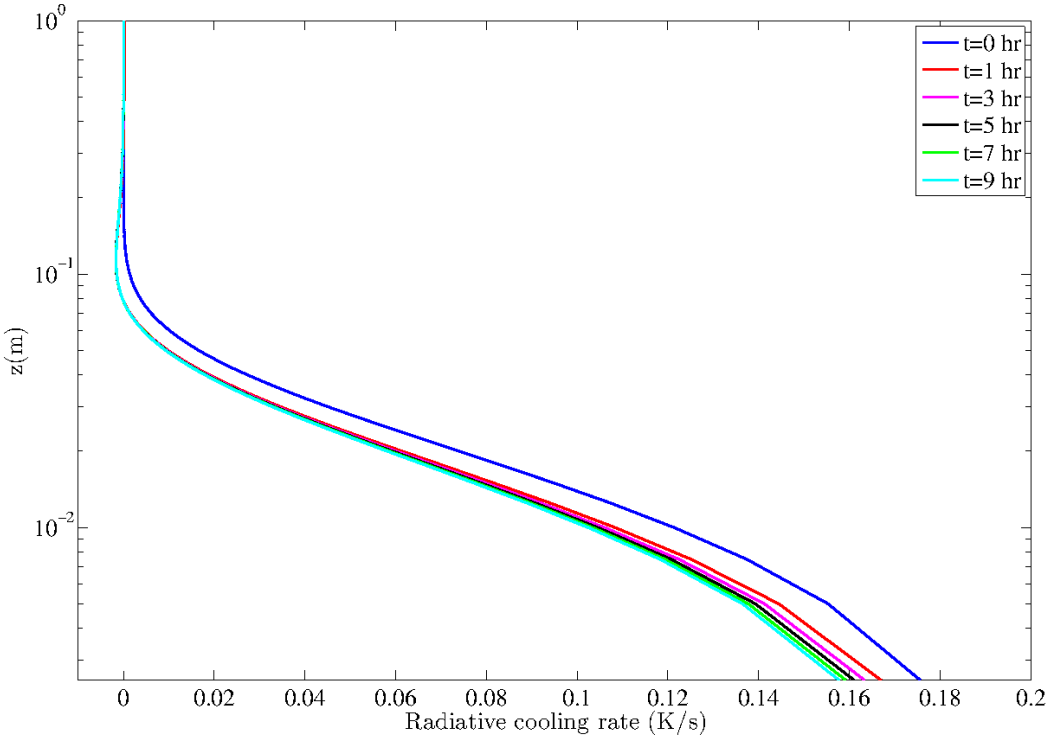

(b) Radiative cooling rate

Figure 5.27: The evolution of an LTM-type starting from an adiabatic lapse-rate profile for a surface emissivity $\epsilon_g = 1$, and ground cooling rate of $\beta = 1.5\,K\mathrm{hr}^{\frac{-1}{2}}$ and the water vapor mixing ratio specified to be $q = 0.005$. The aerosol optical thickness is 0.02, $R_f = 25$ and radiative relaxation time scale is 183 s and $R_f = 25$ Plot (a) shows the temperature profile at different instants, and plot (b) shows the corresponding radiative cooling-rate profiles. The dashed lines are the profiles obtained with water vapor as the participating medium and exhibit a monotonic variation in temperature with height.

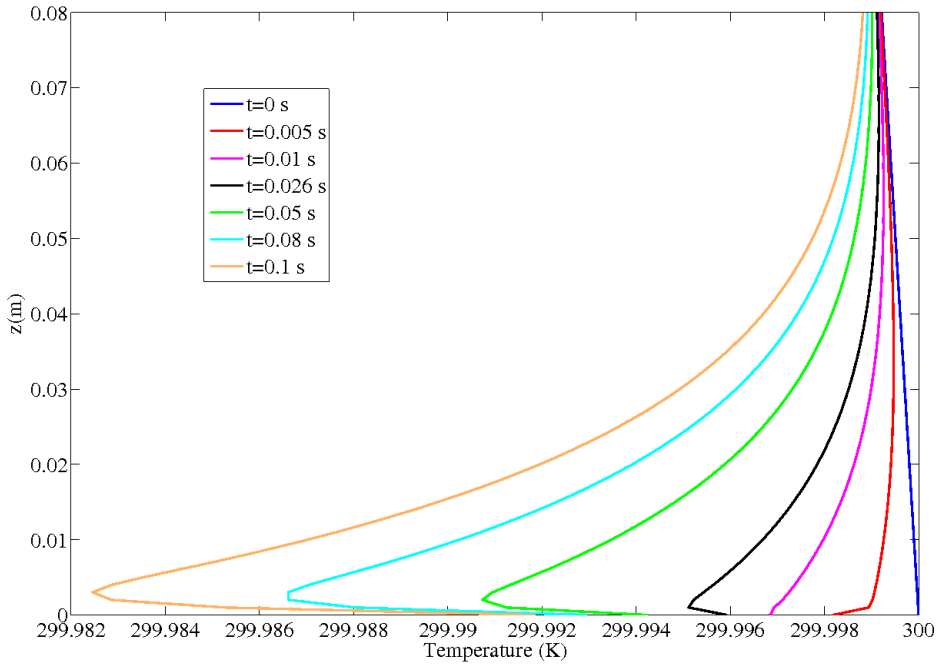

Figure 5.28: The short-time evolution, leading to an LTM-type profile starting from an adiabatic lapse-rate profile for a surface emissivity $\epsilon_g = 1$, a ground cooling rate of $\beta = 1.5\,K\mathrm{hr}^{\frac{-1}{2}}$ and a water-vapor mixing ratio specified to be $q = 0.005$. The aerosol optical thickness is 0.02, $R_f = 25$ and radiative relaxation time scale is 183 s Plot shows the transition from an inversion profile to LTM-type profile.

.

The predicted temperature profiles show warming effect of water vapor in the lowest meters of the NBL. In the Newtonian cooling approximation we haven't considered the direct effect of water vapor in altering the flux divergence profiles, but the effect of water vapor emission is included in estimating the brightness temperature T_{sky}. The warming effect arises because of the following reason. At the initial instant, ground always cools faster than the air layers and this leads to an inversion profile. The water vapor heats up the lowest layers in the strongly absorbing part of the spectrum and this results in a moderate warming. In the case of a foam surface, this warming can overwhelm the weaker minima obtained using the Newtonian cooling approximation.

5.7 Conclusion

In this chapter, we have presented numerical simulations that show the emergence of the Ramdas layer in a heterogeneous night-time atmosphere. To begin with, the coupled air-soil problem is solved in a simplified approximation by considering a concentrated layer of suspended aerosol particles close to the ground as the chief radiatively participating agent. The concentrated layer is assumed to be in the optically thin regime and modelled using a Newtonian cooling approximation. In the limit where one neglects the conduction among the air layers, it is shown that the nature of the temperature profile near the ground (either inversion or LTM-type) is governed by the Ramdas-Zdunkowski factor defined as the ratio of the air to surface cooling

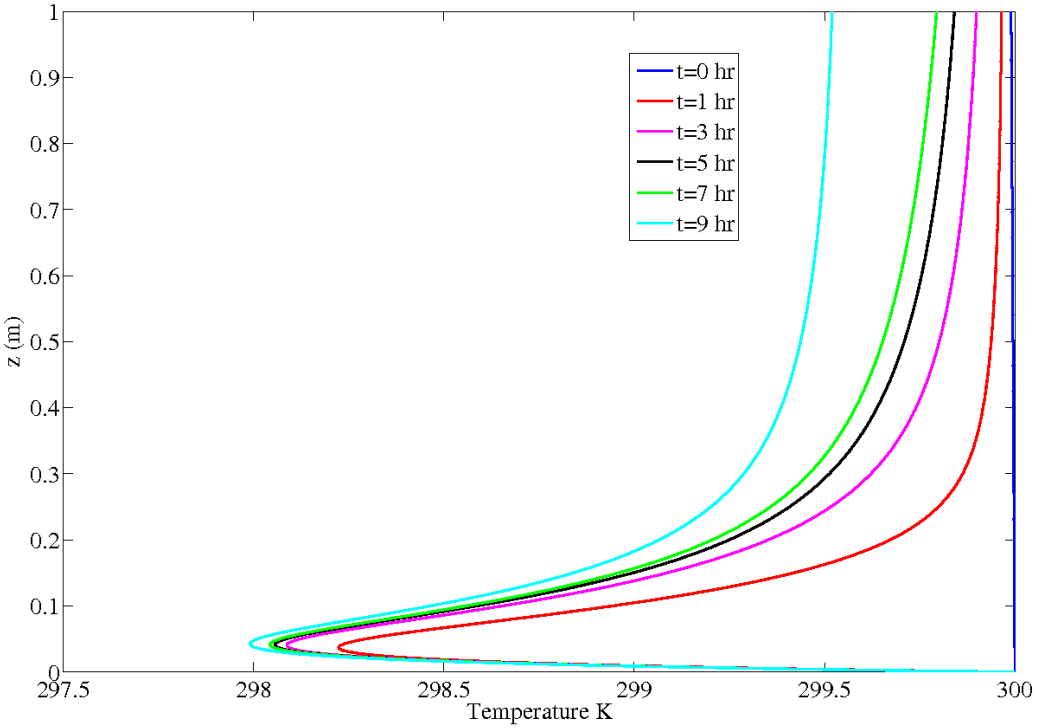

(a) Temperature profile

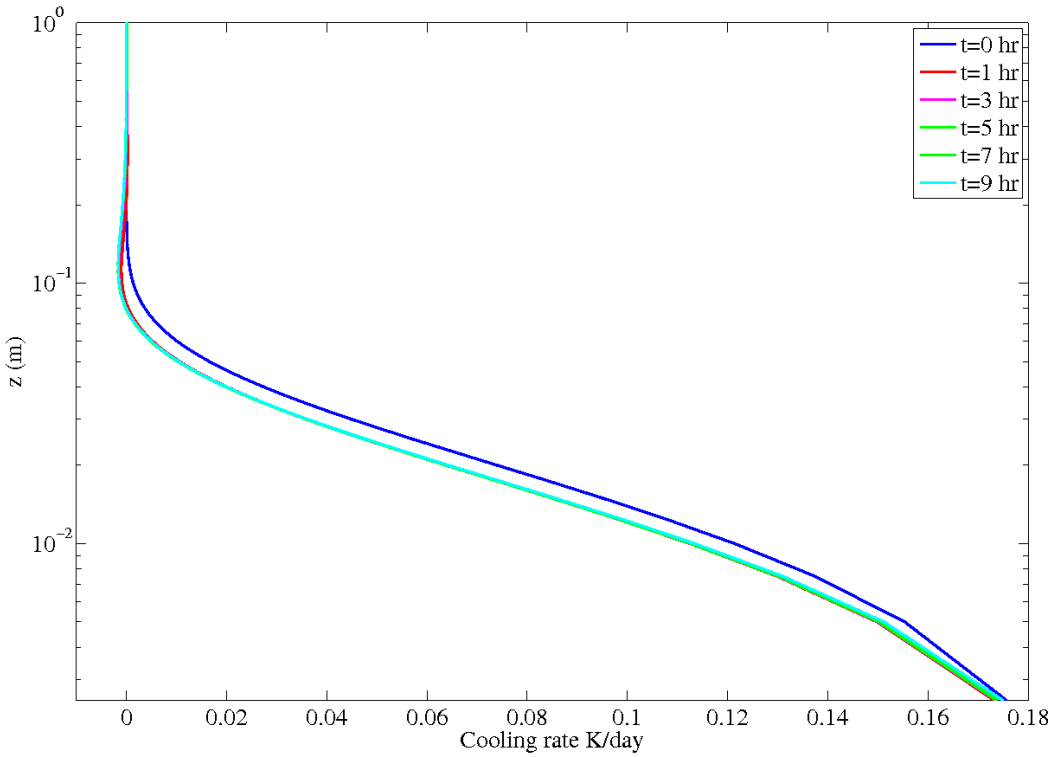

(b) Radiative cooling rate

Figure 5.29: The evolution of LTM-type profile starting from an adiabatic lapse-rate profile for a surface emissivity $\epsilon_g = 1$, a ground cooling rate of $\beta = 0\,K\mathrm{hr}^{\frac{-1}{2}}$ and a water-vapor mixing ratio specified to be $q = 0.005$. The aerosol optical thickness is 0.02, radiative relaxation time scale is 183 s and $R_f = \infty$. Plot (a) is the temperature profile at different instants and plot (b) shows the corresponding radiative cooling-rate profiles.

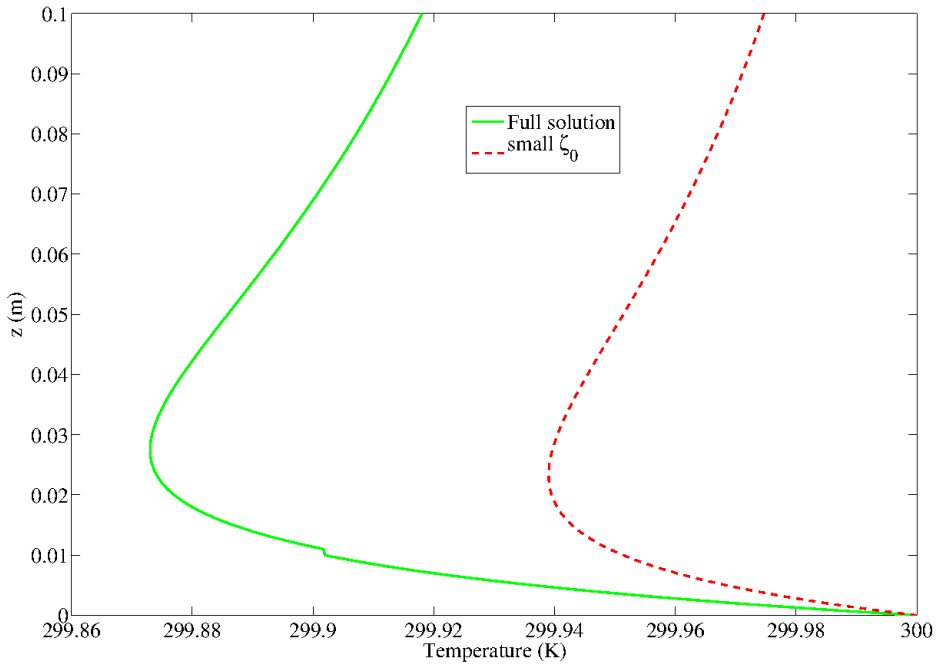

Figure 5.30: Comparison of the temperature profile obtained using a full numerical solution with ground temperature fixed for an exponential concentration profile, with a scale height of 1 cm and a relaxation time at the ground of 2000 s, with the small- ζ_0 analysis described in 4.6.2 in chapter 4. The estimated T_{sky} is 255 K and ζ_0 is 0.02.

rate. The role of water vapor alone in establishing the structure of the NBL as a function of the surface emissivity and the surface cooling rate is discussed. Importantly, it has been shown that water vapor cannot produce an LTM-type profile in a night-time atmosphere for any value of the surface emissivity or ground cooling rate. Full numerical simulations with both water vapor and aerosol particles have been carried out to determine the structure of the NBL. Above a critical $R_f \approx O(1)$, the simulations predict an LTM-type profile over a black surface. The intensity of the minimum increases with a decrease in the surface emissivity, which is consistent with the observations by Mukund *et al.* (2013).

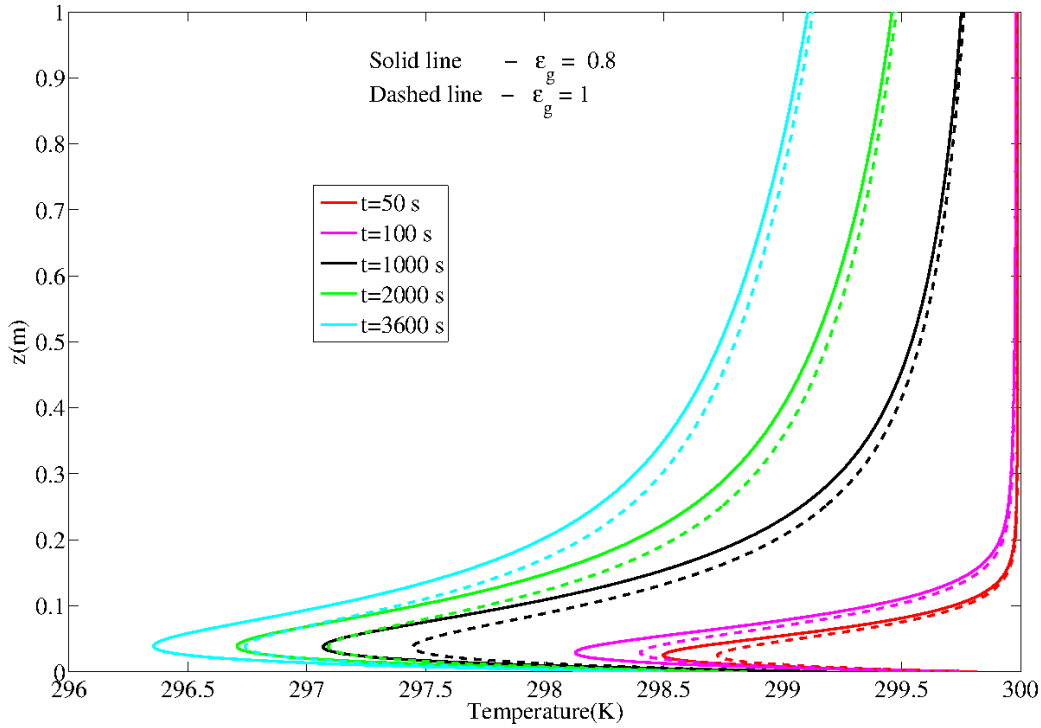

(a) Temperature profile

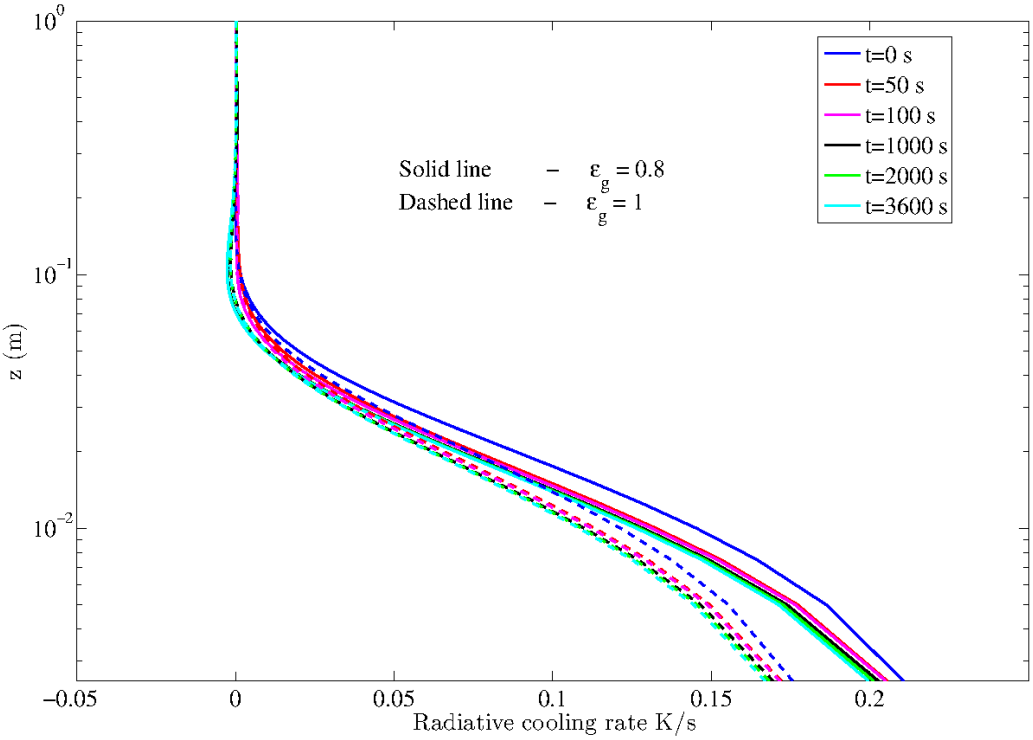

(b) Radiative cooling rate

Figure 5.31: The evolution of an LTM-type starting from an adiabatic lapse-rate profile for different surface emissivity $\epsilon_g = 1 \text{and} 0.8$ and ground cooling rate is assumed to be $\beta = 1.5\,K\text{hr}^{\frac{-1}{2}}$ and the water vapor mixing ratio is specified to be $q = 0.005$. The aerosol optical thickness is 0.02 and radiative relaxation time scale is 183 s Plot (a) is the temperature profile at different instants and plot (b) shows the corresponding radiative cooling-rate profiles.

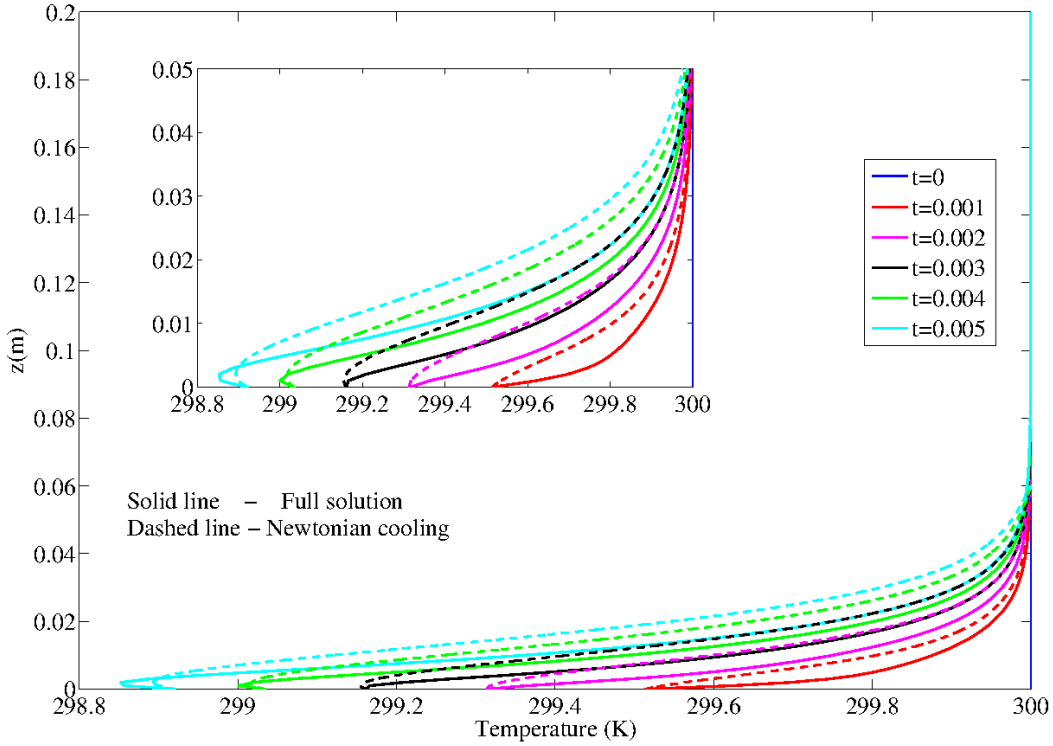

(a) Temperature profile

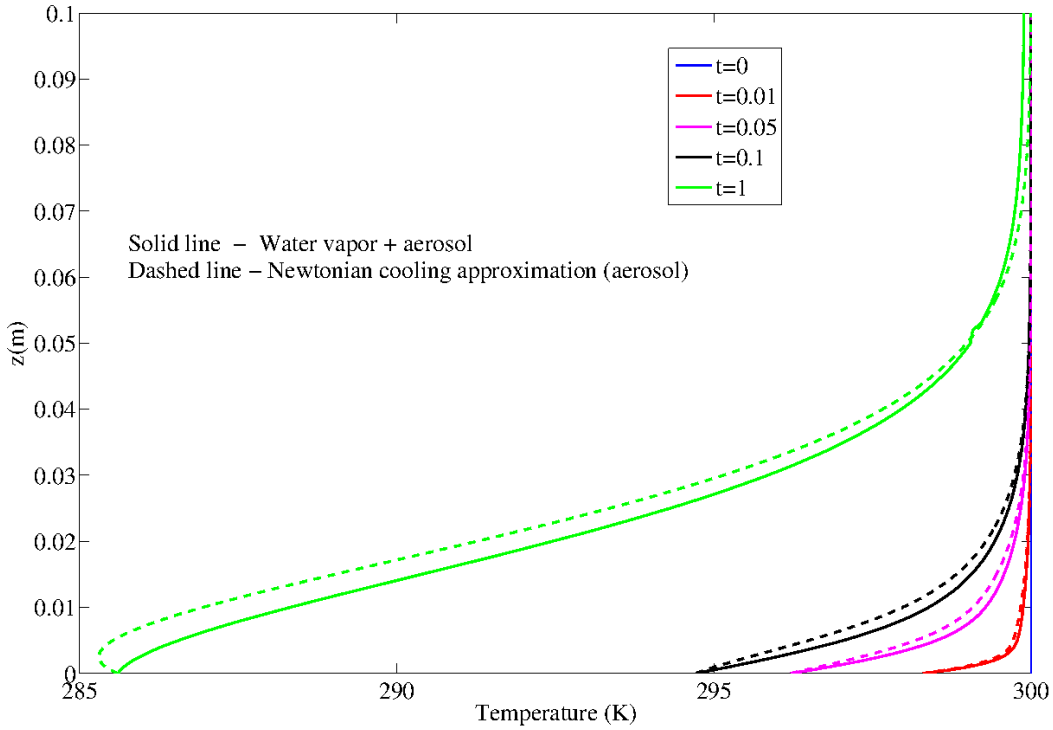

(b) Radiative cooling rate

Figure 5.32: The evolution of an LTM-type starting from an isothermal profile for different R_f values (R_f = 16and1.4) and ground temperature is specified from the solution obtained in section 5.4.2. The number density of aerosol particles is assumed to be 10 s which corresponds to a concentration of 6×10^{12}particlesm^{-3}. The optical thickness of aerosol layer is 0.1 and the ground emissivity $\epsilon_g = 1$.

Chapter 6

Laboratory Simulation of Ramdas layer

A portion of material in this chapter is reproduced in Proceedings of the 21^{st} National and 10^{th} ISHMT ASME Heat and Mass Transfer Conference

6.1 Abstract

The aerosol-induced radiative forcing manifests in a non-trivial manner even outside of the configuration, described briefly in chapter 4, and that leads to LTM-type profiles in the laboratory. Experiments to study the effects of this forcing have therefore been carried out with unfiltered air in the two-plate geometry with coupled radiative-conductive boundary condition (this is a classical configuration since, with an unstable stratification, the two-plate geometry is used for the study of Rayleigh-Benard convection). In this chapter, we theoretically analyze the effect of a heterogeneous radiatively participating medium (the heterogeneity arising due to a varying concentration of suspended aerosols in the unfiltered air used in the experiments), contained between parallel plates of an infinite horizontal extent, and maintained at (different) constant temperatures. The temperatures of the plates correspond to a stable stratification, and we examine the resulting radiative-conductive equilibria that exhibit a monotonic variation of temperature. The predicted equilibrium temperature profiles compare well with experimental observations, and show that the radiative forcing due to suspended aerosols lead to pronounced deviations from the expected (linear) conduction profile. The deviation is also asymmetric with the asymmetry being crucially dependent on the plate emissivities. As will be seen, this is in sharp contrast to earlier observations, in the same configuration, for pure gases. We also study the role of the aerosol-induced radiative forcing in the context of the LTM-type profile produced in the laboratory set-up, with de-coupled radiative and conductive boundary conditions, that is, the 'laboratory Ramdas layer'. In particular, we examine the relaxation response of the Ramdas layer to a 'cloud' event.

6.2 Introduction

Laboratory experiments were originally designed to reproduce the Ramdas layer under controlled conditions so that one can avoid the vagaries of weather and advective effects from the surrounding environs. Further, as discussed in an earlier chapter (see chapter 4), since there is no existing theory which can explain the origin and all other aspects of the phenomenon in a satisfactory manner, laboratory experiments can help shed light on the fundamental issues. The details about the experimental set-up and the observed temperature profiles are explained in

Mukund (2008), Mukund *et al.* (2010) and Singh (2013). In this chapter, after a brief description of the experimental set-up, we focus on the theoretical modelling of these experiments.

The work in this chapter may be divided into two parts based on the nature of the experiments. First, to study the radiative effects of aerosol particles outside the LTM scenario, experiments have been conducted in the traditional two-plate geometry, the plates being maintained at different constant temperatures with an intervening inhomogeneous radiatively participating medium - unfiltered air. The configuration is similar to the classical Rayleigh-Benard problem except that the boundary temperatures now correspond to a stable stratification. For this set-up, fixing the plate temperatures also fixes the radiative boundary conditions, and the conductive and radiative boundary conditions are thereby coupled. The experimental results exhibits a significant deviation from the linear conduction profile. Moreover the deviation is asymmetric, and the nature of the asymmetry is found to be a sensitive function of the plate emissivities. The equilibrium profiles range from being bottom heavy to top heavy in character depending on the ratio of plate emissivities and the optical thickness of the medium. The second set of experiments (the 'three-plate configuration' where the 'third' plate refers to the cold source) attempts to mimic the LTM conditions in the atmosphere. Towards this end, a cold source is added that then interacts with the aerosol-laden air-layers via a transparent upper plate. The addition of a separate source helps de-couple the radiative and conductive boundary conditions. As discussed in chapter 4, this de-coupling naturally occurs in the atmospheric context, but must be enforced in the laboratory in order to reproduce LTM-type profiles under laboratory conditions.

6.3 The two-plate geometry

There have been several earlier studies that have attempted to study the stabilizing role of radiation on the onset of Rayleigh-Benard convection. To begin with, we discuss a couple of early studies those by Goody (1956) and Spiegel (1960) that set the tone for the later work, both theoretical and experimental, on this problem. In a seminal paper, Goody (1956) examined analytically the effect of radiation on the onset of convection in a (compositionally) homogeneous gray medium in the optically thick and thin approximations, and with the boundaries assumed to be free-slip surfaces. He showed that the inclusion of a radiative source term introduced two modifications (a) a non-linear base-state temperature profile with a reduced de-stabilizing gradient in the bulk; (b) an additional (radiative) relaxation mechanism for a rising fluid parcel. Both effects are stabilizing, but for typical parameter values, only lead to a modest enhancement in the critical Rayleigh number. Later, Spiegel (1960), using dimensional arguments, defined a radiative Rayleigh number in terms of the ratio of radiative time scale to the convective time scale, that characterized the onset of convection in a gray homogeneous medium of arbitrary optical thickness. The characterization in terms of a radiative Rayleigh number became possible since the effect of thermal conduction was neglected in this analysis. Spiegel (1960) demonstrated that overstability (that is, onset of instability via oscillating modes) cannot occur in a radiatively participating medium, and the principle of exchange of stabilities therefore holds similar to the conventional Rayleigh-Benard problem [Chandrasekhar (1981)]. The threshold for convection to occur was found to depend on the optical thickness and the stabilization was found to be

minimal in the limits of large and small optical thicknesses.

On the experimental front, Gille & Goody (1964) studied the onset of convection in thin horizontal layers of dry air, and radiatively participating ammonia gas, sandwiched between parallel plates. The temperature profiles and heat fluxes measured in the quiescent gas, before the onset of instability, were found to compare well with theoretical predictions which was based on a non-gray random band model. The measured temperature profile was a non-linear function of the vertical coordinate, 'symmetric' about the center of the domain, and the maximum deviation from the linear conduction profile was only about 4% of the imposed temperature difference. Further, the effect of surface emissivities was studied (the two bounding surfaces always had the same emissivity). When the surfaces became reflective, the profile continued to be symmetric about the center, and there was a moderate increase in the deviation from the conduction profile. The critical Rayleigh numbers obtained for ammonia gas were found to be significantly larger than those obtained for dry air.

Similar experiments have been carried out later by Schimmel *et al.* (1970), Novotny & Olsofka (1970) and Hutchison & Richards (1999) to study the effect of radiation on the base state and on the onset of convection using different radiatively participating gases.

Schimmel *et al.* (1970) had carried out measurements of heat transfer in four participating gas mixtures: pure carbon dioxide, pure nitrous oxide, a mixture of carbon dioxide and nitrous oxide and a mixture of carbon dioxide and methane. Theoretical predictions for the coupled problem were made using three different radiation models: a gray gas model, a gray band model and an exponential wideband model. The predictions of the wideband exponential model matched the measurements under all conditions, while the other two models performed rather poorly. The observed profiles were again symmetric about the center of the test section and the maximum deviation from the conduction profile was about 0.25 K (the normalized deviation being about 2.5%). Novotny & Olsofka (1970) extended this work by looking at the effect of mixing a non-participating gas with a participating one.

More recently, Hutchison & Richards (1999) measured the heat transfer across carbon dioxide and air layers before and after the onset of convection. They observed an increase of 7 to 20 % increase in the threshold Rayleigh number for the onset of convection. They carried out a theoretical analysis based on an using exponential wideband model with the predicted non-linear profile again being symmetric, and the maximum deviation from the conduction profile being about 0.04 K (the normalized deviation from the conduction profile being about 0.4%).

On the theoretical side, later analyses have aimed at extending the study by Goody (1956). Christophorides & Davis (1970) included the effect of conduction and examined the stability in the optically thin limit and the stability analysis was carried out for rigid-rigid boundary conditions. Arpaci & Gozum (1973) included the effects of non-grayness of the participating medium and plate emissivities on the stability. The non-grayness was characterized by Rossland and Planck mean absorption coefficients. Bdeoui & Soufiani (1997) modeled radiation using correlated k-distribution methods and compared the linear stability analysis with direct numerical simulations (DNS) results.

The stability analysis has been recently extended to the atmospheric context by Larson [Larson (2000);Larson (2001)] by accounting for the exponential variation of the absorption coefficient

with altitude . The linear stability analysis was done in which case, as shown by Spiegel (1960), the system stability may be interpreted in terms of a radiative Rayleigh number as the ratio of radiative time scale to the convective time scale [1] provided conduction among air layers was neglected. A nonlinear stability analysis was carried out for the Rayleigh-Benard problem with radiation, and it has been shown that, in the pure radiation case, there will not be any subcritical instabilities.

Aston *et al.* (2000), and Chan *et al.* (2000) have also analyzed the base-state and stability of a radiatively participating medium in various asymptotic limits (conduction or radiation dominant atmosphere, and either in the optically thick or thin limit). The results were then compared with the full numerical solution of the non-linear equations.

References	Details	Height of domain	Emissivity	Maximum deviation
Gille & Goody (1964)	Ammonia $\Delta T = 7K$	1.987cm 5.048 cm	$\epsilon = 0.224, 0.35$ 0.48	0.28 K
Schimmel (1969)	CO_2 $\Delta T = 10K$	1cm	$\epsilon = 0.04$	0.25 K
Hutchison & Richards (1999)	CO_2 $\Delta T = 10K$	2.5cm	$\epsilon = 0.04$	0.04 K

Table 6.1: Summary of laboratory experiments which have attempted to study the role of radiation on the onset of convection. In all the experimental set-up the surfaces are of the same emissivity that is $\epsilon_1 = \epsilon_2$ and denoted as ϵ and ΔT is the temperature difference between the plates.

The gist of the above literature survey is that radiation is found to enhance the stability to Rayleigh-Benard convection. The base state of the system is itself modified due to radiation, and radiation also acts as an additional heat transfer mode for perturbations. Both act to enhance the stability. The modifications to the base state depends on the boundary emissivities and the optical thickness of the participating medium, and reflective surfaces were found to produce large deviations from the conduction profile.

In almost all the above studies, the radiatively participating medium is assumed to be homogeneous in the theoretical analysis. The exception is, the analysis by Larson (2000) who considered inhomogeneity of the participating medium, that is, water vapor with a scale height is 2.7 km. Conduction among air layers was still neglected in the analysis. The results from the previous chapters 4 and 5 emphasize the the role of the medium heterogeneity in determining the thermal structure of the nocturnal boundary layer under calm cloudless conditions [Mukund *et al.* (2010)], as also in producing laboratory LTM-type profiles. In section 6.3.1, we therefore

[1] The radiative Rayleigh number(Ra_R) , originally derived by Spiegel (1960) is more general than the one obtained by Larson (2000) in the sense that the radiative diffusivity used by Larson (2000) to define Ra_R is appropriate only in the optically thin limit. On the other hand, Spiegel (1960) obtained the radiative time scale which is valid for any optical thickness. The radiative time scale for any perturbation to decay in a radiating gray medium of an arbitrary optical thickness ($\hat{\alpha}$) is given by $\tau_R^{-1} = \frac{16\hat{\alpha}\sigma T^3}{h\rho C_p}\left(1 - \frac{\hat{\alpha}}{h}\cot^{-1}\frac{\hat{\alpha}}{h}\right)$ where h is the domain height.In the optically thin limit where $\hat{\alpha} \ll 1$, $\tau_R = \frac{\rho C_p}{16\alpha\sigma T^3}$, and in the other limit where $\hat{\alpha} \gg 1$, $\tau_R = \frac{3\hat{\alpha}\rho C_p h}{16\sigma T^3}$. In the optically thin limit, of course, both Ra_R definitions are the same.

present the analysis leading to radiative-conductive equilibria for a heterogeneous medium in the two-plate geometry. In section 6.3.2, the predicted equilibrium profiles are compared with experimental observations for unfiltered air in the two-plate geometry. In section 6.4 a simple, analytically tractable theoretical analysis is presented to predict equilibrium profiles. Section 6.5 presents the theoretical modeling for the laboratory Ramdas layer that arises in the three-plate geometry and its response to an abrupt blocking of the radiative sink. The latter would correspond to a 'cloud event' in the atmospheric context. Finally, section 6.6 presents a summary of the main findings.

6.3.1 Theoretical Formulation

As mentioned earlier, two sets of experiments have been carried out to study the radiative forcing by the suspended aerosol particles. Experimental procedures and the results obtained are discussed in detail by Singh (2013) and Mukund *et al.* (2013). In the first set of experiments, the radiatively participating heterogeneous medium is sandwiched between two parallel opaque plates. Hence, fixing the temperature of the top plate fixes the conductive as well as radiative boundary conditions. To study the effect of boundary emissivity on the aerosol forcing, an Aluminium foil is used to cover either the bottom or top plate to reduce the plate emissivity. In the other set of experiments a cold source is added which mimics the uppermost colder air layers in the atmosphere and now the participating medium can interact with the sky through the transparent upper plate. This de-couples the conductive and radiative boundary conditions. In this section, we present results for the two-plate configuration where the conductive and radiative boundary conditions are coupled.

The theoretical analysis involves several simplifying assumptions. We work within a plane parallel formulation where the radiatively participating heterogeneous medium is confined between infinite parallel plates (the infinite horizontal extent is consistent with the insulating boundary conditions on the sidewalls of the experimental test section). The plates are assumed to be isothermal, and are gray diffuse emitters and reflectors. Since a stable temperature stratification is maintained in the experiments, the heat transfer is assumed to be due to conduction and radiation alone. We also assume the participating medium to be gray. The dominant radiative forcing in the experiments arises from suspended aerosol particles and the gray medium assumption is a reasonable one in this case, since the absorption coefficients of solids and liquids in general are far smoother functions of the wavelength (in the IR range) when compared to gases. The gray medium assumption is expected to be even better for a polydisperse suspension of aerosols, since the distribution of sizes acts to further smoothen the absorption coefficient.

Governing Equation

The one-dimensional energy balance in the medium is:

$$\rho C_p \frac{\partial T}{\partial t} = k \frac{\partial^2 T}{\partial z^2} - \frac{dF_z}{dz}, \tag{6.1}$$

where k is the thermal conductivity, ρC_p the medium heat capacity, and F_z the vertical component of the net radiative flux. Since radiation is a non local phenomenon, the governing equation

for radiative transfer is an integro-differential equation in the general case. However, with the use of the Milne-Eddington differential approximation [Goody (1956), Larson (2001)], one may obtain a differential equation governing F_z as:

$$\frac{d^2F_z}{dz^2} - \frac{1}{\alpha}\left(\frac{d\alpha}{dz}\right)\frac{dF_z}{dz} - 3\alpha^2 F_z = 4\alpha\sigma\frac{dT^4}{dz} \tag{6.2}$$

Here, α is an effective absorption coefficient that includes contributions from both radiatively participating gases as well as suspended particulates. When radiative forcing due to aerosol particles is dominant, then the contribution of the gases may be neglected, and one may write $\alpha = A\alpha_h n(z)$ where $n(z)$ is the aerosol number density field, and $A\alpha_h$ is the absorption cross section of a single aerosol particle. The above expression for α is valid in the dilute limit, when the aerosol contribution is linearly related to the number density. The number densities, inferred from a match with experimental observations, do fall in the dilute regime, and any form of radiative interactions between aerosol particles (absorption or scattering) is therefore neglected.

The Milne-Eddington equation is obtained by taking the first two (zeroth and first) moments of radiative transfer equation involving $I(\Omega)$, where Ω denotes the angular dependence of the intensity. For a plane-parallel formulation, taking the first moment involves multiplying by cosine of the angle between the vertical and the direction of intensity and then integrating over the entire solid angle. This is a subset of the general P_N approximation where the intensity is expressed in terms of a spherical harmonics expansion, and taking moments of the radiative transfer equation leads to a set of coupled ODE's which is the closed by a suitable approximation (N stands for the number of terms in the Legendre polynomial series used to represent the radiant intensity). Thus, the Milne-Eddington is also called the P_1 approximation [Siegel & Howell (2002)]. It can be seen from (6.2) that the governing Milne-Eddington equation reduces to the exact equation both in the optically thick and thin limits, and it has been shown by citeSpiegel1966 that this method is reasonably accurate for intermediate optical thicknesses. In the optically thick limit the above equation reduces to a local flux-gradient relation that is, $F_z = -\dfrac{4\sigma}{3\alpha}\dfrac{dT^4}{dz}$. In the optically thin limit one obtains $\dfrac{d^2F_z}{dz^2} = 16\sigma T^3\dfrac{dT}{dz}$, and if we integrate this once substituting the boundary conditions from (6.7), then one finds $\dfrac{dF_z}{dz} = -\left[\sigma T_1^4 + \sigma T_2^4 - 2\sigma T^4\right]$.

Since the temperature difference between the boundaries is small in relation to the absolute temperature equation (6.2) may be linearized, and combined with the energy (6.1). At steady state, the resulting non-dimensional equation governing the temperature field is

$$\frac{d^3\theta}{dz^3} - \frac{1}{\hat{\alpha}}\left(\frac{d\hat{\alpha}}{dz}\right)\frac{d^2\theta}{dz^2} - 3\hat{\alpha}^2\left(\frac{d\theta}{dz}\right) - 3\hat{\alpha}\chi\left(\frac{d\theta}{dz}\right) = 3\hat{\alpha}^2\eta\psi \tag{6.3}$$

where $\chi = \dfrac{16\sigma T_c^3 h}{3k}$, $\hat{\alpha} = \alpha h$ and $\eta = \dfrac{\sigma T_c^4 h}{k(T_1 - T_0)}$. Here, $\theta = \dfrac{T - T_0}{T_1 - T_0}$ is the normalized temperature, T_c is the absolute temperature scale that may be taken as the mean of the bottom and top plate temperatures, h is the separation between the plates, T_0 and T_1 are the bottom and top plate temperatures, respectively, ψ is the (constant) total heat flux, $\hat{\alpha}$ is the dimensionless optical thickness in units of the inverse separation between the plates, $\dfrac{\chi}{\hat{\alpha}}$ is the ratio of the

radiative to thermal conductivities, and η denotes the ratio of radiative to conductive fluxes. The independent dimensionless parameters that govern the temperature profiles are the optical thickness ($\hat{\alpha}$) and the ratio of radiative to thermal conductivities $\frac{\chi}{\hat{\alpha}}$. The ratio of radiative to conductive fluxes(η) can be interpreted in terms of $\hat{\alpha}$, χ and the temperature ratio $\dfrac{T_c}{T_1 - T_0}$. The temperature ratio appears as an independent parameter because one scales the radiative flux with σT_c^4. However, if one uses $\sigma T_c^3 (T_1 - T_0)$ as the relevant scale for the net flux, the ratio of temperatures may be eliminated and the only remaining parameters are $\hat{\alpha}$ and χ. As discussed in the previous section and shown by Spiegel (1960), in the optically thin limit where $\hat{\alpha} \ll 1$, $\hat{\alpha}^2\chi$ is the ratio of conductive to radiative time scales, while in the other optically thick limit ($\hat{\alpha} \gg 1$), χ is the ratio of conductive to radiative time scales.

Since there are 4 unknowns (3 integration constants associated with the third-order differential equation and the unknown total heat flux), four boundary conditions are needed. The first two are no-slip conditions at the top and bottom boundaries: $\theta = 0$ at $z = 0$ and $\theta = 1$ at $z = 1$. As mentioned earlier, fixing the plate temperatures fixes both the conductive and radiative boundary conditions. These latter boundary conditions are obtained by taking the radiative balance for a layer of air near the boundaries. Using the Milne-Eddington approximation [Goody (1956)] the radiative flux divergence and flux can be written in terms of upwelling and downwelling intensities as follows:

$$F_z = \pi \left(I^{\uparrow} - I^{\downarrow} \right), \tag{6.4}$$

$$\frac{dF_z}{dz} = 4\pi\alpha B - 2\pi\alpha \left(I^{\uparrow} + I^{\downarrow} \right). \tag{6.5}$$

Near the boundaries, either $I^{\uparrow}$ or $I^{\downarrow}$ can be specified and the other component of the intensity may be eliminated using (6.4) and (6.5). Thereby, one may obtain a relation between F_z and $\dfrac{dF_z}{dz}$. For example, near a bottom boundary, $I^{\uparrow}$ is the radiosity from the plate which is known. One can thus obtain the required boundary conditions, originally given by [Goody (1956)] for a black surface, and that can be generalized to gray surfaces easily. These are given by:

$$\left.\frac{dF_z}{dz}\right|_{z=0} = 4\alpha(0) \left(\frac{1}{\epsilon_1} - \frac{1}{2} \right) F_z(0), \tag{6.6}$$

$$\left.\frac{dF_z}{dz}\right|_{z=h} = -4\alpha(h) \left(\frac{1}{\epsilon_2} - \frac{1}{2} \right) F_z(h). \tag{6.7}$$

Using the steady-state energy equation one can write the net radiative flux as $F_z = \psi + k\dfrac{dT}{dz}$, and the flux divergence as $\dfrac{dF_z}{dz} = k\dfrac{d^2T}{dz^2}$. The radiative boundary conditions, (6.7) in terms of the non- dimensional temperature, are given by:

$$\left.\frac{d^2\theta}{dz^2}\right|_{z=0} = \left(2v_1\hat{\alpha}\eta\psi + 2v_1\hat{\alpha}\,\frac{d\theta}{dz} \right)\Bigg|_{z=0}, \tag{6.8}$$

$$\left.\frac{d^2\theta}{dz^2}\right|_{z=1} = \left(-2v_2\hat{\alpha}\eta\psi - 2v_2\hat{\alpha}\,\frac{d\theta}{dz} \right)\Bigg|_{z=1}, \tag{6.9}$$

where

$$v_1 = 2\left(\frac{1}{\epsilon_1} - \frac{1}{2}\right), \tag{6.10}$$

$$v_2 = 2\left(\frac{1}{\epsilon_2} - \frac{1}{2}\right), \tag{6.11}$$

where ϵ_1 and ϵ_2 are the bottom and top plate emissivities, respectively.

Equation (6.3) can be solved numerically using a linear shooting method [F.Gerald & Wheatley (2003)]. The numerical code is validated using the known analytical result for a gray homogeneous medium. The analysis in this case becomes possible because $\frac{d\hat{\alpha}}{dz} = 0$ and (6.2) reduces to a constant coefficient differential equation. The solution for the two-plate geometry, in the linearized approximation, and for bounding black surfaces is given by Goody (1956):

$$\theta(z) = \frac{Le^{pz}}{p} - \frac{Le^{(1-z)p}}{p} - \frac{\eta\psi z}{1+\chi} - \frac{L(1-e^p)}{p}, \tag{6.12}$$

where

$$L = 2\hat{\alpha}\chi\left[p(e^p-1) + 2\hat{\alpha}(e^p+1) + \frac{4p\chi(e^p-1)}{3\hat{\alpha}(1+\chi)}\right]^{-1},$$

and $p = \sqrt{3\hat{\alpha}^2(1+\chi)}$ is the inverse of the conductive boundary layer thickness.

6.3.2 Results and Discussion

Equilibrium temperature profiles

The radiative-conductive equilibrium temperature profiles obtained are shown in Figure 6.1a for differing combinations of boundary emissivities, and an exponential absorptivity stratification given by $\hat{\alpha}(z) = 1.4e^{\frac{-z}{0.05}} + 0.05$. The particular functional form mimics a steeply varying concentration of large particles embedded in a uniform field of smaller particles. The same temperature profiles are plotted as a deviation from the corresponding linear conduction profile in figure 6.1b. Equilibrium temperature profiles for the different boundary emissivity combinations are shown in figures 6.2a, 6.2b, 6.3a and 6.3b, where we also compare these profiles to experimental measurements [Singh (2013)], and in addition, contrast them with the temperature profiles obtained using equation (6.12) for a homogeneous medium with an optical thickness $\hat{\alpha} = 1.4$ (corresponding to the peak value of the heterogeneous medium). The results show that the heterogeneous equilibria, besides deviating significantly from a linear conduction profile, also exhibit a pronounced *asymmetry* even when the two boundaries have identical emissivities. Any asymmetry in the corresponding homogeneous equilibria profiles, for identical boundary emissivities, can arise only due to nonlinear effects; these are $O(\Delta T)/T_0$ which is roughly 1%, and much smaller than the asymmetries observed. Thus, the observed asymmetry is solely due to the radiative effects of the inhomogeneous aerosol concentration field.

The nature of the asymmetry, in fact, depends crucially on the boundary emissivities. Considering the case of identical boundary emissivities first, for the Black-Black configuration (see figure 6.2a), the concentrated aerosol layer close to the bottom plate interacts strongly with

the downwelling flux from the warmer upper boundary, and thence, attains a higher temperature. This leads to a 'bottom-heavy' equilibrium profile. On the other hand, for the Al-Al configuration shown in figure 6.2b, where both the bounding surfaces have low emissivities, emission of the aerosol-laden air layers close to the bottom plate dominates the boundary emission. The concentrated aerosol layer may now be interpreted as a 'bottom plate', with higher effective emissivity (Note that this interpretation makes it identical to the asymmetric Al-Black configuration described below in the region above the aerosol layer). Near the top plate, the reflected component consists of colder radiation from this bottom plate and absorption of this colder radiation leads to a top-heavy profile. The homogeneous equilibrium is symmetric about the center in both these cases. Now, we move on to the asymmetric emissivity configurations (Al-Black and Black-Al). For the Al-Black configuration, the deviation from the conduction profile, close to the bottom plate, is further enhanced because the bottom boundary (Al) has a low-emissivity (see figure 6.3a), and the upwelling flux from the reflective bottom surface is now dominated by the warmer emission originating from the upper boundary. The asymmetry for the Al-Black configuration, shown in figure 6.3a, in fact, strong enough that the deviation from the conduction profile remains single-signed; in sharp contrast to the corresponding solution for a homogeneous medium. The opposite occurs for the Black-Al configuration (see figure 6.3b) where the deviation, while remaining single-signed, is now negative, since the high-emissivity surface is at a lower temperature.

Temperature gradient and Flux divergence

The comparison between observations and theoretical predictions for the temperature gradients and radiative flux divergences, for all four configurations considered, are shown in figures 6.4 and 6.5 respectively. Figure 6.4 indicates a large temperature gradient near the bottom plate. The gradient magnitude, just above the low-emissivity bottom boundary (Al-Black configuration), is $O(100)Km^{-1}$. The radiative-flux divergence profile shows a region of intense radiative heating near the bottom surface that decays over a length scale of $O(10\,mm)$ and the maximum heating occurs over the low emissivity boundary for the asymmetric configuration (Black-Al). It is evident that, for the assumed exponential distribution of aerosol particles, the temperature profiles, gradients and flux divergences match well with the experiments.

In order to understand the dependence on the aerosol radiative forcing in more detail, the equilibrium temperature profiles are shown in figure 6.6, for a varying aerosol concentration with the scale height fixed, with black boundaries. As expected, the maximum deviation from the conduction profile increases with increasing concentration. Similarly, for low emissivity boundaries ($\epsilon_1 = \epsilon_2 = \epsilon = 0.05$; see figure 6.7), with increasing concentration, the air layers near the top surface interact more efficiently with "effective emissivity" plate near the bottom and attain a lower temperature.

6.4 Analytical solutions for the heterogeneous radiative-conductive equilibria:

In the last section, using a full numerical solution, we examined the role of an inhomogeneity in altering the temperature profile (from the symmetric profile known for a homogeneous medium)

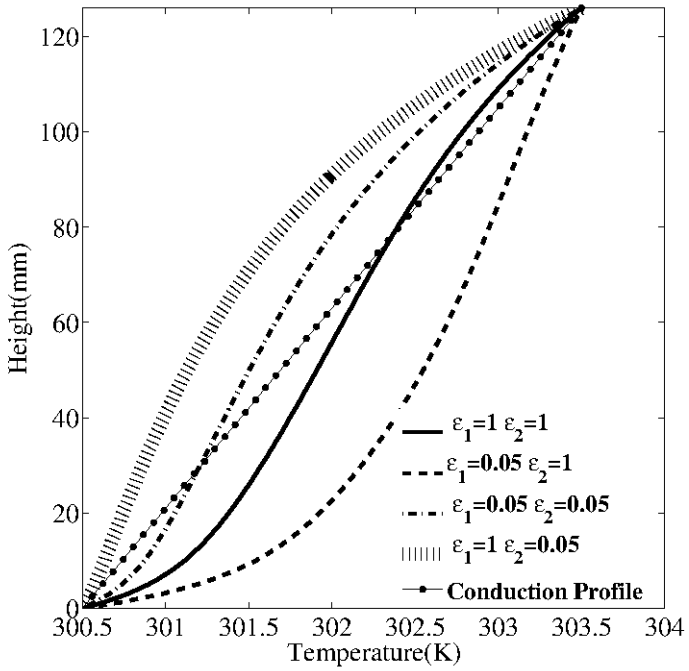

(a) Equilibrium temperature profiles for varying plate emissivities.

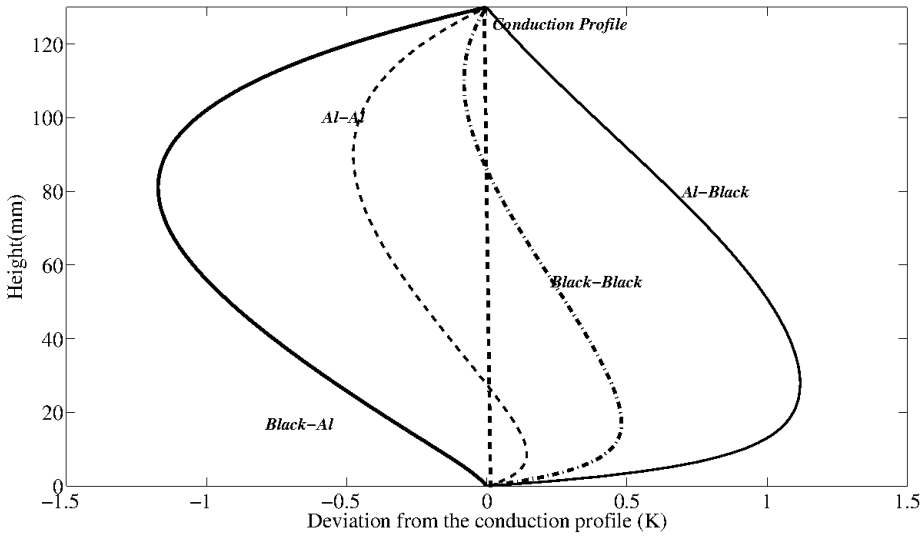

(b) Deviation from the conduction profile over different surfaces.

Figure 6.1: Plot (a) shows the equilibrium temperature profile in the two-plate geometry for varying plate emissivities where plot (b) shows the corresponding deviation from the conduction profile.

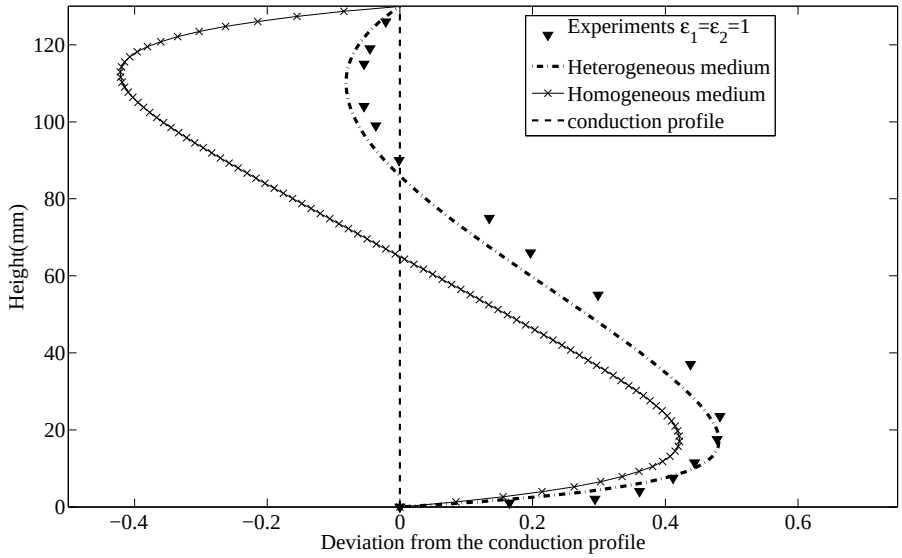

(a) Black-Black $\epsilon_1 = 1, \epsilon_2 = 1$

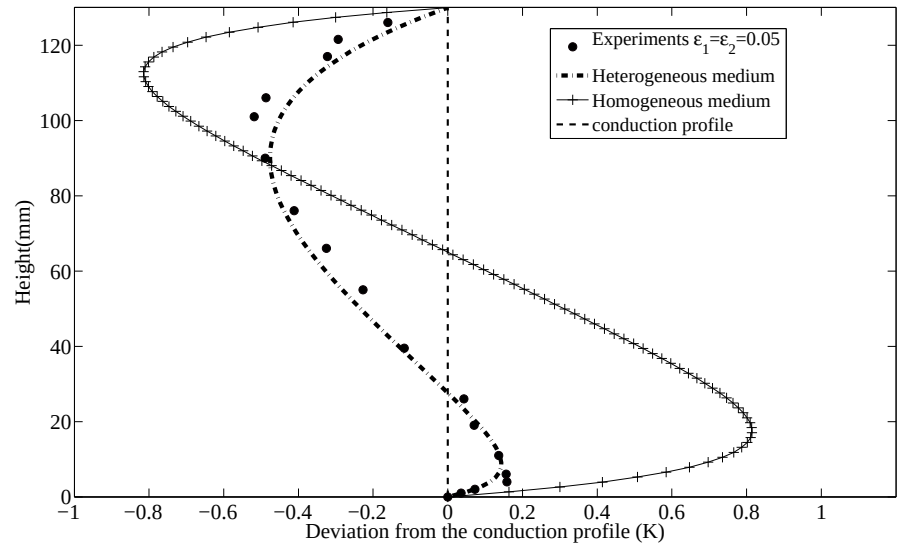

(b) Al-Al $\epsilon_1 = 0.05, \epsilon_2 = 0.05$

Figure 6.2: Deviation from the conduction profile over different surfaces. The theoretical results compare well with experimental observations for an assumed exponential distribution of aerosol particles; the resulting optical thickness distribution is $\hat{\alpha}(z) = 1.4\mathrm{e}^{\frac{-z}{0.05}} + 0.05$. The corresponding result for a homogeneous participating medium is shown for comparison.

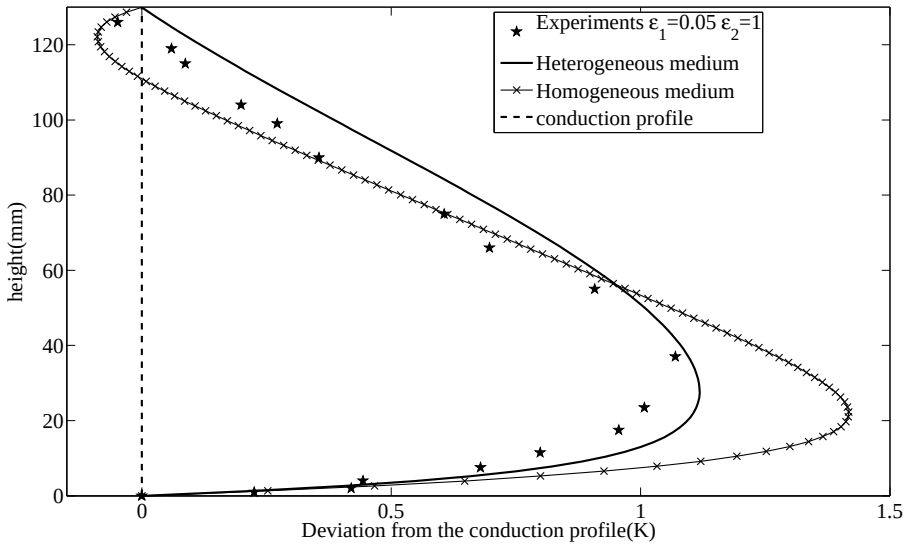

(a) Al-Black $\epsilon_1 = 0.05, \epsilon_2 = 1$

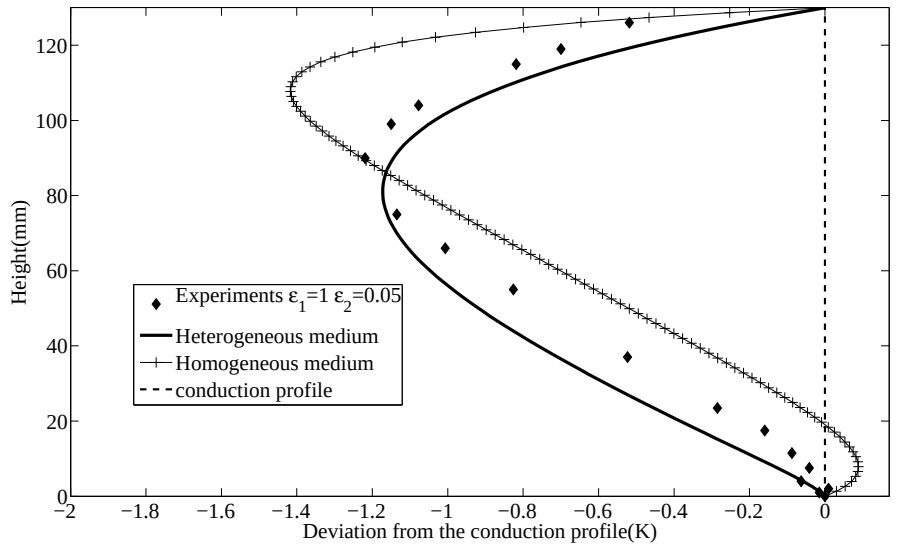

(b) Black-Al $\epsilon_1 = 1, \epsilon_2 = 0.05$

Figure 6.3: Deviation from the conduction profile over different surfaces. The theoretical results compare well with experimental observations for an assumed exponential distribution of aerosol particles; the resulting optical thickness distribution is $\hat{\alpha}(z) = 1.4\mathrm{e}^{\frac{-z}{0.05}} + 0.05$. The corresponding result for a homogeneous participating medium is shown for comparison.

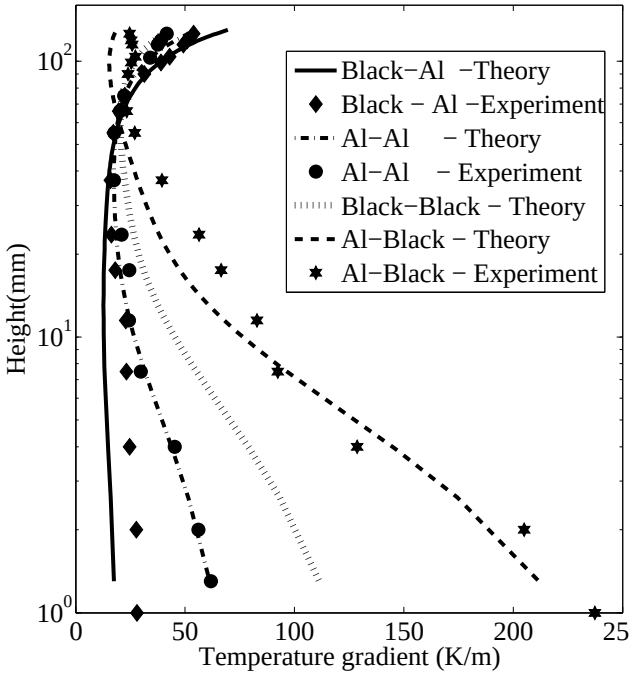

Figure 6.4: A comparison of the theoretical and experimental temperature gradient profiles over different surfaces.

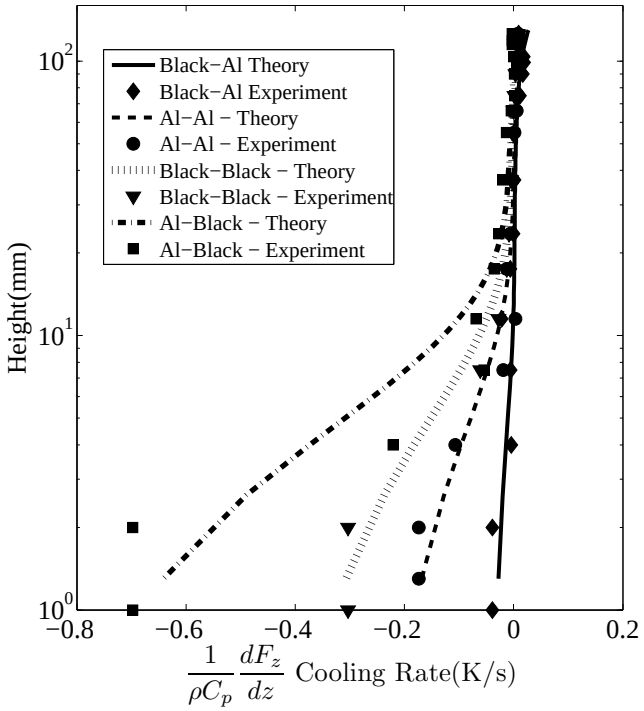

Figure 6.5: A comparison of the theoretical and experimental radiative flux-divergence profiles over different surfaces.

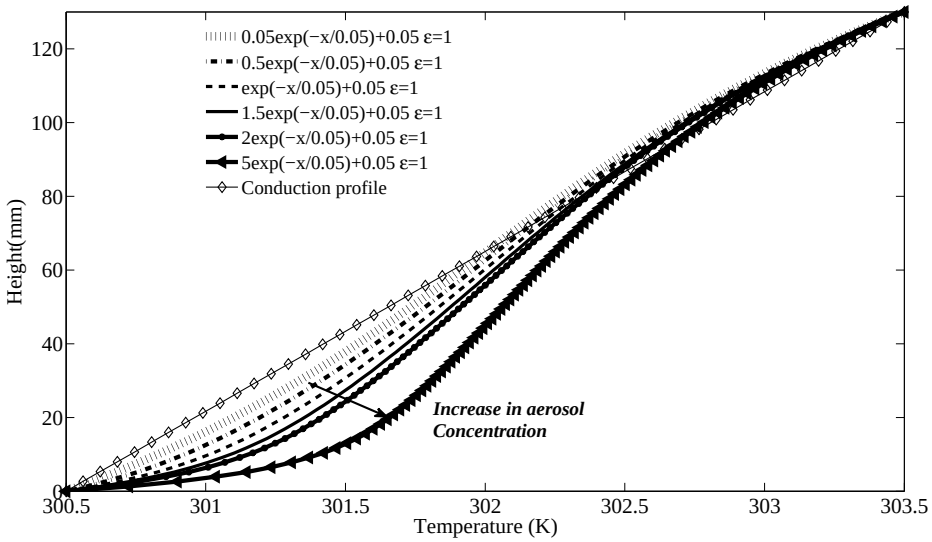

Figure 6.6: Variation of the equilibrium temperature profiles, for varying parameters in the aerosol concentration profile, for black bounding surfaces.

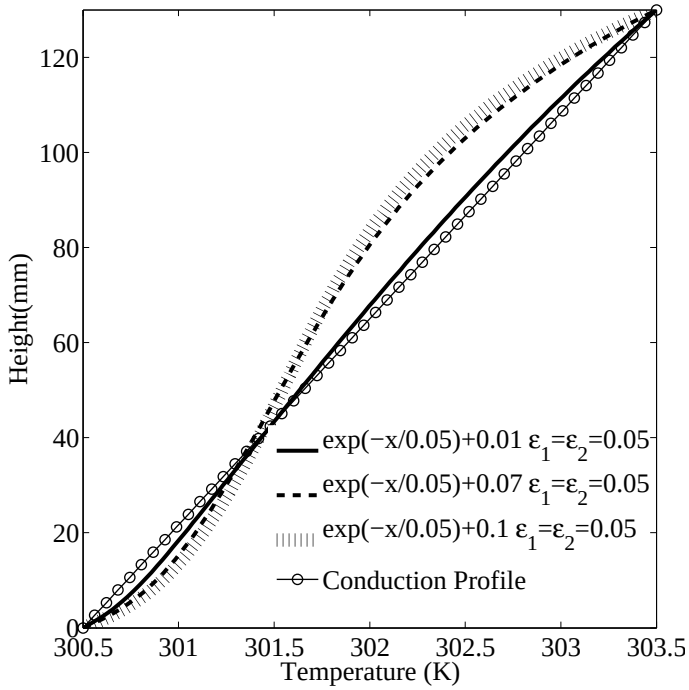

Figure 6.7: Temperature profile for different uniform distribution of aerosol. The bounding surfaces are assumed to have equal emissivity and the assumed value is 0.05

between two plates maintained at different (constant) temperatures. It is of interest to see whether the trends observed with regard to the dependence of the asymmetric equilibria on the boundary emissivities can be predicted using a simple theoretical analysis. In order to motivate the assumptions that lead to an amenable theoretical analysis, we first note that the participating medium must be optically thin based on the length scale that characterizes the aerosol concentration profile. For instance, in the case of the black-black configuration, the presence of a 'bottom-heavy' deviation profile implies that the aerosol layer interacts strongly with the top warmer boundary and this can be explained only if we consider the medium to be optically thin. Further, the other parameter which determines the temperature profile in the test section is the ratio between conductive and radiative time scale. The large deviations from the linear conduction profile, observed in the experiments, clearly imply that radiation and conduction are comparable in magnitude. To begin with, for simplicity, first, we present a special case where the radiative forcing of the suspended aerosol particles is assumed to be weak, and thereby, conduction to be dominant throughout the domain at leading order. Such an assumption allows one to treat the radiative source term as a regular perturbation about a linear conduction profile. Physically, the above problem can be thought of change in temperature of a single aerosol particle, which is close to its conductive equilibrium temperature, due to a weaker radiative interactions both with the boundaries and with the medium. Our goal here is to predict qualitatively the trends observed in the experiments as a function of the boundary emissivities (for instance, the transition from bottom heavy to top-heavy with decreasing surface emissivity). It turns out that the simplified solution obtained via a regular perturbation approach predicts the correct trend in asymmetry and there is, in fact, a near quantitative match with the observations (although the latter do not lie in the weak forcing regime) in some scales. Later we extend the analysis to include an arbitrary ratio of conductive to radiative time scales, but with the medium still assumed to be optically thin and this follows the experimental observations in all cases. This method is, in fact, same as that of the 'Newtonian cooling' or the 'cooling to space' method commonly employed in the atmospheric context.

6.4.1 Regular Perturbation problem

For the conduction dominant and optically thin limit, $\hat{\alpha}_0^2\chi$ is the relevant small parameter which is the ratio of conductive to radiative time scales. The relevant length scale is the scale height of the aerosol concentration profile H, and the ratio of radiative to conductive time scale $\hat{\alpha}_0^2\chi$ is based on the this length scale [2]. The steady state energy equation, in terms of the above small

[2] In principle, the relevant length scale for the radiative heat transfer is the scale height of aerosol layer and for conduction, the domain height is the relevant length scale. The radiative forcing is proportional to $\sigma T_c^3(T_1 - T_0)$ where T_c is the mean temperature across the domain and T_0 and T_1 are the bottom and top plate temperature and since the medium is in the optically thin limit this is the relevant scale for the net radiative flux. (In the optically thin limit the full governing integral equation reduces to the Newtonian cooling approximation where, the net flux is proportional to the temperature difference). The final non dimensional equation is

$$\frac{d^2\theta}{dz^2} = \frac{\sigma T_c^3 \alpha h^2}{k}\frac{dF_z}{dz} \tag{6.13}$$

where θ is the normalized temperature and α is the absorption coefficient. Indeed the prefactor is nothing but the ratio of conductive time scale to radiative time scale in the optically thin limit based on test section height h. In the above scaling analysis, we recognize in the optically thin limit the radiative flux divergence is proportional

parameter, that characterizes the conduction dominant, optically thin limit is given by:

$$\frac{d^2\theta}{dz^2} = \hat{\alpha}_0^2 \chi \frac{dF_z}{dz}. \tag{6.14}$$

Hence, the normalized temperature profile can be written as

$$\theta(z) = \theta_0(z) + (\hat{\alpha}_0^2\chi)\theta_1(z) + (\hat{\alpha}_0^2\chi)^2\theta_2(z) + ... \tag{6.15}$$

where θ_0 is the leading order solution and since $\hat{\alpha}_0^2\chi$ is very small (for conduction to be dominant), the leading-order solution as expected is the linear conduction profile and estimating θ_1 directly gives the deviation from the conduction profile.

Leading-order solution

At leading order, the governing equation is

$$\frac{d^2\theta_0}{dz^2} = 0, \tag{6.16}$$

and the boundary conditions are the constant temperatures fixed at both the plates:

1. $\theta_0 = 0$ at $z = 0$,
2. $\theta_0 = 1$ at $z = g$ where $g = \dfrac{h}{H}$.

The leading order solution is evidently a linear conductive profile:

$$\theta_0 = \frac{z}{g}. \tag{6.17}$$

First correction

At the next order, $\dfrac{d^2\theta_1}{dz^2}$ will be forced by the radiative flux divergence at the leading order. Thus the governing equation is at $O(\hat{\alpha}^2\chi)$ is:

$$\frac{d^2\theta_1}{dz^2} = \left.\frac{dF_z}{dz}\right|_{leading\ order}, \tag{6.18}$$

with homogeneous boundary conditions:

1. $\theta_1 = 0$ at $z = 0$,
2. $\theta_1 = 0$ at $z = g$.

Now, using the Milne-Eddington equation one can find the net radiative flux at leading order. The non-dimensional Milne Eddington equation for the inhomogeneous medium is given by:

$$\frac{d^2F_z}{dz^2} - \left(\frac{1}{\hat{\alpha}}\right)\left(\frac{d\hat{\alpha}}{dz}\right)\frac{dF_z}{dz} - 3\hat{\alpha}^2F_z = 16\hat{\alpha}\,\frac{d\theta_0}{dz}. \tag{6.19}$$

to the optical thickness based on the aerosol scale height. It is worth noting, though radiation acts over a length scale of $O(H)$, the resultant parameter which discriminates whether conduction is dominant doesn't involve H; again this is expected from the physical grounds where we are treating the problem as a regular perturbation that is conduction is the dominant mode of heat transfer and the relevant length scale should be the height of the domain.

In the optically thin limit, we can neglect terms of $O(\hat{\alpha}^2)$ in (6.19), and the reduced governing equation is given by:

$$\frac{d^2F_z}{dz^2} - \left(\frac{1}{\hat{\alpha}}\right)\left(\frac{d\hat{\alpha}}{dz}\right)\frac{dF_z}{dz} = 16\hat{\alpha}\,\frac{d\theta_0}{dz}, \quad (6.20)$$

and the corresponding radiative boundary conditions are:

$$\left.\frac{dF_z}{dz}\right|_{z=0} = 4\hat{\alpha}(0)\left(\frac{1}{\epsilon_1} - \frac{1}{2}\right)F_z|_{z=0}\,, \quad (6.21)$$

$$\left.\frac{dF_z}{dz}\right|_{z=g} = -4\hat{\alpha}(1)\left(\frac{1}{\epsilon_2} - \frac{1}{2}\right)F_z|_{z=g}\,. \quad (6.22)$$

These are the non-dimensionalized versions of the equations (6.7) described in section 6.3.1. Since we know the forcing from the leading order solution, equation (6.20) can be reduced to a first order differential equation in the radiative flux divergence, and can be therefore solved for any concentration profile. For purposes of simplicity, we only present results for an exponential distribution of optical thicknesses, that is, $\hat{\alpha}(z) = \hat{\alpha}_0 \mathrm{e}^{\frac{-z}{H}}$, and an exponential distribution of optical thickness superposed on a uniform background of the form $\hat{\alpha}(z) = \hat{\alpha}_0 + \hat{\alpha}_1 \mathrm{e}^{\frac{-z}{H}}$, the latter being relevant to the experiments.

Case I : $\hat{\alpha}(z) = \hat{\alpha}_0 \mathrm{e}^{\frac{-z}{H}}$

The net radiative flux is given by

$$F_z = -c_1\mathrm{e}^{-z} - \frac{16\hat{\alpha}_0(z+1)\mathrm{e}^{-z}}{g} + c_2. \quad (6.23)$$

The deviation from the conduction profile for is given by

$$\theta_1 = c_1\mathrm{e}^{-z} + \frac{16}{g}(z+2)\mathrm{e}^{-z} + c_3 z + c_4, \quad (6.24)$$

where, for a surface emissivity ϵ the constants are given by

$$c_1 = 2v_1c_2 \quad (6.25)$$

$$c_2 = \frac{-8\left[1 + \frac{2}{g}v_2\hat{\alpha_0}(1-(g+1)\mathrm{e}^{-g})\right]}{v_1 + v_2 + 2v_1v_2\hat{\alpha_0}(1-\mathrm{e}^{-g})} \quad (6.26)$$

$$c_4 = -\left[c_1 + \frac{32}{g}\right], \quad (6.27)$$

$$c_3 = -\frac{c_4}{g}, \quad (6.28)$$

where v_1 and v_2 are defined earlier (see (6.10) and (6.11)).

For a black surface the above expression reduces to:

$$c_1 = \frac{-8\left(1+\frac{2\hat{\alpha}_0}{g}\right)}{1+\hat{\alpha}_0}, \tag{6.29}$$

$$c_2 = \frac{c_1(1+2\hat{\alpha}_0)+32\hat{\alpha}_0^2/g}{2\alpha_0}, \tag{6.30}$$

$$c_4 = -8(\frac{4}{g}-1), \tag{6.31}$$

$$c_3 = -\frac{c_4}{g}. \tag{6.32}$$

The resultant temperature profile have been plotted and compared with the full solution obtained using linear shooting method described earlier for $\hat{\alpha} = 0.05\mathrm{e}^{\frac{-z}{0.05}}$, both over black-black and Al-Al surfaces in figure 6.8a and 6.8b respectively. The regular perturbation works very well even for $O(1)$ optical thickness radiation dominant medium. The corresponding results for a simple exponential distribution of aerosol optical thickness $\hat{\alpha}(z) = 1.4\mathrm{e}^{\frac{-z}{0.05}}$ is shown in figure 6.11a and 6.11b.

Case II : $\hat{\alpha}(z) = \hat{\alpha}_0 + \hat{\alpha}_1\mathrm{e}^{-z/H}$

For the profile consists of an exponential with a uniform background concentration which was used to match the theory with the results for the two-plate experiments, radiative flux is given by:

$$F_z = c_1(\hat{\alpha}_0 z - \hat{\alpha}_1\mathrm{e}^{-z}) + (16/g)\left[\hat{\alpha}_0 z^2/2 - \hat{\alpha_1}(z+1)\mathrm{e}^{-z}\right] + c_2. \tag{6.33}$$

The resultant temperature profile is given by

$$\theta = c_1(\hat{\alpha}_0 z^2/2 + \hat{\alpha}_1\mathrm{e}^{-z}) + (16/g)\hat{\alpha}_0 z^3/3 + 16\hat{\alpha}_1(z+2)\mathrm{e}^{-z} + c_3 z + c_4. \tag{6.34}$$

The constants are given by

$$c_1 = 2v_1c_2, \tag{6.35}$$

$$c_2 = \frac{-8\left[1+\frac{2}{g}v_2(0.5\hat{\alpha}_0 g^2\hat{\alpha}_1(1-(g+1)\mathrm{e}^{-g}))\right]}{v_1+v_2+2v_1v_2(\hat{\alpha}_0 g+\hat{\alpha}_1(1-\mathrm{e}^{-g}))}, \tag{6.36}$$

$$c_3 = -\frac{c_4}{g} \tag{6.37}$$

$$c_4 = -\frac{c_1\hat{\alpha}_1}{\hat{\alpha}_0+\hat{\alpha}_1} - 32\hat{\alpha}_1. \tag{6.38}$$

Finally, we compare the temperature profiles given by equation (6.34) with the experimental profiles, corresponding to the four boundary-emissivity configuration (Black-black,Al-Al,Black-Al,Al-Black), in figures, 6.10a to 6.11b. The regular perturbation solution describes correctly the transition in the nature of the profile from a bottom-heavy one to the top-heavy one as the surface emissivity in the symmetric configuration is changed from 1 to 0.05. It is nevertheless clear from figures 6.10a - 6.11b that the uniform background in the optical thickness distribution is crucial to agreement with experiments. However, in all cases there remains a significant quantitative discrepancy between the numerical solution and the regular perturbation analysis. In general, the solution obtained using the regular perturbation overpredicts the deviation from

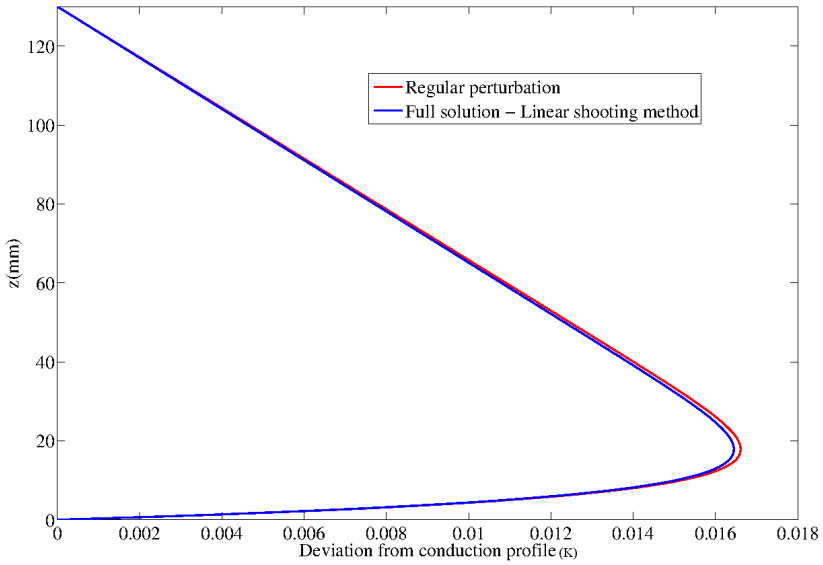

(a) Black-Black $\epsilon_1 = 1, \epsilon_2 = 1$

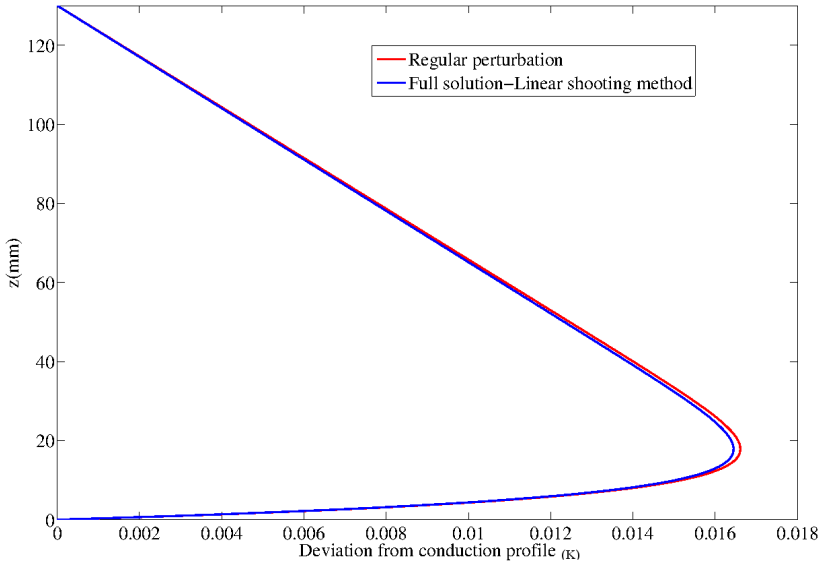

(b) Al-Al $\epsilon_1 = 0.05, \epsilon_2 = 0.05$

Figure 6.8: Deviation from the conduction profile over different surfaces. The results obtained using regular perturbation method (see equation 6.24) are compared with full numerical solution for an assumed distribution optical thickness given by $\hat{\alpha}(z) = 0.05\mathrm{e}^{\frac{-z}{0.05}}$.

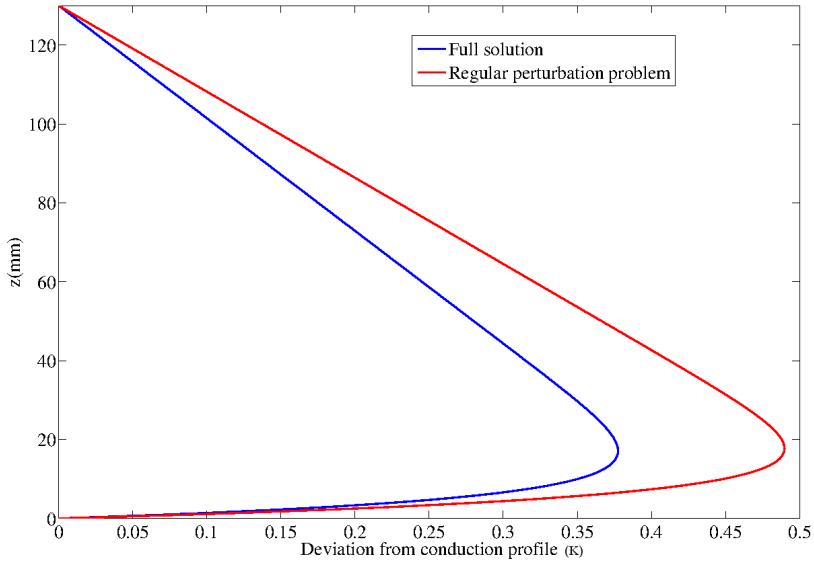

(a) Black-Black $\epsilon_1 = 1, \epsilon_2 = 1$

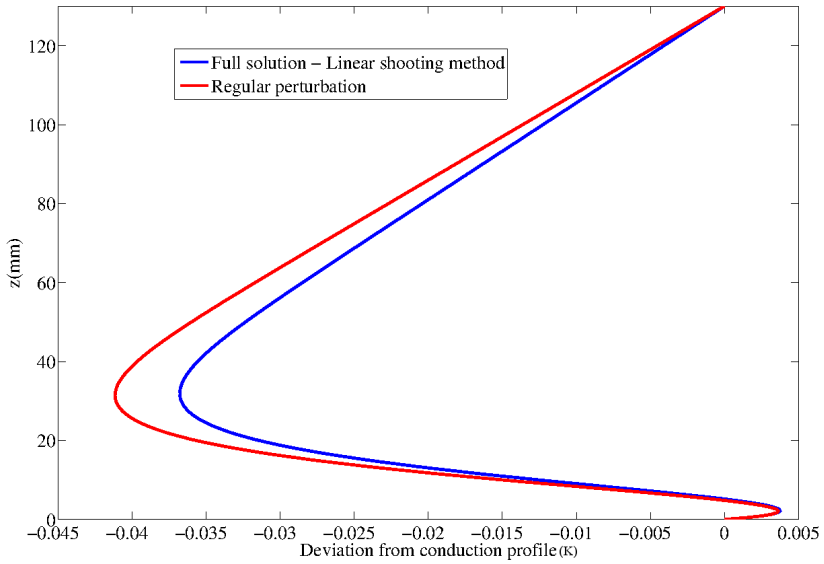

(b) Al-Al $\epsilon_1 = 0.005, \epsilon_2 = 0.005$

Figure 6.9: Deviation from the conduction profile over different surfaces. The results obtained using regular perturbation method (see equation 6.24) are compared with full numerical solution for an assumed exponential distribution of aerosol particles; the resulting optical thickness distribution is $\hat{\alpha}(z) = 1.4\mathrm{e}^{\frac{-z}{0.05}}$.

the conduction profile, although the qualitative change in the temperature profile with changing boundary emissivity for both symmetric and asymmetric configurations. This deficiency is remedied in the next sub-section where we describe an exact solution that is only restricted to the optically thin regime.

6.4.2 Radiative conductive equilibria for arbitrary $\hat{\alpha}^2\chi$

In the above analysis, we assumed the radiative forcing of aerosol particles to be weak, and that conduction was the dominant mechanism in determining the temperature profile in the test section. Herein, we relax that assumption and obtain the temperature profile for an arbitrary ratio of radiative to conductive time scales; the medium is still optically thin. The non-dimensional Milne-Eddington equation in the optically thin limit with the necessary boundary conditions was presented in the previous section (see (6.20) and (6.22)). As mentioned earlier, in this limit the governing equation for radiative transfer can be reduced to a first order differential equation, and can therefore be solved for an arbitrary concentration profile. But, the temperature profile can be obtained only for a certain family of concentration profiles because, on substitution, the resulting energy equation contains a variable coefficient (reflecting the variation of concentration profile with height) which can be solved only for certain concentration profiles. The results will be presented for an exponential variation of aerosol particle concentration with an uniform background and will be compared with the full numerical solution as well as the regular perturbation problem.

The solution of the Milne-Eddington equation (6.20), for an arbitrary concentration profile is given by:

$$F_z \;=\; c_1\hat{\alpha}_0\int_0^z f(z')dz' \;+\; 16\hat{\alpha}_0\int_0^z f(z')\theta(z')dz' + c_2. \tag{6.39}$$

Here, c_1 and c_2 are constants obtained by substituting the radiative boundary conditions (6.22) at both boundaries. Here, $f(z)$ denotes the functional form of the concentration profile. The constants are given by

$$c_1 \;=\; 2c_2v_1, \qquad \text{where} \tag{6.40}$$

$$c_2 \;=\; \frac{-8\left[1+2v_2\alpha_0\displaystyle\int_0^g f(z')\theta(z')dz'\right]}{v_1+v_2+2v_1v_2\alpha_0\displaystyle\int_0^g f(z')dz'}. \tag{6.41}$$

After substituting the flux-divergence in the energy equation, the resultant temperature profile is governed by the following differential equation:

$$\frac{d^2\theta}{dz^2} \;-\; 16\chi f(z)\left(\theta \;-\; \frac{v_1\left[1+2v_2\alpha_0\displaystyle\int_0^g f(z')\theta(z')dz'\right]}{v_1+v_2+2v_1v_2\alpha_0\int_0^g f(z')dz'}\right) \;=\; 0. \tag{6.42}$$

The radiative flux-divergence is proportional to $(\theta-\theta_{rad})$, but θ_{rad}, the radiative equilibrium

temperature now involves an unknown temperature profile (arises because of the cumulative emission of air layers which can't be neglected in the limit of low emissive surfaces), but still a constant (not a function of z), we can define $x(z) = \theta(z) - \dfrac{v_1\left[1 + 2v_2\alpha_0\int_0^g f(z')\theta(z')dz'\right]}{v_1 + v_2 + 2v_1v_2\alpha_0\int_0^g f(z')dz'}$ and the resultant equation is given by

$$\frac{d^2x}{dz^2} - 16\chi f(z)x = 0. \tag{6.43}$$

For the concentration profile consists of an exponential with a uniform background ($f(z) = f_1 + f_2e^{-z/H}$, where $f_1 = \frac{\hat{\alpha}_0}{\hat{\alpha}_0+\hat{\alpha}_1}$ and $f_2 = \frac{\hat{\alpha}_1}{\hat{\alpha}_0+\hat{\alpha}_1}$), the above equation which can be solved by using suitable variable transformation. The resultant temperature profile is given by

$$x(z) = c_3 I_{8\sqrt{f_2\chi}}\left(8\sqrt{f_2\chi}e^{\frac{-z}{2}}\right) + c_4 Y_{8\sqrt{f_2\chi}}\left(8\sqrt{f_2\chi}e^{\frac{-z}{2}}\right), \tag{6.44}$$

where $I_n(x)$ and $Y_n(x)$ are the modified Bessel functions of the first and second kind, respectively. The boundary conditions are the fixed temperatures at the two boundaries. If we substitute the resultant temperature profile in θ_{rad} and using the boundary conditions, we can obtain two equations in terms of unknown constants which can be solved. The resultant temperature profile is compared with the full solution and the above solution compares very well with the full solution in figures 6.10a and 6.11b and works better than the regular perturbation analysis. This is expected since the perturbation analysis has been solved for the limit where conduction is the dominant mechanism.

6.5 Laboratory simulation of the Ramdas layer

In this section we will describe the theoretical modeling of the laboratory Ramdas layer. In the previous analysis, concerning the experiments in the two-plate geometry, the boundaries were assumed to be opaque and fixing the top plate temperature also fixes the radiative boundary condition. However, in the atmospheric context, as explained in chapter 4, the near-surface aerosol laden layers interact effectively with the uppermost air layers, and this implies that the radiative and conductive or convective boundary conditions are de-coupled. The conductive or convective boundary condition is fixed by local heat transport mechanisms either molecular conduction or turbulent activity inside the nocturnal boundary layer, while the effective radiation temperature (denoted, for instance, by T_{sky} in the analysis in section 4.6.2) is fixed in part, by the distant much colder upper layers of the atmosphere. As argued by Mukund (2008), in order to produce LTM on much smaller length scales relevant in the laboratory, this de-coupling should be achieved.

The only earlier effort that achieves this de-coupling of the radiative and conductive boundary condition is that of Whitehead & Chen (1970). The authors achieved this de-coupling in their study of penetrative convection on the laboratory scale. To establish the desired non-monotonic density stratification from the initial stable stratification, the participating medium, mineral oil, was heated by an overlying heating lamp. To maintain the top temperature, an overlying layer of

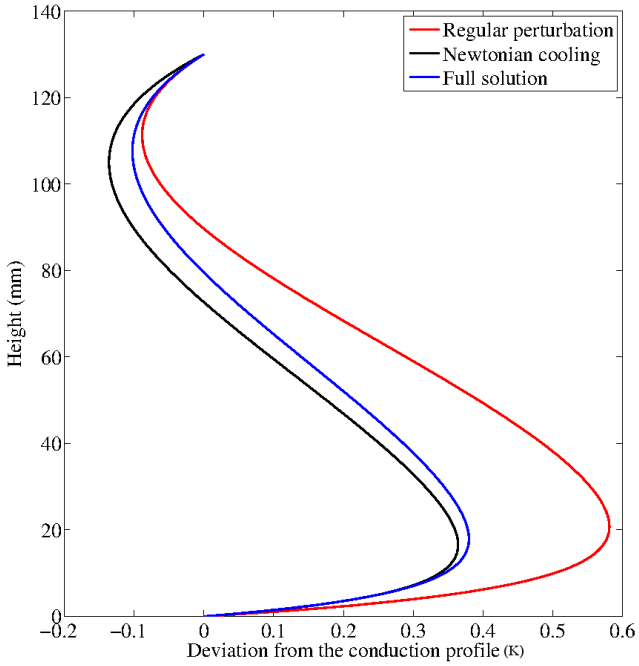

(a) Black-Black $\epsilon_1 = 1, \epsilon_2 = 1$

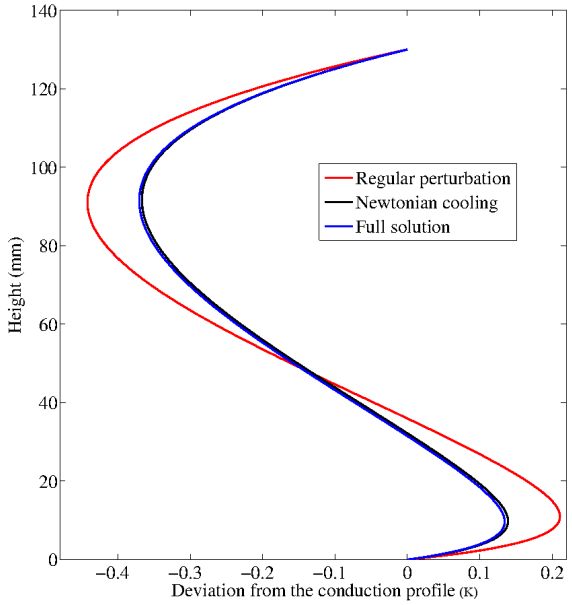

(b) Al-Al $\epsilon_1 = 0.05, \epsilon_2 = 0.05$

Figure 6.10: Deviation from the conduction profile over different surfaces. The results obtained using regular perturbation method (see equation 6.24) and Newtonian cooling approximation for arbitrary ratio of conductive to radiative time scales are compared with full numerical solution for an assumed distribution optical thickness given by $\hat{\alpha}(z) = 0.05 + 1.4\mathrm{e}^{\frac{-z}{0.05}}$.

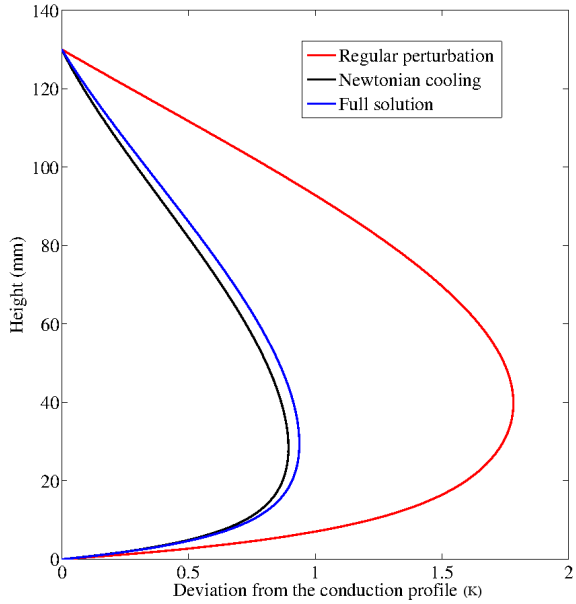

(a) Al-Black $\epsilon_1 = 0.05, \epsilon_2 = 1$

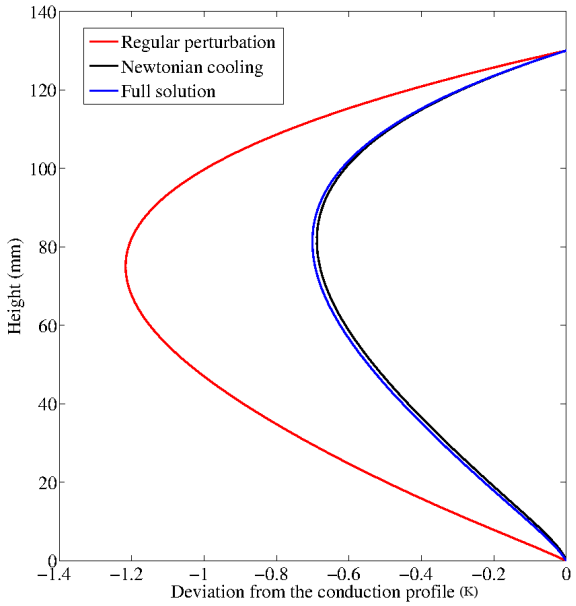

(b) Black-Al $\epsilon_1 = 1, \epsilon_2 = 0.05$

Figure 6.11: Deviation from the conduction profile over different surfaces. The results obtained using regular perturbation method (see equation 6.24) and Newtonian cooling approximation for arbitrary ratio of conductive to radiative time scales are compared with full numerical solution for an assumed distribution of optical thickness given by $\hat{\alpha}(z) = 0.05 + 1.4\mathrm{e}^{\frac{-z}{0.05}}$.

radiatively transparent fluid kerosene was used as a coolant. Apart from fixing the top conductive temperature, kerosene serves as a transparent medium through which warmer radiation from the lamp can pass through, thereby de-coupling the radiative boundary condition from conductive boundary condition. The topmost mineral oil layers absorb the warmer radiation, and since the top temperature is fixed, the temperature distribution exhibits an 'elevated maximum' leading to a region of unstable stratification near the top boundary. The resulting convection near the top boundary 'penetrates' into the stably stratified region below. Although the experiments establish the effect of non-local radiative heating in changing the base state, these effects were not modelled in their theoretical studies to study their role in stabilization. For the laboratory LTM-type profiles discussed below, radiative cooling plays a crucial role both in setting up the base state and in its enhanced stability to perturbations.

Experiments by Tiwari (2006), Mukund (2008) and Singh (2013) have successfully reproduced LTM-type temperature profiles under laboratory conditions by enforcing the aforementioned de-coupling. The experimental set-up is shown in figure 6.12. The set-up consists of a test section, an air circulation region and a 'sky' region which consists of an ice- water mixture to mimic the uppermost cold layers in the atmosphere, and thus helps enforce the crucial element of de-coupled boundary conditions. The test section is bounded by two plates, where the bottom plate mimics the ground in the atmospheric context, while the temperature of the 'top plate' (a polythene sheet), which is independently controlled by circulating air at the required temperature, mimics the local boundary condition prevalent at the top of the (developing) inversion layer in the night-time atmosphere. The transparent polythene sheet also allows for the participating medium in the test section to interact (radiatively) with the cold 'sky'. All temperature measurements were taken in the test section using a thermocouple ensemble. setting. Experiments in the set up allowed one to conclusively prove that aerosol particles are necessary to explain the phenomenon of an elevated minimum [Mukund *et al.* (2013)]. The initial LTM-type profile is formed in unfiltered air, a heterogeneous participating medium, the heterogeneity arising due to a varying concentration of aerosol particles (this variation with height arises due to a balance between sedimentation and laminar or turbulent diffusion). Next, a *HEPA* filter is used for varying durations to progressively filter out the particles of size less than $0.3\mu m$. The LTM intensity decreases with an increasing duration of filtering, and for an hour-long duration of filtering, the medium becomes sufficiently homogeneous for the temperature profile to conform to a linear conduction profile. Further, the role of surface properties and the response of the aerosol laden layers to both a 'gust episode' and a 'cloud event' were also investigated [Mukund *et al.* (2013)].

Recent experiments by Prasanna (2012) have studied the role of radiation on convective transfer via experiments where the medium interacts with a radiative sink. However, the temperature of the top plate (polythene sheet) in these experiments is determined by the interaction of the polythene sheet with the overlying cold sink, and was not independently maintained as necessary in the LTM experiments described above. These experiments were mostly aimed at assessing the feasibility of using participating gases in passive cooling technology. The idea behind this method is to achieve cooling by exposing the participating medium that emits effectively in the atmospheric window, to a cold radiative sink. The effect of the surface emissivity of the

bottom plate was also studied.

The theoretical model for the base-state temperature profile described here mimics the laboratory set-up in the Mukund (2008) and Singh (2013) experiments. The model reduces to a determination of the temperature profiles in two radiatively participating media bounded by three constant-temperature surfaces. As in the experiments, the bottom surface represents the ground, while the top surface represents the sky. For theoretical convenience, however, the air circulation region, together with the bounding polythene sheets has been modeled as a single intermediate surface of fixed temperature that therefore acts as a physical boundary between the two media. This is achieved by incorporating a heat sink (a delta function) of the required strength at the appropriate location, that then acts to de-couple the radiative and convective boundary conditions. The strength of this heat sink is given by

$$q_s = \psi_1 - \psi_2 \tag{6.45}$$

where ψ_i (i=1 and 2) are the heat fluxes in each medium on either side of the polythene sheet. This intermediate surface may be transparent or semi-transparent, and the surface-absorptivity in the latter case is to be regarded as a lumped parameter characterizing the combined absorption of the two polythene sheets with the circulation section in between.

We have modeled radiation using the Milne-Eddington approximation as in the previous section. To characterize the nature of the equilibrium profiles and to gain some insight into the influence of the various parameters, in section 6.5.1, we initially present the analysis for the case of a gray homogeneous medium and where, in addition, the surfaces are assumed to be diffuse emitters and reflectors. Later, in section 6.5.2 we will present the results for a heterogeneous medium between two parallel plates, and where the heterogeneity interacts with the colder source. These will then be compared with the experimental results of Singh (2013). In the laboratory case, since the temperature difference between the test section is small, the linearized energy equation works very well. Indeed, the results for the homogeneous medium, based on the linearized equations, have been shown to agree very well with the full non-linear numerical simulation by Mouli (2007).

6.5.1 Homogeneous medium

Herein, we present the results for a gray radiatively homogeneous participating medium. In this case one can write down the Milne-Eddington equation as follows:

$$\frac{d^2F_z}{dz^2} - 3\alpha_i^2 F_z = 4\alpha_i\sigma\frac{dT^4}{dz}, \tag{6.46}$$

where α_i, i=1 and 2, are the absorption coefficient with i=1 corresponding to the participating medium in the test section and i=2 denoting the absorption coefficients of the medium between the (upper) polythene sheet and sky. Combining (6.46) with the energy equation (6.1), one can write down the non-dimensional normalized governing equations in terms of temperature alone as follows:

$$\frac{d^3\theta_i}{dz^3} - \left(1 + 3\hat{\alpha_i}^2\chi_i\right)\left(\frac{d\theta}{dz}\right) = 3\hat{\alpha_i}^2\eta\psi + q_s\eta\delta(z-g). \tag{6.47}$$

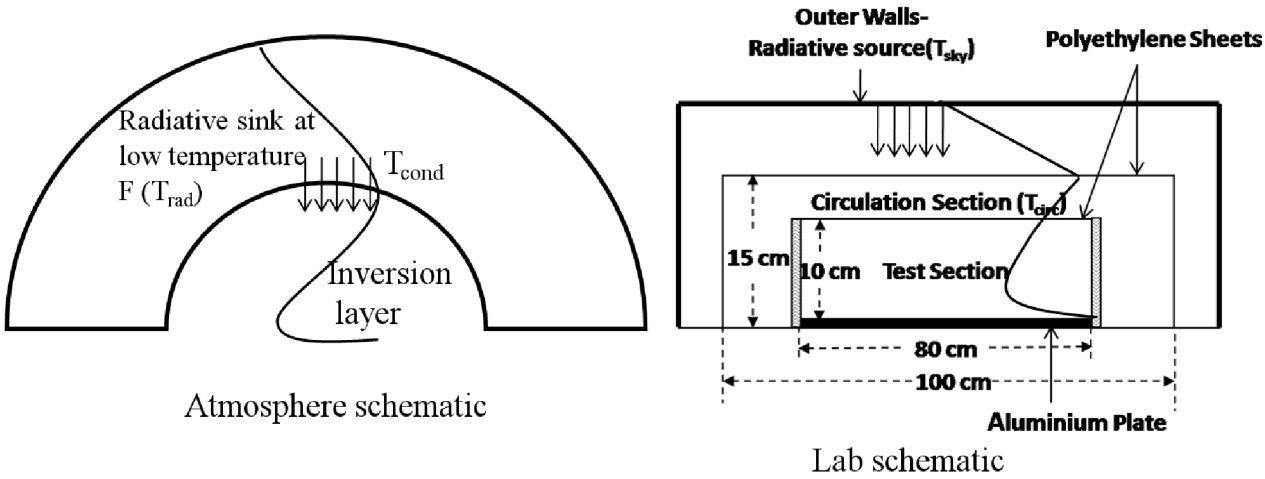

(a) Atmospheric temperature profile and corresponding experimental set-up

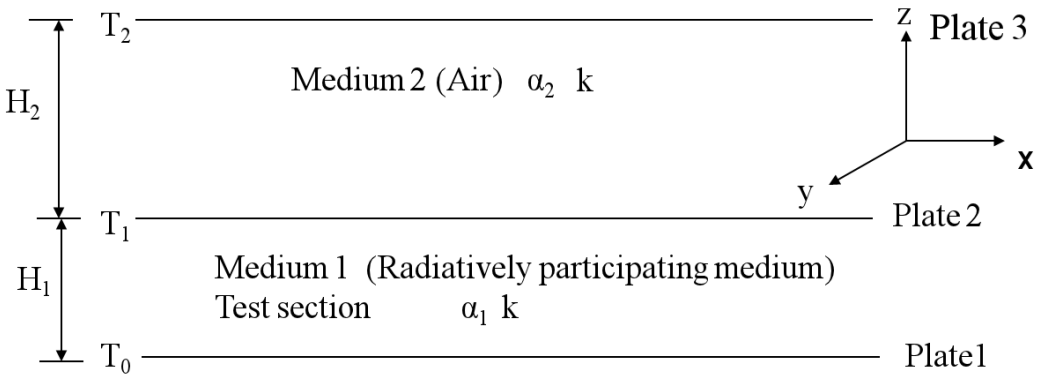

(b) Theoretical model

Figure 6.12: Schematic showing the night time temperature profile and the corresponding laboratory set-up [Tiwari (2006); Mukund *et al.* (2013)]. The corresponding theoretical modeling is shown in figure(b)

Here, $\theta = \dfrac{T - T_0}{T_2 - T_0}$ is the normalized temperature with the characteristic length scale used in the above scaling being $H_1 + H_2$. Here, the $\hat{\alpha}_i$s are constant and they can be included in the definition of the χ_i s which are now and defined as $\chi_i = \dfrac{16_c^3}{3\hat{\alpha}_i k}$ and, can directly be interpreted as the ratio of radiative to thermal conductivities. The parameters η and ψ are the ratio of the radiative flux to the conductive flux and total heat flux, respectively. The relevant non dimensional parameters are the optical thickness in both medium and χ the ratio of radiative to thermal conductivities in both medium.

The individual governing equations for the temperature profile in each domain can be written down as

$$\frac{d^3\theta_1}{dz^3} - \left(1 + 3\hat{\alpha_1}^2\chi_1\right)\left(\frac{d\theta_1}{dz}\right) = 3\hat{\alpha_1}^2\eta\psi_1 \quad , \; 0 < z < \frac{H_1}{H_1 + H_2} \tag{6.48}$$

$$\frac{d^3\theta_2}{dz^3} - \left(1 + 3\hat{\alpha_2}^2\chi_2\right)\left(\frac{d\theta_2}{dz}\right) = 3\hat{\alpha_2}^2\eta\psi_2 \quad , \; \frac{H_1}{H_1 + H_2} < z < 1 \tag{6.49}$$

There are a total of 8 unknowns (6 integration constants associated with the pair of third-order differential equations and the unknown constant fluxes in each domain), and one needs 8 boundary conditions to determine the radiative-conductive equilibrium temperature profile throughout the domain. The boundary conditions are as follows:

1. $\theta = 0$ z = 0,
2. $\theta = \theta_p$ z = g,
3. $\theta = 1$ z = 1,

   where $g = \dfrac{H_1}{H_1 + H_2}$ and $\theta_p = \dfrac{T_1 - T_0}{T_2 - T_0}$ is the fixed non-dimensional temperature of the intermediate surface. The radiative boundary conditions at the bottom and top plates are given by

4. $$\left.\frac{d^2\theta_1}{dz^2}\right|_{z=0} = \left(2v_1\hat{\alpha_1}\eta\psi_1 + 2v_1\hat{\alpha_1}\,\frac{d\theta_1}{dz}\right)\Bigg|_{z=0}, \tag{6.50}$$

5. $$\left.\frac{d^2\theta_2}{dz^2}\right|_{z=1} = \left(-2v_2\hat{\alpha_2}\eta\psi_2 - 2v_2\hat{\alpha_2}\,\frac{d\theta_2}{dz}\right)\Bigg|_{z=1}, \tag{6.51}$$

   in non-dimensional form, as before, (see (6.7) in section 6.3.1) where ϵ_1 and ϵ_2 are the bottom and top plate emissivities, respectively, and

$$v_1 = 2\left(\frac{1}{\epsilon_1} - \frac{1}{2}\right), \tag{6.52}$$

   and

$$v_2 = 2\left(\frac{1}{\epsilon_2} - \frac{1}{2}\right). \tag{6.53}$$

   The matching boundary conditions at the second plate ($z = g$) are obtained by taking a radiation balance for infinitesimal thin layers above and below at the semi-transparent plate (see figure 6.13), whence one obtains:

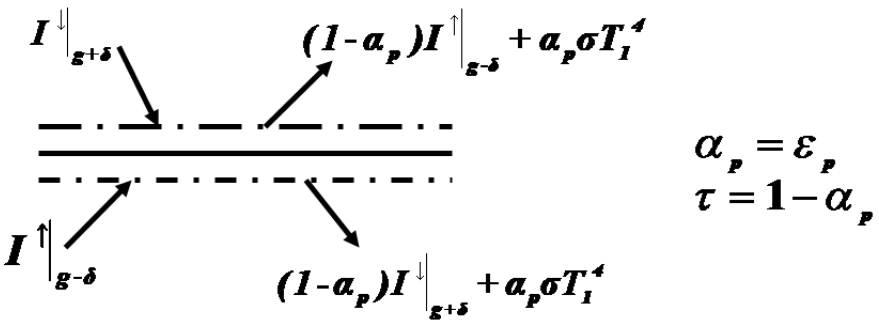

Figure 6.13: Radiative balance at the semi-transparent plate

$$I^{+}\big|_{g+\delta} = (1-\alpha_p)\, I^{+}\big|_{g-\delta} + \alpha_p \sigma T_1^4, \tag{6.54}$$

$$I^{-}\big|_{g-\delta} = (1-\alpha_p)\, I^{-}\big|_{g+\delta} + \alpha_p \sigma T_1^4. \tag{6.55}$$

Here, α_p is the emissivity of polythene sheet. Substituting (6.54) and (6.55) in (6.4) and (6.5) and eliminating the other component of intensity one can write down the radiative balance in terms of the flux as:

$$\frac{1}{\alpha_1}\frac{dF_z}{dz}\bigg|_{g-\delta} - \frac{1}{\alpha_2}\frac{dF_z}{dz}\bigg|_{g+\delta} + \frac{2\alpha_p}{2-\alpha_p}\left[F_z\big|_{g-\delta} + F_z|_{g+\delta}\right] = 0, \tag{6.56}$$

$$\frac{1}{\alpha_1}\frac{dF_z}{dz}\bigg|_{g-\delta} - \frac{1}{\alpha_2}\frac{dF_z}{dz}\bigg|_{g+\delta} + \frac{2(2-\alpha_p)}{\alpha_p}\left[F_z\big|_{g-\delta} - F_z|_{g+\delta}\right] = 0. \tag{6.57}$$

The non dimensional form is

6.

$$\frac{1}{\hat{\alpha_1}}\frac{d^2\theta_1}{dz^2}\bigg|_{g-\delta} - \frac{1}{\hat{\alpha_2}}\frac{d^2\theta}{dz^2}\bigg|_{g+\delta} + \frac{2\alpha_p}{2-\alpha_p}\left[\eta\psi_1 + \frac{d\theta}{dz}\bigg|_{g-\delta} + \eta\psi_2 + \frac{d\theta}{dz}\bigg|_{g+\delta}\right] = 0, \tag{6.58}$$

7.

$$\frac{1}{\hat{\alpha_1}}\frac{d^2\theta_1}{dz^2}\bigg|_{g-\delta} - \frac{1}{\hat{\alpha_2}}\frac{d^2\theta}{dz^2}\bigg|_{g+\delta} + \frac{2(2-2\alpha_p)}{\alpha_p}\left[\eta\psi_1 + \frac{d\theta}{dz}\bigg|_{g-\delta} - \eta\psi_2 - \frac{d\theta}{dz}\bigg|_{g+\delta}\right] = 0. \tag{6.59}$$

For a transparent polythene sheet ($\alpha_p = 0$) the above relations reduce to

$$\frac{d\theta}{dz}\bigg|_{g-\delta} - \frac{d\theta}{dz}\bigg|_{g+\delta} = \eta(\psi_2 - \psi_1), \tag{6.60}$$

$$\frac{1}{\hat{\alpha_1}}\frac{d^2\theta}{dz^2}\bigg|_{g-\delta} = \frac{1}{\hat{\alpha_2}}\frac{d^2\theta}{dz^2}\bigg|_{g+\delta}. \tag{6.61}$$

One can directly write down the relations for a transparent polythene sheet based on the continuity of the radiative fluxes and flux divergences at $z = g$.

The above constant coefficient equations can now be solved analytically and the temperature

profile in the two domains are of the form:

$$\theta_1 = \frac{c_1 e^{p_1 z}}{p_1} - \frac{c_2 e^{-p_1 z}}{p_1} - \frac{\eta \psi_1 z}{(1+\chi_1)} + c_3, \tag{6.62}$$

$$\theta_2 = \frac{d_1 e^{p_2 z}}{p_2} - \frac{d_2 e^{-p_2 z}}{p_2} - \frac{\eta \psi_2 z}{(1+\chi_2)} + d_3. \tag{6.63}$$

As defined earlier, $p_1^2 = 3\hat{\alpha_1}^2(1+\chi_1)$ and $p_2^2 = 3\hat{\alpha_2}^2(1+\chi_2)$ denote the non dimensional conductive boundary layer thicknesses now measured in units of (H_1+H_2). Using the boundary and matching conditions above, one can obtain the constants in the (6.62) and (6.63) and these constants are given in appendix B. The results for different parameter values are presented in what follows.

Results

The radiative conductive equilibria for the entire domain, as given by (6.62) and (6.63), are plotted in figure (6.14a). Only the test-section temperature profiles are shown in figure 6.14b for different optical thicknesses ($\hat{\alpha_1}$). The ground temperature is taken to be $T_0 = 300.5\,K$, while the polythene and sky temperatures are assumed to be $T_1 = 303.5\,K$ and $T_2 = 282.5\,K$, respectively. Further, the second plate is assumed to be transparent ($\alpha_p = 0$) and the two boundaries are assumed to be black ($\epsilon_1 = \epsilon_2 = 1$) - these values are taken from the experiments. For small optical thicknesses ($\hat{\alpha_1} \ll 1$), the medium is transparent and the profile is close to a linear conduction profile. As the optical thickness increases, the medium interacts with the colder sky, and above a threshold value of $\hat{\alpha_1} \approx 0.05$, there is an elevated minima, that is, an LTM-type profile. The height and the intensity of the minima increases as one increases the optical thickness of the medium (the intensity and the height being defined with respect to the bottom plate). This is expected as the topmost layers of the medium in the test section, on account of their increased absorptivity, interacts effectively with the colder radiation and the minimum temperature occurs closer to the top plate. The trend involving the increase in intensity of the minimum reverses when $\hat{\alpha}$ is increased beyond values of order unity. This is due to the attenuation of colder radiation that reaches any given location in the test section because of a shielding effect, that is, the absorption of colder radiation by the top most air layers in the test section. The height of the minimum will, however, be still close to the top plate.

Next, we study the effect of the boundary emissivities on the LTM characteristics. To begin with, the emissivity of the bottom plate is varied with the emissivity of the top plate (sky) assumed to be unity, and the polythene sheet assumed to be transparent. The optical thicknesses of both media are assumed to be 0.05 (in the optically thin limit). The equilibrium temperature profiles for different bottom surface emissivities are shown in figure 6.15a. When the surface emissivity is reduced the intensity of the minimum increases. This is because the reflected component now consists of downwelling radiation from the colder sink and the effective absorption of this colder radiation is responsible for the increase in intensity. On the other hand, if one decreases the emissivity of the second plate (sky), the intensity of the minima decreases (see figure 6.15b). This is due to the effective colder radiation, is available to the medium in the test section, being reduced due to weaker emission. Next, the transmissivity of the polythene sheet is changed to see its effect on the LTM intensity and the resulting profiles are shown in

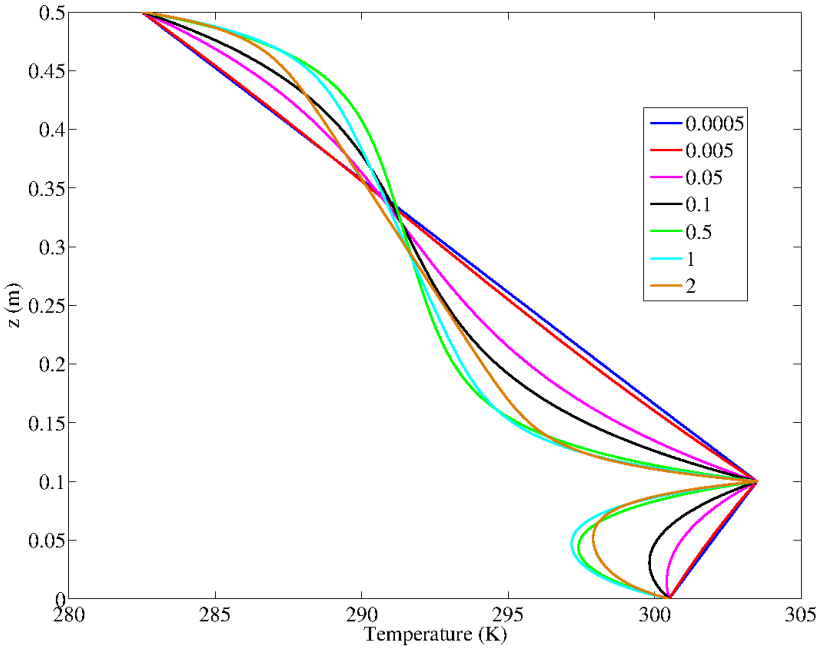

(a) Absolute temperature profile in the entire domain

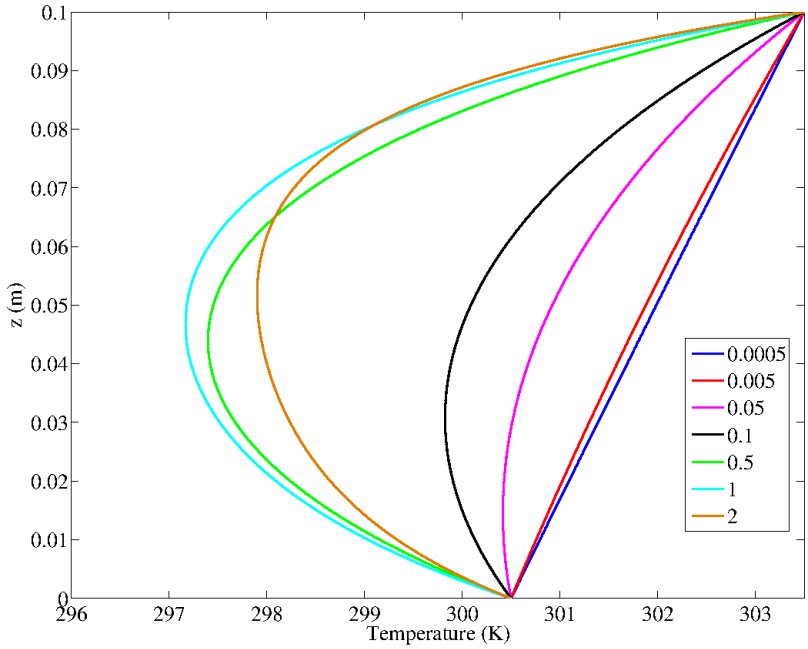

(b) Absolute temperature profile in the test section

Figure 6.14: Plot (a) shows temperature profile for various optical thickness ($\hat{\alpha}$) in the entire domain while in plot(b) the equilibrium profile only in the test section is plotted. The polythene sheet is assumed to be fully transparent. The bottom and top plate is assumed to be black. The temperatures of the plates are assumed to be $T_0 = 300.5\,K, T_1 = 303.5\,K$ and $T_2 = 282.5\,K$

figure 6.16a. When the transmissivity of the polythene sheet is reduced, the intensity of the minimum decreases (note that the polythene sheet is maintained at the highest temperature). The temperature profiles for different sky temperatures is presented in figure 6.16b. When the sky temperature is increased the intensity of minima starts decreasing, and one eventually has a monotonic temperature profile.

In the above analysis, we have neglected convection in the second domain despite it being unstably stratified. For the temperature difference between the polythene sheet and sky ($\approx 20\,K$) and the height of the second medium, the estimated Rayleigh number is $O(10^8)$. The quantitative significance of the above analysis is therefore limited, since, on one hand, there will be a sensible heat flux on account of convective fluctuations, and on the other hand, the radiative flux will be modified on account of the expected modification to the mean temperature profile. Hence, the present analysis is more for purposes of illustrating the dependence of the equilibrium profile on the different physical parameters. Importantly, since the participating medium is air which is transparent in the IR range, the detailed nature of the temperature profile in the domain 2 doesn't play a significant role and the boundary emission dominates the interaction between the air layers. Hence, despite the convective instability in the second medium one may model the equilibrium profile in the test section by incorporating the source (sky) as a radiative boundary condition at the polythene sheet itself which we do in the next section.

The length scale and intensity of the LTM are expected to be insensitive to the aforementioned details, and are expected to behave in a manner similar to that shown in figure 6.16b. The experimentally measured temperature profile, obtained by Mukund (2008), is as shown in figure 6.17. The measured intensity for a black bottom surface is about 0.5 K and the height of the minima is about 8 mm. For the same intensity, this length scale is only 25% of that characterizing the homogeneous LTM. Clearly, LTM-type profiles in a homogeneous medium cannot capture both the intensity and the height of the minimum. Physically, this should be expected, since the homogeneous medium is largely transparent on length scales of the order of the test section height. Since photon mean free paths are much larger than the height scale of interest, the only relevant length scale for the homogeneous equilibrium is the height of the test section, and hence, the height of the homogeneous medium is expected to scale with the test section height.

6.5.2 Heterogeneous medium

In the last section, we presented the results for a radiatively gray homogeneous participating medium, sandwiched between two plates, which can effectively interact with the colder sink. The most important inference, from the analysis, is the disparity in the length scale characterizing the height of the laboratory LTM in relation to that observed in experiments, clearly pointing to the role of medium heterogeneity. In this section, we therefore analyze the equilibrium temperature profile, in the de-coupled system under consideration, when the participating medium is rendered heterogeneous due to a varying concentration of (suspended) aerosol particles. Thus, the absorption coefficient is now a function of height z, and the same absorption coefficient stratification as that used in the two-plate experiments described earlier in section 6.3.2 is used. Such an assumption is consistent with a similar 'preparation' being used for the unfiltered air

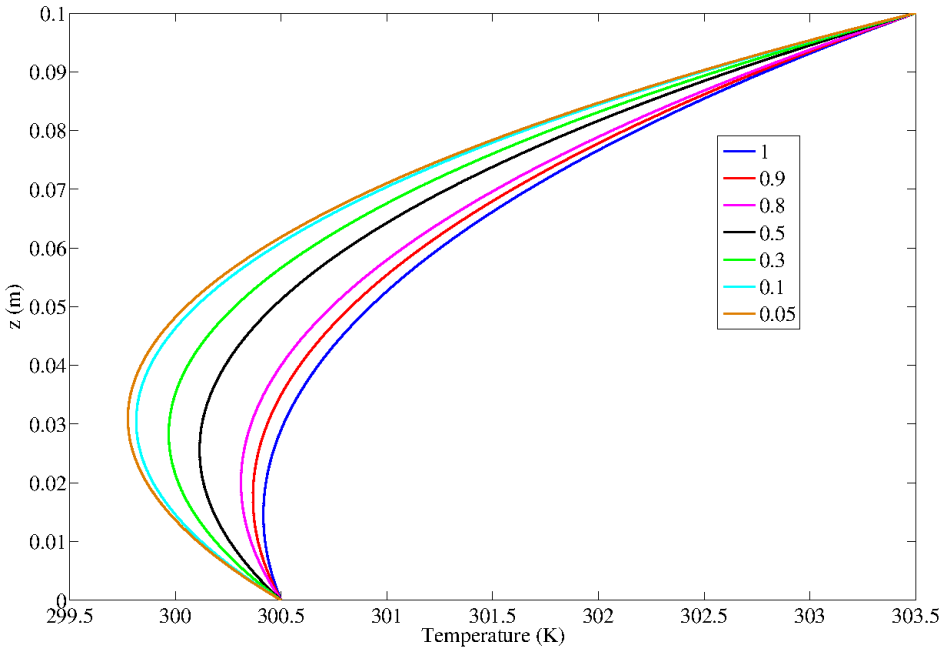

(a) Temperature profile for different bottom plate emissivities

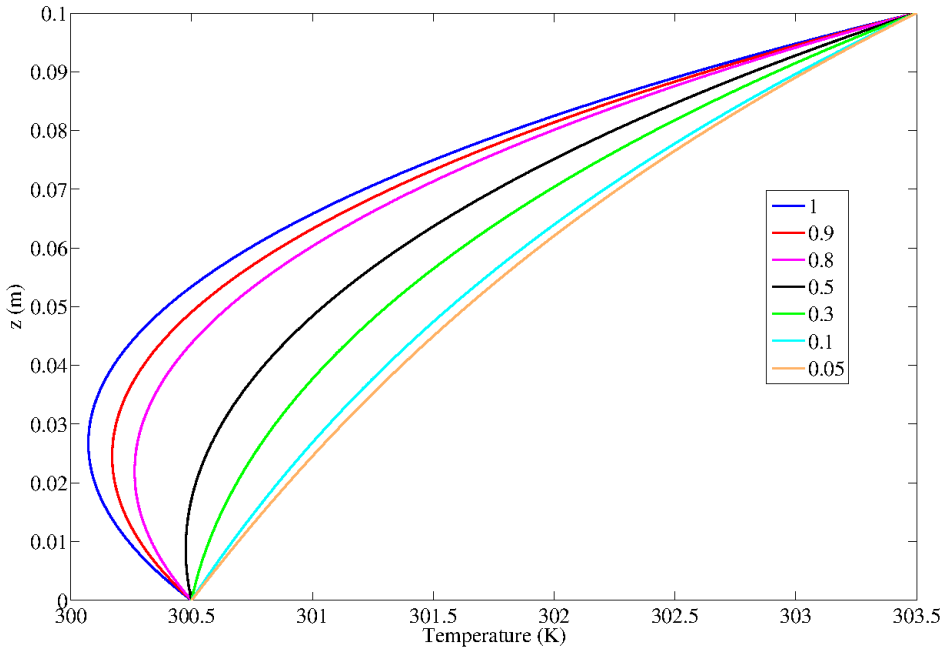

(b) Temperature profile for different top plate emissivities

Figure 6.15: Plot (a) shows temperature profile for different bottom plate emissivities. The optical thickness is $\hat{\alpha} = 0.05, T_0 = 300.5\,K, T_1 = 303.5\,\text{and}\,T_2 = 282.5\,K$. The polythene sheet is assumed to be fully transparent and top plate is assumed to be black. Plot(b) shows temperature profile for different top plate emissivities and the bottom plate is assumed to be black. The rest of the parameters are same as above.

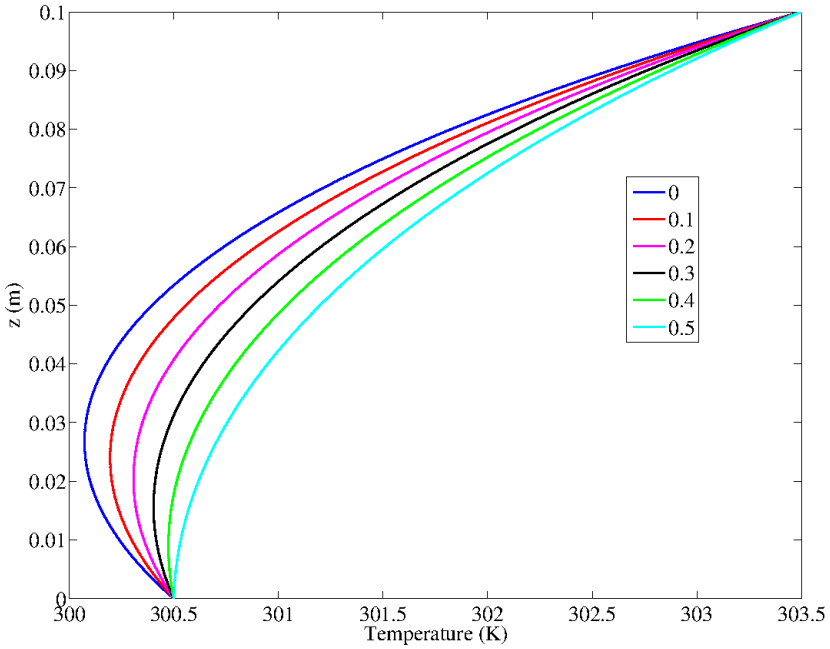

(a) Temperature profile for different polythene transmissivities

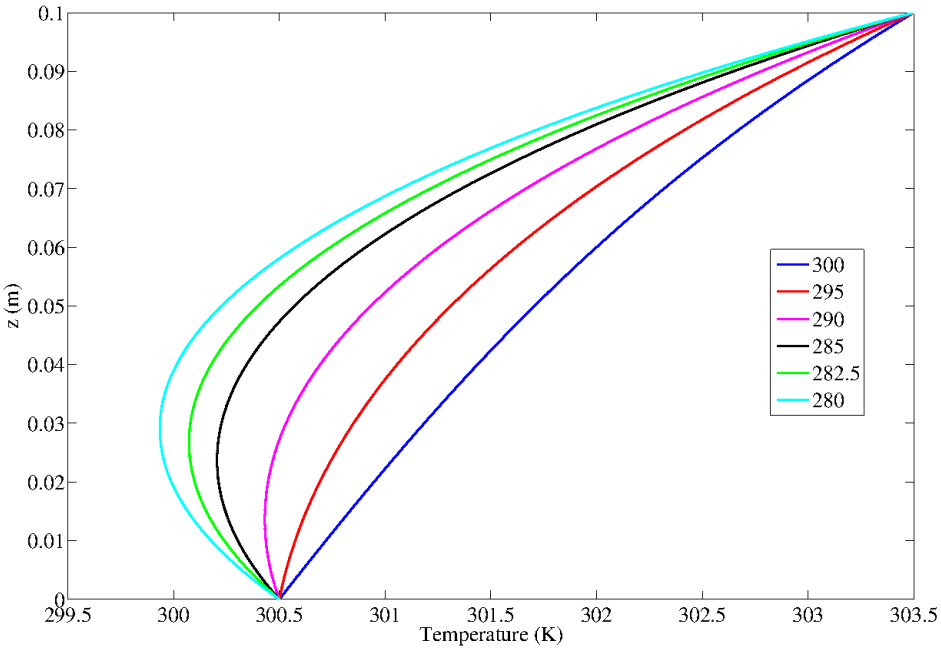

(b) Temperature profile for different polythene transmissivities

Figure 6.16: Plot (a) shows temperature profile for different polythene transmissivities. The optical thickness is $\hat{\alpha} = 0.05, T_0 = 300.5\,K, T_1 = 303.5\,K$ and $T_2 = 282.5\,K$. The bottom and top plates are assumed to be black. while plot (b) shows the temperature profiles for different sky temperature. The rest of the parameters are same as above.

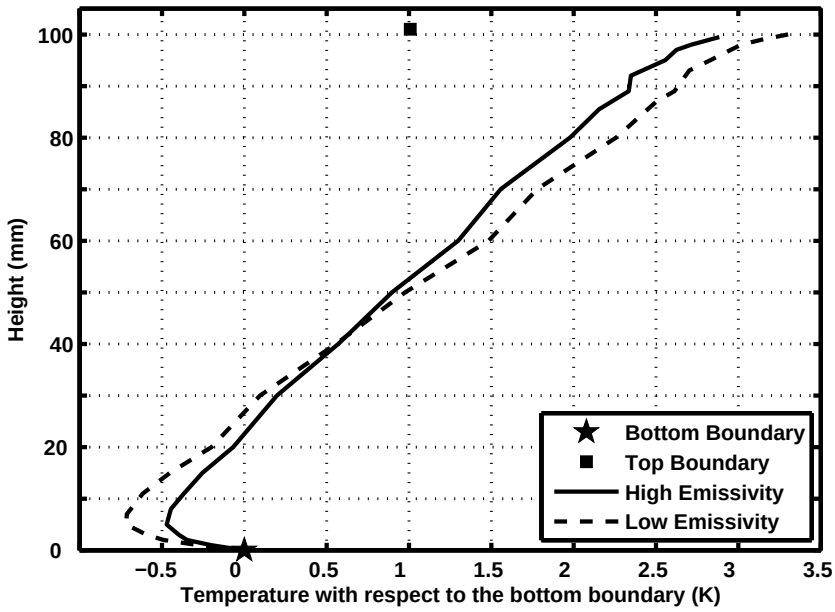

Figure 6.17: Typical LTM profiles observed in laboratory for two different surface emissivities [Mukund (2008)].

medium in all experiments. In the earlier section, intended more for illustrative purposes, we considered the radiative-conductive equilibrium that results in medium 2 despite the very stringent limitation imposed by the unstable stratification. Here, recognizing the transparency of this medium, and the small magnitude of its emission in relation to the cold source itself, we do not treat the medium 2 explicitly. Instead the effect of the cold source is incorporated via the radiative temperature of the downwelling intensity at the polythene sheet, this temperature being different from the sheet emission temperature. Thus, we assume the downwelling intensity at the polythene sheet is given by σT_2^4 and emission from the plate is σT_1^4. If one substitutes these in equations (6.4) and (6.5), the resultant boundary condition is given by

$$\left.\frac{dF_z}{dz}\right|_{z=h} = 4\alpha(h)\sigma\epsilon_p T_1^4 - 4\alpha(h)(1-\epsilon_p)\sigma T_2^4 - 2\alpha\, F_z|_{z=h}\,. \tag{6.64}$$

The non dimensional form of the of the boundary condition in terms of the normalized temperature profile, is

$$\left.\frac{d^2\theta}{dz^2}\right|_{z=1} = 4\eta\hat{\alpha}(1)\epsilon_p\hat{T}_1^4 - 4\eta\hat{\alpha}(1)(1-\epsilon_p)\hat{T}_2^4 - 2\hat{\alpha}\eta\psi - 2\hat{\alpha}\left.\frac{d\theta}{dz}\right|_{g-\delta}. \tag{6.65}$$

Here, $\hat{T}_1$ and $\hat{T}_2$ are the non-dimensional temperatures of the polythene sheet and top plate (sky), respectively. The governing equation, (6.3), along with the conductive boundary condition at both the boundaries, the bottom radiative condition, and equation (6.65), can again be solved numerically using the linear shooting method described earlier in section 6.3.

The resultant temperature profile along with the experimental observations are shown in figures 6.18 and 6.19 (LHS plots) for a high and low emissivity bottom surface, respectively.. The results show good agreement between theory and experiments, and consistent with the measurements, a higher intensity LTM is observed for the low emissivity surfaces. The corresponding

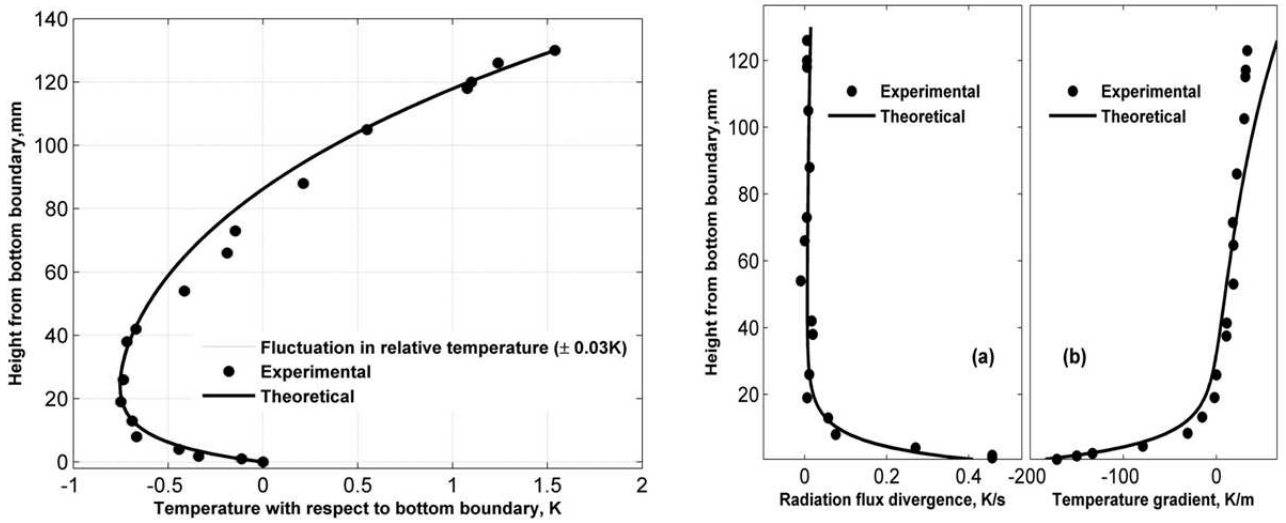

(a) Temperature profile

(b) Temperature gradient and radiative flux divergence

Figure 6.18: Temperature profiles in the test-section for black ($\epsilon_g \approx 0.9$) bottom boundary T_2 is held 280 K, while T_g is at 300 K. solid symbols correspond to experimental observation . solid curve represent the result of theoretical calculation, where optical thickness distribution is $\hat{\alpha}(z) = 1.4\mathrm{e}^{\frac{-z}{0.05}} + 0.05$. Radiative flux divergence and temperature gradient with respect to height in fig (a) and fig (b) respectively.

radiative flux divergence and temperature gradients profiles are plotted, in figures 6.18 and 6.19 (RHS plots). The temperature gradients are $O(100\,\mathrm{Km}^{-1})$. Note that the gradient and radiative cooling rate values are an order of magnitude smaller than the field values. The intensity and the height of the minima are again smaller than the observed values in the field. As mentioned earlier in section 6.3.2, the main reason for these differences is the compressed vertical scale in the laboratory set-up, which enhances the conductive fluxes (by a factor of 8-10) in relation to radiative fluxes.

Simulation of a cloud event

Apart from reproducing LTM on laboratory scales, the response of the aerosol-laden air layers to a 'gust episode' and to a 'cloud' event has been studied extensively in the laboratory [Mukund *et al.* (2013)]. The theoretical modeling for the 'cloud' event is presented here by studying the relaxation response of the laboratory LTM to a change in the radiative boundary condition. This change is achieved, experimentally, by a 'blocking experiment', where an opaque sheet is inserted above the air circulation section to prevent any interaction between the aerosols and the cold sink. This resembles a passing cloud-cover in the atmospheric context. The expected response is a transition from an initial LTM-type profile, arising from an interaction with a distant cold sink, to a two-plate profile characteristic of a heterogeneous medium and the particular combination of boundary emissivities (bottom plate and the polythene sheet). As seen earlier in section 6.3, the latter profile, although asymmetric, does not exhibit an elevated minimum.

The 'cloud event' is simulated theoretically within the simplified framework, where the radiative flux divergence is given by a Newtonian cooling approximation, by incorporating a sudden change in the radiative sink temperature at a certain instant of time (this assumes that the

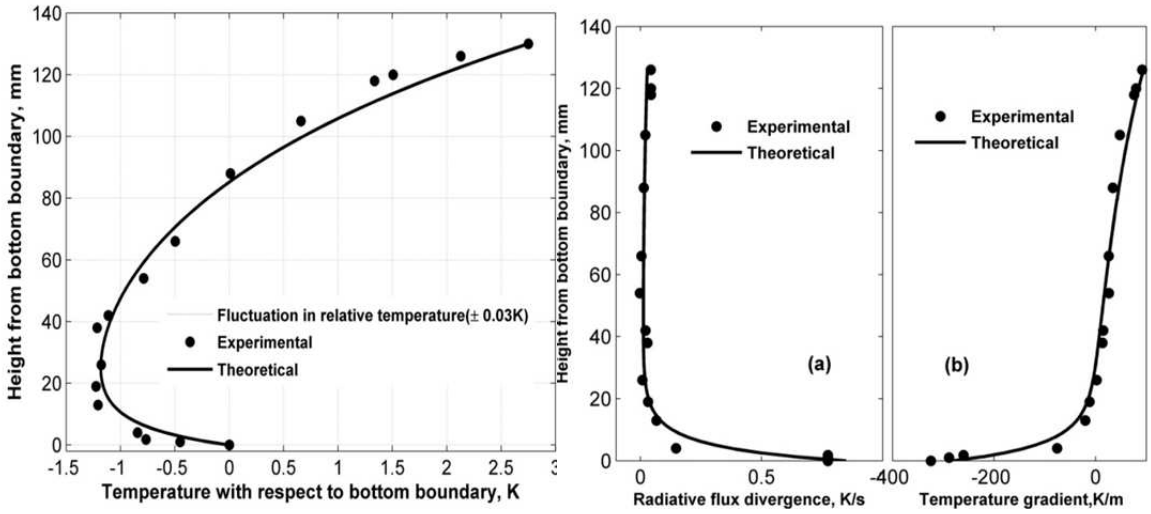

(a) Temperature profile (b) Temperature gradient and radiative flux divergence

Figure 6.19: Temperature profiles in the test-section for black ($\epsilon_g \approx 0.05$) bottom boundary T_2 is held 280 K, while T_g is at 300 K. solid symbols correspond to experimental observation . solid curve represent the result of theoretical calculation, where optical thickness distribution is $\hat{\alpha}(z) = 1.4e^{\frac{-z}{0.05}} + 0.05$. Radiative flux divergence and temperature gradient with respect to height in fig (a) and fig (b) respectively.

time scale for moving the opaque sheet into position is much smaller than any characteristic relaxation time of the system). It has already been seen, in the context of the two-plate problem, that the Newtonian cooling approximation is a very good assumption (this has also been verified by comparing the solution, with this approximation,

$$\frac{k}{\rho C_p}\frac{d^2T_e}{dz^2} = \frac{T_e - T_{rad1}}{\tau_{rad(z)}}, \tag{6.66}$$

where T_{rad1} is the radiative sink temperature that leads to an LTM-type profile and τ_{rad} is the intrinsic radiative time scale that is proportional to the local aerosol concentration. The unsteady energy equation is

$$\frac{\partial T}{\partial t} = \frac{k}{\rho C_p}\frac{\partial^2 T}{\partial z^2} - \frac{T - T_{rad2}}{\tau_{rad}}, \tag{6.67}$$

where T_{rad2} is the hypothetical isothermal radiative equilibrium that the medium would attain at the end of the blocking period in the absence of conductive boundary conditions. Since we have $T = T_e(z)$ at t = 0, the problem is more conveniently formulated in terms of a perturbation about the initial radiative-conductive equilibrium. The resulting equation for the perturbation temperature, $\theta' = T - T_e(z)$, is

$$\frac{\partial \theta'}{\partial t} = \frac{k}{\rho C_p}\frac{\partial^2 \theta'}{\partial z^2} - \frac{\theta' - \Delta T(z)}{\tau_{rad}} \tag{6.68}$$

where $\Delta T(z)$ is the difference in the radiative equilibrium temperatures before and after blocking. The evolution from an LTM-type profile to one that does not exhibit an elevated minimum, due to a 'cloud event', is shown in figure 6.20, It is evident from figure 6.20a, which shows the

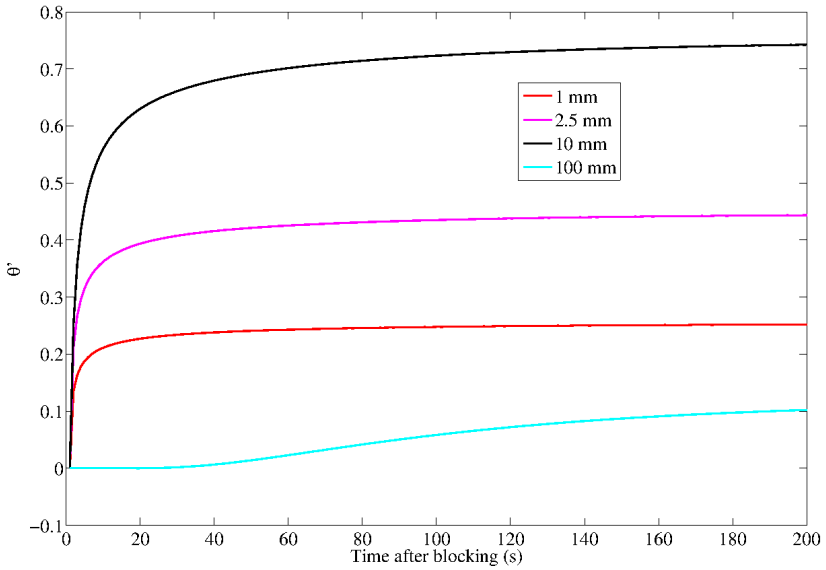

(a) Temperature trace

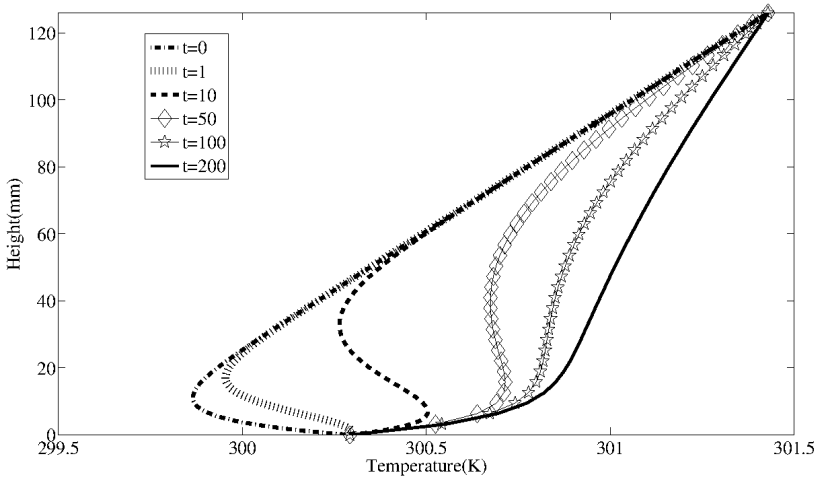

(b) Absolute temperature profile

Figure 6.20: Evolution of the laboratory LTM-type profile due to a screening of the radiative sink.

perturbation temperature-time series at different vertical location, that the concentrated aerosol-laden air layers near the bottom plate, on account of their enhanced emissivities, equilibrate faster than the upper layers due to radiation.

6.6 Conclusions and outlook

Theoretical predictions for the equilibrium temperature profiles arising in a radiatively participating heterogeneous medium sandwiched between two horizontal plates have been presented. The results compare favorably with experiments [Singh (2013)], and show that a significant and asymmetric deviation from the linear conduction profile occurs due to suspended aerosol particles (in unfiltered air). Variation in the boundary emissivities leads to qualitative differences in the nature of the asymmetry in the equilibrium profiles. The radiative forcing predicted and

that measured in the experiments, exceed that obtained in similar laboratory experiments, but with purified gases such as CO_2 and NH_3, by at least an order of magnitude. Thus, the results in this chapter emphasize the importance of aerosol-induced radiative forcing on laboratory length scales. It has already been shown, in the atmospheric context, that the existence of such a heterogeneity, is necessary to explain the origin of an eighty-year-old paradox - the Ramdas layer (see chapter 4). Finally, we have also simulated the Ramdas layer on the laboratory scale and its response to a 'cloud' event. The response is spatially very heterogeneous with the air layers containing the highest aerosol concentrations, and outside the conductive boundary layer, heating up at the fastest rates.

Chapter 7

Conclusions and Future Work

This thesis focusses on the role of radiative heat transfer in determining the nocturnal boundary layer (NBL) that develops over land, in particular, the thermal structure of the lowest meters of the NBL. Detailed conclusions are provided at the end of each chapter. However an overview is provided here followed by a list of future studies that needs to be taken up.

In chapter 2, we have shown that the extension of the broadband flux-emissivity scheme over a non-black surface is erroneous. The error arises, because of an incorrect use of flux-transmissivity to attenuate the reflected component. The error results in a spurious cooling in the opaque-bands near the surface and exaggerate the role of ground emissivity on radiative cooling-rate profiles. We have obtained a correct transmissivity that eliminates the aforementioned spurious cooling, and predicts that there is no qualitative difference in the NBL structure that develops over black and gray surfaces.

In chapter 3, we extend the correct broadband flux-emissivity scheme to include the multiple reflection between two reflective surfaces that are relevant in both laboratory (a configuration commonly employed to study the interaction of radiation with other heat transport mechanisms) and atmospheric contexts (interaction of a cloud cover with a gray surface). The emissivity scheme is also extended to incorporate directional characteristics of both medium and surface emissions, and this avoids the diffusivity-factor approximation that is typically used to replace the angular integral in the monochromatic fluxes. Further, we have shown that the error is not only restricted to the broadband flux-emissivity schemes and in fact, present in all the frequency parameterized schemes that doesn't fully resolve the finest scale in the spectrum that is, the elementary line width.

The origin of a micrometeoritic paradox called Ramdas layer is discussed in chapter 4. A relatively recent theory so called VSN model, which attempts to explain the origin of this phenomenon is based on broadband flux-emissivity scheme. This is a serious instance, where the aforementioned spurious cooling is interpreted as a reason for the origin of this phenomenon. However, this cooling is spurious and the inevitable conclusions are preferential cooling of air layers cannot occur in a compositionally homogeneous atmosphere and inhomogeneity on the length scale of the Ramdas layer is necessary to explain the origin of this phenomenon. The field observations by Mukund *et al.* (2013) conclusively proves that there is an intrinsic cooling mechanism associated with the lowermost air layers and they cool faster than the ground. The steep variation of suspended aerosol particles near the ground which effectively interacts with the uppermost colder air layers could be a candidate for this inhomogeneity. Recent experiments by Singh (2013), shows that suspended aerosol particles are indeed necessary to explain the origin of this phenomenon.

In chapter 5 and 6 we studied the role of aerosol radiative forcing in determining the structure of NBL, both in the atmospheric and laboratory contexts. In the former case, the NBL

temperature profile was shown to primarily depend on a non dimensional parameter called Ramdas-Zdunkowski factor which is the ratio of air and ground cooling rates. This helps in discriminating between the inversion and the LTM-type regimes. Theoretical analysis which includes the radiative forcing by aerosol particles successfully predicted the LTM-type profile. The role of aerosol radiative forcing is studied under laboratory conditions by Singh (2013). The theoretical temperature profiles predicted by solving the energy equation, with the Milne-Eddington approximation for the radiative flux, and that includes the radiative forcing of the suspended aerosols, matched well with experiments and the role of surface emissivity is studied in altering the temperature profile.

The present work has opened up some interesting questions which require further investigations and some of them are mentioned below.

1. The role of aerosol radiative forcing on the stability of the Ramdas layer has to be carried out in a consistent manner. The estimated Rayleigh number is $O(10^4)$ times the threshold for the onset of Rayleigh-Benard convection. Although, the role of radiation in stabilizing Rayleigh-Benard convection has been studied extensively in the literature [Goody (1956);Larson (2000)], the role of the radiative forcing due to a particulate inhomogeneity, that is itself convected by an imposed perturbation, and in addition, sediments and diffuses relative to the flow, has not been studied. Further, in the case of Ramdas layer, radiation is the main agent that establishes this unstable temperature profile. Recent experiments by Singh (2013) shows this layer is not quiescent and there is an overturning instability although there is still a significant radiation-induced stabilization. Hence, understanding the role of radiation in stabilizing this layer is an interesting extension to carry out.

2. The intensity and height of the minimum are sensitive to turbulence levels and a passage of cloud cover. The response of aerosol-laden layers to a 'gust episode' which is a 'homogenization event' and a 'cloud event' (which blocks the interaction of lowermost layers with the cold sky) needs to be studied.

3. In chapter 5, we solved the equation with the ground temperature specified as a function of time. However, this is reasonably good for high R_f surfaces. A full air-soil coupled problem will avoid this restriction and ground temperature will be determined from the surface energy budget that also includes the radiative effects of water vapor.

4. In micrometeorology, experimental sites need a large fetch to height ratio to measure the vertical temperature profile and fluxes intrinsic to that surface. Otherwise the measurements will be contaminated due to advection. Not many theoretical studies have been carried out to include the effect of radiation in determining the fetch. In the light of above, one has to include the role of aerosol particles to determine the fetch.

Appendix A

Governing equation for two-band formulation

In this Appendix, we present the derivation of net fluxes used in section 4.6.2 to obtain the equilibrium temperature profile. The flux divergence is given by

$$\frac{dF}{du} = \int_0^u \frac{d\epsilon^f(u-u')}{du}\frac{d(\sigma T^4)}{du'}du' + \int_u^{u_t}\frac{d\epsilon^f(u'-u)}{du}\frac{d(\sigma T^4)}{du'}du' - \sigma T^4(u_t)\frac{\epsilon^f(u_t-u)}{du}. \quad \text{(A.1)}$$

Here, $\epsilon^f(u)$ includes the contributions of both water vapor and aerosol. The derivative of the flux-emissivity may be obtained using $\frac{d\epsilon^f(u)}{du} = -\frac{d\tau^f(u)}{du}$:

$$\frac{d\tau^f(u)}{du} = \tau_{aerosol}(z)\frac{d\tau^f_{wv}(u)}{du} + \tau^f_{wv}(u)\frac{d\tau^f(z)_{aerosol}}{dz}, \quad \text{(A.2)}$$

with $\tau_{aerosol}(z) = \mathrm{e}^{\int_0^z \alpha(z')dz'} = \mathrm{e}^{\int_0^z A\alpha_h n(z')dz'}$

To obtain the equation for small ζ_0 analysis, we will restrict to two bands that is, window and non-window bands. The contributions in each band can be written separately as follows:

In the non-window band the flux-divergence is given by

$$\frac{dF}{du} = f_{nw}\left[\int_0^u \frac{d\epsilon^f_{nw}(u-u')}{du}\frac{d(\sigma T^4)}{du'}du' + \int_u^{u_t}\frac{d\epsilon^f_{nw}(u'-u)}{du}\frac{d(\sigma T^4)}{du'}du' - \sigma T^4(u_t)\frac{\epsilon^f_{nw}(u_t-u)}{du}\right]. \quad \text{(A.3)}$$

In the above expression, the effect of suspended aerosol particles is neglected in the non-window band. Similar expression can be obtained in the window band also. If one integrates by parts and assuming the balance close to the ground then

$$\frac{dF}{du} = A\alpha_h n(z)\sigma f_w\left[2T^4 - T_g^4 - \hat{T}^4_{sky}\right], \quad \text{(A.4)}$$

where

$$\hat{T}_{sky} = \left[\int_0^{u_t} T^4(u')(AQ_{ext}n(u'))e^{-\alpha_w u'}\,du'\right]^{\frac{1}{4}}, \quad \text{(A.5)}$$

Appendix B

Solution for gray homogeneous solution

In this appendix, we present the analytical solution for a gray homogeneous medium in the three-plate configuration. The governing equation and the boundary conditions are presented in chapter 6 in section 6.5.1. The temperature profile in each domain is given by

$$\theta_1 = \frac{c_1 \mathrm{e}^{p_1 z}}{p_1} - \frac{c_2 \mathrm{e}^{-p_1 z}}{p_1} - \frac{\eta \psi_1 z}{(1+\chi_1)} + c_3, \tag{B.1}$$

$$\theta_2 = \frac{d_1 \mathrm{e}^{p_2 z}}{p_2} - \frac{d_2 \mathrm{e}^{-p_2 z}}{p_2} - \frac{\eta \psi_2 z}{(1+\chi_2)} + d_3. \tag{B.2}$$

Here, we write down the constants for a gray homogeneous medium. The unknown constants can be obtained by substituting the above temperature profile in the boundary conditions listed in chapter 6 and that results in 8 equations with 8 unknown constants. First, using the boundary conditions available for each domain, the solution for the temperature profile is obtained in terms of the unknown fluxes in each domain.

1. $c_2 = A_1\psi_1 + B_1$,
2. $c_3 = C_1\psi_1 + D_1$,
3. $c_1 = E_1\psi_1 + F_1$,
4. $d_2 = A_2\psi_2 + B_2$,
5. $d_3 = C_2\psi_2 + D_2$,
6. $d_1 = E_2\psi_2 + F_2$,

   Where

$$A_1 = \frac{\eta g p_1 (p_1 - 2\hat{\alpha}_1) - 2\hat{\alpha}_1 \eta \chi_1 (\mathrm{e}^{p_1 g} - 1)}{(1+\chi_1)\left[2p_1 \sinh p_1 g + 4\hat{\alpha}_1 \cosh p_1 g - 4\hat{\alpha}_1\right]},$$

$$B_1 = \frac{\theta_p p_1 (p_1 - 2\hat{\alpha}_1)}{\left[2p_1 \sinh p1g + 4\hat{\alpha}_1 \cosh p1g - 4\hat{\alpha}_1\right]},$$

$$C_1 = \frac{-4\hat{\alpha}_1(1+\chi_1)A_1 + 2\eta\hat{\alpha}_1\chi_1}{p_1(1+\chi_1)(p_1 - 2\hat{\alpha}_1)},$$

$$D_1 = \frac{-4\hat{\alpha}_1 B_1}{p_1(p_1 - 2\hat{\alpha}_1)},$$

$$E_1 = A_1 - C_1 p_1,$$

$$F_1 = B_1 - D_1 p_1,$$

$$A_2 = \frac{-\left[2\hat{\alpha}_2\eta\chi_2(\mathrm{e}^{p_2 g} - \mathrm{e}^{p_2}) + \eta p_2 \mathrm{e}^{p_2}(g-1)(p_2 + 2\hat{\alpha}_2)\right]}{(1+\chi_2)\left[2p_2 \sinh p_2(1-g) + 4\hat{\alpha}_2 \cosh p_2(1-g) - 4\hat{\alpha}_2\right]},$$

$$B_2 = \frac{p_2 \mathrm{e}^{p_2}(p_2 + 2\hat{\alpha}_2)(1-\theta_p)}{\left[2p_2 \sinh p_2(1-g) + 4\hat{\alpha}_2 \cosh p_2(1-g) - 4\hat{\alpha}_2\right]},$$

$$C_2 = \frac{+4\hat{\alpha}_2(1+\chi_2)\mathrm{e}^{-p_2} A_2 + 2\eta\hat{\alpha}_2\chi_2 +_2 (p_2 + 2\hat{\alpha}_2)}{p_2(1+\chi_2)(p_2 + 2\hat{\alpha}_2)},$$

$$D_2 = 1 + \frac{4\hat{\alpha}_2 B_2 \mathrm{e}^{-p_2}}{p_2(p_2 + 2\hat{\alpha}_2)},$$

$$E_2 = \frac{A_2(1+\chi_2)\mathrm{e}^{-p_2 g} + \eta g p_2 - C_2 p_2(1+\chi_2)}{(1+\chi_2)\mathrm{e}^{p_2 g}},$$

$$F_2 = \frac{\theta_p p_2}{\mathrm{e}^{-p_2 g}} + \frac{B_2 \mathrm{e}^{-p_2 g}}{\mathrm{e}^{p_2 g}} - \frac{D_s p_2}{\mathrm{e}^{-p_2 g}}.$$

The above constants are in terms of the unknown fluxes. We use the matching condition at the polythene sheet, to obtain these constants. For a semi-transparent polythene sheet the unknown constants are

Semi transparent plate:

$$\psi_1 = \frac{ab_{12} + a_{12} b}{a_{12} b_{11} + b_{12} a_{11}},$$

$$\psi_2 = \frac{ba_{11} - ab_{11}}{a_{12} b_{11} + b_{12} a_{11}},$$

where

$$a_{11} = E_1 \mathrm{e}^{p_1 g}\left(\frac{p_1}{\hat{\alpha}_1} + P\right) - A_1 \mathrm{e}^{-p_1 g}\left(\frac{p_1}{\hat{\alpha}_1} - P\right) + \frac{\eta P \chi_1}{1+\chi_1} - \frac{1}{1+\chi_1},$$

$$a_{12} = E_2 \mathrm{e}^{p_2 g}\left(\frac{p_2}{\hat{\alpha}_2} - P\right) - A_2 \mathrm{e}^{-p_2 g}\left(\frac{p_2}{\hat{\alpha}_2} + P\right) - \frac{\eta P \chi_2}{1+\chi_2} - \frac{1}{1+\chi_2},$$

$$a = -F_1 \mathrm{e}^{p_1 g}\left(\frac{p_1}{\hat{\alpha}_1} + P\right) + B_1 \mathrm{e}^{-p_1 g}\left(\frac{p_1}{\hat{\alpha}_1} - P\right) + F_2 \mathrm{e}^{p_2 g}\left(\frac{p_2}{\hat{\alpha}_2} - P\right) - B_2 \mathrm{e}^{-p_2 g}\left(\frac{p_2}{\hat{\alpha}_2} + P\right),$$

$$b_{11} = E_1 \mathrm{e}^{p_1 g}\left(\frac{p_1}{\hat{\alpha}_1} + q\right) - A_1 \mathrm{e}^{-p_1 g}\left(\frac{p_1}{\hat{\alpha}_1} - q\right) + q\eta\left(1 - \frac{1}{1+\chi_1}\right),$$

$$b_{12} = E_2 \mathrm{e}^{p_2 g}\left(\frac{p_2}{\hat{\alpha}_2} - a\right) - A_2 \mathrm{e}^{-p_2 g}\left(\frac{p_2}{\hat{\alpha}_2} + q\right) + q\eta\left(1 - \frac{1}{1+\chi_2}\right),$$

$$b = -F_1 \mathrm{e}^{p_1 g}\left(\frac{p_1}{\hat{\alpha}_1} + q\right) + B_1 \mathrm{e}^{-p_1 g}\left(\frac{p_1}{\hat{\alpha}_1} - q\right) - F_2 \mathrm{e}^{p_2 g}\left(\frac{p_2}{\hat{\alpha}_2} - q\right) + B_2 \mathrm{e}^{-p_2 g}\left(\frac{p_2}{\hat{\alpha}_2} + q\right),$$

Here $P = \dfrac{2\alpha_p}{2-\alpha_p}$ and Here $q = \dfrac{2(2-\alpha_p)}{\alpha_p}$.

Transparent plate $\alpha_p = 0$

- $\psi_1 = \dfrac{a_{12} b - a b_{12}}{a_{12} b_{11} - b_{12} a_{11}},$
- $\psi_2 = \dfrac{ba_{11} - ab_1 1}{a_{12} b_1 1 - b_{12} a_1 1},$

$$a_{11} = \eta + E_1 \mathrm{e}^{p_1 g} + A_1 \mathrm{e}^{-p_1 g} - \frac{\eta}{1+\chi_1},$$

$$a_{12} = \eta + E_2 \mathrm{e}^{p_2 g} + A_2 \mathrm{e}^{-p_2 g} - \frac{\eta}{1+\chi_2},$$

$$a = -(F_1 \mathrm{e}^{p_1 g} + B_1 \mathrm{e}^{-p_1 g} - F_2 \mathrm{e}^{p_2 g} - B_2 \mathrm{e}^{-p_2 g}),$$

$$b_{11} = \hat{\alpha_2}(E_1 P_1 \mathrm{e}^{p_1 g} - A_1 P_1 \mathrm{e}^{-p_1 g}),$$

$$b_{12} = \hat{\alpha_1}(E_2 \mathrm{e}^{p_2 g} - A_2 P_2 \mathrm{e}^{-p_2 g}),$$

$$b = \hat{\alpha_1}(F_2 P_2 \mathrm{e}^{p_2 g} - B_2 P_2 \mathrm{e}^{-p_2 g}) - \hat{\alpha_2}(F_1 P_1 \mathrm{e}^{p_1 g} - B_1 P_1 \mathrm{e}^{-p_1 g}) \ .$$

References

Abraha, M. G. & Savage, M. J. 2008 Comparison of estimates of daily solar radiation from air temperature range for application in crop simulations. *Agric Forest Meteorol* **148-3**, 401–416.

Abramowitz, M. & Stegun 1990 *Handbook of mathematical functions*. Dover.

Aczel, J. 1996 *Lectures on functional equations and their applications*. Academic Press.

Albani, F. 1951 Investigaciones sobre la distribución vertical de las temp. minimas en las capas de aire próximas al suelo. *Arch. Fitotécnico del Uruguay* **4**, 361–376.

Andre, J. C. & Lacarrère, P. 1980 Simulation dètaillèe de la couche limite atmosphèrique. comparison avec la situation des 2 et 3 juillet 1977 à voves. *La Mètèorologie* **22**, 5–49.

Andre, J. C. & Mahrt, L. 1981 The nocturnal surface inversion and influence of clear-air radiative cooling. *J. Atmos. Sci.* **39**, 864–878.

Arpaci, V. S. & Gozum, D. 1973 Thermal stability of radiating fluids: the bénard problem **16-5**, 581–588.

Aston, J. A. G., Chan, W. L., Moore, D. R. & Walton, I. C. 2000 Radiative transfer in a static model atmosphere. *Geophys. Astrophys. Fluid Dynmnics* **93** (3-4), 253–287.

Bader, D., Cove, C., Gutowski, W., Held, I., Kunkel, K., Miller, R., Tokmakian, R. & Zhang, M. 2008 Climate models: an assessment of strengths and limitations. *US Department of Energy Publications* p. 8.

Bdeoui, F. & Soufiani, A. 1997 The onset of rayleigh-bÃ©nard instability in molecular radiating gases. *Phys.Fluids* **9-12**, 3858–3872.

Bignell, K. 1970 The water-vapour infra-red continuum. *Quart.J.R.Met.Soc.* **96**, 390–403.

Bohren, C. F. & Clothiaux, E. 2006 *Fundamentals of atmospheric radiation*. Wiley. com.

Brawand, H. & Kohnke, H. 1952 Micro-climate and water vapor exchange at the soil surface. *Proc. Soil. Sci. Soc. Amer.* **16**, 195–198.

Brooks, D. L. 1950 A tabular method for the computation of temperature change by infrared radiation in the free atmosphere. *J.atmos.Sci* **7-5**, 313–321.

Brubaker, K. L. & Entekhabi, D. 1996 Analysis of feedback mechanisms in land-atmosphere interaction. *Water.Res.* **32-5**, 1343–1357.

Brunt, D. 1932 Notes on radiation in the atmosphere. i. *Quart.J.Roy.Meteor.Soc.* **58** (247), 389–420.

Businger, J. A., Wyngaard, J. C., Izumi, Y. & Bradley, E. F. 1971 Flux-profile relationships in the atmospheric surface layer. *Bound.-Lay. Meteorol.* **28-2**, 181–189.

Cess, R. D. 1974 Radiative transfer due to atmospheric water vapor: Global considerations of the earth's energy balance. *J.Quant.spectros.radiat.transfer* **14-9**, 861–871.

Chan, W. L., Moore, D. R. & Aston, J. A. G. 2000 Linear convective instability in a radiating model atmosphere. *Geophys. Astrophys. Fluid Dynmnics* **93** (3-4), 289–322.

Chandrasekhar, S. 1960 *Radiative transfer*. Dover.

Chandrasekhar, S. 1981 *Hydrodynamic and hydromagnetic stability*. Dover.

Chou, M. D. & Arking, A. 1980 Computation of infrared radiative cooling rates in water vapor bands. *J. Atmos. Sci.* **37-4**, 855–867.

Chou, M. D., Ridgway, W. L. & Yan, M. M. 1993 One-parameter scaling and exponential-sum fitting for water vapor and co_2 infrared transmission functions. *J. Atmos. Sci.* **50-14**, 2294–2303.

Christophorides, C. & Davis, S. H. 1970 Thermal instability with radiative transfer. *Phys.Fluids* **13**, 222.

Clarke, R. H., Dyer, A. J., Brook, R. R., Reid, D. G. & Troup, A. J. 1971 *The Wangara experiment: Boundary layer data*. CSIRO Australia.

Claude, E. & Guedalia, D. 1985 Influence of geostrophic wind on atmospheric nocturnal cooling. *J. Atmos. Sci.* **42**, 2695–2698.

Clough, S. A., Kneizys, F. X. & Davies, R. W. 1989 Line shape and the water vapor continuum. *Atmos. Environ. Res* **23-4**, 229–241.

Collins, W. D., Hackney, J. K. & Edwards, D. P. 2002 An updated parameterization for infrared emission and absorption by water vapor in the national center for atmospheric research community atmosphere model. *J.Geophys.Res* **107-D22**, 17.1–17.20.

Collins, W. D., Rasch, P. R., Boville, B. A., Hack, J. J., Mcaa, J. R., Williamson, D. L. & Briegleb, B. P. 2006 The formulation and atmospheric simulation of the community atmosphere model version 3 (cam3). *J.Climate* **19**, 2144–2161.

Corradini, C. & Severini, M. 1975 Laboratory experimental check of radiative air cooling theory. *Q. J. Roy. Meteorol. Soc.* **101**, 163â167.

Corrigan, C. E., Roberts, G. C., Ramana, M. V., Kim, D. & Ramanathan, V. 2008 Capturing vertical profiles of aerosols and black carbon over the indian ocean using autonomous unmanned aerial vehicles. *Atmos. Chem. Phys.* **8-3**, 737–747.

Devara, P. C. S. & Raj, P. E. 1993 Lidar measurements of aerosols in the tropical atmosphere. *Advances in atmospheric sciences* **10**, 369–378.

Duynkerke, P. G. 1999 Turbulence, radiation and fog in dutch stable boundary layer. *Bound.-Lay. Meteorol* **90**, 447–477.

Edwards, J. M. 2009a Radiative processes in the stable boundary layer: Part i. radiative aspects. *Bound.-Lay. Meteorol* **131**, 105–126.

Edwards, J. M. 2009b Radiative processes in the stable boundary layer: Part ii. the development of the nocturnal boundary layer. *Bound.-Lay. Meteorol* **131**, 127–146.

Ellingson, R. G., Ellis, J. & Fels, S. B. 1991 The intercomparison of radiation codes used in climate models : Longwave results. *J. Geo. Res.* **96-D5**, 8929–8953.

Elliott, W. P. 1963 The height variation of vertical heat flux near the ground. *Q. J. Roy. Meteorol. Soc.* **90-385**, 260–265.

Fels, S. B., Kiehl, J. T., Lacis, A. A. & Schwarzkopf, M. D. 1991 Infrared cooling rate calculations in operational general circulation models:comparisons with benchmark computations. *J. Geo. Res.* **96-D5**, 9105–9120.

F.Gerald, C. & Wheatley, P. O. 2003 *Applied Numerical Analysis*. Pearson.

Fleagle, R. G. 1953 A theory of fog formation. *J.Mar.Res* **12**, 43–50.

Fleagle, R. G. 1955 The temperature distribution near a cold surface. *J. atmos. Sci.* **13-2**, 160–165.

Frank, M. & Klar, A. 2011 *Radiative Heat Transfer and Applications for Glass Production Processes*. Springer Berlin Heidelberg.

Freeman, K. P. & Liou, K. N. 1979 Climatic effects of cirrus clouds. *Advances in geophysics.* **21**, 231–287.

Funk, J. P. 1960 Measured radiative flux divergence near the ground at night. *Q. J. Roy. Meteorol. Soc.* **86**, 383–389.

Gaevskaya, G. N., Kondrati'ev, K. Y. & Yakushevskaya, K. E. 1962 Radiative heat flux divergence and heat regime in the lowest layer of the atmosphere. *Archiv fü r Meteorologie, Geophysik und Bioklimatologie Serie B* **12,1**, 95–108.

Garand, L. 1983 Some improvements and complements to the infrared emissivity algorithm including a parameterization of the absorption in the continuum region. *J. Atmos. Sci* **40-1**, 230–243.

Garcia, V., Mira, M., Valor, E., Caselles, V., Coll, C. & Galve, J. M. 2009 Angular dependence of the emissivity of bare soils in the thermal infrared. In *Geoscience and Remote Sensing Symposium, 2009 IEEE International, IGARSS 2009*, , vol. 3, pp. III–133. IEEE.

Garratt, J. R. 1994 *The Atmospheric Boundary Layer*. Cambridge University Press.

Garratt, J. R. & Brost, R. A. 1981 Radiative cooling effects within and above the nocturnal boundayr layer. *J. Atmos Sci.* **38**, 2730–2746.

Geiger, R. 1995 *The climate near the ground*. Harvard University Press.

Gille, J. & Goody, R. M. 1964 Convection in a radiating gas. *J.Fluid.mech* **20-1**, 47–79.

Goody, R. M. 1956 The influence or radiative transfer on cellular convection. *J.Fluid.mech* **1**, 424–435.

Goody, R. M. 1964 *Atmospheric radiation*. Clarendon Press,Oxford.

Gopalakrishan, S. G., Sharan, M., McNider, R. T. & Singh, M. P. 1997 Study of radiative and turbulent processes in the stable boundary layer under weak wind conditions. *J. Atmos Sci.* **55**, 954–960.

Ha, K. J. & Mahrt, L. 2003 Radiative and turbulent fluxes in the nocturnal boundary layer. *Tellus* **55A(4)**, 317–327.

Hess, M., Koepke, P. & Schult., I. 1998 Optical properties of aerosols and clouds: The software package opac. *Bull. Am. Meteorol. Soc.* **79-5**, 831–844.

Hoch, S. W. 2005 Radiative flux divergence in the surface boundary layer, a study based on observations at summit, greenland. PhD thesis, Swiss Federal Institute of Technology ETH, Zurich, Zurich, Switzerland.

Hottel, H. C. & Egbert, R. B. 1941 The radiation of furnace gases. *Trans. ASME* **63**, 297–307.

Hutchison, J. E. & Richards, R. F. 1999 Effect of nongray gas radiation on thermal stability in carbon dioxide. *J.Thermophys Heat.tr.* **13-1**, 25–32.

José, A. S. & Cuenca, J. 1999 Angular variation of thermal infrared emissivity for some natural surfaces from experimental measurements. *App. Optics* **38** (18), 3931–3936.

Justin, C. P., Salvucci, G. D., Phillips, N. G. & Daley, M. J. 2009 Mechanisms of moisture stress in a mid-latitude temperate forest: Implications for feedforward and feedback controls from an irrigation experiment. *Ecol.Model.* **220**, 968–978.

Kaimal, J. C. & Finnigan, J. J. 1994 *Atmospheric Boundary Layer Flows: Their Structure and Measurement*. Oxford University Press.

Koračin, D., B.Grisogono & Subanovič, N. 1989 A model of radiative heat transfer effects in the atmospheric boundary layer. *Geofizika* **6,1**, 75–86.

Lacis, A. A. & Oinas, V. 1991 A description of the correlated k distribution method for modeling nongray gaseous absorption, thermal emission, and multiple scattering in vertically inhomogeneous atmospheres. *J.Geophys.Res.Atmospheres (1984–2012)* **96** (D5), 9027–9063.

Lake, J. V. 1956 The temperature profile above bare soil on clear nights. *Q. J. Roy. Meteorol. Soc.* **82**, 187–197.

Larson, V. E. 2000 Stability properties of and scaling laws for a dry radiative-convective atmosphere. *Q. J. Roy. Meteorol. Soc.* **126**, 145–171.

Larson, V. E. 2001 The effects of thermal radiation on dry convective instability. *Dyn. Atmos. Oceans* **34**, 45–71.

Lettau, H. H. 1979 Wind and temperature profile prediction for diabatic surface layers including strong inversion cases. *Bound.-Lay. Meteorol.* **17**, 443–464.

Lieske, B. J. & A.Stroschein, L. 1967 Measurements of radiative flux divergence in the arctic. *J. Clim. Appl. Meteorol.* **15,1-2**, 67–81.

Liou, K. N. 2002 *An introduction to atmospheric radiation*. Academic Pres, N.Y.

Liou, K. N. & Ou, S. C. 1981 Parameterization of infrared radiative transfer in cloudy atmospheres. *J. Atmos. Sci.* **38**, 2707–2716.

Liou, K. N. & Ou, S.-C. S. 1983 Theory of equilibrium temperatures in radiative-turbulent atmospheres. *J. atmos. Sci* **40** (1), 214–229.

Liou, K. N. & Sasamori, T. 1975 On the transfer of solar radiation in aerosol atmospheres. *J. Atmos. Sci.* **32**, 2166–2177.

Liou, K. N. & Wittman, G. D. 1979 Parameterization of the radiative properties of clouds. *J. Atmos.Sci.* **36** (7), 1261–1273.

Lützke, R. 1960 Unter welchen bedingungen hebt sich das nachtliche, temperatur minimum von der bodenoberflache ab? *Anggewandte Met.* **4**, 1–10.

Mahrt, L. & Vickers, D. 2006 Extremely weak mixing in stable conditions. *Bound.lay.meteorol.* **119-1**, 19–39.

McClatchey, R. A., Fenn, R. W., Selby, J. E. A., Volz, F. E. & Garing, J. S. 1972 The optical properties of the atmosphere. *AFCRL* **72**, –.

Morcrette, J. J. 1977 Calcul des flux infrarouges et des taux de refroidissement radiatif en atmosphère nuageuse. PhD thesis, University of Lille, France.

Mouli, M. C. 2007 Interaction between conduction, free convection and gas radiation. Master's thesis, Indian Institute of science, Bangalore, India.

Mukund, V. 2008 Field observations and laboratory simulation of the lifted temperature minimum. PhD thesis, Jawaharlal Nehru Centre for Advanced Scientific Research, Bangalore, India.

Mukund, V., Ponnulakshmi, V. K., Singh, D. K., Subramanian, G. & Sreenivas, K. R. 2010 Hyper-cooling in the nocturnal boundary layer: the ramdas paradox. *Phys.Scripta* **T142**, 014041.

Mukund, V., Singh, D. K., Ponnulakshmi, V. K., Subramanian, G. & Sreenivas, K. R. 2013 Field and laboratory experiments on aerosol-induced cooling in the nocturnal boundary layer. *Q.J.Roy.Meteor.Soc.* .

Narasimha, R. 1991 When and why air can be cooler than ground below: A theory for the ramdas effect. *J. Indian Inst. Sci.* **71**, 475–483.

Narasimha, R. 1994 The dynamics of the ramdas layer. *Curr. Sci.* **66**, 16–23.

Narasimha, R. & Vasudevamurthy, A. S. 1995 The energy balance in the ramdas layer. *Bound.-Lay. Meteorol* **76**, 307–321.

Nieuwstadt, F. T. M. 1984 The turbulent structure of the stable, nocturnal boundary layer. *J.atmos.sci* **41,14**, 2202–2216.

Nieuwstadt, F. T. M. & Tennekes, H. 1981 A rate equation for the nocturnal boundary-layer height. *J.atmos.sci* **38,7**, 1418–1428.

Nkemdirim, L. C. 1978 A comparison of radiative and actual nocturnal cooling rates over grass and snow. *J. Appl. Meteorol* **17-11**, 1643–1646.

Novotny, J. L. & Olsofka, F. A. 1970 The influence of a non-absorbing gas in a radiation-conduction interaction. *AIAA 5th Thermophysical Conference* .

Oke, T. R. 1970 The temperature profile near the ground on calm clear nights. *Q. J. Roy. Meteorol. Soc.* **96**, 14–23.

Penner, J. E., Chen, Y., Wang, M. & Liu, X. 2009 Possible influence of anthropogenic aerosols on cirrus clouds and anthropogenic forcing. *Atmos. Chem. Phys* **9**, 879–â896.

Prasanna, S. 2012 Studies on the effects of surface radiation and radiation in participating medium on natural convection. PhD thesis, Indian Institute of technology Madras, Bangalore, India.

Ptashnik, I. V., Shine, K. P. & Vigasin, A. A. 2011 Water vapour self-continuum and water dimers:1.analysis of recent work. *J.Quant.spectros.radiat.transfer* **112**, 1286–1303.

Ragothaman, S., Narasimha, R. & Vasudevamurthy, A. 2001 The dynamical behavior of the lifted temperature minimum. *Il Nuovo Cimento* **24**, 353–375.

Räisänen, P. 1996 The effect of vertical resolution on clear-sky radiation calculations: tests with two schemes. *Tellus* **48-3**, 403–423.

Raj, E. P., Devara, P. C. S., Maheskumar, R. S., Dani, K. K. & Saha, S. K. 2001 Spatio-temporal variations in lidar-derived aerosol concentrations at pune during indoex-ifp. *Curr. Sci.* **80**, 112–114.

Ramakrishna, T. V. B. P. S., Sharan, M., Gopalakrishnan, S. G. & Aditi 2003 Mean structure of the nocturnal boundary layer under strong and weak wind conditions: Epri case study. *J.Appl.meteorol.* **42**, 952–969.

Ramanathan, K. R. & Ramdas, L. A. 1935 Derivation of angstrom s formula for atmospheric radiation and some general considerations regarding nocturnal cooling of air layers near the ground. *Proc.Indian.Acad.Sci.* **11**, 822–829.

Ramanathan, V. 1976 Radiative transfer within the earth's troposphere and stratosphere: A simplified radiative-convective model. *J.Atmos.Sci* **33-7**, 1330–1346.

Ramanathan, V. & Downey, P. 1986 A nonisothermal emissivity and absorptivity formulation for water vapor. *J. Geo. Res* **91-D8**, 8649–8666.

Ramdas, L. A. & Atmanathan, S. 1932 The vertical distribution of air temperature near the ground during night. *Beitr. zur Geophysik* **37**, 116–117.

Raschke, K. 1957 Über das nächtliche temperaturminimum über nackten boden in poona. *Met. Rundschau.* **10**, 1–11.

Rissmann, J. 1998 Der einflußlangwelliger strahlungsprozesse auf das bodennahe temperaturprofil. PhD thesis, Institut für Meteorologie der Universita ät Leipzig, Leipzig, Germany.

Rodgers, C. D. 1967 The use of emissivity in atmospheric radiation calculations. *Q. J. Roy. Meteorol. Soc.* **93-395**, 43–54.

Rodgers, C. D. & Walshaw, C. D. 1966 The computation of infra-red cooling rates in planetary atmosphere. *Q. J. Roy. Meteorol. Soc.* **92**, 67–92.

Running, S. W., Justice, C. O., alomonson, V., Hall, D., Barker, J., Kaufmann, Y. J., Strahler, A. H., Huete, A. R., Muller, J. P., Vanderbilt, V., Wan, Z. M. & Teillet, P. 1994 Terrestrial remote sensing science and algorithms planned for eos/modis. *Int. J. Remote Sens.* **15-17**, 3587–3620.

Savijärvi, H. 2006 Radiative and turbulent heating rates in the clear-air boundary layer. *Q. J. Roy. Meteorol. Soc.* **132**, 147–161.

Savijärvi, H. 2009 Stable boundary layer: Parametrizations for local and larger scales. *Q. J. Roy. Meteorol. Soc.* **135**, 914–921.

Savijärvi, H. 2013 High-resolution simulations of the night-time stable boundary layer over snow. *Quart.J.Roy.Meteor.Soc.* .

Schaller, E. 1977 Time and height variability of the sensible heat flux in the surface layer. *Bound.Lay. Meteorol.* **11**, 329–354.

Schiesser, W. E. & Griffiths, G. W. 2009 *A compendium of partial differential equation models: method of lines analysis with Matlab*. Cambridge University Press.

Schimmel, W. P. 1969 Interferometric study of the interaction of gaseous radiation with conduction between parallel horizontal plates. PhD thesis, University of Notre Dame, Notre Dame, United States.

Schimmel, W. P., Novotny, J. L. & Olsofka, F. A. 1970 Interferometric study of radiation-conduction interaction. *Proc.4th int. Heat Transfer Conference* **3**.

Siegel, R. & Howell, J. R. 2002 *Thermal radiation heat transfer*. Taylor and Francis, N.Y. London.

Singh, D. K. 2013 The impact of aerosols and land surface properties on the lifted temperature minimum in the nocturnal atmospheric boundary layer â field and laboratory experiments. PhD thesis, Jawaharlal Nehru Centre for Advanced Scientific Research, Bangalore, India.

Siqueira, M. B. & Katul, G. G. 2010 A sensitivity analysis of the nocturnal boundary-layer properties to atmospheric emissivity formulations. *Bound.-Lay. Meteorol.* **134-2**, 223–242.

Snyder, W. C., Wan, Z., Zhang, Y. & Feng, Y. Z. 1998 Classification based emissivity for land surface temperature measurement from space. *Int.J. of remote sensing* **19**, 2753–2774.

Sparrow, E. M. & Cess, R. D. 1967 *Radiation Heat Transfer*. Brooks/Cole Publishing Co.

Spiegel, E. A. 1960 The convective instability of a radiating fluid layer. *Astrophys. J.* **132**, 716â728.

Steeneveld, G. J. 2007 Understanding and prediction of stable atmospheric boundary layers over land. PhD thesis, Wageningen Universiteit, Netherlands.

Stephens, G. L. 1978 Radiation profiles in extended water clouds. i: Theory. *J. Atmos. Sci.* **35**, 2111–2122.

Stephens, G. L. 1984 The parameterization of radiation for numerical weather predictions and climate models. *Mon. Weather. Rev.* **112**, 826–867.

Stephens, J. J. 1961 Spectrally averaged total attenuation,scattering,and absorption cross sections for infrared radiation. *J.Meteorol* **18**, 822–828.

Stull, R. B. 1988 *An introduction to boundary layer meteorology*. Springer.

Sun, J., Burns, S. P., Delany, A. C., Oncley, S. P., Horst, T. W. & Lenschow, D. H. 2003 Heat balance in the nocturnal boundary layer during cases-99. *J. Appl.Meteorol.* **42-11**, 1649–1666.

Sutton, O. G. 1953 *Micrometeorology*. McGraw-Hill, N.Y.

Tiwari, P. 2006 Laboratory simulation of lifted temeprature minimum. PhD thesis, Jawaharlal Nehru Centre for Advanced Scientific Research, Bangalore, India.

Turner, J. S. 1973 *Buoyancy Effects in Fluids*. Cambridge University Press.

Varghese, S. 2003 Band model computation of near-surface logwave fluxes. PhD thesis, Jawaharlal Nehru Centre for Advanced Scientific Research, Bangalore, India.

Varghese, S., Vasudevamurthy, A. S. & Narasimha, R. 2003b A fast accurate method of computing near-surface longwave fluxes and cooling rates in the atmosphere. *J. Atmos. Sci.* **60**, 2869–2886.

Vasudevamurthy, A. S., R.Narasimha & S.Varghese 2005 An asymptotic analysis of a simple model for the structure and dynamics of the ramdas layer. *Pure Appl. Geophys.* **162**, 1831–1857.

Vasudevamurthy, A. S., Srinvasan, J. & Narasimha, R. 1993 A theory of the lifted temperature minimum on calm clear nights. *Proc. Roy. Soc. Lond* **23**, 183–206.

Vincenti, W. G. & Traugott, S. C. 1971 The coupling of radiative transfer and gas motion. *Ann.Rev.Fluid.Mech.* **3** (1), 89–116.

Viskanta, R. & Mengüç, M. P. 1987 Radiation heat transfer in combustion systems. *Prog. Energ.Combust Sci.* **13** (2), 97–160.

Wang, K., Wan, Z., Wang, P., Sparrow, M., Liu, J., Zhou, X. & Haginoya, S. 2005 Estimation of surface longwave radiation and broadband emissivity using moderate resolution imaging spectroradiometer (modis) land surface temperature/emissivity products. *J. Geophys. Res.* **110**, D11109.

Wang, W., Liang, S. & Augustine, J. A. 2009 Estimating high spatial resolution clear-sky land surface upwelling longwave radiation from modis data. *IEEE Trans. Geosci. Remote Sens.* **47**, 1559–1570.

Welch, R. & Zdunkowski, W. 1976 A radiation model of the polluted atmospheric boundary layer. *J. Atmos. Sci.* **33**, 2170–2184.

Whitehead, J. A. & Chen, M. M. 1970 Thermal instability and convection of a thin fluid layer bounded by a stably stratified region. *J.Fluid.Mech* **40**, 549–576.

Yu, T. W. 1978 Determining height of the nocturnal boundary layer. *J.Appl.Meteorol.* **17**, 28–33.

Zdunkowski, W. 1966a The nocturnal temperature above the ground. *Beitr.Phys.Atmos* **39**, 247–253.

Zdunkowski, W., Henderson, D. & Hales, J. 1966 The effect of atmospheric haze on infrared radiative cooling rates. *J. Atmos. Sci.* **23**, 297–304.

Zdunkowski, W. & Johnson, F. G. 1965 Infrared flux divergence calculations with newly constructed radiation tables. *J. Appl.Meteorol.* **4-3**, 371–377.